Surface-Enhanced Spectroelectrochemistry using Synchrotron Infrared Radiation

A dissertation submitted to the
College of Graduate and Postdoctoral Studies
in partial fulfillment of the requirements
for the degree of Doctor of Philosophy
in the Department of Chemistry
University of Saskatchewan
Saskatoon

By
Tyler A. Morhart

Permission to Use

In presenting this dissertation in partial fulfillment of the requirements for a Postgraduate degree from the University of Saskatchewan, I agree that the Libraries of this University may make it freely available for inspection. I further agree that permission for copying of this dissertation in any manner, in whole or in part, for scholarly purposes may be granted by the professor or professors who supervised my dissertation work or, in their absence, by the Head of the Department or the Dean of the College in which my dissertation work was done. It is understood that any copying or publication or use of this dissertation or parts thereof for financial gain shall not be allowed without my written permission. It is also understood that due recognition shall be given to me and to the University of Saskatchewan in any scholarly use which may be made of any material in my dissertation.

Disclaimer

Reference in this dissertation to any specific commercial products, process, or service by trade name, trademark, manufacturer, or otherwise, does not constitute or imply its endorsement, recommendation, or favoring by the University of Saskatchewan. The views and opinions of the author expressed herein do not state or reflect those of the University of Saskatchewan, and shall not be used for advertising or product endorsement purposes.

Requests for permission to copy or to make other uses of materials in this dissertation in whole or part should be addressed to:

Department of Chemistry
University of Saskatchewan
110 Science Place
Saskatoon, Saskatchewan
Canada
S7N 5C9

OR

Dean
College of Graduate and Postdoctoral Studies
University of Saskatchewan
116 Thorvaldson Building, 110 Science Place
Saskatoon, Saskatchewan S7N 5C9 Canada

Abstract

Electrochemical reactions are inherently heterogeneous, occurring at the interface between a solid electrode and an electrolyte solution. Therefore, detailed mechanistic understanding requires the electrode/solution interface (ESI) to be interrogated. Doing so with spectroelectrochemical techniques generally encounters several analytical challenges. Sampling the ESI requires a surface-sensitive spectroscopy capable of addressing a buried interface, placing strong limitations on photon energy and spectroelectrochemical cell design. Furthermore, dynamic measurements are fundamentally limited by the finite rise time of the electrode. For many important processes with characteristic timescales in the milli- to microsecond regime, achieving a suitably low rise time requires the use of an electrode with critical dimensions in the hundreds of micrometers, i.e. a microelectrode.

In this thesis, I develop the spectroscopic platform necessary to perform surface-sensitive, time-resolved infrared measurements in the milli- to microsecond regime. I will make the case that an infrared spectroelectrochemical technique, namely attenuated total reflectance surface-enhanced infrared absorption spectroscopy (ATR-SEIRAS), is applicable because it is intrinsically surface-sensitive, yields detailed information on molecular structure, and is compatible with a range of electrocatalytic metals. I will show that the small size of the microelectrode requires an unconventional infrared source, namely highly focused synchrotron radiation.

This thesis will present the characterization of a new internal reflection element which is fully compatible with ATR-SEIRAS and easily amenable to microfabrication. A custom horizontal microscope endstation will be developed at the mid-IR beamline at the Canadian Light Source. Its general utility beyond the primary goal of this thesis will be demonstrated with imaging experiments of a simple interfacial reaction in a microfluidic device. Finally, a 500 µm wide linear microelectrode compatible with ATR-SEIRAS will be fabricated and preliminary kinetic measurements of a model electrochemical process, namely the potential-induced desorption of 4-methoxypyridine, will be discussed.

Acknowledgements

I am immensely grateful to have worked with Prof. Ian Burgess during the course of my graduate studies. Although the late nights at CLS and soul-searching beamtime post-mortems have driven us close to madness, I am thankful for your boundless enthusiasm for this work.

The day-to-day work of science is so much easier when you do it with friends. To the current and past members of the Burgess group, thank you all for your curiosity and humour. During my graduate work, the group is/was: Amanda Quirk, Jessica Sigrist, April Woods, Osai Clarke, Kaiyang Tu, Ian Andvaag, Bipin Unni, Burke Barlow, Sajna Simon, Bao Guo, Mike Lardner, Erick Lins, Anthony Ojukwu, Theo Olumorin, Melissa Shaw, David Chukwu, Grace Flaman, Abby Unrau, Jarvis Stobbs, and Nicole Boyle. Special mention for Kaiyang Tu, who can literally run synchrotron experiments in his sleep, and who was instrumental in obtaining results for the final chapter.

Thanks also to the brilliant technical staff who have worked in the Physics Machine Shop over the years: Ted Toporowski, Blair Chomyshyn, Jill Cornish, James McGregor, Dustin Archdekin, and Ian Knutson. Thank you for treating my ridiculous designs with more respect than they deserved. My thanks as well to glassblower Rick Elvin, who never failed to amaze me with his skill and precision, and Garth Perry, for fielding electronics questions.

This project, like many at the University of Saskatchewan, is a synchrotron project. Walking into a billion dollar facility and getting anything done is only possible with the help of excellent beamline staff. My thanks to Scott Rosendahl, Stuart Read, and Tim May of the mid-IR beamline, and Garth Wells and Michael Jacobs of the SyLMAND beamline. Thanks as well to Ferenc Borondics who is now at SOLEIL. Thanks are also due to Jenni Briggs of PIKE Technologies for excellent input on the VeeMAX III optics and Lorenz Sykora of IRUBIS GmbH for his discussions of the microgrooved Si wafers for ATR-FTIR.

To my advisory committee, Professors Tom Ellis, Tim Kelly, and Sven Achenbach, I thank you for your thoughtful input and questioning as this project has progressed. I wish to specifically note the excellent input on microfabrication in SyLMAND that I received from Prof. Sven Achenbach.

To my parents, Shelly and Kevin: without your love and encouragement, none of this would have been possible. If I have any success, it is only because of the traits and skills I learned from the two of you. And love and thanks as well to my sister Danni - yes, yes, I know you save people's lives and all that but come on, I did some really cool stuff. Just look at the pictures. And finally, to Robyn, Fallon, and Jordan - thank you for bringing grace and acceptance to our family merger.

As I write these lines in the spring of 2021, the COVID-19 pandemic is (hopefully) coming to an end, with widespread deployment of vaccines across Canada and other wealthy nations. Although this bizarre time has seemed designed to test the bonds between loved ones, I could think of no better person to be trapped at home with than my wife, Rosalyn. Words fail to describe someone as surprising and dynamic as you. For your kindness, generosity of spirit, and brilliance, I give you my unending gratitude and love.

For my mother, Shelly Jean Morhart, and the people who miss her.

Contents

Permission to Use i

Abstract iii

Acknowledgements iv

Contents vi

List of Tables ix

List of Figures x

List of Abbreviations xvi

1 Introduction 1
- 1.1 The Central Role of the Electrode-Solution Interface . . . 1
- 1.2 The Challenge of Studying the ESI . . . 3
- 1.3 Thesis Scope . . . 5

2 Background 7
- 2.1 Introduction . . . 7
- 2.2 Infrared Spectroscopy . . . 7
  - 2.2.1 Theory . . . 7
  - 2.2.2 Instrumental Aspects of Fourier-Transformed Infrared Spectroscopy . . . 10
  - 2.2.3 Sampling Methods . . . 14
  - 2.2.4 Time-Resolved Methods . . . 16
- 2.3 Electrochemistry . . . 17
  - 2.3.1 Introduction . . . 17
  - 2.3.2 The Electrode/Solution Interface . . . 17
  - 2.3.3 Electrochemical Measurements . . . 19
  - 2.3.4 Microelectrodes . . . 20
  - 2.3.5 Photolithography as a Fabrication Method for Microelectrodes . . . 22
- 2.4 Spectroelectrochemistry with ATR-SEIRAS . . . 23
  - 2.4.1 Spectroelectrochemistry . . . 23
  - 2.4.2 Introduction to ATR-SEIRAS . . . 24
  - 2.4.3 Theory . . . 27
  - 2.4.4 Experimental Setup . . . 29
  - 2.4.5 Thin Film Electrodes . . . 31
  - 2.4.6 Non-Faradaic Adsorption of 4-Methoxypyridine as an ATR-SEIRAS Probe System . . . 34

3 Synchrotron-Sourced ATR-SEIRAS with an Infrared Microscope 37
- 3.1 Introduction . . . 37
- 3.2 Experimental . . . 39
  - 3.2.1 Materials . . . 39
  - 3.2.2 Spectroelectrochemical Cell Design . . . 39
  - 3.2.3 ATR-SEIRAS Thin-Film Preparation . . . 41
  - 3.2.4 Spectroelectrochemical Measurements on Large Au Thin-Film Electrodes . . . 42
  - 3.2.5 Optical Modelling . . . 43
  - 3.2.6 Determination of Au Surface Roughness . . . 43
  - 3.2.7 Microelectrode Preparation . . . 43

3.2.8 Spectroelectrochemistry with Individually Addressable Microelectrodes . . . 44
3.3 Results and Discussion . . . 45
3.3.1 Estimation of Beamspot Size by 3D Geometric Ray-Tracing . . . 45
3.3.2 Observation of Femtomole Quantities of Adsorbed MOP . . . 48
3.3.3 Challenges in Transitioning to Microelectrodes . . . 50
3.4 Conclusions . . . 52

4 Microgrooved Si Internal Reflection Elements for ATR-SEIRAS 54
4.1 Introduction . . . 54
4.2 Experimental . . . 56
4.2.1 Materials . . . 56
4.2.2 Spectroelectrochemical Cell Design . . . 56
4.2.3 ATR-SEIRAS Thin-Film Electrode Preparation . . . 57
4.2.4 Spectroelectrochemical Measurements . . . 57
4.2.5 Geometric Ray Tracing . . . 58
4.3 Results and Discussion . . . 59
4.3.1 Optical Properties of Microgrooved Si IREs . . . 59
4.3.2 Electrochemical ATR-SEIRAS measurements . . . 61
4.3.3 Performance Comparison between Si hemisphere and Microgrooved IRE . . . 66
4.4 Conclusions . . . 66

5 Design and Commissioning of a Horizontal ATR Microscope Endstation 69
5.1 Introduction . . . 69
5.2 Experimental . . . 70
5.2.1 Materials . . . 70
5.2.2 Fabrication of a Model Microfluidic Device and Transmission Slit . . . 71
5.2.3 Spectroscopic Measurements . . . 71
5.2.4 Total Least Squares Deconvolution . . . 72
5.2.5 Optical Modelling . . . 73
5.3 Results and Discussion . . . 73
5.3.1 Design Considerations of the Horizontal ATR Microscope Endstation . . . 73
5.3.2 Quantification of Beamspot Size . . . 77
5.3.3 Single-Point Measurements with a Sub-Millimeter Beamspot . . . 78
5.4 Conclusions . . . 81

6 Chemical Imaging of a Simple Interfacial Reaction on Flow 83
6.1 Introduction . . . 83
6.2 Experimental . . . 85
6.2.1 Materials . . . 85
6.2.2 Microfluidics Device Fabrication . . . 85
6.2.3 ATR-FTIR Imaging . . . 86
6.2.4 *In Situ* Microfluidic Device Operation . . . 87
6.3 Results and Discussion . . . 87
6.3.1 Characterization of Imaging Capabilities . . . 87
6.3.2 Steady-State Chemical Imaging in a Microfluidic Channel . . . 92
6.4 Conclusions . . . 93

7 ATR-SEIRAS Microspectroscopy of a Model Electrochemical Process on a Microelectrode 96
7.1 Introduction . . . 96
7.2 Experimental . . . 97
7.2.1 Materials . . . 97
7.2.2 Microelectrode Template Fabrication . . . 98
7.2.3 Static Spectroelectrochemical Measurements and *in situ* Au Deposition . . . 98
7.2.4 Step-Scan Measurements . . . 100

7.3 Results and Discussion . . . 100
7.3.1 Cyclic Voltammetry of Early-Stage Au Electrodeposition on the Microband Electrode 100
7.3.2 Spectroscopic Monitoring of ATR-SEIRAS Activity During Electrodeposition . . . 101
7.3.3 Demonstration of Spatially-Resolved ATR-SEIRAS Measurement of a Microband Electrode . . . 103
7.3.4 Time-Resolved Spectroelectrochemistry with Step-Scan FTIR . . . 105
7.4 Conclusions . . . 109

8 Conclusions and Future Work **111**
8.1 Conclusions . . . 111
8.2 Future Work . . . 113
8.2.1 Technical Developments . . . 113
8.2.2 Static and Dynamic Spectroelectrochemistry . . . 114
8.2.3 Electrochemical Microfluidics . . . 116

References **117**

Appendix A Magnification in Macro- and Micro-ATR Experiments **131**
A.1 Introduction . . . 131
A.2 Definitions . . . 131
A.3 Optical Geometries in Micro- and Macro-ATR . . . 132
A.3.1 Micro-ATR . . . 132
A.3.2 Macro-ATR . . . 133
A.3.3 Summary of the Differences between Macro- and Micro-ATR . . . 136
A.4 Magnification in This Thesis . . . 136

List of Tables

2.1 Selected areas of application for ATR-SEIRAS 25
2.2 Selected normal modes of 4-methoxypyridine observed in ATR-FTIR measurements 36

List of Figures

1.1 a) Simplified schematic of a direct-methanol fuel cell. At right, methanol (CH_3OH) in electrolyte solution is fed to the anode where it is oxidized, liberating electrons and protons. Electrons are captured by an external circuit to do useful work, while protons diffuse across a polymer electrolyte membrane (middle). At left, oxygen is reduced at the cathode to water. b) A microscopic illustration of the reaction occuring at the electrode-solution interface of the anode. Methanol and water react at the surface of precious metal catalyst nanoparticles. The reaction mechanism and intermediates, and therefore the number electrons extracted per methanol n, depend strongly on fuel cell operating conditions and catalyst design. 2

1.2 The ATR-SEIRAS method. a) A macroscopic view of the experimental setup. The infrared beam passes through an infrared-transparent prism and is totally internally reflected at the electrode/solution interface. The solution-facing side of the prism is coated with a nanostructured metal thin film electrode. b) Microscopic view of ATR-SEIRAS. Molecules are shown adsorbed at the surface of the metal thin film. Infrared light couples with the metal film resulting in increased signal strengths from surface adsorbed molecules. 4

2.1 Molecular vibration illustrated with the simple harmonic oscillator model, shown here with the stretching mode of HCl driven by infrared radiation. The H-Cl bond is shown displaced to a new internuclear displacement r from its equilibrium bond length r_e. By definition for this molecule, q is along the molecular bond axis. 8

2.2 Energy levels of a simple harmonic oscillator superimposed on a parabolic potential. 8

2.3 a) Schematic of a Michelson interferometer. b) Detector response to monochromatic radiation passing through a Michelson interferometer as a function of optical path difference. c) As b) but with polychromatic light. The oscillating signal now decays rapidly at large OPD. 11

2.4 Simplified construction of *etendue*, $G = S\Omega$. The source area S radiates light which is captured in the solid angle Ω, in this case a spherical cap. Ω is related to the emission angle, θ. 13

2.5 Brilliance curves for synchrotron radiation and conventional globar i.e. a blackbody radiator. The Mid-IR wavelength range is approximately from 10 to 3 µm. The brilliance of the synchrotron source is uniformly higher than that of the globar. Insets visualize source emission. Adapted from reference 34. 13

2.6 FT-IR sampling methods with generalized sample materials. Refractive index n_1 is often that of air, but for buried interfaces n_1 will be that of the solvent. a) Transmission mode. The IR beam is incident on a sample material with complex refractive index n_2 which absorbs some light. b) External reflection mode. The IR beam is reflected off the surface of the material. c) Internal reflection mode. The IR beam travels through the material with refractive index n_2, generally chosen to be IR-transparent, and reflects off the interface shown at top, probing a small region of the sample placed at that interface. 15

2.7 Attenuated total reflection. a) Instead of probing the sample material with complex refractive index n_1, the IR beam travels through an IR-transparent crystal (n_2) and undergoes total internal reflection at the principal reflecting plane. b) The evanescent wave penetrates into the sample medium, decaying exponentially. c) Schematic of a common optical accessory for ATR experiments (PIKE VeeMAX III). The central mirrors move up and down (symbolized by arrows,) dynamically adjusting the AOI. The accessory is approximately 30 cm on a side and fits in the sample compartment of a standard laboratory FT-IR instrument. 16

2.8 The electrode-solution interface, ESI. Anions (dark circles with $-$) are specifically adsorbed alongside a layer of solvent molecules (open white circles). Solvated cations (white circles with $+$) occupy the diffuse part of the double layer. Adapted in part from reference 2 18

2.9 A typical three-electrode cell configuration. The working, counter, and reference electrodes are shown immersed in the electrolyte. The solution may be sparged with inert gas to remove dissolved oxygen and maintain an inert atmosphere in the cell; components necessary for this are not shown. 19

2.10 Double layer charging. a) An RC equivalent circuit used to model the electrical double layer. b) Plot of potential realised at the electrode-solution interface as a function of time, depicting an ideal instantaneous step and cases where RC is small and large. 20
2.11 The ATR-SEIRAS method. a) A macroscopic view of the experimental setup. The infrared beam passes through an infrared-transparent prism and is totally internally reflected at the electrode/solution interface. The solution-facing side of the prism is coated with a nanostructured metal thin film electrode. b) Microscopic view of ATR-SEIRAS. Molecules are shown adsorbed at the surface of the metal thin film. Infrared light couples with the metal film resulting in increased signal strengths from surface adsorbed molecules. 24
2.12 Dependence of SEIRAS signal intensity on angle of incidence. SEIRAS enhancement peaks at high AOI. Adapted from reference 18. 27
2.13 Schematic of the Bruggeman effective medium used by Osawa to describe the mechanism of ATR-SEIRAS. 28
2.14 SEIRAS selection rule. At left, a horizontal dipole p is shown which induces an image dipole p_{img} of equal magnitude but opposite direction. The net dipole is zero and no SEIRAS signal is observed. At right, the image dipole is parallel and a net dipole exists, rendering the signal observable. 29
2.15 Schematic of the glass castle ATR-SEIRAS cell, shown mounted on the variable angle ATR accessory. 30
2.16 Two modes of MOP adsorption on Au surfaces. 34

3.1 Comparison of reflection versus transmission geometry. a) A 15× Schwarzchild objective operating in reflection mode. b) The achievable AOI is too low for ATR-SEIRAS. b) Transmission. The hemisphere is rotated by 90° so that the principal reflecting plane is parallel with the optical axis. While operating the microscope in transmission mode, the beampath through the Si hemisphere undergoes total internal reflection. The AOI is much higher than in a) and is suitable for ATR-SEIRAS. 38
3.2 Experimental geometry of the ATR-SEIRAS experiment using the FT-IR microscope. a) Photograph of the Hyperion FT-IR microscope. The white arrow indicates the sample stage where the spectroelectrochemical cell was placed. b) Cross section of the Schwarzchild objectives and the cell at focus. 40
3.3 Spectroelectrochemical cell design for ATR-SEIRAS compatible with the FT-IR microscope at the Mid-IR beamline. Component numbering is discussed in the main text. 41
3.4 Cyclic voltammogram of the Au film electrode in 0.1 M $HClO_4$. Scan rate = 20 $mV\,s^{-1}$ . . . 43
3.5 Custom-machined Si spherical segment used in microelectrode experiments. 44
3.6 Ray-tracing simulation setup. 45
3.7 Power falling on the detector as a function of displacement from $(x, y, z) = (0, 0, 0)$. 46
3.8 Ray-tracing simulation of beamspot at the detector under "perfect alignment" (left) and maximum counts (right). 46
3.9 Ray-tracing simulation of beamspot at the detector for two cases. Top (a) and (b) depicts the half-blocked beam without the hemisphere present, and bottom (c) and (d) with the hemisphere in the beampath. (d) Shows the shape of the focused spot on the principal reflecting plane of the hemisphere. 47
3.10 Ray-tracing simulation of beamspot at the detector under "perfect alignment" (left) and maximum counts (right). 48
3.11 Spectral noise as a function of the nominal radius of the focused beamspot illuminating the principal reflecting plane. Noise is calculated as standard deviation of a 100% transmission line. 49
3.12 ATR spectrum of 0.1 M aqueous MOP on the unmodified Si hemisphere (top, black) and potential difference absorbance ATR-SEIRAS spectra of surface-adsorbed MOP. Coloured spectra are labelled with their nominal spot radius. 50
3.13 Signal-to-noise ratio of the C-O-C asymmetric stretch at 1305 cm^{-1}as a function of nominal spot radius. 51

3.14 a) Photograph of multiple individually addressable microband electrodes prepared on the Si spherical segment optic. b) An optical micrograph collected at the region indicated with a white arrow in a). In this image, the Au microbands appear light orange. 52

4.1 Schematic of the microgrooved IRE. a) Isometric drawing showing the dimensions of the IRE and a cross-section revealing the grooves. Infrared radiation is incident from the groove side. b) Cross-section showing the groove angle, crystallography, and position of sample material. . 55

4.2 Cross section of the modified spectroelectrochemical cell for the microgrooved IRE. The inset is an exploded view showing the IRE as it is sandwiched between the wafer holder (bottom) and the teflon liquid cup (top). Numbering is discussed in the text. 57

4.3 Cross section of a single groove showing the definition of angles used in this chapter. 59

4.4 Infrared transparency of a conventional 25 mm diameter Si hemisphere and a microgrooved IRE at $AOI = 55^{\circ}$. Spectra are referenced to the reflected spectrum from a gold mirror. . . . 60

4.5 Comparison of ATR spectra collected with a hemisphere (black) and a microgrooved IRE (red). The shorter pathlength of the microgrooved IRE improves signal-to-noise at low frequencies. . 61

4.6 Variation of optical throughput as a function of AOI using a Si hemisphere. Single beams are shown at left and the maximum intensity at about 1750 $cm^{-1}$is plotted at right. 62

4.7 Polarisation dependence for reflection at the Si/air interface of a microgrooved IRE. Angles are defined in Figure 4.3. 63

4.8 ATR-SEIRAS spectra of MOP obtained on microgrooved IRE. a) Potential difference absorbance spectra collected at various AOI. Reference and sample spectra were collected at -700 and +200 mV, respectively. b) Signal-to-noise ratio of the C-O-C asymmetric stretching mode at approximately 1310 $cm^{-1}$with a dotted line fit to guide the eye. 64

4.9 Two-dimensional geometric ray-tracing of light incident on the wafer at three different AOI. Rays are incident from the left and reflect off a simple mirror. The proportion of rays undergoing double bounces increases with AOI. 65

4.10 Ray diagram of beam projected on wafer. 65

4.11 Comparison of ATR-SEIRAS spectra of MOP using the 25 mm diameter Si hemisphere (red) and microgrooved IRE (black). Spectra were collected with AOI = 55° for the microgrooved IR and 68° for the hemisphere. 67

5.1 Schematic of the open-channel microfluidic device. 71

5.2 Picture of the 3D ray-tracing simulation geometry. The beam is generated at left and is focused onto the microgrooved IRE by a BaF_2 lens (blue) and then is collimated by an equivalent lens before being focused onto the detector. The detector size is matched to the MCT/A detector used in this chapter. Rays are colour-coded by intersection for clarity. 74

5.3 Two-dimensional ray-tracing of a Schwarzchild objective (not to scale) in reflection mode with a) a flat mirror at the sample position and b) a microgrooved IRE placed such that the incident radiation is focused on the principal reflecting plane. The blue rays in (b) indicate returning rays which are off-centre and do not reach the detector. 74

5.4 Left: CAD drawing of the horizontal ATR microscope. The red arrow indicates the direction that IR is incident. The inset depicts the sampling optics and the sample holder, which is compatible with the microfluidic devices used in this chapter and Chapter 6 and the spectroelectrochemical cell used in Chapter 7. The IRE is mounted such that the grooved side faces down (negative z-axis) toward the incident beam. Right: schematic of optical layout 75

5.5 Determination of the beamspot profile at focus with a slit. a) Schematic of the experiment showing the focusing beam incident on a CaF_2 wafer with a 400 µm wide transmission slit in an otherwise Au-coated surface. b) Profile of the transmitted intensity falling on the detector. c) Recovered beam profile (black dots) after total least squares deconvolution. The Gaussian fit (solid red line) has FHWM = 130 µm. 77

5.6 a) The microgrooved IRE showing the experimental geometry with the beam incident on a single groove. b) Detected power as a function of IRE translation along the x and y coordinates. c) ATR experiment showing the OH-stretch and hydrocarbon bands of ethanol plotted as a function of y position. The variation in the OH-stretching mode is co-plotted in red alongside the detected power in (b). 79

5.7 3D raytracing depicting the beampath through the microgrooved IRE. Note that the coordinate system is the same as that used in Figure 5.2, and here the z direction is equivalent to the y direction in other figures. a) Position 1, where the IRE is placed at $z = 0$ µm and maximum intensity falls on the detector. The majority of rays undergo single reflection. b) Position 2, $z = +400$ µm (approximately one half of a groove period) and minimum intensity falls on the detector. The majority of rays undergo multiple internal reflections. c) Normalized intensity falling on the detector as a function of translation along y. The total range of z is 700 µm, or one groove period. A sinusoidal oscillation is observed which matched the experiment shown in Figure 5.6. 80

5.8 a) Schematic of the 400 µm-wide water-filled microfluidic channel patterned in 10 µm thick layer of SU-8. b) Peak ATR absorbance of characteristic H_2O (blue) and SU-8 (red) as a function of x translation. The deconvolved beam profile is shown as an inset and has FWHM = 70 µm. c) Representative spectra at the positions marked in b) with arrows. Spectral features from water and SU-8 are marked in blue and red, respectively. 81

6.1 Modified HATR end station modified for chemical imaging. a) CAD image with mirrors labelled and the focal plane array's position indicated. b) Plan view of the horizontal microscope. 87

6.2 Illumination of the FPA detector by placing a mirror at the sample positions. Axes are labelled with pixel number. a) Signal intensity calculated by integrating the single beam intensity around 3100 cm^{-1}. b) Standard deviation of the noise in the same region as (a). c) The signal-to-noise ratio calculated form the preceding images. 88

6.3 External reflection imaging of USAF target. a) Simplified beampath depicting image compression along the y axis. The IR beam (pink rays) is incident from left on the USAF target at an AOI $\theta = 50°$. The beam is projected along the y-direction into an elliptical form with semiaxis d'. b) Illustration of the effect of off-normal illumination. In the top image, the beam samples an extended area. The reflected beam is compressed along the y-axis, resulting in apparent image compression at the detector. c) Optical micrograph of the USAF target group 2 element 5 imaged in (d). Reflected power image of group 2 element 5 in the USAF target. 89

6.4 c) Cartoon of the microgrooved IRE decorated with a photoresist checkerboard. b) SEM image of the fabricated checkerboard. The square voids in the photoresist are visible with slight shadows in them. c) Full absorbance image of water in the open voids of the checkerboard. The image was obtained by integrating the OH-stretching mode of water. 90

6.5 Cropped and rotated section of Figure 6.4c showing the image formed from a single groove period. Three regions of interest (ROI) are indicated on the figure. The optical paths leading to the three ROI are explained in Figure 6.6. 90

6.6 Geometric ray-tracing through multiple grooves. The three ROI from 6.5 are shown to arise from differing paths through (or off) the microgrooved IRE. ROI1 arises from light undergoing a single bounce to interrogate the primary imaged area, but light in ROI2 results from the overlap of multiple internal reflections which image primary and secondary areas. ROI3 comes from external reflection on the terraces and carries no analytical signal. 91

6.7 ATR imaging of the microfluidic device. a) Schematic of the co-flow channel employed in this chapter. The white rectangle indicates the area imaged in panel b). The inset shows a photograph of the finished device. b) Composite colour-mapped image of H/D exchange in the microchannel under flow. From left to right, integrated band intensities are colour-mapped as follows: H_2O - blue, HOD - orange, D_2O - red. Pixels with no analytical signal are shown in grey. The region shown was extracted from ROI1 on the detector. c) Representative spectra from locations marked with arrows. The asterisk denotes the characteristic H-O-D bending mode. d) Profiles extracted by integrating the relevant bending modes along the line defined by the arrows in (b). 92

6.8 Geometric ray-tracing with light incident at 55°. With a sufficiently focused small beam, all rays undergo a single bounce through one groove. 94

7.1 Schematic of the microband electrode layout (white) on the microgrooved Si IRE (grey). The dotted circle represents the area which is exposed to electrolyte solution in the assembled spectroelectrochemical cell. 98

7.2 Spectroelectrochemical cell for use with microgrooved IREs on the HATR endstation. a) Cross-section illustration of the complete cell, with numbering indicating critical components. b) Detailed view of the region surrounding the microgrooved IRE, indicating the method of electrical contact and the positioning of the incoming IR beam. 99

7.3 Cyclic voltammetry of ITO microband electrode during Au electrodeposition. 100

7.4 a) Depiction of the procedure used to find the microband. A section of the microgrooved IRE is shown with the beam incident on a single groove. The ITO microelectrode is shown in purple. b) Plot of absorbance difference, $\Delta(Absorbance)$, at 1250 cm^{-1}versus x (along a groove face). The strong change in absorbance at $x = 13.5$ mm indicates that the beam is illuminating the microelectrode as its potential is modulated. 102

7.5 *In situ* electrodeposition of Au nanoparticles followed by ATR-SEIRAS. a) Absorbance spectra collected during the electrodeposition process. Growth in vibrational peaks of MOP over time indicate the increasing signal enhancement of the SEIRAS-active nanoparticle film. b) Peak height of the C-O-C asymmetric stretch (marked with an asterisk in (a)) with deposition time. 103

7.6 a) Potential difference absorbance measurements collected at varying positions across the width of the microband. Spectra on the microband are coloured red, while those off the microband are coloured grey. b) The peak of the C-O-C asymmetric bend as a function of position across the width of the band. 104

7.7 SEM micrograph showing the edge of the microband. The ITO microband is at the top of the image and the Si substrate is at the bottom. The region very near the edge (approximately 15 um) has a very high nanoparticle density and the very edge of the electrode is coated in a near-continuous network of nanoparticles. 105

7.8 Frequency-dependent measurement noise in step-scan measurement with a microband electrode.107

7.9 Processed results of the step scan experiment. a) Representative ATR-SEIRAS absorbance spectra at long time. The derivative shape of the spectral bands from MOP is a result of excess Au deposition. b) Absorbance transient of the v_{8a} ring vibration at 1610 cm^{-1}(red) overlaid on the desorptive potential step applied to the microband electrode (grey). 108

A.1 Numerical aperture. Radiation with wavelenght λ is focused in a cone characterized by half-angle θ in a medium of refractive index n. 131

A.2 ATR imaging geometries. a) Micro-ATR uses a hemispherical IRE in combination with a focusing objective to image a small area. b) Macro-ATR uses a prism and flat mirrors to interrogate a large area with a collimated beam. 132

A.3 Geometric ray-tracing to visualize magnification in micro-ATR. a) Simplified IR microscope showing two beampaths from points on the source. The red path travles from the focal point of lens $L1$ (on-axis) while the blue path propagates from a point 1.5 mm to the left (off-axis). b) Expanded view of the hemisphere's effect on the off-axis beam. The blue beam in air would follow the dotted path, but due to refraction the beam follows the solid path through the hemisphere. Surface normals are drawn as black dashed lines. c) Graphical depiction of magnification. Due to the high refractive index's effect on the two beampaths, an imaged object (magenta arrow) at sample (top image) is mapped to a larger image at the detector (bottom). The magnification factor is equal to $n_{Si} = 3.4$. 134
A.4 Geometric ray-tracing to visualize magnification in macro-ATR. 135

List of Abbreviations

AFM	atomic force microscope
AIRES	anomalous infrared effects
AO	active optics
AOI	angle of incidence
ATR-FTIR	Attenuated total reflectance Fourier Transform Infrared spectroscopy
ATR-SEIRAS	Attenuated total reflectance surface-enhanced infrared absorption spectroscopy
BEMT	Bruggeman effective medium theory
CE	counter electrode
CLS	Canadian Light Source
CTE	coefficient of thermal expansion
CV	cyclic voltammetry
DAC	data acquisition card
DC	direct current
DLaTGS	deuterated L-alanine doped triglycine sulfate
DMFC	direct methanol fuel cell
DOF	degrees of freedom
ESI	Electrode/solution interface
ESR	electron spin resonance
fcc	face-centered cubic
FOV	field-of-view
FPA	focal plane array
FTIR	Fourier tranformed infrared spectroscopy
FWHM	full-width at half-maximum
HATR	horizontal attenuated total reflectance
IHP	inner Helmholtz plane
IR	infrared
IRE	internal reflection element
ITO	indium tin oxide
IUPAC	International Union of Pure and Applied Chemistry
MCT	mercury cadmium telluride
Mid-IR	Mid-Infrared Beamline (01B1-1) at CLS
MOP	4-methoxypyridine
NA	numerical aperture

Nd:YAG	Neodymium yttrium aluminum garnet
OAP	off-axis parabolic
OHP	outer Helmholtz plane
OPD	optical path difference
PEEK	polyether ether ketone
PGMEA	propylene glycol monomethyl ether acetate
PMMA	polymethyl methacrylate
PPS	polyphenylene sulfide
PVC	polyvinyl chloride
QCL	quantum cascade laser
QRE	quasireference electrode
RE	reference electrode
ROI	region of interest
SEC	spectroelectrochemistry
SECM	scanning electrochemical microscopy
SEM	scanning electron microscopy
SERS	surface-enhanced Raman spectroscopy
SIR	synchrotron infrared radiation
SNR	signal-to-noise ratio
SPP	surface-plasmon polariton
STM	scanning tunneling microscopy
SyLMAND	Synchrotron Laboratory for Micro and Nano Devices Beamline (05B2-1) at CLS
TA	transverse acoustic
TDM	transition dipole moment
TFE	thin-film electrode
TIR	total internal reflection
TO	transverse optical
TTL	transistor-transistor logic
UME	ultramicroelectrode
USAF	United States Air Force
UV	ultraviolet
VSFG	vibrational sum frequency generation
WE	working electrode

1 Introduction

1.1 The Central Role of the Electrode-Solution Interface

The continued development and application of new chemical transformations, particularly those from which we can extract useful energy, can be considered a hallmark of human progress. It is by harnessing energy in greater and greater quantities that we have transformed the planet, leveraging its resources to provide material wealth at a scale unprecedented in human history. Around the world, extractive industries produce raw materials which are processed into ever more valuable products. In the process, harmful by-products are produced, not least of which is carbon dioxide (CO_2) and other greenhouse gases such as methane, along with an array of other pollutants. The growing awareness of our collective effect on the environment, urged on by the burgeoning environmental movement of the last several decades, has pressured governments, private industry, and individuals to begin to change their behaviour at massive scale. This is an extraordinary challenge which is certain to define the coming decades as the world grapples with anthropogenic climate change, mass extinctions, and habitat loss.

Energy usage plays a key role in the problems facing humanity. Although this is a many-faceted problem which seems to touch every academic field, the manipulation of matter, extraction of useful energy, and application of energy as input to create valuable products indicates that chemistry must play a central role. Many forms of energy extraction apply the heat emitted by a chemical reaction to drive a turbine, producing electricity. A geographically relevant example is the Queen Elizabeth Power Station in Saskatoon, SK, which burns natural gas and accounts for around 15% of the province's electrical power as it serves the City of Saskatoon.[1] The harmful effects of carbon-intensive energy sources such as natural gas or coal are well-established in the academic and popular press, and it is enough to say that the status quo must change. This has motivated a concerted, decades-long effort to establish new energy generation and storage technologies.

The problems of storage and generation of electrical energy land squarely in the domain of electrochemistry, the branch of chemistry which seeks to understand and exploit the interaction of electrical and chemical effects.[2] The behaviour of electrochemical systems is dominated by the processes occuring at the interface between two components: the *electrode*, a solid electronic conductor, and the *electrolyte*, an ionic conductor which is usually a liquid solution of salts. Understanding the structure and changes of the *electrode-solution interface* (ESI) is central to any fundamental or applied problem in electrochemistry. This includes energy applications like batteries, fuel cells, or CO_2 electroreduction but also the myriad industrial implementations of electrochemical technology[3] e.g. the chlor-alkali process or metal electrorefining.

Consider an example of the ESI in a promising energy generation application, namely that of a generalized direct methanol fuel cell (DMFC)[4,5] shown in Figure 1.1. In a typical DMFC illustrated in Figure 1.1a, a composite anode is composed of nanoparticles of a precious metal catalyst (typically Platinum-containing alloys) supported on the surface of an inexpensive porous carbon electrode. The anode is in contact with a porous polymer electrolyte (the perfluoropolymer Nafion® is typical) which transports protons generated by the anode half-reaction. Methanol is oxidised to CO_2 at the anode surface, liberating up to six electrons which are conducted through the electrode and travel through an external circuit to do useful electrical work. The half-reaction occurring at the anode is nominally

$$CH_3OH\,(aq) + H_2O\,(l) \xrightarrow{\text{Pt/Ru catalyst}} 6\,e^- + 6\,H^+(aq) + CO_2(g)$$

and a microscale illustration of the reaction occurring at the anode's ESI is depicted in Figure 1.1b.

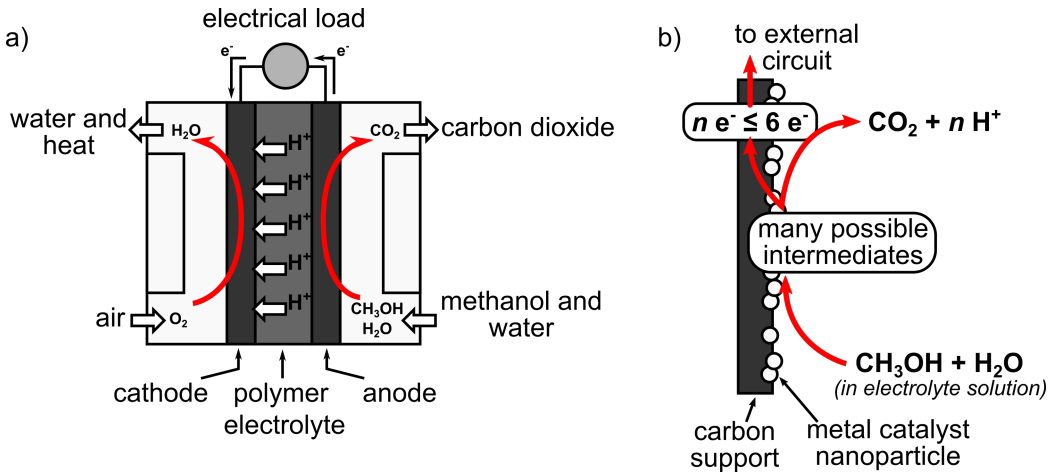

Figure 1.1: a) Simplified schematic of a direct-methanol fuel cell. At right, methanol (CH_3OH) in electrolyte solution is fed to the anode where it is oxidized, liberating electrons and protons. Electrons are captured by an external circuit to do useful work, while protons diffuse across a polymer electrolyte membrane (middle). At left, oxygen is reduced at the cathode to water. b) A microscopic illustration of the reaction occuring at the electrode-solution interface of the anode. Methanol and water react at the surface of precious metal catalyst nanoparticles. The reaction mechanism and intermediates, and therefore the number electrons extracted per methanol n, depend strongly on fuel cell operating conditions and catalyst design.

The simplified discussion above offers little insight into the true nature of the reaction occurring at the ESI. A complex, multi-step mechanism has been put forth[4] involving an array of adsorption motifs, intermediates, and by-products. Discussion of the detailed mechanism is outside the scope of this introduction, but the point is that overall the performance of the DMFC is dominated by what happens at the ESI. The reaction rate, and thus the rate at which useful energy can be extracted, is directly impacted by the mechanism by which oxidation occurs. Any attempt to improve the DMFC, or indeed any electrochemical technology, must proceed from detailed understanding of the processes occuring at the ESI.

1.2 The Challenge of Studying the ESI

The ESI can be investigated by purely electroanalytical methods which monitor electrical observables such as impedance, currents, and potentials. Detailed theories have been developed to link the macroscopic quantities measured to the microscopic changes occurring at the ESI, both in terms of molecules assembling or reacting at the surface or in changes in the electrode structure itself. However, these techniques are only indirect measurements i.e. they are not directly sensitive to chemical structure, and conclusively identifying reaction intermediates or even components of a complex mixture requires exceedingly careful experimental design, if it is possible at all. Furthermore, the observables monitored are generally averages over the entire ESI. For example, measuring the current passing through the ESI yields an average over many microscopic sites, and interpretation of the results requires careful consideration of the differing reactivities of contributing microenvironments.

Although the indirect methods of pure electrochemistry do yield valuable information, any method which can provide direct chemical information about the ESI is clearly of great benefit. A natural choice is the application of *spectroscopy*, where the ESI is probed by studying its interaction with photons. Application of spectroscopic techniques to electrochemical systems, *spectroelectrochemistry*, has become a major subfield of electrochemistry, and a broad discussion of its development and outlook has been offered recently by Lozeman *et al.*[6] Light-matter interactions depend strongly on the energy of the input photons, allowing a variety of information to be gleaned by coupling one of the many well-developed spectroscopies with electrochemical techniques. For example, X-ray techniques can report on oxidation state and local coordination environment of the metal atoms of the electrode.[7–9] Ultraviolet and visible photons probe electronic structure in reacting molecules, and advances in visible frequency lasers have allowed application of powerful pump-probe techniques for monitoring reaction dynamics with extremely high time resolution (femtoseconds or better).[10–12]

Vibrational spectroscopy, and infrared spectroscopy in particular, directly probes molecular structure and is uniquely suited to monitor structural changes during the course of reactions. Since its introduction in 1980,[13] infrared spectroelectrochemistry has been productively applied to the study of electrochemical systems. The study of surfaces with infrared spectroelectrochemistry poses some fundamental challenges to the experimentalist. There are generally lower absolute numbers of molecules to interrogate on a surface than in the bulk. Infrared photon-matter interaction is already fairly weak, so signal-to-noise ratios (SNR) in surface-sensitive FTIR spectroelectrochemistry are usually very low. Furthermore, fundamental processes in electrochemical reactions tend to have timescales in the milli- to microsecond regime, so any attempt to elucidate reaction dynamics requires time-resolved measurements with corresponding time resolution. For example, on these timescales mass transport to the electrode surface from the bulk occurs,[14,15] along with adsorption or desorption of reactants, intermediates, and products.[16] The orientation of molecules on a catalytic surface is often critically important, and reorientation of adsorbed molecules occurs on a finite timescale.[17]

This thesis is motivated by the desire to obtain dynamic information about electrochemical reactions and process occurring at the electrode/solution interface on the micro- to millisecond timescale. This poses a number of requirements which will be further explored in Chapter 2 and are summarized here.

Any *in situ* study of the ESI must be a surface-sensitive one. This thesis will employ a surface-sensitive FTIR spectroelectrochemical technique developed by Masatoshi Osawa in the late 1980s.[18] Attenuated total reflectance surface-enhanced infrared absorption spectroscopy (ATR-SEIRAS) exploits the interaction of infrared photons with a nanostructured metal film, typically around 20 nm thick, deposited on an IR-transparent internal reflection element. By working in the Kretschmann configuration, where light is totally internally reflected off the metal/solution interface without ever passing through the electrolyte solution (Figure 1.2a), losses due to strong absorption of IR light by liquid media are avoided entirely. Furthermore, the optical properties of the metal film enhance the IR absorption cross-section of molecules at the metal surface by a factor ranging from 10 - 100×, greatly improving signal-to-noise and rendering the technique surface-sensitive, Figure 1.2b.

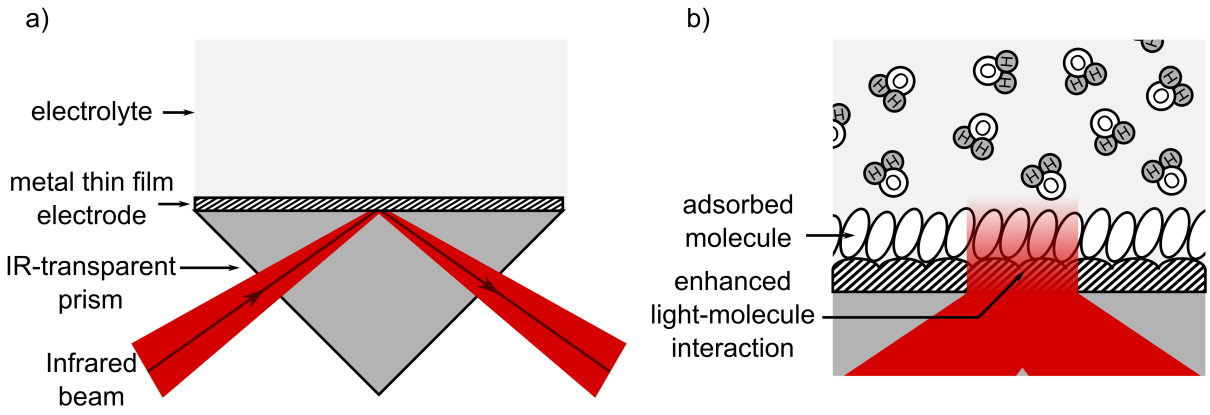

Figure 1.2: The ATR-SEIRAS method. a) A macroscopic view of the experimental setup. The infrared beam passes through an infrared-transparent prism and is totally internally reflected at the electrode/solution interface. The solution-facing side of the prism is coated with a nanostructured metal thin film electrode. b) Microscopic view of ATR-SEIRAS. Molecules are shown adsorbed at the surface of the metal thin film. Infrared light couples with the metal film resulting in increased signal strengths from surface adsorbed molecules.

Time-resolved FTIR techniques are well-developed, both in the greater literature and the Burgess group.[19–21] A range of timescales can be covered with a conventional FTIR spectrometer. The *rapid-scan* FTIR technique can achieve time-resolution down to milliseconds, and microsecond resolution can be achieved with the technically demanding *step-scan* technique. A key experimental consideration is the need to rapidly trigger the process of interest before beginning to collect spectroscopic data, thereby avoiding convolution of early datapoints with the changing electrode potential. This is accomplished by applying a potential step to the working electrode. However, it will be shown quantitatively in Chapter 2 that the so-called *electrode rise time*, the length of time which passes before a real electrode actually reaches the desired potential, depends directly on the electrode area. For the timescales required here, it will be necessary to use so-called *mi-*

croelectrodes, electrodes with critical dimensions in the hundreds of micrometers, in order to rapidly trigger electrochemical experiments.

Microelectrodes present their own problems for FTIR spectroelectrochemistry. The small size of typical microelectrodes requires a highly focused, bright IR source, and Chapter 2 will demonstrate that this exceeds the capabilities of conventional, lab-scale infrared sources. While conventional sources have high photon flux, for optical reasons they cannot be focused to a sufficiently small spot on the surface of a microelectrode. This dramatically decreases the signal-to-noise of a potential FTIR spectroelectrochemical experiment. Instead, it is necessary to use a specialized infrared source capable of focusing infrared light to sufficiently small spot sizes. In this thesis, infrared radiation from a synchrotron source (the Canadian Light Source) will be shown to be necessary.

1.3 Thesis Scope

In short, the goal of this thesis is to develop the analytical tools necessary to perform ATR-SEIRAS microspectroscopy experiments using synchrotron infrared radiation. Pertinent theory and background will be discussed in Chapter 2. Quantitative discussions of infrared spectroscopy and relevant sampling methods, electrochemistry and some salient features of microelectrodes, and the ATR-SEIRAS technique will be presented. It was intended that the experimental platform developed here would be compatible with the time-resolved methods being separately developed by my colleague Dr. Kaiyang Tu, a fellow graduate student at the time.

Chapter 3 will present an early attempt at integrating existing instrumentation at the Mid-IR beamline of CLS with ATR-SEIRAS and will serve to highlight the two main technical challenges encountered in this thesis: (1) the need for robust, reproducible control of the infrared spot size and position, and (2) the difficulties associated with preparing thin film microelectrodes for ATR-SEIRAS. Chapter 3 concludes with a discussion on what is needed experimentally to solve these problems, setting the course for the remaining chapters.

Challenge (1) is essentially a problem of optical design and will be dealt with over the course of Chapters 4 and 5. In Chapter 4 a newly available microstructured internal reflection element (IRE) will be shown to be highly compatible with ATR-SEIRAS. The advantages in improved spectral throughput at low frequencies and compatibility with microfabrication techniques will be discussed, as well as the impact of the differing beampath on the ATR-SEIRAS signal enhancement. In Chapter 5, a custom horizontal microscope endstation will be developed at the Mid-IR beamline expressly for use with the novel IRE. The optical and spectroscopic performance of the microscope will be characterized by quantifying spot size and by interrogating a simple open channel microfluidic device.

Although this thesis was motivated narrowly by the desire to achieve surface-sensitive FT-IR microspectroscopy on a microband electrode for the purposes of time-resolved spectroelectrochemistry, it was recognized

that the horizontal microscope was generally applicable to infrared imaging as well. This will be demonstrated in Chapter 6, where an interfacial reaction between two co-flowing streams of liquid will be imaged. The chapter will present the fabrication of a microfluidic device integrated with the novel IRE and demonstrate the general utility of the horizontal microscope for imaging studies as well as spectroscopy.

Finally, challenge (2), the preparation of a mechanically stable microelectrode compatible with ATR-SEIRAS, will be dealt with in Chapter 7. By making use of some excellent contemporaneous work from a fourth-year student (Ian Andvaag, now a Masters candidate in the Burgess lab) that developed electrodeposited Au nanoparticles on conductive metal oxide adhesion layers for ATR-SEIRAS, a protocol will be developed for preparing SEIRAS-active microband electrodes. The highly focused beamspot provided by the horizontal microscope and fine control over its position will be further demonstrated in a proof-of-concept experiment addressing a microband electrode. Working in collaboration with Tu, a preliminary time-resolved experiment will be presented and ongoing challenges will be discussed.

Finally, Chapter 8 will summarize the results of this thesis and draw conclusions. Continuing technical improvements will be proposed. Implications for static and dynamic electrochemical studies, including insights into electrocatalytic reactions and electrochemical pattern formation, will be discussed along with applications in electrochemical microfluidics.

2 Background

2.1 Introduction

This chapter will describe the theory of infrared spectroscopy and some instrumental aspects and sampling methods relevant to this thesis. Some topics from electrochemistry will be introduced with particular attention paid to the properties and fabrication of microelectrodes. This will lay the groundwork for a discussion of an infrared spectroelectrochemical technique, ATR-SEIRAS, which is central to the work described in subsequent chapters. The benefits and drawbacks of the technique will be discussed along with a brief examination of the difficulties of preparing the metal thin film electrodes on which the technique relies.

2.2 Infrared Spectroscopy

This section will first review some of the relevant theory for infrared spectroscopy. Then, the Michelson interferometer will be discussed along with its advantages over dispersive instrument designs. A discussion of infrared sources will motivate the use of synchrotron radiation in this thesis. Detectors for infrared spectroscopy will be reviewed, along with a brief discussion of sampling methods, in particular the Attenuated Total Reflection (ATR) method.

2.2.1 Theory

Infrared spectroscopy yields detailed information about chemical structures by probing the interaction between infrared radiation and molecular vibrational modes. In a typical infrared (IR) spectroscopy experiment, IR radiation is absorbed at discrete frequencies as vibrational modes are excited in the molecule. Detailed treatments of the quantum mechanics underlying this phenomenon and experimental details are given in textbooks such as those in references 22, 23, and 24; a survey of IR spectroscopy is given below where relevant results are stated without derivation.

Molecular vibrations, defined as periodic displacements of atomic nuclei, are often treated with the simple harmonic oscillator (SHO) model of quantum mechanics, Figure 2.1. This simple model offers enough descriptive power to understand the IR spectra shown in this thesis. An illustrative example is that of a heteronuclear diatomic molecule (e.g. HCl) where the H-Cl bond is assumed to behave as a spring according to Hooke's law:

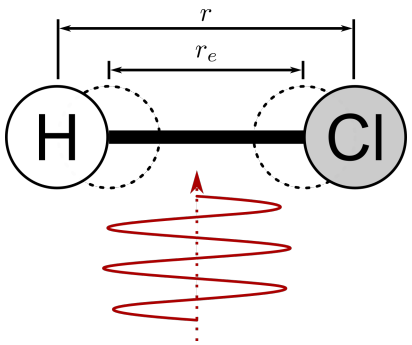

Figure 2.1: Molecular vibration illustrated with the simple harmonic oscillator model, shown here with the stretching mode of HCl driven by infrared radiation. The H-Cl bond is shown displaced to a new internuclear displacement r from its equilibrium bond length r_e. By definition for this molecule, q is along the molecular bond axis.

$$f = -kq$$

where the restoring force f is proportional to the internuclear displacement $q = r - r_e$ (r and r_e are the internuclear distance and equilibrium bond length, respectively) and the force constant k. It is worth noting here that q happens to lie parallel to the bond axis in this diatomic molecule, but more generally q is parallel to the normal mode coordinate. That is to say, q may not be along any one bond in a polyatomic molecule. The potential energy V is obtained by integrating the expression $dV = -fdq$ to find

$$V(q) = -\frac{1}{2}kq^2$$

which is a parabola centered at $q = 0$, Figure 2.2.

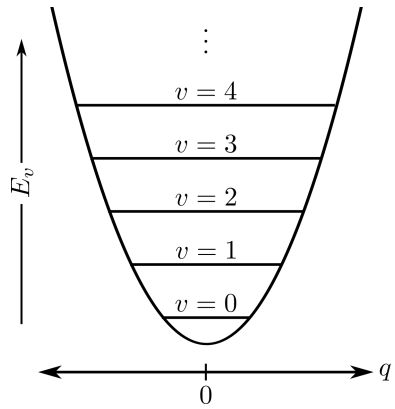

Figure 2.2: Energy levels of a simple harmonic oscillator superimposed on a parabolic potential.

Spectroscopic experiments report on the energy difference ΔE between different quantized levels of the system under study. In order to obtain an analytical description of the spectroscopic observable, ΔE, the energy of a given vibrational mode must be quantified. This requires finding a solution Ψ to the Schrodinger equation $\hat{H}\Psi = E\Psi$, where $\hat{H}$ is the Hamiltonian operator and E is its energy eigenvalue. The H-Cl bond

has only one degree of freedom along the bond axis so it is enough to solve the Schrodinger equation in one dimension. For a one-dimensional harmonic oscillator, the Schrodinger equation is

$$-\frac{\hbar^2}{2\mu}\frac{d^2\psi}{dq^2} + V(q)\psi(q) = E\psi(q)$$

where $\hbar$ is the reduced Planck constant, $\mu = m_H m_C l/(m_H + m_C l)$ is the reduced mass. We use the potential $V(q) = -\frac{1}{2}kq^2$ and rearrange slightly to have

$$\frac{d^2\psi}{dq^2} + \frac{2\mu}{\hbar^2}\left(E - \frac{1}{2}kq^2\right) = 0 \qquad -\infty < q < \infty$$

Solution of this second order differential equation yields wavefunctions $\Psi_v(q)$ quantized by vibrational quantum number v. They have the general form

$$\Psi_v(q) = N_v H_v(\alpha^{1/2}q)e^{-\alpha q^2/2}$$

where the constant α is

$$\alpha = \left(\frac{k\mu}{\hbar^2}\right)^{1/2}$$

and the normalization constant N_v is

$$N_v = \frac{1}{(2^v v\nu!)^{1/2}}\left(\frac{\alpha}{\pi}\right)^{1/4}$$

and $H_v(\alpha^{1/2}q)$ are *Hermite polynomials* with degree v.

The important point for this discussion is that, for a simple harmonic oscillator which has the wavefunctions given above, the energy is quantized according to

$$E_v = h\nu(v + \frac{1}{2}) \qquad v = 0, 1, 2, \cdots$$

where

$$\nu = \frac{1}{2\pi}\left(\frac{k}{\mu}\right)^{1/2}$$

which has frequency units. Figure 2.2 depicts the results of the simple harmonic oscillator model, showing a parabolic potential with equally spaced energy levels E_v labelled with their vibrational quantum numbers $v = 1, 2, \cdots$.

Solution of the time-dependent Schrodinger equation $\hat{H}\Psi = i\hbar\partial\Psi/\partial t$ yields insight into the lineshape and selection rules for IR spectroscopy. Ultimately, the probability P at time t of transition from state ψ_1 to ψ_2 with energies E_1 and E_2 can be expressed as

$$\frac{P}{t} = \frac{E_0^2(M_{21})^2}{4\hbar}\left[\delta(hn - \Delta E) + \delta(\Delta E + hv)\right]$$

where we have defined $M_{21} = \int \psi_2 \mu_z \psi_1 d\tau$ as the *transition dipole moment*. Here μ_z is the dipole moment component along the z-axis. This equation, Fermi's Golden Rule, offers several key insights. First is that the probability of observing a transition is proportional to the square of the exciting electric field amplitude, E_0. This implies that one way to improve the effective absorption cross section is to increase the magnitude of the electric field in the region of the absorbing molecule. Second, a transition occurs when the energy of the incident photon $h\nu$ is equal to the energy difference between two states $\Delta E = E_2 - E_1$ i.e. the photon energy is resonant with the transition energy. Third, although it is not obvious from the equation, absorption is sensitive to polarization. Light must be polarized along the direction of the normal mode (the z-axis the case of HCl as shown above) for absorption to occur; polarizing orthogonal to the normal mode prevents absorption. This point will be important when discussing ATR-SEIRAS in a later section. Finally, and particularly important, is that only vibrational transitions which have non-zero transition dipole moments are observed, which is the selection rule for infrared spectroscopy. Molecules which have non-zero transition dipole moments can be said to be IR-active.

The preceding discussion has focused on a linear species for simplicity, but for a non-linear molecule with N nuclei, there are generally $3N - 6$ normal modes, some or all of which may be IR-active depending on the symmetry of the particular vibrational mode. As shown above, the frequency of a normal mode depends strongly on the masses and arrangement of the nuclei involved via the reduced mass μ. As a result, IR absorption is an excellent technique for determining chemical structures and how they change during reactions. Indeed, there is a well-developed empirical and theoretical understanding of the characteristic vibrational frequencies (called *group frequencies*) of chemical functional groups, allowing relatively simple interpretation of spectral data in terms of structural features of molecules under study. Sample preparation is generally straightforward, irradiation with IR light is non-destructive, and spectra can be obtained in a few minutes with commercially available instruments.

2.2.2 Instrumental Aspects of Fourier-Transformed Infrared Spectroscopy

2.2.2.1 The Michelson Interferometer

The heart of a Fourier Transformed Infrared (FT-IR) instrument is the Michelson interferometer, a schematic of which is shown in Figure 2.3a. Broadband IR light is incident on a beamsplitter and the beam is divided along two paths. Both beams reflect off of mirrors, one of which moves, before re-combining at the beamsplitter, passing through a sample material, and ultimately being focused onto a detector. As the position of the moving mirror is scanned back and forth, the two beams interfere either constructively or destructively. For a monochromatic source, the result is a sinusoidal function of the *optical path difference* (OPD), shown in Figure 2.3b. For a broadband source containing many wavelengths, the so-called interferogram is composed of a rapidly varying signal contained in a finite envelope which goes effectively to zero at large OPD, figure 2.3c.

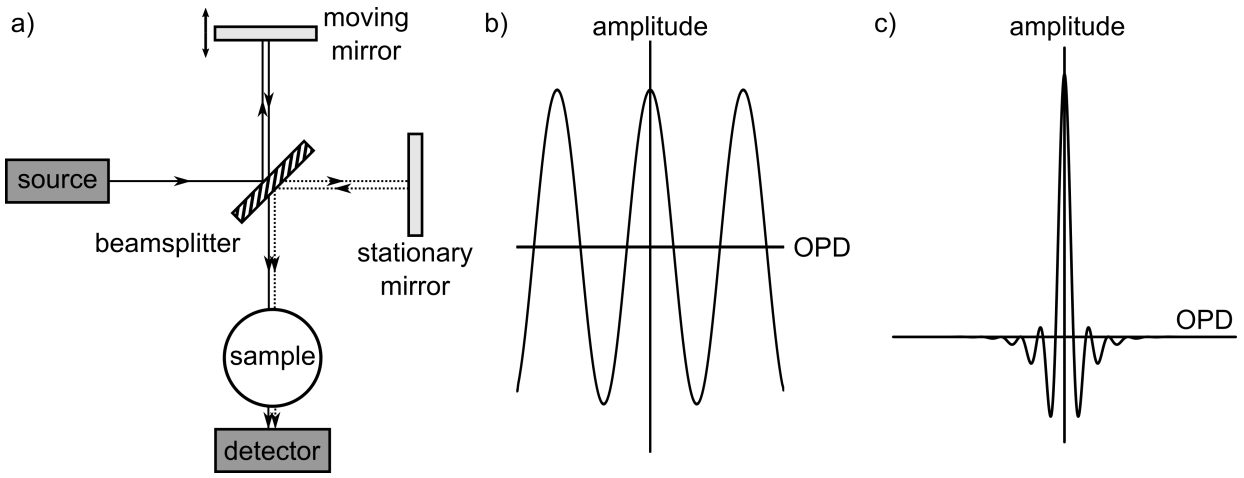

Figure 2.3: a) Schematic of a Michelson interferometer. b) Detector response to monochromatic radiation passing through a Michelson interferometer as a function of optical path difference. c) As b) but with polychromatic light. The oscillating signal now decays rapidly at large OPD.

Contained in the interferogram is information on the attenuation of light by the sample at each wavelength. Fourier-transforming the interferogram yields a more easily interpreted frequency spectrum. Collecting interferograms with and without the sample in the beampath, I_S and I_0 respectively, allows an absorption spectrum to be calculated by $A = -\log(I_S/I_0)$. By convention, the OPD is recorded in units of centimeters and so FT-IR spectra are presented with frequency units of inverse centimeters called *wavenumbers*, cm^{-1}.

2.2.2.2 Advantages of FT-IR over Dispersive Instruments

In contrast to the FT-IR instrument, many spectroscopies use dispersive instruments to collect spectra. For example, in a typical UV-Visible spectrometer, a white light source is directed to a monochromator, dispersing the wavelengths in space, before passing through a slit to select a "single" wavelength. The filtered beam is incident on a sample material before reaching a detector; scanning the wavelengths allows a complete spectrum to be measured. Using interferometry offers several key advantages compared to dispersive instruments.

The **Connes advantage** is that the resolution of an FT-IR instrument is much better than a dispersive instrument. In a dispersive setup, the resolution is limited by the slit width, whereas in a Michelson interferometer all wavelengths are sampled at once, and resolution is limited by the pathlength of the interferometer's moving mirror.

The **Jacquinot advantage** is that the power reaching the detector is much higher than that which would pass through a slit. This is extremely important as FT-IR measurements are detector noise-limited. Driving up the power falling on the detector element increases the signal-to-noise of the measurement.

The **Fellgett (multiplex) advantage** comes from the simultaneous sampling of all wavelengths, significantly decreasing measurement time compared to a dispersive instrument. The Fellgett advantage has consequences for the signal-to-noise ratio (SNR) of experimental data. The important point for the experi-

mentalist is that because detector noise is random, multiple measurements can be averaged to increase SNR. In practice, many replicate interferograms are collected and averaged to improve SNR. Typical collection times are on the order of a minute or two.

2.2.2.3 Infrared Sources

The vast majority of commercial FT-IR spectrometers rely on the *globar* as an IR source. Globars are solid ceramic rods (usually silicon carbide) which are electrically heated to between 1000 and 1650 °C. The globar emits IR light as a thermal blackbody, peaking at a wavelength which depends on the operating temperature of the globar, typically around 1000 to 2000 cm^{-1}. The emission is broadband, covering the mid-IR region (loosely, 4000 to 600 cm^{-1}). This region spans the typical range in which molecular vibrations occur and therefore the globar is a common choice.

A key drawback of the globar is its low brilliance. Brilliance measures the flux density per solid angle through which light is emitted and has units of photon s^{-1} per 1% bandwidth cm^{-2} sr^{-1}. Although globars emit a large number of photons, they are emitted isotropically i.e. into a large solid angle, resulting in low brilliance. This has significant consequences for microspectroscopy experiments such as those completed in this thesis. To understand this, we must introduce the geometric *etendue*, G, depicted in Figure 2.4. The etendue is defined as $G = S\Omega$ where S is the source area and Ω is the solid angle into which light is emitted. G, which is also called the optical invariant, is a conserved quantity in an optical system. In other words, the etendue of the source G_{source} and that at sample G_{sample} can at best be equal, $G_{source} \geq G_{sample}$; optical losses result in $G_{sample} > G_{source}$. A typical globar is 10 × 1 mm^2 and the maximum usable light emitted by a globar is contained within a half-sphere which has solid angle $\Omega = 2\pi$ sr. So, $G_{globar} = 0.63$ sr cm^2. Assuming that all of the light could be focused to a spot with no optical losses, and noting that collecting all of the emitted light in a half-sphere would require an extremely high numerical aperture, a spot size of 10 mm^2 is formed. The beam cannot be focused further than this and instead must be apertured which necessarily reduces flux at sample. The practical consequence is that trying to focus a globar to a spot diameter around 100 µm or less results in significant losses in photon flux, drastically reducing SNR and in some cases preventing meaningful measurement.

In contrast to the globar, synchrotron infrared radiation (SIR) such as that collected at the Mid-IR beamline at CLS[25,26] is highly brilliant. The principle of synchrotron radiation is based on radiation emission by moving charges. While an electron oscillating in vacuum emits a dipole radiation pattern, accelerating it to near relativistic speeds and forcing it to travel through a bending magnet results in a significant compression of the radiation pattern, resulting in a highly collimated, intense beam of light ranging from far-IR to hard X-rays. In contrast to the low brilliance of globars, SIR is typically four or five orders of magnitude more brilliant. This is chiefly due to the very small solid angle into which SIR is emitted; although a globar emits more photons, they are emitted isotropically compared to the tightly collimated beam produced by a synchrotron.

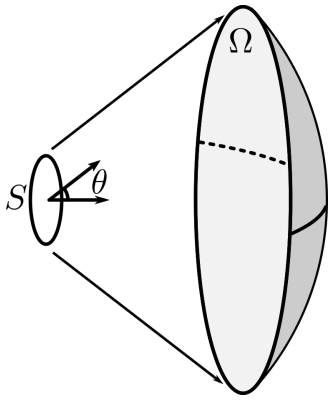

Figure 2.4: Simplified construction of *etendue*, $G = S\Omega$. The source area S radiates light which is captured in the solid angle Ω, in this case a spherical cap. Ω is related to the emission angle, θ.

Both the source size S_{source} and solid angle Ω_{source} are very small for SIR. At the mid-IR beamline of CLS, the geometric etendue is measured at $G_{CLS} = 4.1 \times 10^{-5}$ sr cm^2 around 1600 cm^{-1}. As a result, focusing a SIR beam to a diffraction-limited spot is possible without significant loss of IR intensity. This has resulted in a substantial literature on FT-IR microspectroscopy addressing problems in cell biology, condensed matter physics, and chemistry.[27–32]

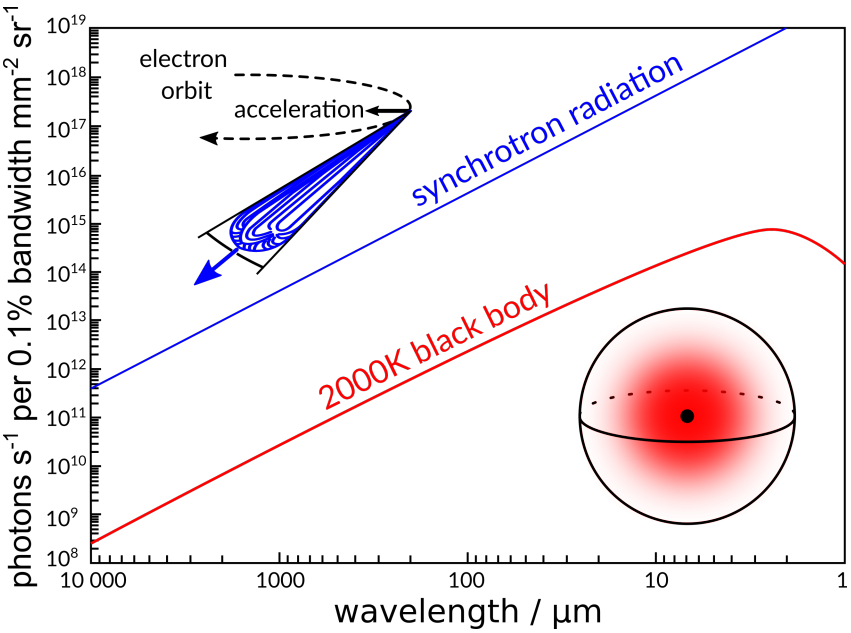

Figure 2.5: Brilliance curves for synchrotron radiation and conventional globar i.e. a blackbody radiator. The Mid-IR wavelength range is approximately from 10 to 3 µm. The brilliance of the synchrotron source is uniformly higher than that of the globar. Insets visualize source emission. Adapted from reference 34.

2.2.2.4 Single-Element and Imaging Detectors

Infrared photon detection is challenging due to their low energies. Many common detectors such as bolometers or deuterated L-alanine doped triglycine sulfate (DLaTGS) detectors rely on thermal detection mechanisms, while the very common mercury cadmium telluride (MCT) detector relies on photoconduction. The figure of merit for a detector is specific detectivity, D^*, units $\mathrm{cm\,Hz^{1/2}\,W^{-1}}$, which essentially measures detector sensitivity. While higher D^* offers better sensitivity, often this comes with the tradeoff of lower spectral bandwidth. MCTs offer high detectivity compared to thermal detectors while still spanning the mid-IR spectrum. Furthermore, they respond very rapidly (typically microseconds or better) allowing rapid data collection and time-resolved spectroscopies.

In a photoconducting MCT detector, a voltage is applied to the semiconducting MCT element. When infrared photons strike the sensor, electrons in the conduction band are excited into the valence band and travel in the potential gradient as a photocurrent. Because of their very low bandgap, such detectors are highly susceptible to thermal noise. In order to improve SNR, MCT detectors must be cooled with liquid nitrogen, reducing dark currents. A single sensor element is typically mounted behind an IR-transparent window with the detecting element in contact with the nitrogen reservoir to maintain low temperature.

The majority of work described in this thesis relies on single-element MCT detectors as described above. However, for the imaging work presented in Chapter 6, a two-dimensional focal plane array (FPA) detector is used. Focal plane array detectors are essentially charge-coupled devices with the pixels made up of miniaturized MCT elements. A typical FPA (such as the one used in Chapter 6) incorporates a 64 × 64 pixel array of MCT sensors, with each sensor measuring 40 × 40 μm^2. Data acquisition speed has advanced rapidly since their introduction in 1995, and hypercubes of 4096 spectra at 8 cm^{-1}resolution can be collected in about 5 minutes.

2.2.3 Sampling Methods

2.2.3.1 Transmission and External Reflection

The simplest FT-IR measurement mode is transmission, where the beam passes through a sample before impinging on a detector. IR absorption in condensed matter is generally very strong. For example, a layer of water around 20 µm can completely attenuate IR transmission around the H_2O bending and stretching modes. Powdered materials can be diluted into an IR-transparent KBr pellet to avoid excessive absorption, but working with condensed media in transmission mode requires methods to minimize the optical path length to dimensions around 10 µm. Transmission cells which accomplish this have been reported for biological[30] and electrochemical experiments[19,20,33–35], but fabrication can be very challenging. External reflection experiments reflect the IR beam from the sample surface before collecting it at the detector. This method can be very useful, particularly for solid samples, but reflection from solid-liquid interfaces face the same problems as transmission measurements.

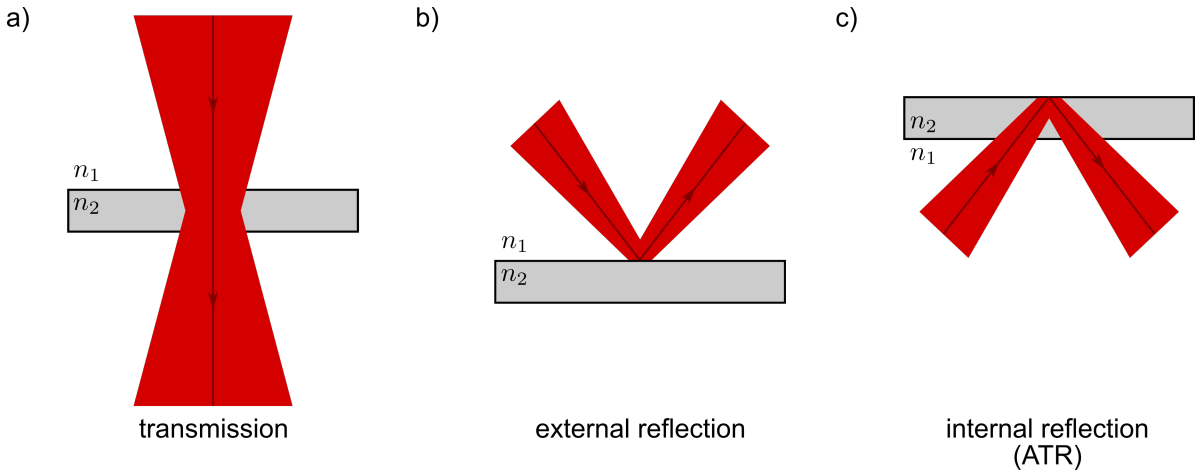

Figure 2.6: FT-IR sampling methods with generalized sample materials. Refractive index n_1 is often that of air, but for buried interfaces n_1 will be that of the solvent. a) Transmission mode. The IR beam is incident on a sample material with complex refractive index n_2 which absorbs some light. b) External reflection mode. The IR beam is reflected off the surface of the material. c) Internal reflection mode. The IR beam travels through the material with refractive index n_2, generally chosen to be IR-transparent, and reflects off the interface shown at top, probing a small region of the sample placed at that interface.

2.2.3.2 Attenuated Total Reflection

The attenuated total reflection (ATR) geometry is highly amenable to strongly absorbing samples such as condensed media.[36] ATR relies on total internal reflection, wherein the IR beam is passed through an IR transparent prism, often called an ATR element, at an angle of incidence (AOI) greater than the critical angle, $\theta_c = \arcsin n_2/n_1$. The beam is totally internally reflected at the prism-sample interface as shown in Figure 2.7a. Maxwell's equations require continuity of the electric field across the interface, and solving for the field on the sample side reveals an exponentially decaying wave of the form $E(z) = E_0 e^{-z/d_p}$, Figure 2.7b. The penetration depth d_p is the distance over which the wave decays to $1/e$ of its original value. For a beam incident at AOI θ with wavelength λ, the depth of penetration is

$$d_p = \frac{\lambda}{2\pi n_1 \sqrt{\sin^2\theta - (n_2/n_1)^2}}$$

Apparent in this equation is that the penetration depth scales linearly with wavelength and decreases with increasing AOI. As a rule of thumb, the penetration depth is roughly $\lambda/4$, or about 1 or 2 µm in the mid-IR. The short interaction distance is beneficial for studies of condensed media, returning high quality spectra without danger of excessive absorption losses from the sample.

A variety of optical accessories for ATR-FTIR measurements are available commercially. One common variable angle accessory is shown in Figure 2.7c, which makes use of a moving mirror system and matched parabolic mirrors to adjust the angle of incidence over a wide range.

Finally, this sampling method lends itself to a unique hybrid technique, ATR-SEIRAS, which is highly

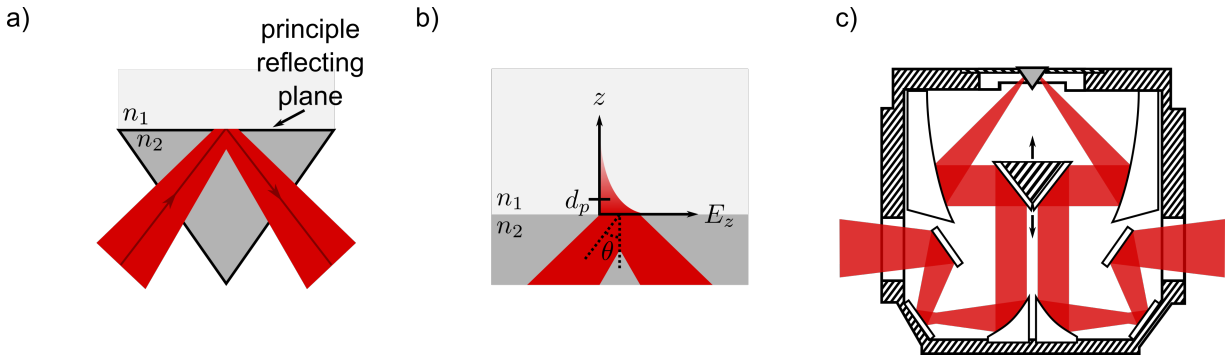

Figure 2.7: Attenuated total reflection. a) Instead of probing the sample material with complex refractive index n_1, the IR beam travels through an IR-transparent crystal (n_2) and undergoes total internal reflection at the principal reflecting plane. b) The evanescent wave penetrates into the sample medium, decaying exponentially. c) Schematic of a common optical accessory for ATR experiments (PIKE VeeMAX III). The central mirrors move up and down (symbolized by arrows,) dynamically adjusting the AOI. The accessory is approximately 30 cm on a side and fits in the sample compartment of a standard laboratory FT-IR instrument.

compatible with electrochemistry. (See Section 2.4.)

2.2.4 Time-Resolved Methods

Conventional FT-IR instruments can easily collect spectra with time resolution on the scale of minutes or more with no modification. Temporal regimes down to many milliseconds are accessed with the *rapid scan* technique, while timescales down to a few hundred nanoseconds are accessed with *step scan.*

Dynamic measurements using the *rapid-scan* technique can be obtained by simply driving the moving mirror at high velocities and collecting interferograms during the course of a dynamic process. Co-adding and averaging many interferograms improves SNR, but this requires the process under study to be reset and triggered many times (typically 128 or more). The factor limiting time resolution in rapid scan is the drive velocity of the moving mirror, which imposes a practical limit of a few tens of milliseconds.

In contrast, the *step-scan* technique is limited not by the relatively slow drive velocity of the moving mirror, but instead by the bandwidth of the MCT detector. In step-scan measurements, the process under study is triggered while the moving mirror is held at a single position. The detector transient is collected as the process evolves, the mirror position is incremented, the process is reset, and the measurement is repeated. Interferograms at each time are reconstructed from the set of detector transients, with the temporal resolution limited by the detector response rate. As most modern MCTs have bandwidths in the gigahertz range, this has allowed some workers to achieve nanosecond time resolution [37,38] and microsecond resolution is achievable with relative ease. However, in contrast to rapid-scan, where the studied process must be reset a few hundred times, a far greater number of repetitions is needed for step-scan. A typical interferogram usually contains about 1000 mirror positions, and collecting a relatively modest 128 interferograms for each time point still requires 128,000 repetitions. This points to an obvious need for excellent stability and repeatability of the

experimental system under study.

2.3 Electrochemistry

2.3.1 Introduction

Electrochemistry is often defined as "the branch of chemistry concerned with the interrelation of electrical and chemical effects." [2] This statement encompasses a truly massive array of modern technologies, industries, and fields. The application of electrochemistry is critical to the modern economy, playing a central role in energy (e.g. batteries and fuel cells), material production (e.g. chloralkali process, electrowinning and refining of metals), material failure (corrosion), and environmental and biological sensing (e.g. gas sensors, insulin test strips). Beyond these well-established major industries, many niche applications exist which are too numerous to name.

The successful application of these myriad technologies rests on fundamental understanding of the physics and chemistry of electrochemical processes. The scientific study of electrochemistry seeks to understand the factors which control those processes: electrical potentials, charge (at interfaces and transferred between reactants), mass transport, reaction rates, and electrode surface structure are a few of the considerations which come to mind.

The electrode/solution interface was briefly discussed in the introduction to this thesis, but a more technical description is offered here. After that, a short discussion of electrochemical measurements will be presented followed by a quantitative description of the properties of microelectrodes and their fabrication methods.

2.3.2 The Electrode/Solution Interface

Central to the study of electrochemistry is the electrode/solution interface (ESI), namely its structure and dynamics under application of electrical potentials. The behaviour of the ESI dominates the behaviour of electrochemical systems. In general, the ESI is defined as an interface between two phases. One, the *electrode*, is a solid electronic conductor, and the other, the *electrolyte*, is an ionic conductor. For the purposes of this thesis, the electrode is always metallic Au and the electrolyte is an aqueous solution of ions, though solid electrolytes are of great importance in energy materials.

The ESI can be modelled as a parallel plate capacitor, where application of a potential results in buildup of excess charge density on the metal, σ^M, and a corresponding equal but opposite charge density is induced in the solution side, σ^S, with the condition that $\sigma^M = -\sigma^S$. The electrical double layer which forms is associated with a double layer capacitance, C_d.

A microscopic depiction of the ESI is presented in Figure 2.8. On the solution side of the interface, several layers are shown. The layer immediately adjacent to the metal is the Stern layer. This contains

specifically adsorbed molecules: usually solvent molecules, but sometimes other molecules which have shed their solvation shell such as electrolyte anions as shown in the figure. (Section 2.4.6 introduces a pyridine derivative which exhibits this behaviour and has useful spectroscopic features.) The *inner Helmholtz plane* is defined as the plane running through the locus of the electrical centers of the specifically adsorbed ions. The *outer Helmholtz plane* is drawn through the locus of centers of the nearest solvated ions; these ions are said to be non-specifically adsorbed. Finally, beyond this layer there is an extended region called the *diffuse layer* composed of thermally agitated non-specifically adsorbed ions which extends from the OHP to bulk solution. The thickness is a function of ionic strength, but for ionic strengths used in this thesis (above 0.01 M) the thickness is below 100 Å.

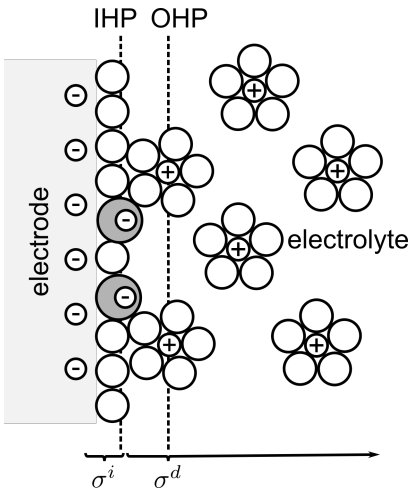

Figure 2.8: The electrode-solution interface, ESI. Anions (dark circles with −) are specifically adsorbed alongside a layer of solvent molecules (open white circles). Solvated cations (white circles with +) occupy the diffuse part of the double layer. Adapted in part from reference 2

Defining the excess charge density in the IHP as σ^i and the excess charge density in the diffuse layer (inclusive of the OHP) as σ^d, it is apparent that the excess charge density on the solution side of the double layer is $\sigma^S = \sigma^i + \sigma^d$ so that $\sigma^M = -\sigma^S = -\sigma^i - \sigma^d$. While Figure 2.8 shows specifically adsorbed anions, it is important to note that specific adsorption of cations and neutral species can occur as well. In any case, the charge from species in the inner Helmholtz plane is balanced by electrolyte ions in the diffuse part of the double layer. This offers a route to understanding the mechanism by which the electrochemist exerts control over the structure and changes in the ESI: by modulating the potential applied to the metal, and thus the excess charge density σ^M, the solution side responds by restructuring under the influence of the large electric field at the ESI, with charged particles moving between the bulk solution and the electrical double layer to balance the charge. In the absence of faradaic reactions accompanied by electron transfer (i.e. a *non-faradaic process*), this process is called *double layer charging* and has a characteristic timescale which will be discussed in detail in Section 2.3.4, where it will be shown to be central to the experimental program of this thesis.

2.3.3 Electrochemical Measurements

Studying and affecting the microscopic properties of the ESI requires interfacing it with macroscopic experimental methods. This section will briefly describe some typical experimental setups germane to the work presented in this thesis.

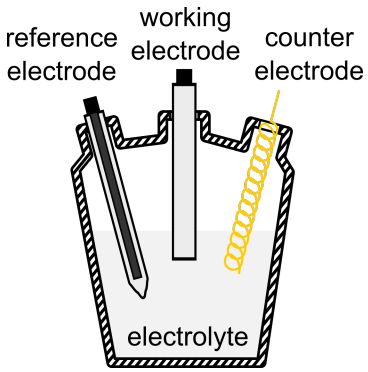

Figure 2.9: A typical three-electrode cell configuration. The working, counter, and reference electrodes are shown immersed in the electrolyte. The solution may be sparged with inert gas to remove dissolved oxygen and maintain an inert atmosphere in the cell; components necessary for this are not shown.

Electroanalytical methods monitor macroscopic observables such as electrical potentials, currents, and impedances, with well-developed theories connecting them to microscopic changes. Most commonly, electroanalytical measurements are made using a three-electrode configuration, Figure 2.9. The electrode at which the process of interest takes place is called the *working electrode, WE*. Depending on the needs of the experiment (e.g. in electrocatalysis) it may be reactive, but often it is an inert metal such as Au or Pt. (This thesis exclusively employs Au working electrodes.) Paired with the WE is the *counter electrode, CE,* (sometimes also called an auxiliary electrode) which passes current to balance the flow of charge at the WE. The choice of CE material is generally made on the basis of convenience and compatibility with the experiment; for example, electrodes which may form products that interfere with processes at the WE are generally avoided. For that reason, inert metals such as Pt or Au are often chosen. Finally, a *reference electrode, RE,* is selected and the potential of the working electrode is measured relative to the RE. The RE is chosen to provide a stable potential under the experimental conditions. The body of the electrochemical cell usually comprises a borosilicate glass vessel containing the electrolyte in which the WE and CE are immersed. Ground glass ports (not shown in Figure 2.9) admit two glass tubes which are used to sparge the solution with inert gas (usually Ar), removing dissolved O_2. In some cells, the RE is separated from the main cell volume by a reference arm incorporating a ground glass joint to mitigate ion migration from the reference solution. In aqueous media, electrolyte salts are usually chosen on the basis of good solubility and non-interference with WE processes. NaF and $KClO_4$ are common choices, with the former exhibiting less specific adsorption than the latter.

Electrochemical observables are measured with a potentiostat. To do so, the potentiostat drives the

necessary current through the WE/CE pair to maintain the desired potential difference across the WE/RE pair. The circuit measuring the WE/RE potential difference acts as a high impedance feedback loop. Many electroanalytical techniques rely on applying a particular potential function to the working electrode, so all potentiostats incorporate an analog function generator along with necessary components to digitize the analog response of the working electrode and interface with a data collection computer.

2.3.4 Microelectrodes

In section 2.3.2 the double layer charging time was briefly mentioned. In this section, the double layer charging time will be further developed by considering the response of an electrode to a potential perturbation.

A common experiment in kinetics is to perturb a thermodynamic property of a system (pressure, temperature, potential, etc.) and monitor the changes which occur as the system relaxes to a new equilibrium state. In electrochemistry, we speak often of "triggering" a process by applying a potential jump, say from some potential at which the system is static to one at which a reaction occurs. In pure electroanalytical chemistry, the current which flows upon application of a potential step is monitored, or additional information can be obtained by coupling a spectroscopic technique. In either case, it is desirable to have the potential step be applied almost instantaneously relative to the characteristic timescale of the reaction. If this is not the case, the system's kinetic response is convolved with the time-varying potential and extracting meaningful kinetic data is at best extremely challenging.

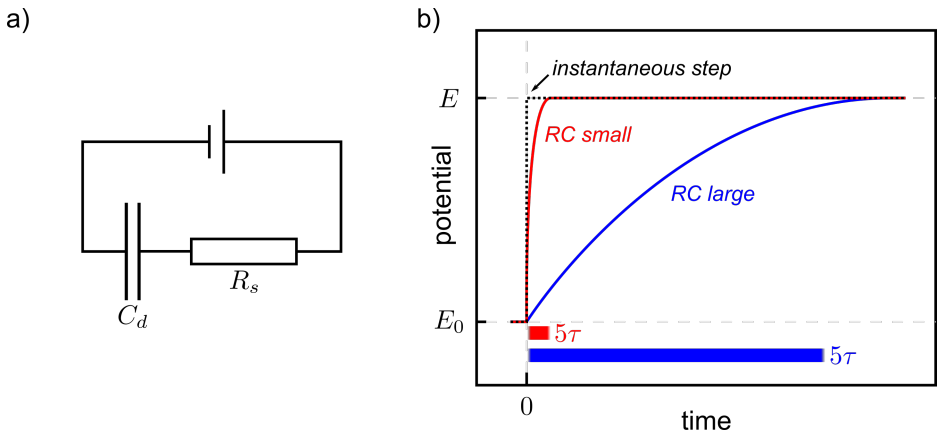

Figure 2.10: Double layer charging. a) An RC equivalent circuit used to model the electrical double layer. b) Plot of potential realised at the electrode-solution interface as a function of time, depicting an ideal instantaneous step and cases where RC is small and large.

To understand the potential response of the working electrode, the equivalent circuit in an electrochemical experiment can be examined. In the three-electrode configuration, the WE is grounded and the potential of the RE is controlled in order to apply the desired potential difference. In the absence of Faradaic charge transfer from solution-phase analytes, the response of the electric double layer can be modelled as a simple RC circuit as shown in Figure 2.10a. The equivalent circuit models the interface with a double layer capacitance

C_d and a solution resistance R_s. As an aside, it is noteable that the CE has a much larger geometric area than the WE, and its corresponding double layer capacitance $C_{d,CE}$ will be very large. However, $C_{d,CE}$ can be neglected in the following analysis by virtue of the design of the potentiostat. Although the potential step is applied across the WE/RE pair, the resulting current is forced to flow between the CE/WE pair. In this arrangement, the potential of the counter electrode fluctuates in order to force the necessary current to flow, but the time constant of that circuit has no bearing on that of the WE/RE circuit.

Then, in response to a potential step of magnitude E_{step}, the time-dependent interfacial potential $E(t)$, Fig 2.10b, is

$$\frac{E(t)}{E_{step}} = 1 - \exp\left(\frac{-t}{R_s C_d}\right)$$

which is plotted in Figure 2.10b for two values of $R_s C_d$.

Upon application of a potential step the interfacial potential rises exponentially with a characteristic timescale $\tau = R_s C_d$, where the interface is greater than 99% charged after 5τ. Therefore, achieving an "instantaneous" potential step requires τ to be reduced so that 5τ is much shorter than the characteristic time scale of the experiment. As an example, if one wished to collect data with microsecond resolution it would be necessary to reduce τ to 200 ns or less.

Inspecting $\tau = R_s C_d$, it is apparent that control of τ relies on minimizing the solution resistance and the double layer capacitance. The solution resistance is a function of the ionic strength of the electrolyte, but for aqueous systems this is practically limited to around 10 - 100 Ω by the solubility of electrolyte salts. The double layer capacitance, however, is a function of the electrode area. The capacitance per unit area of the Au/electrolyte interface is around 50 µF/cm^2. Considering that a 500 µm by 5 mm band electrode has $C_d \approx 1.25$ µF and taking $R_s = 10$ Ω, a time constant $\tau = C_d R_s \approx 12.5$ µs can be achieved, which allows time resolution of several tens of microseconds. Such an electrode, with one critical dimension in the range of hundreds of micrometers, is often called a microelectrode, with those having critical dimensions below 25 µm being called ultramicroelectrodes (UMEs).

The low RC time constants of (ultra)microelectrodes can pose problems for electrochemical experiments. A time constant on the order of $\tau \approx 10$ µs implies that the potentiostat electronics must have a bandwidth of at least 100 kHz or better. A slower instrument would simply not be able to apply a suitably fast step. In practice, high-end potentiostats such as the HEKA PGSTAT590 used in this thesis have a user-adjustable bandwidth control. The two highest settings on the PGSTAT590 are 100 kHz and MAX, where the latter applies no bandwidth limiting circuit and simply allows the system to drive potentials as fast as its electronics allow. Because this is higher than 100 kHz, the temporal response is more than suitable for the experiments completed in this thesis.

(Ultra)microelectrodes have been used extensively in electroanalysis, in part for the low rise time detailed above but also because their small size permits sampling of minute quantities of material. Perhaps the most consequential application has been in scanning electrochemical microscopy (SECM) as pioneered by Bard

and coworkers.[39–41] SECM takes inspiration from other scanning probe microscopies (e.g AFM, STM) to collect nanoscale images of surface reactivity. The small size of the UME tip has been key to achieving high spatial resolution electrochemical imaging.

Other work has exploited a collector-generator geometry similar to the familiar rotating ring disk electrode. Compton *et al.* have reviewed the status of planar collector-generator electrodes supported insulating surfaces.[42] In particular, references therein show that interdigitated arrays of microelectrodes can be used for calibration-free measurements of both bulk analyte concentration and diffusion coefficient. Similar experimental work from the Fritsch group has used this property to discriminate between dopamine and norepinephrine.[43]

The finite rise time of the working electrode raises an issue central to the motivation of this thesis: in order to do time-resolved spectroelectrochemistry with high time resolution (few microseconds or less), it is necessary to work with micro- or even ultramicroelectrodes. However, section 2.2.2.3 demonstrated that conventional thermal sources, which have low brilliance, are incapable of focusing on such small spots with good efficiency. Instead, such a task requires highly brilliant synchrotron infrared radiation to achieve useful photon flux on such a confined area.

2.3.5 Photolithography as a Fabrication Method for Microelectrodes

Because traditional machining techniques simply cannot achieve sufficient quality at small scales, UMEs in the academic literature have been prepared in a variety of creative ways. Although methods of fabrication for nano-, ultramicro-, and microelectrodes are varied, the focus here will be on those prepared by in a planar geometry on an insulating substrate. To that end, photolithography is a superb choice for its flexibility and fidelity.

The tools necessary to prepare microelectrodes on dielectrics or semiconductors have existed for many decades now in the microelectronics industry. Indeed, there has been a long-standing campaign to miniaturize metal interconnects on chips to keep up with decreasing transistor size.[44,45] The extensive use of Si as a substrate in microfabrication is highly beneficial for the goals of this thesis, as Si is a common material for internal reflection elements used in ATR and ATR-SEIRAS (*vide infra*).

Microelectrodes in this thesis were prepared by direct-write ultraviolet photolithography at the SyLMAND beamline at CLS.[46] Although the direct-write system was installed in SyLMAND to support ongoing research and development in x-ray lithography mask preparation,[47,48] the system is generally amenable to UV photolithography fabrication. UV photolithography is a fabrication method by which microscale structures are selectively patterned on flat substrates. The technique proceeds by several processing steps. First, the substrate is cleaned, usually with a solvent or by reactive ion etching, then a UV-sensitive polymer solution called a photoresist is spin-coated. The resist-coated wafer may be soft-baked on a hot plate depending on the resist chemistry before being selectively exposed with UV radiation. For positive-tone resists, irradiation generates a photoacid from a precursor chemical in the resist. During a post-exposure bake, the high tem-

peratures drive cleavage of the polymer backbone, rendering exposed regions of the resist soluble. Immersion in a solvent called the developer removes the resist from these regions, leaving a photo-resist coated wafer which has been selectively patterned. The resist layer can act as a mask for subsequent etching or material deposition steps.

2.4 Spectroelectrochemistry with ATR-SEIRAS

2.4.1 Spectroelectrochemistry

Although classical electroanalytical techniques have many benefits, and have yielded deep insight into some aspects of electrochemical systems, they lack direct structural information. This observation has motivated the coupling of spectroscopy to electrochemical techniques, resulting in the varied field of *spectroelectrochemistry, (SEC)*. A key feature of work in spectroelectrochemistry is the large number of *in situ* techniques. While *ex situ* studies such as scanning electron microscopy of catalytic surfaces before and after use, or vibrational spectroscopy of an electrodeposited film certainly offer useful information about the start and end points of a process, *in situ* measurements offer a more accurate picture of what is actually happening at the ESI. An excellent discussion of the fundamentals of *in situ* SEC methods is given in a technical report by the IUPAC Commission on Electrochemistry[49] which surveys the field until 1998. Several comprehensive reviews have appeared in recent years. Zhai *et al.* have discussed major developments in several commonly applied SEC methods, including UV-visible and near-infrared methods, as well as more niche techniques exploiting x-ray, vibrational, and fluorescence techniques.[50] Of particular note in Zhai *et al.* is the focus on the practical details of spectroelectrochemical cell construction: integrating a complete three-electrode cell into a setup which is compatible with the unique optical demands of a given technique. This is a significant component of the day-to-day work of the SEC practitioner and has merited a thorough review of its own.[51]

Many of the recent reviews have focused on key sub-fields, a few of which are highlighted here. Garoz-Ruiz *et al.* have reviewed the use of SEC for quantitative chemical sensing studies.[52] Dunsch has traced the early influences of electron spin resonance (ESR) on SEC and highlighted the usefulness of hyphenated ESR-SEC techniques when studying elementary electrochemical reaction mechanisms, particularly on organic electronics.[53] Cowan and Hardwick discuss the use of vibrational and nonlinear techniques to probe lithium-ion and lithium-oxygen batteries.[54] Finally, Lozeman *et al.* have written a tutorial review for the new practitioner which highlights the techniques they believe have the most potential for the future.

Notably in Lozeman *et al.*, the authors identify FT-IR spectroelectrochemistry as being particularly promising for the future. The advantages of infrared spectroscopy have been discussed in section 2.2, particularly its chemical sensitivity and lack of vacuum requirement, and in 1968 the bulk of solution was interrogated using a thin-layer cell by Heineman *et al.* incorporating optically transparent electrodes.[55] However, infrared spectroelectrochemistry came into its own starting in 1980 with work from Bewick, Kunimatsu, and Pons which applied infrared spectroscopy to the ESI for the first time.[13] In that paper, they identified one of

the major challenges of IR-SEC, namely the strong attenuation of IR light by solvent layers. This put strong limits on the pathlength (and thus the thickness) of a spectroelectrochemical cell designed for transmission or external reflection. The confined geometry of thin-layer cells imposes difficulties in fabrication and alters mass transport characteristics of electrochemical reactions. When comparing results to theory, the restricted diffusion obviates the use of analytical solutions derived assuming semi-infinite diffusion, requiring careful numerical modelling. Although this has been done successfully by several groups, an internal reflection technique (ATR-SEIRAS, *vide infra*) was fairly quickly developed which avoided these difficulties.

2.4.2 Introduction to ATR-SEIRAS

Attenuated total reflection surface-enhanced infrared absorption spectroscopy, or ATR-SEIRAS, is a surface-sensitive vibrational spectroscopy which is well-suited to the study of electrochemical systems, Figure 2.11. Since its introduction in the 1980s by Masatoshi Osawa, the technique has a found a core user base of around a dozen groups with approximately another seventy-five groups employing it for one or two publications. As such, electrochemical ATR-SEIRAS is a relatively niche technique, with approximately 250 peer-reviewed publications to date, especially when compared to a related technique, surface enhanced Raman spectroscopy (SERS). (At the time of writing there are about 1500 research papers on electrochemical SERS alone.)

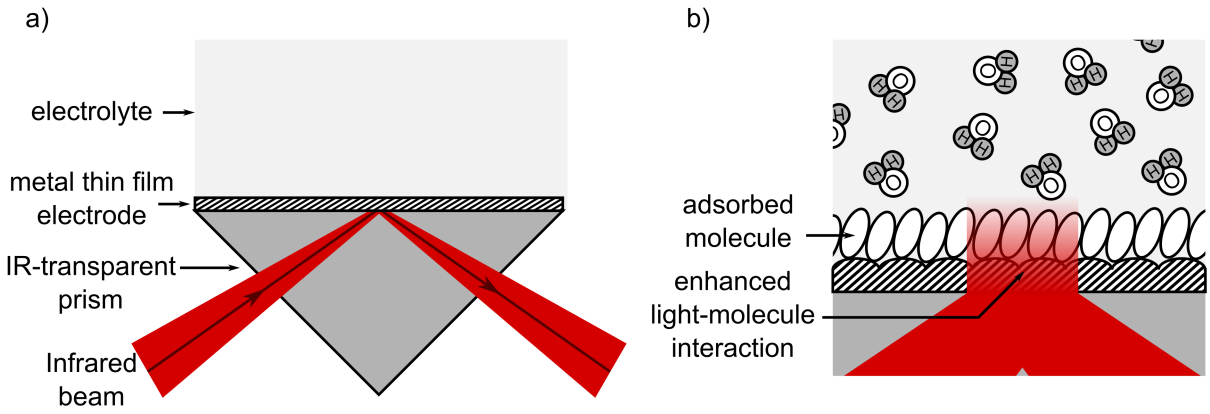

Figure 2.11: The ATR-SEIRAS method. a) A macroscopic view of the experimental setup. The infrared beam passes through an infrared-transparent prism and is totally internally reflected at the electrode/solution interface. The solution-facing side of the prism is coated with a nanostructured metal thin film electrode. b) Microscopic view of ATR-SEIRAS. Molecules are shown adsorbed at the surface of the metal thin film. Infrared light couples with the metal film resulting in increased signal strengths from surface adsorbed molecules.

ATR-SEIRAS relies on the interaction of IR light with a metallized ATR element to enhance the absorption cross section of molecules adsorbed at the metal/electrolyte interface. Enhancement factors on the order of 10 - 100 are typical[56], about three orders of magnitude lower than most SERS experiments, but this is enough to provide submonolayer detection limits. As a result, by varying the potential applied to the metal film, which acts as the working electrode, detailed information can be collected on the structure of molecules,

Table 2.1: Selected areas of application for ATR-SEIRAS

application	examples	references
electrocatalysis	small molecule electrooxidation	57–62
	catalyst poisoning	63–65
	electroreduction	66–68
	potential oscillations during electrocatalysis	60
self-assembly	thiols	69
	viologens	70
	aromatic carboxylic acids	71
	pyridine	72,73
	interfacial water structure	74
bioelectrochemistry	supported lipid bilayers	75,76
	membrane proteins	77–79
	respiratory proteins	80
	bacteria	81

their adsorption geometries, and electrogenerated products. This has significant consequences for catalytic studies, as the SEIRAS effect has been demonstrated on a variety of catalytically relevant metals such as Au, Pt, Ag, Ru, Rh, Ni, and Cu (see references in 56), although oxide formation can cause experimental complications for some of these.

2.4.2.1 Applications of ATR-SEIRAS

Table 2.1 summarizes some representative electrochemical ATR-SEIRAS references along three major themes of application: electrocatalysis, bioelectrochemistry, and self-assembly.

ATR-SEIRAS is uniquely suited to studying electrocatalytic reactions on metal surfaces. The breadth of compatible metals (and alloys), submonolayer detection limits, and excellent molecular structural sensitivity inherent to vibrational spectroscopy make it a powerful tool to tease apart electrooxidation mechanisms of small molecules[57–62] and catalyst poisoning[63–65] for fuel cell applications or electroreduction reactions for CO_2[66], O_2[67], or N_2[68] reduction. Because it is highly amenable to *in situ* or *operando* measurements in real electrolytes, it is an excellent complement to surface characterization tools that require high vacuum conditions such as STM or X-ray spectroscopies.

Although the ATR-SEIRAS literature is dominated by electrocatalysis work, the study of molecular self-assembly has benefited from the same features. The surface selection rules of ATR-SEIRAS can be used to extract detailed information on the orientation of adsorbed molecules such as thiol self-assembled monolayers.[69] Information beyond molecular orientation can be collected because molecular vibrations in condensed matter are highly sensitive to their local environment. This has allowed detailed study of the

adsorption and self-assembly of organic molecules with[70,82] and without[72,73] redox activity. Fundamental questions about the structure of the electric double layer have been explored by determining the structure of water at the Au/electrolyte interface as well.[74]

Finally, a fascinating body of work has accumulated in bioelectrochemistry. Surface modification with biocompatible ligands and subsequent adsorption of proteins has been developed extensively by the Armstrong group[83–85], and there has been great effort by Vincent *et al.* to couple electrochemical techniques to vibrational techniques[86–89]. Using ATR-SEIRAS, detailed studies of the immobilization of redox active protein on a Au surface[78] and its conformational changes[79] have been completed. Complex I, a respiratory protein, has also been studied in a similar fashion.[80] These methods are also extensible to redox-active bacteria.[81] Furthermore, the potential-dependent hydration of phospholipid bilayer membranes[75] has been investigated, and, when coupled with neutron reflectometry, ATR-SEIRAS has yielded insight into the position and redox behaviour of ubiquinone in model membranes.[76]

2.4.2.2 Comparison to Other Surface-Sensitive Vibrational Spectroscopies

A variety of spectroscopic techniques exist for interrogating surfaces and interfaces. A general problem posed by the electrode/solution interface is that it is usually buried. The interface in question is bounded on one side by a metallic solid and on the other by a liquid. On their own, or in contact with atmosphere or vacuum, these materials can be interrogated but the metal/liquid interface is a challenging one to sample. Bulk metals are opaque into x-ray wavelengths, and liquids are transmissive only in certain frequency ranges. Furthermore, the lower dimensionality of surfaces compared to the bulk reduces the number of molecules which can be sampled and generally decrease signal compared to bulk measurements.

As stated earlier, surface-enhanced Raman spectroscopy (SERS) has been productively applied to electrochemical measurements. Visible frequency lasers used in SERS rarely encounter problems of absorption by electrolyte, except by strongly coloured analytes, and near-IR radiation is transmitted by water. Indeed, SERS has great potential to be used alongside SEIRAS due to the complementary nature of the spectra. Dual-mode SERS and SEIRAS measurements were recently demonstrated by my colleague Osai Clarke.[90] Although SERS offers many similar benefits to SEIRAS, it is unsuitable for fluorescent materials or those which are very sensitive to intense visible frequency radiation.

An extremely powerful surface-sensitive technique is vibrational sum-frequency generation (VSFG).[91,92] In VSFG, a visible and infrared frequency laser overlap spatially at an interface. Because the interface has broken centrosymmetry by definition, emission of a sum-frequency photon is possible, effectively allowing the second order nonlinear susceptibility of the interface to be probed. Vibrational information encoded in this quantity is used in a manner similar to the interpretation of other vibrational spectra. Despite the advantages, there are real challenges to the technique. In homodyne-detected VSFG, submonolayer detection is generally much poorer than SERS or SEIRAS and spectral lineshapes are convolved with both real and imaginary parts of the susceptibility, only the latter of which contains absorption information. The development of heterodyne

detection methods[93–95] has greatly improved detection limits and allowed unambiguous determination of the imaginary component of the susceptibility, but is severely limited by instrumental complexity, the need for very precise phase references, and the complex phase offset introduced by metal surfaces.[96]

2.4.3 Theory

The mechanism of ATR-SEIRAS was initially the subject of some debate. One early explanation was to draw an analogy to surface-enhanced Raman spectroscopy (SERS), where incident photons couple to surface plasmon-polariton modes in structured metal nanoparticles. Excitation of such modes induces a greatly enhanced local electric field which falls off very rapidly near the particle. Because the probability of a molecule absorbing an IR photon scales with $|E|^2$, it was suggested that the increased local electric field is responsible for signal enhancement.[97] Although this has been verified for SERS,[98] the evidence for this mechanism for ATR-SEIRAS is not convincing. Osawa *et al.* summarized the evidence against this mechanism in the mid-eighties.[99] They noted that for metal thin films in the Kretschmann configuration, surface plasmon polariton (SPP) excitation occurs resonantly at AOI very near the critical angle, θ_c. However, they had observed that SEIRAS enhancement was greatest at near-grazing AOI as shown in Figure 2.12,[100] far from θ_c. This provided strong evidence against the SPP description.

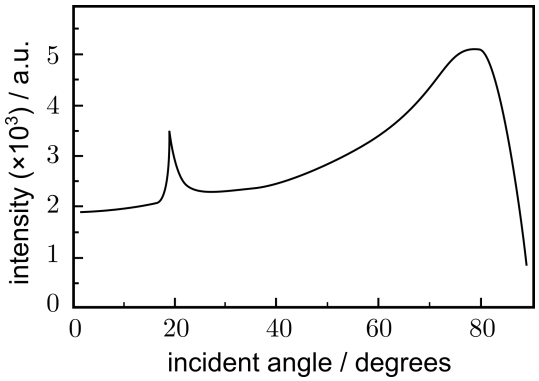

Figure 2.12: Dependence of SEIRAS signal intensity on angle of incidence. SEIRAS enhancement peaks at high AOI. Adapted from reference 18.

A successful theoretical description of the enhancement mechanism with semi-quantitative results was developed by Osawa and coworkers starting in the late eighties.[18,99,100] The model describes the perturbation of the metal thin film's optical properties, namely its permittivity ϵ, by the presence of an adsorbed analyte. From there, the Fresnel reflection equations could be used to calculate the reflectivity of the interface with and without analyte present.

In order to describe the optical properties of the metal film in the presence and absence of analyte, Osawa *et al.* used an effective medium approximation (EMA), a schematic of which is shown in Figure 2.13. The ATR element (Si in Figure 2.13) was modelled as a semi-infinite layer with permittivity ϵ_{Si}. The thin film was modelled in two parts: a uniform thin metal film (typically 10 nm) with complex permittivity ϵ_m,

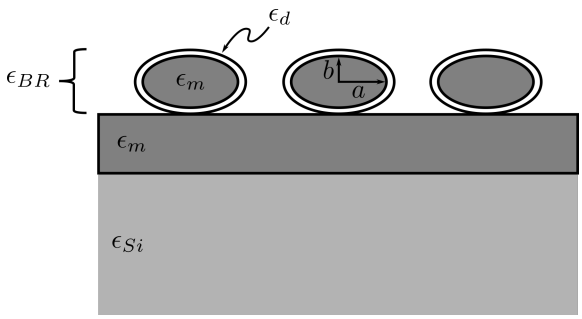

Figure 2.13: Schematic of the Bruggeman effective medium used by Osawa to describe the mechanism of ATR-SEIRAS.

and a composite layer whose permittivity ϵ_{BR} was described by the Bruggeman effective medium theory (BEMT).[101] The composite layer was composed of a layer of uniform, randomly oriented prolate ellipsoids with the same permittivity as the metal film, ϵ_m, and aspect ratio $\eta = a/b$, where a and b are the radii of the long and short axes of the ellipsoid, respectively. The ellipsoids occupy a fraction F of the composite layer in a host medium of permittivity ϵ_h. Using the BEMT, the permittivity of the composite film is

$$\epsilon_{BR} = \epsilon_h \frac{3(1-F) + F\alpha}{3(1-F) - 2F\alpha}$$

where α is the polarizability of the metal ellipsoid. It is here that the permittivity of the analyte makes its way into the model. The complete expression for α is given in reference 18, but for an ellipsoid surrounded by a molecular layer of permittivity ϵ_d then

$$\alpha_{\perp,\parallel} = f(\epsilon_m, \epsilon_d, \epsilon_{BR}, L_1, L_2, Q)$$

where $\perp$ and $\parallel$ refer to the applied field being perpendicular and parallel to the surface, respectively. The quantities L_1 and L_2 are depolarization factors of the uncoated and coated particles, respectively, and can be calculated with equations given by Stoner *et al.*[102] Q is the volume ratio of uncoated and coated particles V_1/V_2, which incorporates the thickness of the molecular layer.

We can gain some physical insight by considering how a monolayer of molecules modulates the reflectivity of the interface. Consider first the ATR experiment, where we are probing the reflectivity of the Si/liquid interface. Compared to metals, Si is not a very polarizable material. Therefore, adding a monolayer of molecules, which can be imagined as oscillating dipoles, does not affect the optical properties of the Si/liquid interface very much. (One could also consider the interaction of the evanescent wave and the analyte: light-matter interactions for molecular vibrations are generally very weak, so we expect the absorption to be very low.) In the ATR-SEIRAS experiment, light reaching the detector is now reflected off the metal/liquid interface. In contrast to Si, metal films/nanoparticles are generally highly polarizable and so they are very sensitive to their local dielectric environment. Therefore, adding a monolayer of molecules drastically changes the polarizability, and thus the reflectivity, of the metal film at frequencies matching those of the analyte's vibrational resonances.

2.4.3.1 Selection Rules

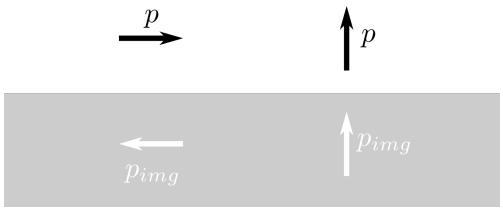

Figure 2.14: SEIRAS selection rule. At left, a horizontal dipole p is shown which induces an image dipole p_{img} of equal magnitude but opposite direction. The net dipole is zero and no SEIRAS signal is observed. At right, the image dipole is parallel and a net dipole exists, rendering the signal observable.

In Section 2.2.1, it was stated that the probability of non-zero IR absorption requires the transition dipole moment, M_{21}, to be nonzero. ATR-SEIRAS imposes another selection rule, depicted graphically in Figure 2.14. Only molecular vibrations with a component of the transition dipole moment normal to the interface are SEIRAS-active. The physical origin of the rule can be explained by the formation of induced image dipoles. Figure 2.14) shows a dipole oriented parallel to the metal-coated interface. The presence of the real dipole induces an image dipole which is equal and opposite, and the net dipole is zero. In contrast, a dipole oriented perpendicular to the interface induces an image dipole which adds constructively so that the net dipole is nonzero.

2.4.4 Experimental Setup

SEIRAS requires integration of a complete three-electrode cell with an FT-IR instrument. This presents some interesting challenges in the construction of a suitable spectroelectrochemical cell. Probably the most significant consideration is electrical contact with the metallized ATR element which serves as the working electrode. In addition, the cell must stand up to the aggressive cleaning procedures employed for typical electrochemical glassware. It should be liquid- and gas-tight to allow the electrolyte to be purged of dissolved oxygen and prevent electrolyte leakage onto sensitive optical components in the ATR accessory.

Spectroelectrochemical cells for ATR-SEIRAS have generally been homebuilt, and those used in this thesis are no different. Below, I'll describe one such cell, the "glass castle," which has been developed through the efforts of several previous students, the essential features of which are captured in Figure 2.15. Modifications to this design to meet specific needs of this thesis are discussed in experimental chapters.

2.4.4.1 "Glass Castle" ATR-SEIRAS cell

The glass castle is designed to mate with a commercial variable angle ATR accessory, the PIKE VeeMAX III. The VeeMAX design accepts the converging beam from the FTIR spectrometer, collimates it, and re-focuses it to a spot in the plane defined by the accessory's top plate.

A custom-machined steel or aluminum top plate features a circular cutout to which the glass castle cell attaches by screws. The top plate positions the assembled cell such that the ATR element is at focus of the

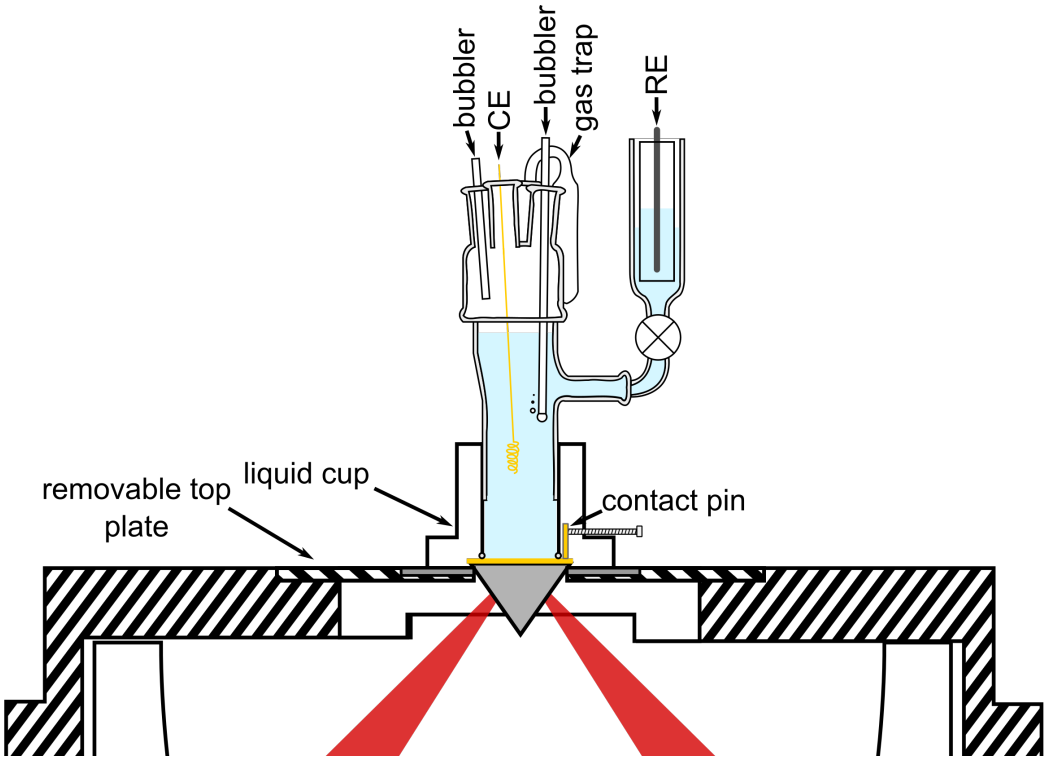

Figure 2.15: Schematic of the glass castle ATR-SEIRAS cell, shown mounted on the variable angle ATR accessory.

ATR accessory. The ATR element is held in a machined polyether ether ketone (PEEK) cradle which allows the IR beam to impinge on the crystal. A Teflon liquid cup is fastened to the cradle, compressing a Viton O-ring onto the metallized surface of the ATR element. This provides a tight seal to retain liquid inside the cell. The O-ring diameter is deliberately much smaller than that of the metallized area. This allows electrical contact to be made with the metal film by Au-coated spring-loaded pins which extend from the body of the liquid cup. A set screw is advanced to touch the pin, providing a stable place to secure an alligator clip for the working electrode.

The liquid-containing portion of the cell is defined by the liquid cup and a glass body which threads into the cup. The body is sealed at a ground glass joint by a cap with ground glass ports for the counter electrode (generally a coiled Au wire) and glass tubes for sparging the solution with inert gas ("below bubbler") and maintaining an inert atmosphere in the cell headspace ("above bubbler"). Generally the solution is only sparged for about 30 minutes immediately prior to an experiment, after which the below bubbler is turned off and inert gas flow is maintained through the above bubbler. A gas trap filled with ultrapure water prevents backflow of atmospheric gases into the cell.

A ground glass joint with a stopcock (also ground glass) connects the main body of cell to the reference arm. The reference arm is filled with electrolyte, open to atmosphere, and incorporates a homemade reference electrode, generally Ag/AgCl in saturated KCl solution. The ground glass stopcock retards Cl^- migration and dissolved O_2 diffusion into the main cell. (Au can be anodically etched in Cl^--containing electrolytes,

which rapidly degrades SEIRAS performance.)

2.4.4.2 Instrumentation

Electrical contact to working, counter, and reference electrodes is made with alligator clips connected by BNC cables to a HEKA PG 590 potentiostat. Data are collected with custom-written Labview software running on a personal computer interfaced to the potentiostat with a National Instruments USB 6351 X-series data acquisition card. FTIR measurements on a conventional FTIR bench are made on Bruker VERTEX 70 FTIR spectrometer with a liquid nitrogen cooled Kolmar MCT detector.

2.4.5 Thin Film Electrodes

A central part of the ATR-SEIRAS experiment is the metallized thin film electrode (TFE) which is deposited on the ATR element. Although there are a variety of metals reported in the literature on several different ATR element materials, by far the most common is Au on Si and this discussion will focus on that combination.

2.4.5.1 Deposition and Texturing Methods for Au/Si Thin Films

There are two major fabrication methods reported in the literature: electroless deposition and metal sputtering. The earliest TFEs for ATR-SEIRAS were prepared by metal sputtering[18,97,103–105] and this method still has many adherents. Metal sputtering is a well-developed technique owing largely to the sustained effort of the microelectronics community. One common implementation, magnetron sputtering, is characterized by relatively high deposition rates, the comparative ease of deposition of conductive, semiconductive, or insulating media, and good coverage.[106] In brief, a large negative voltage (typically hundreds of volts) is applied to a target material in the presence of ions of inert gas. Positively charged ions bombard the target and transfer their energy collisionally to target atoms, ejecting them from the solid target where they eventually deposit on the substrate.

In contrast to sputtering, which is a physical vapour deposition technique reliant on vacuum equipment, electroless deposition exploits galvanic exchange in solution to chemically deposit Au atoms on Si surfaces. (The term "electroless" was coined to denote that although this is an electrochemical reaction there is no external current provided.) Electroless deposition of TFEs for ATR-SEIRAS was first reported by Osawa.[107] This too originally developed in microelectronics.[108] The procedure reported by Osawa involved stripping the native silicon oxide layer in 40 % NH_4F solution for several minutes followed by deposition of Au at 60 °C from a solution containing 0.015M $NaAuCl_4 \cdot 2\,H_2O$ + 0.15 M Na_2SO_3 + 0.05 M $Na_2S_2O_4 \cdot 5\,H_2O$ + 0.05 M NH_4Cl. The exact mechanism is still debated, but it is well known that Au deposition proceeds through the dissolution of Si according to the following half-cell reactions[109]:

$$Si\,(s) + 6\,HF\,(aq) \longrightarrow {SiF_6}^{2-}\,(aq) + 6\,H^+\,(aq) + 4\,e^-$$

$${AuCl_4}^-\,(aq) + 3\,e^- \longrightarrow Au\,(s) + 4\,Cl^-\,(aq)$$

Also relevant is the beneficial effect of HF stripping the native oxide layer on Si. Films deposited from electroless solutions were found by Osawa to be more mechanically stable than those prepared by metal sputtering.

Once the metal TFE has been deposited a second critical preparation step must be undertaken. Empirical enhancement factors of as-prepared films vary, but in most cases they can be improved by a process of electrochemical texturing. This step is given various names in the literature, including electrochemical annealing or sometimes electropolishing. In any case, it involves carefully cycling the potential of the TFE between anodic potentials at which Au oxidation occurs and cathodic potentials just before hydrogen reduction begins. Many aqueous electrolytes are used for this purpose, sulfuric acid and acetic acid being fairly common[57,67,74,110]. It is empirically observed that the signal enhancement of the film usually improves with prolonged cycling, and the claim made in the literature is that cycling the surface in this way promotes mobility of the gold atoms on the surface, allowing the island structure of the film to anneal and increase the size of the islands, thereby improving the enhancement.[111] (There may also be contributions from improving the film cleanliness by desorbing contaminants such as hydrocarbons.) Specific adsorption of electrolyte ions, e.g. sulfate on low-energy gold faces, is often invoked as a mechanistic explanation. The claim is as low energy faces are stabilized, their growth is promoted and sulfuric acid electrolytes have been used to prepare preferentially textured Au(1 1 1) TFEs.[74,111–113]

Although little is said in the literature about the practical aspects of TFE preparation, a brief discussion is relevant for this thesis, as it will motivate some key experimental considerations. The Burgess group has extensive experience with both sputtered and electroless films and I summarize here the collective knowledge as of this writing. Although electroless films do indeed seem to have better mechanical stability (and frequently better signal enhancement by up to a factor of about two), the fabrication process is extremely difficult and highly variable. Reaching a level of skill where one sees consistent success often takes several months of sustained practice and great diligence in preparation of stock solutions. In particular, the gold solution is prepared fresh each time. Even after one becomes skilled in the art, most students will achieve about a 70% success rate; this combines the frequency of prepared films with negligible signal enhancement as well as mechanical film failure before any data is obtained. In contrast, sputtered films are comparatively simple to prepare, though by no means are they foolproof. Process parameters for sputtering are unique to each machine, so sputtering with a new deposition setup inevitably requires time-intensive parameter optimization before good quality films are obtained. That said, generally once the process is optimized it is at least as reproducible as electroless deposition and requires less effort from the student. Avoiding HF is also an advantage.

2.4.5.2 Mechanical Stability of Au/Si Thin Film Electrodes

The mechanical failure of Au/Si thin film electrodes by delamination is a constant threat to ATR-SEIRAS experiments. Understanding the microscopic factors which affect the adhesion of thin films has inspired a

significant body of work, mostly from semiconductor and microelectronics fields.[114,115] Many failure modes have been identified and the challenge of making meaningful measurements of film adhesion has been reviewed at length.[116–118] The fundamental limit is the poor adhesion of Au on Si due to the poor lattice mismatch. The lattice constants of fcc Au and Si are 4.07 and 5.34 Å, respectively,[119,120] and strain due to lattice mismatch can result in considerable film stress.[121]

The exact nature of the Au/Si interface in TFEs for ATR-SEIRAS is debatable. Although some authors in the ATR-SEIRAS literature have invoked a chemical gold silicide bond formed during electroless deposition,[107] evidence for this is mixed. Physical bonding certainly occurs; Prudnikov and coworkers have shown that in general the van der Waals interaction force between metals and semiconductors is attractive.[122] Work in UHV with well-defined single crystal Si wafers at room temperature has shown the formation of gold silicide bonds by high resolution electron spectroscopies,[123,124] and under those conditions the Au/Si interface is not sharply defined but rather a diffuse alloy approximately 2 nm thick (see ref. 124 for a detailed review). However, under conditions used for electroless deposition it is unlikely that a gold silicide bond forms. In reference 107, Osawa invokes Au-Si bond formation to explain the excellent adhesion, but work published at almost the same time by Carraro[109] characterising the electroless Au/Si interface by XPS showed that no such bond forms. (They did, however, observe silicon oxide growth correlated with deposition time.) Au TFEs prepared by sputtering are usually deposited on mechanically polished Si crystals. At ambient conditions, the native oxide layer forms rapidly and investigation of Au sputtered on oxide-coated Si surfaces results in films with poor adhesion and a sharp SiO_2/Au interface with no chemical bonding.[125]

The microscopic factors which drive film failure are likely due to the relatively high stresses in Au thin films on Si. During deposition, the stresses in sputtered films of Au on Si are known to evolve rapidly with thickness from tensile to compressive stress.[117,126] In electrochemical experiments, electrode stress is known to vary with potential due to surface reconstruction of Au, evolution of gas bubbles, or oxidation and reduction of the surface.[127,128] Taken together, these factors likely drive the mechanical delamination of Au thin film electrodes. Furthermore, sputter deposition is known to induce excess compressive stress due to the so-called "atomic peening mechanism", where energetic particles bombard the film during deposition, compressing the film. Thermal stress must also be considered. The coefficient of thermal expansion for Au is about 5 times higher than Si and 20 times higher than SiO_2. With this in mind, one explanation for the weaker adhesion of sputtered Au films for ATR-SEIRAS might be as follows. In our lab, Au layers are sputtered onto Si crystals with the oxide layer intact. Considering the uncontrolled substrate temperature during sputtering, it is possible that subsequent cooling over many tens of degrees results in enough thermal stress to delaminate the films. In contrast, during electroless deposition the oxide layer is stripped and the substrate is only heated about thirty degrees above room temperature. Electroless deposition therefore would seem to provide a small CTE and temperature difference. This further suggests that slow cool-down periods of sputtered films might improve adhesion by allowing strain relaxation.

2.4.6 Non-Faradaic Adsorption of 4-Methoxypyridine as an ATR-SEIRAS Probe System

The focus of this thesis is on validating new approaches to ATR-SEIRAS. To this end, it is desirable to work with a well-understood test sytem which has a well-defined spectroscopic and electrochemical response, is surface-active, relatively benign, and is stable under ambient conditions. The non-faradaic adsorption of a pyridine derivative, 4-methoxypyridine (MOP), is an excellent candidate.

The adsorption of pyridine and its derivatives on metal surfaces is of particular interest in stabilizing Au surfaces during nanoparticle formation.[129–131] For the purpose of this thesis, the potential-dependent adsorption behaviour is most salient.

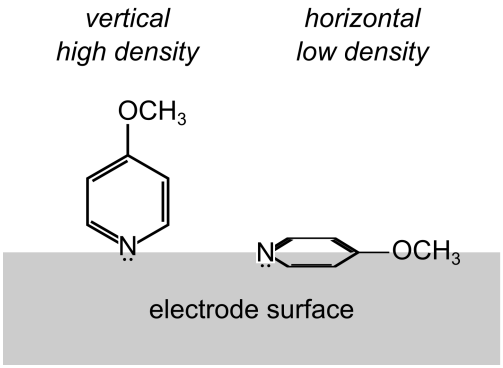

Figure 2.16: Two modes of MOP adsorption on Au surfaces.

Pyridine derivatives adsorb on Au surfaces in two different motifs: a high-coverage σ-type "end-on" motif through the nitrogen lone pair, and a low-coverage π-type "flat" motif through the π system. This is particularly evident on single-crystal Au(111) electrodes[131], but in neutral electrolytes, polycrystalline Au films such as those used for ATR-SEIRAS only exhibit adsorption through the high-density state.[73] In this state, the A'-symmetric normal modes, which are collinear with the principal molecular axis, are parallel to the surface normal, rendering them SEIRAS-active. A complete assignment of the vibrational bands of MOP is given in reference 73 on the basis of DFT simulations and experiment, and the most germane to this work are tabulated in Table 2.2. There are many bands, the strongest of which are noted with an *s* in the fourth column of Table 2.2.

The bands tabulated here are for neat MOP measured in an ATR geometry; the spectroscopic effects of adsorption have been elucidated by Quirk *et al.*[73] It is important to note that while MOP adsorption is potential-dependent, the exact shape of the adsorption isotherm depends on MOP concentration and electrolyte pH.[131] Neutral electrolytes (e.g. NaF and $KClO_4$) and concentrations around 0.1 mM will be used in this thesis, so only those conditions will be described in the following text. MOP can be fully desorbed from the Au/electrolyte interface by application of a suitably negative potential. At potentials below -600 mV vs Ag/AgCl MOP is completely replaced by interfacial water. At more positive potentials,

MOP surface coverage increases until reaching full monolayer coverage around -200 mV vs. Ag/AgCl. It has been found that full coverage also corresponds to maximum SEIRAS signal intensity.[73] Therefore, biasing the working electrode at a suitably negative potential, E_{ref}, collecting a reference spectrum I_{ref}, and repeating with a suitably positive potential E_{sample} to collect I_{sample} allows potential-difference absorption spectra to be calculated, $A = -\log(I_{sample}/I_{ref})$. In such a spectrum, because the reference spectrum is of the MOP-free interface, positive absorbance peaks are visible corresponding to adsorbed MOP.

Two spectroscopic changes have been observed by Quirk *et al.* upon adsorption of MOP onto polycrystalline Au surfaces.[73] First, although the v_{8b} mode at approximately 1567 $cm^{-1}$is A'-symmetric and should be SEIRAS-active, in practice it is tilted substantially with respect to the molecular axis, and this mode is rarely seen in ATR-SEIRAS spectra without excellent signal-to-noise. Second, both the v_{8a} and the C-O-C asymmetric stretching mode (about 1590 and 1280 cm^{-1}, respectively) have a noticeable blueshift by about 20 cm^{-1}. Taken together, these changes are indicative of the spectroscopic interrogation of MOP adsorbed at the Au/electrolyte interface, allowing adsorbed MOP to be differentiated from that in the solution phase.

Table 2.2: Selected normal modes of 4-methoxypyridine observed in ATR-FTIR measurements

description	**symmetry class**	**measured freq.** /cm^{-1}	**literature**[a,b]	**calculated**[c]
ring vibration (v_{8a})	A'	1591	1597, s	1593
ring vibration (v_{8b})	A'	1567	1574, m	1562
ring vibration (v_{19a})	A'		1507,m	1504
CH_3 bend	A"		n/a	1500
ring vibration (v_{18a})	A'	1501	n/a	1493
CH_3 bend	A'	1461	1465,w	1455
CH_3 bend	A'	1442	1445,w	1455
ring vibration (v_{19b})	A'	1418	1423,w	1422
C-O-C (asym stretch)	A'	1281	1289,s	1268
weak, A' (COC asym stretch)	A'	1241	1244,w	1243
ring vibration (v_{9a})	A'	1210	1215,s	1218
COC (sym stretch + ring mode)	A'	1024	1029,s	982
ring breathing (v_1)	A'	989	990,m	966
ring vibration ($v_1 1$)	A"	817	818,s	815
ring vibration (v_5)	A'	800	802,m	776

[a] s = strong; m = medium; w = weak; n/a = not observed.
[b] Peak assignment made on the basis of reference 132.
[c] Calculated peak assignment taken from reference 73. Peak frequencies were multiplied by a factor of 0.985 to account for the harmonic approximation.

3 Synchrotron-Sourced ATR-SEIRAS with an Infrared Microscope

Contributions of the Author

The results described in this chapter have been published in the following peer-reviewed publication:

Tyler A. Morhart, Amanda Quirk, Michael J. Lardner, Tim E. May, Scott M. Rosendahl, and Ian J. Burgess. Femtomole Infrared Spectroscopy at the Electrified Metal-Solution Interface. *Analytical Chemistry*, **2016**, 88, 19, 9351-9354.

I designed the experiments with Ian Burgess with technical input on ATR-SEIRAS from Quirk, spectroelectrochemical cell design from Quirk and Lardner, assistance with synchrotron experiments from Quirk, Lardner, and Rosendahl, and input on optics and ray-tracing from May. I collected and processed all of the data with the following exceptions: voltammetry shown in Figure 3.4 was collected by Quirk and the ray-tracing simulation shown in Figures 3.6 and 3.8 was set up by May with my input. I wrote the first draft of the manuscript and prepared all figures except for Figures 2 and S2 in the published paper. The text and figures shown here were prepared by me.

3.1 Introduction

Faced with the challenge of adapting ATR-SEIRAS to a synchrotron, a technique which to date had been used exclusively with benchtop infrared spectrometers using conventional globar IR sources, it was natural to build on expertise already within the group. ATR-SEIRAS capabilities were already well-developed from the work of Scott Rosendahl, Jessica Sigrist, and Amanda Quirk. The state of the art in the group used relatively large Si hemispherical IREs described in a glass and Teflon spectroelectrochemical cell design discussed in Chapter 2. Au thin film electrodes were prepared primarily by chemical ("electroless") deposition or sputtering in a chamber meant for coating SEM samples (Denton Desk Vacuum IV).

Existing instrumentation at the Mid-IR beamline consisted of a vacuum-purged Bruker Vertex 70v spectrometer coupled by a transfer optics chamber to a Bruker Hyperion FTIR microscope. Rosendahl's graduate work and the ongoing projects of Michael Lardner and Kaiyang Tu had made productive use of the instrumentation and yielded a high level of familiarity in the group. A major component of all three of those individuals' projects comprised designing and building compact spectroelectrochemical cells which fit in the

limited working space between the Schwarzchild objectives. This miniaturization-based approach informed the initial goal to adapt the ATR-SEIRAS cells used in the group to fit under the microscope.

As discussed in Chapter 2, the near-field optical effect on which ATR-SEIRAS relies demands relatively high angle-of-incidence (AOI) for optimal signal enhancement. Accessing such high AOI required careful consideration of the restricted beampath of the IR microscope. The sampling optics are matched Schwarzchild objectives, depicted in cross-section in Figure 3.1a) operating in reflection mode. The incoming beam reflects off the primary spherical mirror (smaller radius of curvature) onto the secondary mirror, which brings the light to focus. In Figure 3.1a, the mirrors are coloured yellow and the housing of the objective is coloured grey. The working distance of the objective is the distance between the focal point and the bottom of the housing, and is at most 25 mm for the objective available at the Mid-IR beamline. The diameter of the primary mirror imposes one limit on the AOI while the width of the secondary mirror imposes the other limit. This is depicted schematically by the marginal rays shown in Figure 3.1. For the 15x objective used here (NA = 0.4), that limits AOI to a range equal to 12 - 24˚ measured from the optical axis.

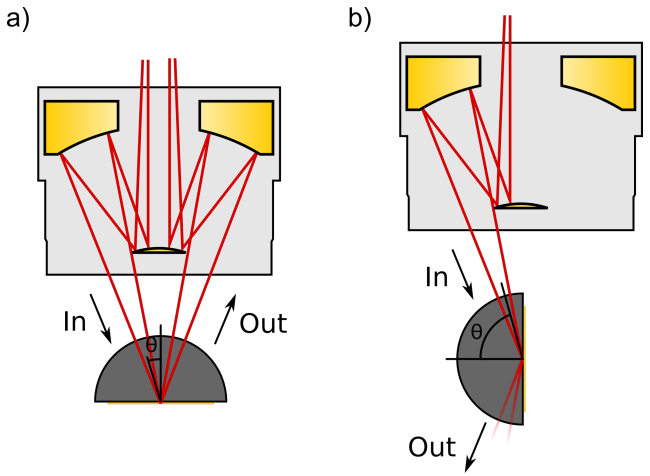

Figure 3.1: Comparison of reflection versus transmission geometry. a) A 15× Schwarzchild objective operating in reflection mode. b) The achievable AOI is too low for ATR-SEIRAS. b) Transmission. The hemisphere is rotated by 90˚ so that the principal reflecting plane is parallel with the optical axis. While operating the microscope in transmission mode, the beampath through the Si hemisphere undergoes total internal reflection. The AOI is much higher than in a) and is suitable for ATR-SEIRAS.

It was recognized by Rosendahl that operating the microscope in reflection mode (incident and collected beam both pass through one objective), did not offer meaningful SEIRAS signal due to the low AOI at the principal reflecting plane, Figure 3.1a. This chapter uses a different optical geometry to access sufficiently high AOI to perform an ATR-SEIRAS microspectroscopy experiment. This is shown in Figure 3.1b. This chapter describes the requirements for spectroelectrochemical cell design and the effect of the unusual sampling geometry on the shape and size of the beamspot. The non-faradaic adsorption of 4-methoxypyridine (MOP) is used as a probe system to demonstrate collection of spectra from spot sizes three orders of magnitude smaller than a conventional ATR-SEIRAS measurement. Early efforts toward patterning and interrogating a

microelectrode will be discussed with attention paid to practical difficulties. These difficulties will motivate a new direction for the thesis work.

3.2 Experimental

3.2.1 Materials

4-methoxypyridine (MOP, 97%, Aldrich) was used as received and made up to 0.1 mM in 50 mM $KClO_4$ supporting electrolyte. $KClO_4$ (Aldrich) was recrystallized twice and stored in a vacuum desiccator until use. Solutions were made up with ultrapure water (18.2 MΩ cm, Millipore) in glassware which had been cleaned in hot, concentrated 3:1 sulfuric:nitric acid and rinsed with copious amounts of ultrapure water. Au wire (Φ 500 µm), Pt wire (Φ 250 µm), and Ag wire (Φ 3 mm) were purchased from Alfa Aesar. Polyvinyl chloride (PVC) and polyphenylene sulfide (PPS) bar stock was purchased from McMaster-Carr.

3.2.2 Spectroelectrochemical Cell Design

Two major needs were identified for a successful design: (1) high angle-of-incidence to maximize signal intensity, and (2) reliable electrical contact with the working electrode. In regular laboratory experiments, the benchtop ATR-SEIRAS cell mated to a variable angle optics accessory (PIKE VeeMAX III), allowing the selection of the angle of incidence to within 1°. At first glance, it seems attractive to try sending the SIR beam to an external output of the spectrometer and couple it directly to the VeeMAX, allowing reuse of an already familiar (and robust) system. However, the requirement to control the spot size to sub-millimeter dimensions would require at minimum the addition of a beam compressor and variable aperture, and at that stage of the project a relatively complex optics project did not seem attractive. (Custom optics will prove necessary based on results shown in the next chapter.) As described in the introduction, it was identified that aligning the hemisphere's principal reflecting plane collinearly with the optical axis would provide an AOI of 66 - 78°. At these more grazing AOI, electric field enhancement is greatly improved, leading to suitably high SEIRAS signal. The experimental geometry implemented in this chapter is shown in Figure 3.2, which includes a photograph of the FT-IR microscope alongside a cross-section of the spectroelectrochemical cell with the microscope optics.

Because of the confined geometry in the microscope sample stage, a new spectroelectrochemical cell was required. For ATR-SEIRAS experiments with a benchtop spectrometer, the "glass castle" ATR-SEIRAS cell (Chapter 2.4.4) was composed of a Teflon body piece mated to a fairly large (over 15 cm in height) piece of glassware which housed the reference and counter electrodes and purge gas connections. The restricted space underneath the microscope objectives imposed a height limitation of about 2.5 cm on the new cell design, rendering the existing glassware useless. Instead of trying to adapt the glassware to fit under the microscope, a compact single-chamber cell was designed(depicted in cross-section in Figure 3.2b and shown

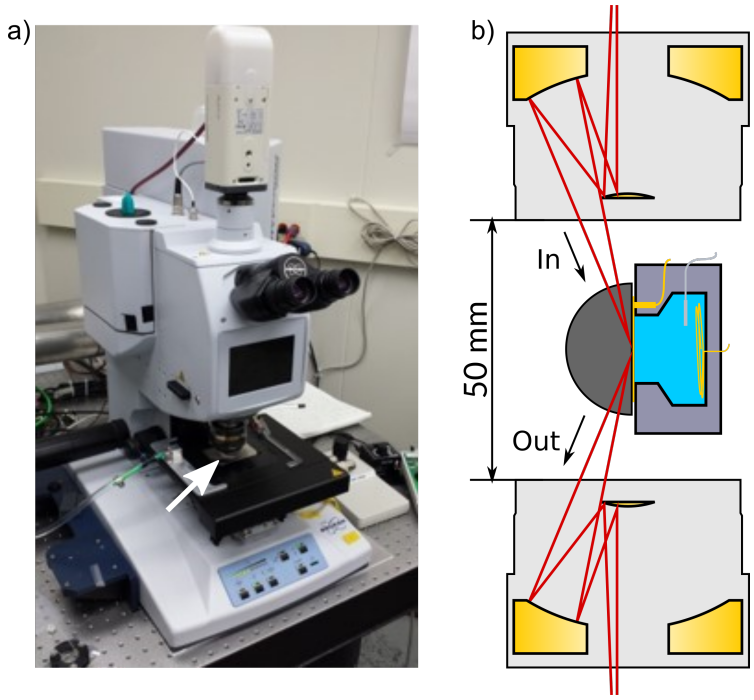

Figure 3.2: Experimental geometry of the ATR-SEIRAS experiment using the FT-IR microscope. a) Photograph of the Hyperion FT-IR microscope. The white arrow indicates the sample stage where the spectroelectrochemical cell was placed. b) Cross section of the Schwarzchild objectives and the cell at focus.

in detail in Figure 3.3). Initial prototypes were prepared in PVC, chosen for its excellent machinability and low cost, while later version were prepared in the highly chemically stable polyphenylene sulfide (PPS). The assembled cell mated to the microscope stage by an aluminum stage plate (2). Electrolyte was injected at ports (3) and (4) via barbed fittings and Tygon tubes (not shown). A circular opening (5) allowed the electrolyte to wet the Au thin film electrode. Electropolishing of the Au film (*vide infra*) was completed using an internal Pt wire quasireference electrode (QRE) (6), but potential difference experiments with MOP used a true Ag/AgCl reference electrode (RE) in the effluent stream (not shown). Physically separating the RE from the WE in this manner increases the uncompensated resistance, a factor which was recognized to affect future time-resolved experiments. However, the non-faradaic adsorption of MOP drew small capacitive currents which decay to zero upon a potential step, so for the purposes of the work in this chapter it was deemed unnecessary to place the RE closer to the WE with a Luggin capillary. A Au coil counter electrode (7) was chosen for its chemical inertness. The surface area of the counter electrode was roughly the same as the exposed working electrode area. The non-faradaic electrochemistry chosen as a test system would draw such minute currents that more careful control of the counter electrode size was not necessary. Furthermore, it was recognized that a microelectrode would be vastly smaller than the counter electrode, so the CE was judged to be appropriate. Finally, electrical contact to the working electrode was made by a spring-loaded pin mounted in a slot (8) facing the hemisphere. Spring-loaded Au-plated pins were used to gently contact

the working electrode and could be retracted during cell assembly, mitigating mechanical damage to the Au film. The final cell design had two redundant pins embedded in the housing of the cell, each connected to a braided copper wire with silver epoxy. Compressing the Au-coated hemisphere onto the pins made secure electrical contact. The hemisphere was held in place with a polypropylene strap.

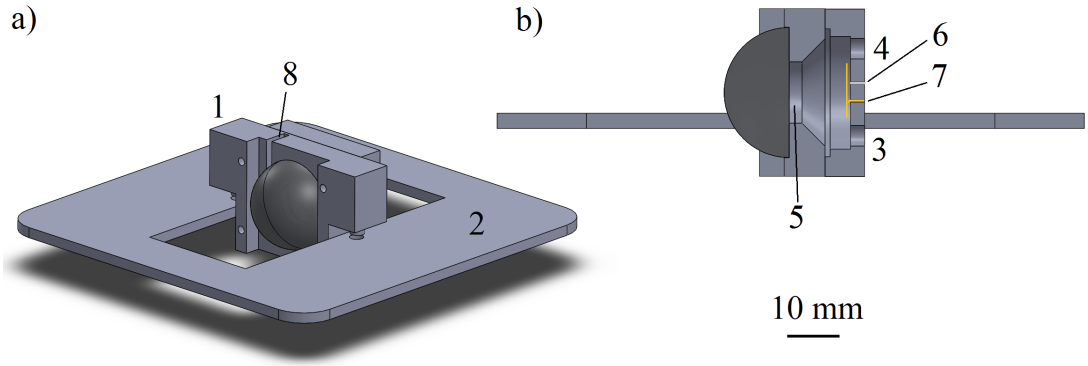

Figure 3.3: Spectroelectrochemical cell design for ATR-SEIRAS compatible with the FT-IR microscope at the Mid-IR beamline. Component numbering is discussed in the main text.

For the proof-of-concept experiments done in this chapter, no inert gas was supplied to purge the electrolyte. This choice was made because the adsorption of MOP is not sensitive to dissolved O_2, although it does exhibit competitive adsorption with OH^-. The Au thin film electrode is highly unstable at the cathodic potentials necessary to generation OH^- from dissolved O_2, so avoiding those potentials prevented the production of OH^-.

3.2.3 ATR-SEIRAS Thin-Film Preparation

Au thin film electrodes were prepared on a 25.4 mm diameter Si hemisphere (ISP Optics). Au deposition was performed using the electroless method reported in Miyake *et al.*[107] with modifications described in Rosendahl *et al.*[133] The hemisphere was manually polished in two steps with 3 and 0.5 µm diamond grit polish (Leco Corporation) for 15 minutes each. The hemisphere was rinsed well with ultrapure water between polishing steps and after completion, then left to dry in a partially covered dish to prevent dust accumulation. Au deposition was performed as follows. The hemisphere was immersed in a 55 °C water bath, leaving the principal reflecting plane above the water level. The exposed plane was then treated with 40% (w/w) NH_4F for 5 min, followed by dropping a solution containing 5 mg $HAuCl_4$, 0.3 M Na_2SO_4, 0.1 M $Na_2S_2O_3$, 0.1 M NH_4Cl, and 2% HF (2:1 v/v) directly on the polished face of the hemisphere. This was allowed to react for 80 s, during which a shiny gold film appeared. The hemisphere was then rinsed with copious amounts of ultrapure water.

As described in Chapter 2, it is necessary to "activate" the metal film by electropolishing. Initially, electropolishing was conducted *ex situ* by exposing the Au film to a 0.1 M $HClO_4$ solution and cycling the potential in a two-electrode configuration versus a Au wire. Then, the electropolished film and hemisphere

was transferred to the SEIRAS cell for use at CLS. A general problem with activation is that the poor mechanical stability of the thin film electrode makes this a highly sensitive process, as prolongued excursions into large positive or negative potentails can stress the film to the point of failure. It was found that the film could not be reliably activated *ex situ*, so instead gold films employed in this chapter were electropolished *in situ* using 50 mM $KClO_4$. Any electrogenerated species were flushed out of the cell by pumping at least 20 mL of electrolyte through the cell (ten times the internal volume).

3.2.4 Spectroelectrochemical Measurements on Large Au Thin-Film Electrodes

Ag/AgCl reference electrodes were prepared freshly before experiments. A 3 mm diameter Ag wire (Alfa Aesar) was oxidised in 10% (v/v) HCl solution versus a Pt electrode in a two electrode configuration. Several hours of oxidation at a roughly +500 mV bias produced a thick, stable coating of AgCl on the surface. This was then sealed in a fritted glass holder containing saturated KCl. The plastic components of the cell were rinsed thoroughly in ultrapure water and dried in air. All electrochemical procedures were performed with a HEKA PGSTAT590 potentiostat and data were collected in a custom Labview program via a USB data acquisition card (NI USB 6351 X-series). Solution was supplied by a syringe pump (New Era Pump Solutions Inc, Model NE-1000) operated manually.

Spectroscopic measurements were completed using a Hyperion 3000 microscope coupled to a Bruker Vertex 70v FTIR spectrometer. The Vertex has both an internal globar and SIR input, allowing the two sources to be compared. Spectra were collected at 4 cm^{-1}resolution and were composed of 128 co-added interferograms. The microscope aperture wheel housed apertures of diameter 3.75 to 0.30 mm, allowing the user to define the size of the beamspot at focus. Two 15x Schwarzchild objectives, NA = 0.4, (Newport) were used for this work.

The spectral noise was quantified by collecting 100% transmission lines, wherein two spectra were collected back-to-back and their ratio taking. Because no changes are induced in the sample, the resulting transmission curve contains only spectral noise, which can be quantified using the standard deviation of about 500 data points between 2460 and 3470 cm-1. This range is chosen to avoid interference due to atmospheric CO_2 and H_2O.

Potential difference spectra were collected as follows. First, a solution containing 1 mM MOP in 50 mM $KClO_4$ electrolyte was injected. Then, the working electrode was biased to -700 mV vs. Ag/AgCl (the reference potential), completely desorbing the MOP. A reference spectrum, I_0, was collected, then the working electrode was biased to 0 mV (the sample potential), adsorbing the MOP as a high-density monolayer. A sample spectrum, I, was collected and an absorbance spectrum was calculated by $A = -\log(I/I_0)$. Signal-to-noise ratio (SNR) was calculated using the peak-to-baseline signal intensity, S, of the C-O-C asymmetric stretching mode and the standard deviation of noise from 1325 to 1425 cm^{-1}, σ, so that $SNR = S/\sigma$. Under this definition, SNR = 3 is required for detection.

3.2.5 Optical Modelling

A commercial 3D geometric ray-tracing package (ZEMAX OpticStudio) was used to help understand the shape and position of the beamspot at focus on the hemisphere. The refractive index of Si was set to 3.4 and monochromatic radiation of 3000 $cm^{-1}$was used. The Schwarzchild objective and condenser were modelled with two perfectly-reflecting spherical mirror sections with dimensions taken from the manufacturer. A point source was used to model the SIR beam and was placed at the back focal length of the objective to illuminate the sample. A ray-counting detector was placed at the conjugate focal point of the condenser.

3.2.6 Determination of Au Surface Roughness

A cyclic voltammogram of the deposited Au film electrode was collected in 0.1 M $HClO_4$ supporting electrolyte at a scan rate of 20 mV s^{-1}, Figure 3.4. The CV shows both oxidation and reduction peaks of the gold surface. The total charge Q passed during reduction of the gold oxide was found by integrating the reduction peak. Dividing by the geometric surface area A of the exposed Au electrode, Q/A, yields a charge density. For the two-electron process required to form a monolayer of AuO, Q/A = 400 mC/cm^2.[134,135] Dividing the experimental value of Q/A by this value yields the surface roughness factor of the gold thin film, 3.2 ± 0.5. This is fairly close to the value of 2.6 that was reported for similar films by Miyake *et al.*[107]

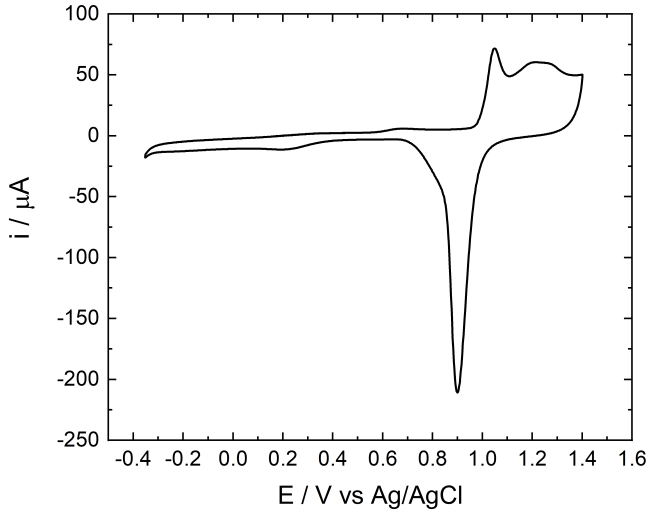

Figure 3.4: Cyclic voltammogram of the Au film electrode in 0.1 M $HClO_4$. Scan rate = 20 mV s^{-1}

3.2.7 Microelectrode Preparation

Microelectrodes were prepared by UV photolithography in the SyLMAND beamline, CLS. The substrate was a custom-manufactured Si spherical segment (ISP Optics) shown in Figure 3.5. The optic was machined from

a 25.4 mm diameter Si hemisphere ground down to a thickness of 6 mm. The principal reflecting plane was mirror polished and the opposite face was ground to a rough finish.

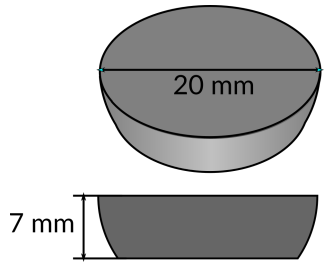

Figure 3.5: Custom-machined Si spherical segment used in microelectrode experiments.

The substrate was first coated with a Au thin film electrode by sputtering in a Denton Desk Vac IV system at a rate of roughly 0.02 nm/s for 15 min. Then, a 500 nm layer of AZ1505 positive-tone photoresist (Microchem) was spin coated onto the substrate using a Solitec Model 5110 spin coater. Following a dynamic dispense of approximately 1 mL of resist at 500 rpm, the spin speed was ramped to 2000 rpm over 5 s before a final spin step at 3000 rpm for 30 s. The coated substrate was baked at 100 °C for 80 s. (The hemispherical section was very thick and heated up more slowly than a typical 0.5 mm thick Si wafer; therefore, to correct for the relatively slow heating of the optic, bake time was measured from the time when changes in the resist coating were visible, indicating reflow occurring at elevated temperature.) The sample was cooled to room temperature and transferred into the Heidelberg Instruments DWL66+ direct write laser system for exposure. The exposure pattern was prepared in LayoutEditor (juspertor GmbH). The pattern consists of 18 individually addressable wide band ultramicroelectrodes. The UME width and pitch were 5 and 10 um, respectively. Each UME was 7500 um long and was connected by a 100 µm wide busbar to a 2.00 mm diameter contact pad.

After exposure, the pattern was developed in AZ400K developer (Microchem GmbH) for 60 s, rinsed with ultrapure water, and gently blown dry with nitrogen. At this stage, the continuous Au film is selectively masked by the photoresist. The excess Au was etched by immersion in a dilute aqua regia bath (3:1:2 v/v HCl:HNO_4:H_2O, reagents from Fisher Scientific) for approximately 7 s, followed by an ultrapure water rinse. The remaining photoresist was removed with acetone and the substrate was rinsed with isopropanol, methanol, and ultrapure water before being dried with nitrogen.

3.2.8 Spectroelectrochemistry with Individually Addressable Microelectrodes

The eighteen individual microelectrodes were connected to an 18-channel selector box, allowing the operator to choose which electrode to electrify. The low potentials and currents employed (1 V and 100 µA were typical upper bounds) did not make any particular demands on wire gauge or other components. Potentials were applied by the HEKA PGSTAT590. Spectra were collected as described above. Several chemical systems were tested but issues fundamental to the electrode design (discussed below) prevented collection of any

meaningful results.

3.3 Results and Discussion

3.3.1 Estimation of Beamspot Size by 3D Geometric Ray-Tracing

In a conventional ATR-SEIRAS experiment employing a benchtop FT-IR and variable angle accessory, the spot size is large enough to illuminate the majority of the Au thin film electrode. In contrast, the goal of synchrotron-based ATR-SEIRAS microspectroscopy would require careful consideration of the spot size when the crystal was focused. The objective was to use the microscope apertures to restrict the size of the beamspot at focus, but exactly what effect the unusual internal reflection geometry would have on the beamspot's shape was unknown. To answer this question and explore questions about the hemisphere's alignment, geometric ray-tracing was used. The simulation geometry is shown in Figure 3.6. A point source (1) was placed at the back focal length of the Schwarzchild objective, marked (2) and modelled only with reflective surfaces. The hemisphere (3) was placed at focus and a ray-tracing detector (4) was placed on the principal reflecting plane as well as a second detector at (5) to model the MCT detector in the microscope. The first problem was to determine how to focus the system when the only feedback available was the detector signal. Silicon has a particularly strong phonon mode at 1108 cm^{-1}, assigned to the asymmetric Si-O-Si stretching mode[136], which is often referred to as the "Silicon cutoff.". In an experimental setting, the shape of the single beam energy curve could be monitored and observation of throughput losses due to the Silicon cutoff indicated the beam was at least passing through the Si hemisphere. However, it was observed that the detector response was highly variable in the y-direction but more-or-less constant in x and z. To understand the sensitivity of the detector response, in the ray-tracing simulation the center point of the hemisphere was placed at the focal point of the Schwarzchild objective (the origin of the simulation shown in Figure 3.6). A 100 × 100 μm^2 ray counting detector (matched to the MCT detector element size) was placed at the conjugate focus. Then, the crystal was translated in small increments in all three Cartesian directions and the number of rays impinging on the detector was counted.

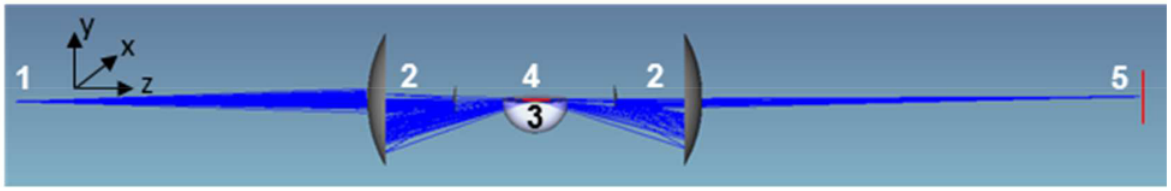

Figure 3.6: Ray-tracing simulation setup.

Figure 3.7 plots the simulated detector response versus displacement from the origin (focal point). For translation along the optical axis (z-axis) or parallel to the principal reflecting plane (x-axis), the detector response is essentially constant, which is consistent with experiment. However, translation of the crystal

"through" the beam (along the y-axis) shows a sharp maximum at 4 µm displacement. This is a surprising result, but inspection of the detector image reveals the cause, Figure 3.8. When the crystal is placed at the origin in "perfect focus", Figure 3.8a shows that only a fraction of the beamspot lies on the detector. In contrast, a small displacement fills the detector, offering maximum signal, Fig 3.8b. The detected signal varies strongly over only 10 µm in the y-axis, and beyond that range is essentially constant at zero. In experiments, it was found that the y-position could be varied by a few tens of microns to one hundred microns. This is likely due to the difficulty of placing the hemisphere center exactly at focus of the Schwarzchild objective.

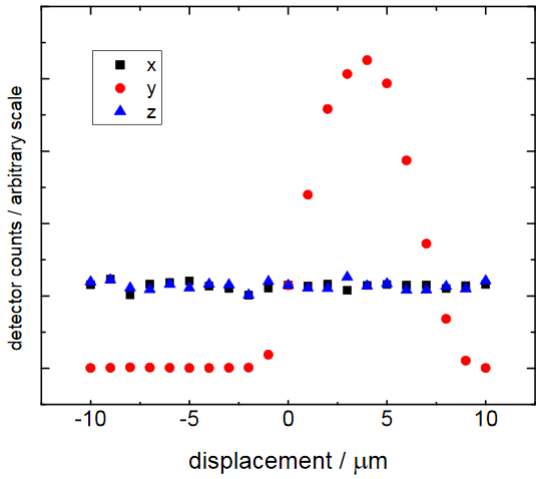

Figure 3.7: Power falling on the detector as a function of displacement from $(x, y, z) = (0, 0, 0)$.

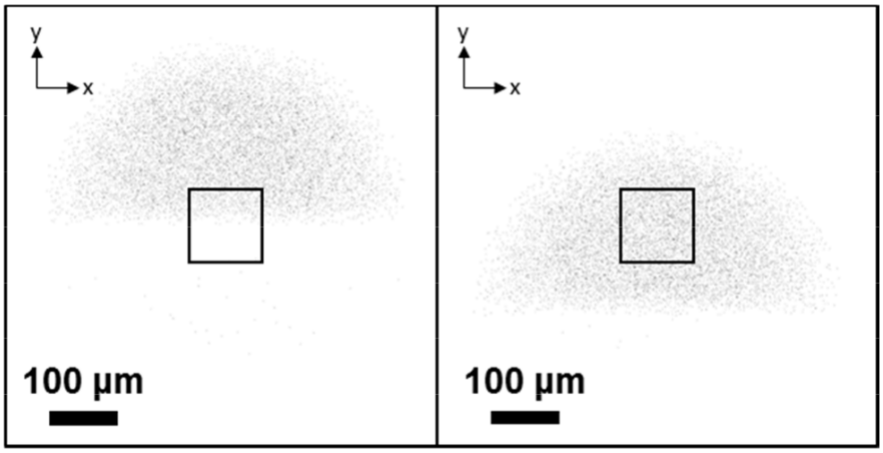

Figure 3.8: Ray-tracing simulation of beamspot at the detector under "perfect alignment" (left) and maximum counts (right).

Understanding the effect of the sampling geometry on the beamspot shape required a second simulation. Figure 3.9a shows the simulation geometry with an imaging detector (red) placed at the objective focus. A stop (not shown) is placed upstream of focus in the simulation to block half the beam in the same manner as the spectroelectrochemical cell. As shown in Figure 3.9b, the beamspot is a half-circle with a radius around

10 µm. Figure 3.9c shows the simulation geometry with the hemisphere (white) placed at focus and the imaging detector placed at the surface of the principal reflecting plane i.e. rotated in the x-z plane. The resulting beamspot is shown in Figure 3.9d. In order to facilitate interpretation, a threshold has been applied to the image so that 95 % of the rays fall in the solid black spot. Compared the half-circular spot shown in Figure 3.9b, the spot on the hemisphere has two key differences. First, because the beamspot is projected on the principal reflecting plane at relatively high AOI, it is slightly elongated along the z-direction (the optical axis). Second, the width of the spot along the x-axis is compressed due to the higher refractive index of Si compared to air.

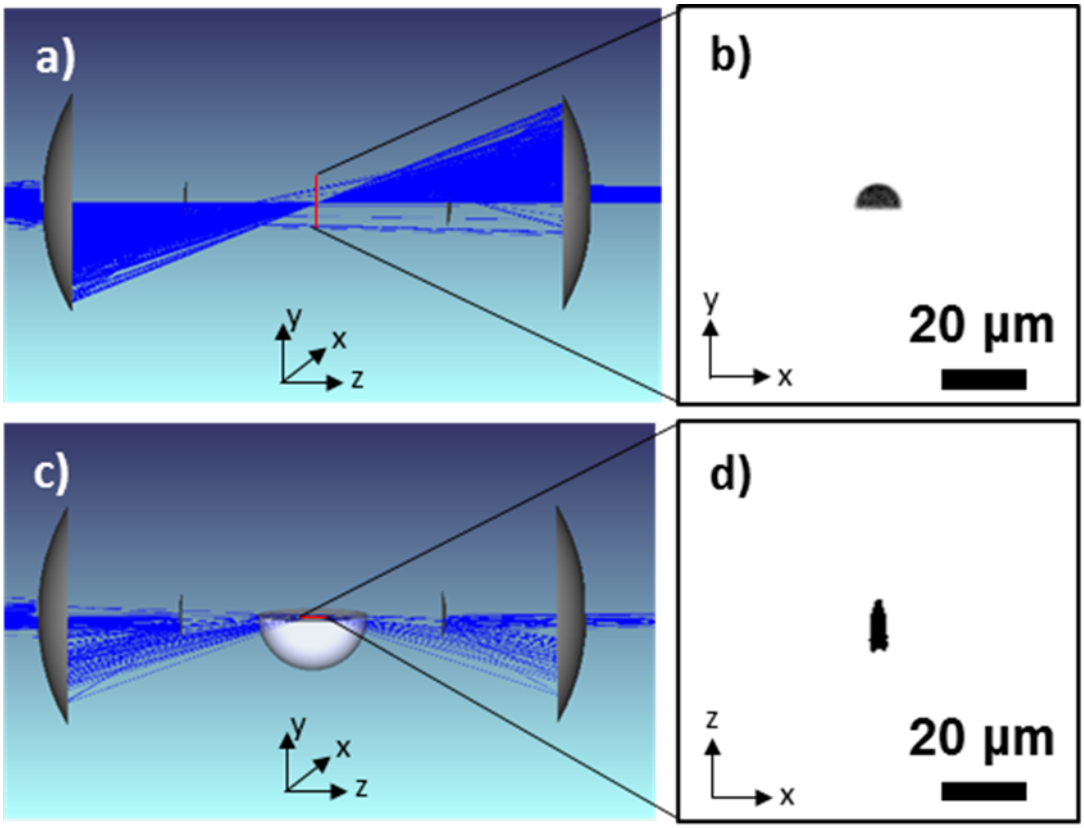

Figure 3.9: Ray-tracing simulation of beamspot at the detector for two cases. Top (a) and (b) depicts the half-blocked beam without the hemisphere present, and bottom (c) and (d) with the hemisphere in the beampath. (d) Shows the shape of the focused spot on the principal reflecting plane of the hemisphere.

As described previously, during experiments the crystal was aligned by maximizing signal on the detector. The images in Figure 3.10 show that this has a very small effect on the shape of the beamspot. Figure 3.10a shows the beamspot with the crystal at $(0, 0, 0)$ (perfect alignment) while 3.10b positions the crystal at $(0, 4, 0)$. In both cases, although there is a subtle difference the shape of the illuminated area is the same within error, 125 ± 10 µm.

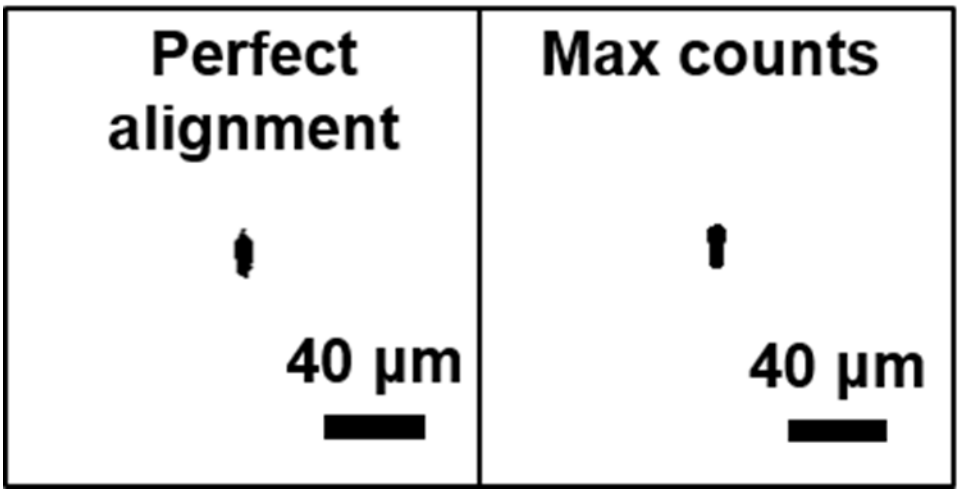

Figure 3.10: Ray-tracing simulation of beamspot at the detector under "perfect alignment" (left) and maximum counts (right).

3.3.2 Observation of Femtomole Quantities of Adsorbed MOP

In ATR-SEIRAS, the signal-to-noise (SNR) of a measurement depends on the intrinsic noise level of the experimental setup (generally detector noise-limited in FT-IR) and the signal magnitude which is a function of the analyte's IR absorption cross section (fixed) and the gold thin film electrode's enhancement factor (also fixed). It follows that decreasing the noise level by providing more photons to the detector increases SNR. To this end, the so-called synchrotron advantage can be quantified by studying measurement noise.[137] Figure 3.11 plots measurement noise, quantified as the standard deviation of a selected region of a 100% transmission curve, as a function of the nominal spot size, r. The quantity r is calculated from the known aperture radius and the 15x compression imparted by the objective. At large spot sizes (high r), the noise is nearly identical, and in fact for even larger spots (beyond the upper limits of this figure) the globar outperforms the synchrotron. However, as the spot size shrinks, the globar spectral noise exhibits a strong dependence on spot size whereas SIR is only weakly dependent. At $r = 10$ µm (the smallest accessible aperture size), the globar is fifteen times noisier than SIR, validating the synchrotron advantage.

In order to demonstrate the utility of synchrotron-sourced ATR-SEIRAS, the non-faradaic adsorption of MOP was studied as a function of spot size. Figure 3.12 plots three potential difference absorbance spectra collected with SIR as a function of spot size and an ATR spectrum (top of Figure 3.12) of 0.1 M aqueous MOP for reference. The latter was collected offline with a conventional FTIR. When interpreting potential difference spectra, upward-going peaks represent increased absorbance in the sample spectrum relative to the background spectrum, whereas downward-going peaks represent decreased absorbance. An arbitrary scalar offset has been added to the spectra to aid interpretation.

Confirmation of surface specificity can be made by inspecting the ATR versus ATR-SEIRAS spectra. As detailed in Chapter 2, the υ_{8a}, υ_{8b}, and υ_{19a} ring modes at 1602, 1573, and 1509 cm-1 are visible in

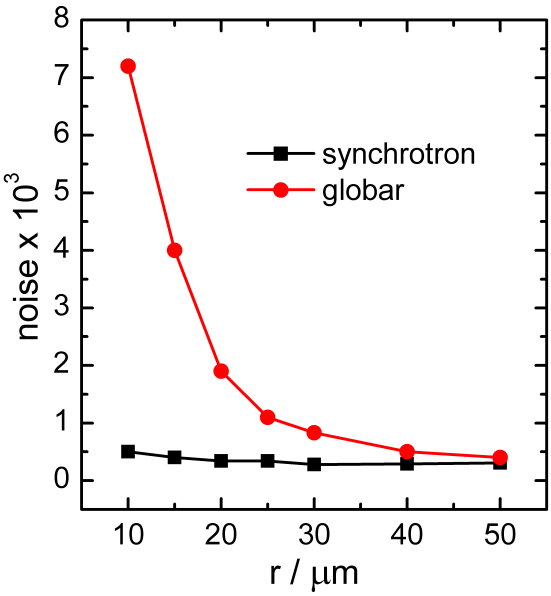

Figure 3.11: Spectral noise as a function of the nominal radius of the focused beamspot illuminating the principal reflecting plane. Noise is calculated as standard deviation of a 100% transmission line.

the ATR spectrum alongside the strong C-O-C asymmetric stretch at 1291 cm-1. However, the v_{8b} mode is not SEIRAS-active and is not observed in the ATR-SEIRAS spectra. In addition, the v_{8a} and C-O-C asymmetric stretch are known to blueshift by roughly 20 cm^{-1}upon adsorption on Au. The dotted line in Figure 3.12 is added to make this shift more obvious. In addition, the broad downward-going band around 1650 cm^{-1}corresponds to the H-O-H bending mode of H_2O which is displaced by adsorbed MOP. Taken together, these observations confirm the surface-sensitivity of the measurement.

The noise levels in the ATR-SEIRAS spectra are only weakly dependent on spot size, which is in keeping with results shown in Figure 3.11. The signal intensity does appear to decrease slightly with decreasing spot size. This may be due to microscale heterogeneity of the Au film. Nevertheless, the SNR is sufficient to positively identify the presence of MOP at even the smallest spot size. Using the spot size calculated from 3D ray-tracing in the previous section, the known surface coverage of MOP ($\Gamma = 6.7 \times 10^{-10}$ mol cm^{-1} REF), and the surface roughness factor of Au (3), the number of MOP molecules interrogated at the smallest spot size is approximately 2.5 fmol or 1.5×10^9 molecules. This is at least three orders of magnitude lower than the ATR measurement presented in Figure 3.12 (I) and over four orders of magnitude lower than a typical ATR-SEIRAS measurement. Quantifying the SNR of C-O-C asymmetric stretching mode at roughly 1300 cm^{-1}as a function of spot size results in the plot shown in Figure 3.13. For relatively large spot sizes, SNR is essentially constant, and even at the smallest accessible spot size it is still about 25. This implies that the limit of detection for MOP is approximately at the level of one femtomole or less. At this spot size, globar SNR is below the critical value for detection.

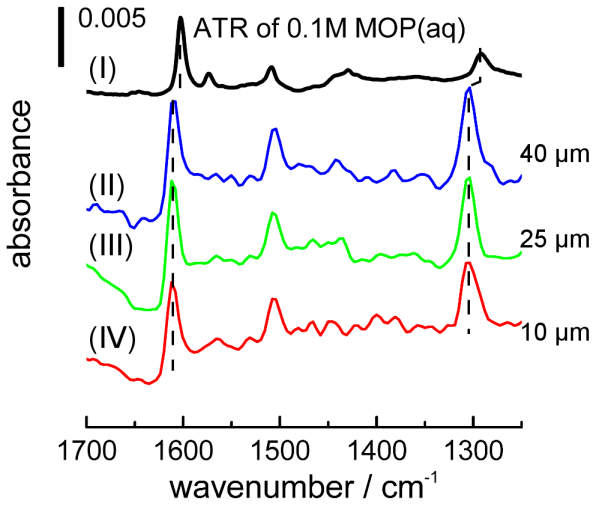

Figure 3.12: ATR spectrum of 0.1 M aqueous MOP on the unmodified Si hemisphere (top, black) and potential difference absorbance ATR-SEIRAS spectra of surface-adsorbed MOP. Coloured spectra are labelled with their nominal spot radius.

3.3.3 Challenges in Transitioning to Microelectrodes

At this point, the first demonstration of synchrotron-sourced ATR-SEIRAS microspectroscopy was complete. All results described to this point have used macroscopic Au films which completely covered the principal reflecting plane of the hemisphere. Critically, although the beamspot size was highly restricted it was still interrogating a small portion of a very large electrode, whereas the goal of the project was to focus a small beamspot on an electrode with one dimension of comparable size. The focus then turned to preparing and illuminating microelectrodes. Considering the small size of the beamspot, it was recognized that the microelectrode would have to be placed exactly at the focal point of the Si hemisphere. At the time, a new direct-write UV laser system had been installed at the SyLMAND facility, potentially offering micron-scale precision in microelectrode positioning. To this end, a custom Si crystal (see Figure 3.5) was purchased which was compatible with the direct-write system. Sample images of prepared microband electrodes are shown in Figure 3.14.

The challenges encountered in transitioning to microelectrodes can be divided along two interconnected themes: electrode fabrication issues and beampath issues. Positioning the beamspot exactly at focus was quickly recognized to be highly challenging. Although the simulations described previously suggest that finding maximum signal on the detector necessarily meant that the crystal was at focus, this was a painstaking process with many degrees of freedom (DOF). Correct positioning of the microscope objective and condenser was required (3 translational DOF each), followed by positioning of the crystal (3 translational DOF, with 3 rotational DOF restricted by the cell design and limited by machining tolerances), and manual fine-tuning of the SIR beam via the active optics (AO) system (4 DOF). It is noteworthy that, at the time, the AO system was less advanced than its current state and required significant manual alignment. All of this was

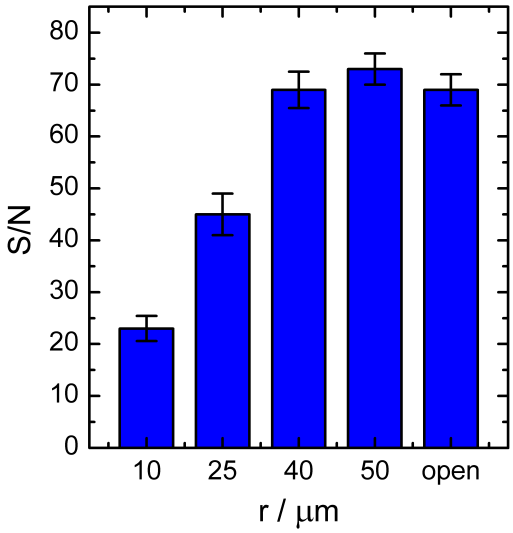

Figure 3.13: Signal-to-noise ratio of the C-O-C asymmetric stretch at 1305 cm^{-1}as a function of nominal spot radius.

to be accomplished with only the signal on the detector (interferogram amplitude and spectral distribution) as feedback.

Compounding these issues was the unreliability of Au films electrodes. In practice, preparing Au films for ATR-SEIRAS is an idiosyncratic process. Electroless deposition in particular requires significant practice and is often highly user dependent, whereas the challenges of physical vapour deposition (sputtering or evaporation) are at least limited to the machine in use. For these reasons, further development used sputtered films. Nevertheless, the poor adhesion of Au on Si renders Au films highly unstable so that films are essentially "one-off" experiments. It is practically impossible to perform a measurement with a given film, then remove the Au-coated crystal from the cell, reassemble it, and repeat a SEIRAS measurement on the same film. Au sticking to the O-ring is often enough to mechanically delaminate the electrode from the crystal. Therefore, there was no way to determine whether a prepared Au film (macroscopic or microelectrode) was SEIRAS-active offline (on a benchtop FTIR) before attempting to use it. Attempts to prepare SEIRAS-active microelectrodes were essentially limited by beamtime: with no other way to verify the activity of a prepared microelectrode, the only option available was to begin beamtime "blind" and determine if an electrode was SEIRAS active on the fly. Furthermore, electrodes which were active at the beginning of a shift often degraded over the course of hours, so that meaningful data comparable to that shown above were almost impossible to obtain. Attempts to mitigate this problem focused on preparing multiple individually addressable electrodes (Figure 3.14) supported on the same crystal. In principle, if a given electrode failed, the beamspot could be translated to illuminate another electrode without having to start from scratch. In practice, the difficulty of preparing SEIRAS-active electrodes in the first place meant that it was often difficult to find an active

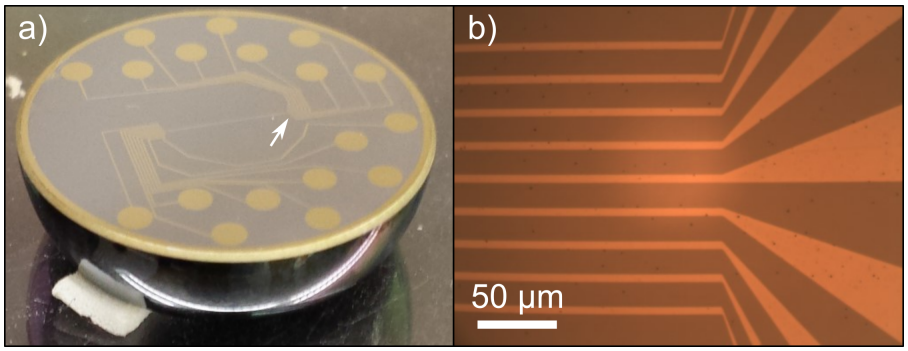

Figure 3.14: a) Photograph of multiple individually addressable microband electrodes prepared on the Si spherical segment optic. b) An optical micrograph collected at the region indicated with a white arrow in a). In this image, the Au microbands appear light orange.

electrode. Furthermore, application of electrical potentials often resulted in complete delamination of the electrodes, likely due to changes in surface stress that come with electrochemical processes at the ESI.[127]

3.4 Conclusions

This chapter reported the development of a spectroelectrochemical cell for synchrotron IR-based electrochemical ATR-SEIRAS measurements. Proof-of-principle measurements at equilibrium conditions used a simple non-faradaic, IR-active probe, 4-methoxypyridine, to verify the experimental design. Using 3D ray tracing simulation and the known surface concentration of MOP, calculations showed that only 2.5 fmol (1.5×10^9 molecules) were interrogated. The detection limit of adsorbed MOP was approximately one femtomole, or roughly 10 % of a monolayer. Collection times for sample and reference spectra were on the order of one minute. These times are comparable to usual measurement times with benchtop instruments, but the microscale spot illuminated in this chapter provides nearly three orders of magnitude improvement in detection limit compared to benchtop methods.

Despite early success, application of this method to kinetic measurements required progression from simply illuminating a miniscule area of a macroscale electrode to the direct measurement of a microelectrode. Reliable preparation of SEIRAS-active microelectrode which were stable under experimental conditions proved highly challenging. Coupled with the time-consuming nature of alignment, this avenue of work proved unproductive.

A better approach may have been to use a Si trapezoidal prism, similar to those used for multi-bounce ATR measurements. Compared to the hemispherical section used above, a prism would have simpler beam steering characteristics. This potentially would have eased the difficulty of positioning the beamspot. However, Au adhesion on Si would remain challenging. There is little evidence in the literature for the use of adhesion layers in ATR-SEIRAS. The only real contribution by Ohta using a Au/Ti system has not seen any experimental uptake despite publication ten years ago as of this writing.[138] Indeed, exhaustive attempts by a fellow graduate student (Kaiyang Tu) to replicate this work yielded no usable results. A Cr adhesion layer may seem useful, but Cr is known to alloy with Au during electrochemical cycling, adversely perturbing electrochemical

response and potentially also the SEIRAS activity.[139] This would remain an open problem until the excellent work of Ian Andvaag in Summer 2019, which is summarized in Chapter 7.

Finally, it is worth considering the microscope optics as a whole. FTIR detectors are photon-limited, and at the small spot sizes used here, the maximum IR throughput is nowhere near the upper bound on the detector's dynamic range. Considering half the beam is lost impinging on the spectroelectrochemical cell, finding a way to recover those photons would contribute a two-fold increase in throughput for a theoretical $\sqrt{2}$ increase in SNR. Doing so would require modifying the beampath of the Schwarzchild objectives or constructing a new set of sampling optics. Results from the next chapter will motivate the latter project in Chapter 7.

The issues identified motivated a re-design of the experimental approach. Two outstanding problems remained: the preparation of a stable, reliable electrode for ATR-SEIRAS, and a more robust approach to positioning the beamspot on the chosen internal reflection element. The second problem motivated the next chapter, wherein a newly available Si microgrooved wafer IRE is applied to ATR-SEIRAS.

4 Microgrooved Si Internal Reflection Elements for ATR-SEIRAS

Contributions of the Author

The results described in this chapter have been published in the following peer-reviewed publication:

Tyler A. Morhart, Bipinlal Unni, Michael J. Lardner, and Ian Burgess. Electrochemical ATR-SEIRAS Using Low-Cost, Micromachined Si Wafers. *Analytical Chemistry*, **2017**, 89, 21, 11818-11824.

I designed the experiments with Ian Burgess. Lardner designed a prototype of the spectroelectrochemical cell. Lardner and Unni assisted with ATR-SEIRAS measurements. Burgess assisted with 2D ray-tracing. I wrote the first draft of the manuscript and prepared all figures except for Figures S3 and S5 - S8. The text and figures in this chapter were prepared by me.

4.1 Introduction

In the previous chapter, a hemispherical internal reflection element (IRE) was employed in a custom-built spectroelectrochemical cell compatible with the microscope endstation housed at the Mid-IR beamline. Although the basic concept of ATR-SEIRAS microspectroscopy was demonstrated, two sets of problems were identified. The first was essentially optical. The complex beam-steering characteristics of the hemispherical (or hemispherical section) IRE presented significant challenges when attempting to address patterned microelectrodes with critical dimensions in the sub-millimeter range. The second hurdle was a fabrication problem. The poor mechanical stability and unreliable spectral response of metal films resulted in precious beamtime being wasted with no clear avenue to pre-testing the films.

Leaving aside the fabrication problem, it was identified that simplifying the optical geometry would allow better control of beamspot positioning. A simple prism was identified as a likely candidate. In contrast to a hemisphere, controlling the beam position with a prism requires only two degrees of translational freedom instead of three. A suitable prism should satisfy the following requirements: 1) infrared transparency (Si, ZnSe, Ge, etc.), and 2) compatibility with lithography techniques for microelectrode fabrication. The second condition was more restrictive and was only met by the entry of a 500 µm thick single-reflection microgrooved Si IRE on the commercial market in 2017. The microgrooved wafer (hereafter abbreviated microgrooved IRE) is shown in Figure 4.1. This device, commercialized by IRUBIS GmbH, is based on earlier work by

Schumacher[140] which used anisotropic Si etching[141] to pattern a linear array of {1 1 1}-terminated v-shaped grooves. The commercialized wafers used in this chapter have a groove angle of 35.26° which is defined by the {1 1 1} and (1 1 0) faces. Schumacher's paper demonstrated their utility as inexpensive ATR crystals with superior throughput in the fingerprint region (below around 1500 cm^{-1}) due to the low Si pathlength. That work illuminated the entirety of the grooved surface i.e. multiple grooves to provide excellent ATR spectra. However, it was recognized in this thesis work that a sufficiently focused beam could illuminate a single groove. In essence, each groove could act as a single-bounce prism. This was extremely attractive, particularly given the innate compatibility of Si with lithographic processes.

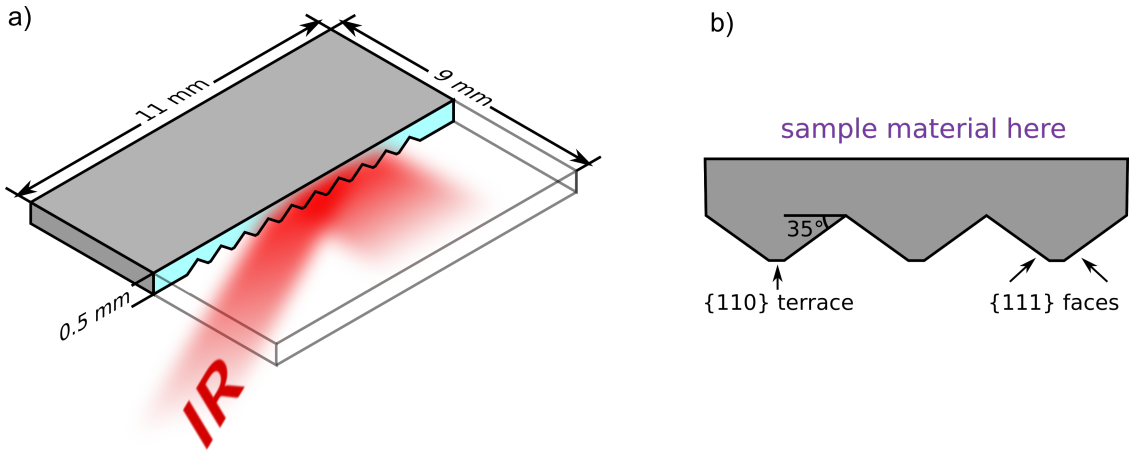

Figure 4.1: Schematic of the microgrooved IRE. a) Isometric drawing showing the dimensions of the IRE and a cross-section revealing the grooves. Infrared radiation is incident from the groove side. b) Cross-section showing the groove angle, crystallography, and position of sample material.

Although the microgrooved wafers were designed for ATR purposes, they had several properties which seemed to recommend them for ATR-SEIRAS generally. They were inexpensive compared to more commonly used hemispheres or prisms, with typical prices being almost a factor of ten lower. (Continued growth in IRUBIS' market share is expected to drive down prices, improving this differential). Their small size and low cost were ideal for preparation of multiple sputtered Au layers in parallel, potentially increasing experimental throughput by cutting down on Au layer preparation time. Furthermore, they retained superior throughput in the fingerprint region. IREs with longer pathlengths attenuate light due to strong phonon modes below 1500 cm^{-1}. This is often colloquially referred to as the "silicon cutoff," and the physical origins of these modes are discussed in the Results section. The poor signal-to-noise that results from the silicon cutoff is a well-known problem in electrochemical ATR-SEIRAS, and several creative mitigation strategies had been described in the literature.[142] Multibounce IREs fabricated from roughly 500 µm Si wafers were reported using microfabrication techniques[140,143–146] or cleaving,[147] although the input beam needs to be well-collimated and the focus must be controlled. More complex methods involved fixing a thin Si wafer to a larger support IRE with better low-frequency throughput. For example, Shao et al. fixed a Pt-coated Si wafer to a highly transparent ZnSe prism and probed superoxide anion generation during oxygen reduction.[148] An improved

version from Xue et al. coupled IR into a 200 µm thick Si wafer by fixing a thin layer of water between the Si wafer and ZnSe support prism.[149] These creative solutions also introduced several new interfaces with dissimilar refractive indices, resulting in significant reflection losses. Furthermore, establishing a gap of consistent thickness is highly challenging and is a common problem found in the Otto configuration used in surface plasmon resonance spectroscopy.[150]

Although it was recognized that the microgrooved IRE's potential for ATR-SEIRAS microspectroscopy was considerable, they had not been demonstrated for use with ATR-SEIRAS. The 35.26° face angle of the grooves and the high refractive index of Si would limit the achievable angle of incidence at the Si/Au interface. Because ATR-SEIRAS enhancement benefits strongly from high AOI, it was an open question whether the ATR-SEIRAS performance of the microgrooved wafers would be sufficient. In this chapter, the performance of microgrooved IREs for electrochemical ATR-SEIRAS is qualified using a macroscopic beamspot under varying AOI.

4.2 Experimental

4.2.1 Materials

Internal reflection elements were purchased from ISP Optics (25 mm diameter Si hemispheres) or IRUBIS GmbH (ATR-elements.com at the time; 10 x 10 mm wafer). Diamond grit polish was purchased from Leco Corporation. $KClO_4$, KCl, $K_3Fe(CN)_6$ and 4-Methoxypyridine (97%, MOP, used as received) were from Sigma-Aldrich. $KClO_4$ was recrystallized twice from water before use. Argon (4.9 purity) was purchased from Praxair.

4.2.2 Spectroelectrochemical Cell Design

The spectroelectrochemical was based on a previously reported design[73] for a silicon hemisphere detailed in Chapter 2. The critical component of that design was the teflon base which sealed onto a Si hemisphere by means of a Viton O-ring under compression. The design described in Chapter 2 was modified slightly to accommodate the much smaller and more brittle microgrooved IRE. Figure 4.1 shows the key design changes made to mitigate breakage. A flat circular Delrin holder (50.8 mm diameter), 1, was machined with a rectangular pocket, 2, to support the wafer. A 1 mm ledge supported the wafer while exposing the entire grooved surface. A series of terrace steps, 3, allow angles of incidence up to 65° relative to the interface normal. The wafer is held off-center in the holder to provide space for contact pins (*vide infra*) and wetting of the surface.

A Teflon base, 4, forms the seal on the wafer and provides an attachment point for the glass components of the cell. The top side is threaded, 5, to match the main glass body. The underside has a pocket inset to hold a soft Viton O-ring, 6, (Durometer 60A). The softer O-ring was chosen to minimize pressure on the

wafer and has been found empirically to decrease cracking. Two other pockets support Au-coated spring-loaded contact pins, 7, which can be held in a retracted position by two #2-56 screws. When in the extended position, the pins contact the Au-modified wafer surface and electrical contact between the pins and screws allows potential control of the Au surface as the working electrode.

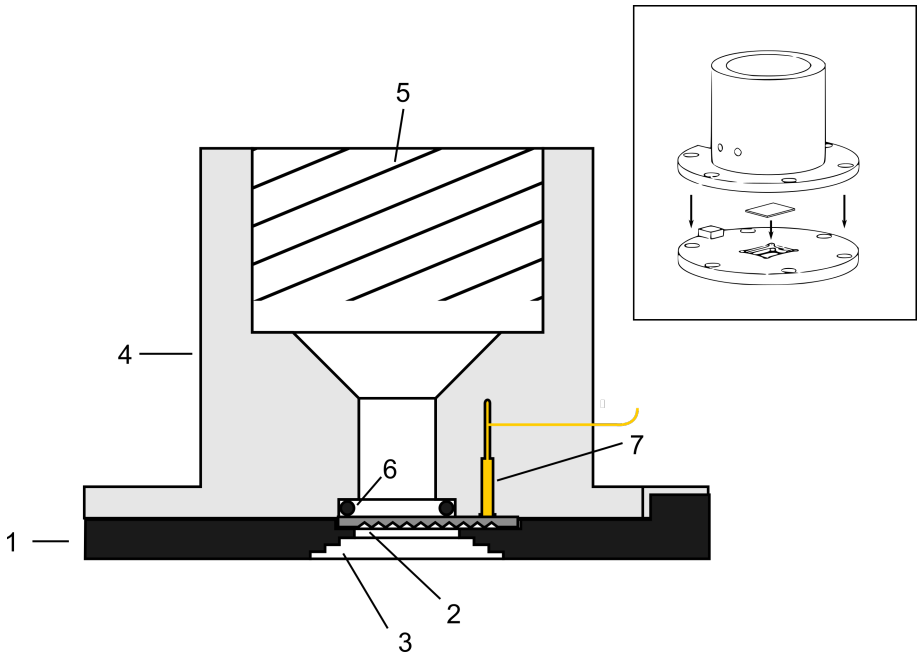

Figure 4.2: Cross section of the modified spectroelectrochemical cell for the microgrooved IRE. The inset is an exploded view showing the IRE as it is sandwiched between the wafer holder (bottom) and the teflon liquid cup (top). Numbering is discussed in the text.

4.2.3 ATR-SEIRAS Thin-Film Electrode Preparation

Internal reflection elements were polished in two 20 minute steps with 3 and 0.5 µm diamond grit polish. IREs were rinsed thoroughly with ultrapure water between and after polishing steps and ultimately dried with flowing Ar. Au layers were prepared by sputtering in a Denton Desk Vacuum IV at a rate of roughly 0.02 nm/s for 15 minutes, yielding Au layers of approximately 20 nm thickness. When testing the microgrooved wafer versus the hemisphere, IREs were co-sputtered to ensure similar performance. The principal reflecting planes were placed at the same height to ensure comparable deposition characteristics.

4.2.4 Spectroelectrochemical Measurements

Glass spectroelectrochemical cell components were washed in a boiling acid bath (2:1 H_2SO_4:HCl) and allowed to cool in the bath to room temperature. Teflon and Viton components were soaked for 30 minutes in freshly prepared piranha (3:1 H_2SO_4:H_2O_2) which had been allowed to cool to room temperature. Cell pieces were rinsed multiple times with ultrapure water and soaked overnight in fresh ultrapure water. Components were

stored in ultrapure water until they were used. The Au-coated IRE was assembled into the relevant cell and filled with 50 mM $KClO_4$ made up in ultrapure water. The cell was fixed on top of a PIKE VeeMAX III variable angle ATR accessory in a Bruker Vertex 70 FTIR. A coiled Au wire was used as the counter electrode and was cleaned by dipping in fresh aqua regia (3:1 HCl:HNO_4). The solution was purged of dissolved oxygen by sparging with Ar for 20 minutes and a blanket of Ar was maintained during experiments.

The Au film was initially textured by a cycling procedure using a Ag pseudoreference electrode to mitigate Au etching due to any residual Cl^- that may be introduced with a Ag/AgCl reference electrode. The WE potential was scanned at 50 mV/s from the open circuit potential (OCP, roughly -200 mV vs Ag) between +200 mV and -200 mV for three cycles. The potential window upper and lower bounds were then widened in 100 mV increments every three cycles. The final potential window was -400 mV to +900 mV, where the upper limit represents the onset of Au oxidation at which surface texturing begins to occur.

After surface texturing, the Ag pseudoreference electrode was replaced with a Ag/AgCl RE. An aliquot of 0.1 M MOP was spiked into the cell so that $[MOP]_{final} = 0.1$ mM. The solution was again sparged with Ar for mixing and to remove dissolved oxygen. Potential difference spectra were collected by poising the WE at E_{des} = -700 mV vs. Ag/AgCl, where the MOP is fully desorbed from the surface,[73] then scanning to E_{ads} = +200 mV vs Ag/AgCl to form a close-packed monolayer of adsorbed MOP. Reference and sample spectra were collected at the negative and positive potentials, respectively. Spectra were collected using a globar source and a MCT/A detector by co-adding and averaging 128 scans at 4 cm^{-1}resolution and a 2 mm aperture. Absorbance spectra were calculated by $A = -\log(I/I_0)$ where I and I_0 are sample and reference spectra respectively.

The signal-to-noise ratio (SNR) for MOP spectra was calculated as follows. The signal, s, is defined as the height of the 1305 cm^{-1} A' C-O-C asymmetric stretch measured from baseline. This band was chosen because it appears in a region with a flat baseline and is well separated from other peaks. The noise, σ, is defined as the standard deviation of the spectral region from roughly 1320 cm^{-1}(the high frequency side of the C-O-C stretch) to 1400 cm^{-1}. In this region the baseline is essentially flat and contains only spectral noise. SNR is defined as $SNR = s/\sigma$, so that a critical value of 3 must be achieved for detection.

4.2.5 Geometric Ray Tracing

Two-dimensional geometric ray-tracing was performed using a freeware software package, Optgeo, available online at (`http://jeanmarie.biansan.free.fr/optgeo.html`). A cross-section of the wafer was defined with frequency-independent real refractive index n = 3.4. The wafer was embedded in a host medium (air) with n = 1 and a subphase was used with n = 1.3 representing water. The incident beam was approximated as a plane wave of ten collimated monochromatic rays incident on one full period of the grooves. Changes to AOI did not change the density of rays. In the figures, only rays which have undergone total internal reflection are shown exiting on the detector side.

4.3 Results and Discussion

4.3.1 Optical Properties of Microgrooved Si IREs

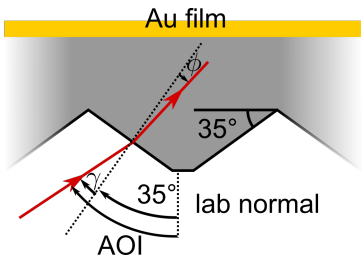

Figure 4.3: Cross section of a single groove showing the definition of angles used in this chapter.

Before evaluating performance of microgrooved wafers for ATR-SEIRAS, the impact of the relatively low face angle must be considered. Figure 4.3 shows a cross-section of one groove with the incident ray marked in red and angles of incidence defined. (Note that while the figure uses single rays, the beam actually converges with an angular spread of roughly 10˚.) As described in the background section, SEIRAS enhancement is greatest at high AOI around 70˚. Intuitively, one would expect the low fixed face angle to restrict the effective AOI at the principal reflecting plane to lower angles. Indeed, by considering Snell's law we see that ϕ, the angle of the transmitted beam with respect to the air/silicon interface is $\phi = \arcsin(n_{air} \sin\gamma / n_{Si})$ where $\gamma = AOI - 35^{\circ}$. Therefore, the angle of incidence at the principal reflecting plane is mapped to a range of angles $34^{\circ} \leq \phi + 35^{\circ} \leq 47^{\circ}$, which is substantially lower than AOI typically used in SEIRAS studies. For pure ATR, this is not problematic as low AOI result in large penetration depths of the evanescent wave, improving signal-to-noise.

The limited AOI range notwithstanding, the short pathlength which results from using such a thin IRE offers attractive benefits for spectroscopy at low wavenumbers. Although Si is often described as IR-transparent, in practice this is only true above approximately 1500 cm^{-1}. Below this frequency, which encompasses most of the fingerprint region, Si IREs (hemispheres and single- or multi-bounce prisms) are found experimentally to suffer substantial throughput losses. Figure 4.4 plots an ATR throughput comparison between the microgrooved wafer and a 12.5 mm radius Si hemisphere at AOI = 55˚. The throughput is plotted as internally reflected light relative to a Au mirror of approximately the same footprint which was placed at the sample plane of the VeeMAX III reflectance accessory. For both crystals, throughput above 1500 $cm^{-1}$is relatively constant. (The positive feature around 2300 $cm^{-1}$is atmospheric CO_2 and can be disregarded.) The Si hemisphere throughput is approximately 0.4 above 1500 cm^{-1}, which is slightly lower than expected purely due to reflection losses at the Si/air interface ($R = 0.30$ for unpolarized light at normal incidence). It is possible that this is due to the slightly smaller footprint of the hemisphere compared to the mirror. The advantage of a shorter pathlength is revealed by the microgrooved wafer's much higher throughput (lower attenuation) below 1500 cm^{-1}. The physical origin of these losses lies in a complex mixture of strongly absorbing phonon

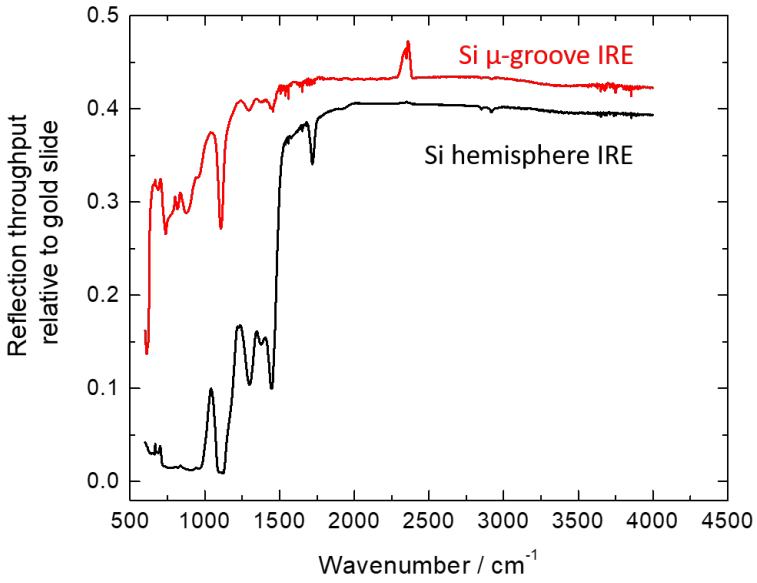

Figure 4.4: Infrared transparency of a conventional 25 mm diameter Si hemisphere and a microgrooved IRE at $AOI = 55°$. Spectra are referenced to the reflected spectrum from a gold mirror.

modes arising from bulk Si and interstitial oxygen defects. The bulk phonon modes are combinations of two transverse optical (TO) modes, one longitudinal optical mode, two transverse acoustic modes, and one longitudinal acoustic mode. Combinations of these modes are visible in the hemisphere spectrum as multiphonon modes at 1446, 1378, and 1298 cm^{-1}.[151] The strong absorption mode at 1108 cm^{-1}arises from asymmetric Si-O-Si vibrations due to interstitial oxygen.[136] The 1719 cm^{-1}mode is further evidence of interstitial oxygen defects[152] and is typically explained as a combination band of the 1108 cm^{-1}Si-O-Si asymmetric stretch and TA and TO modes.[153] However, some recent evidence suggests it does not actually involve the Si-O-Si stretch.[154] Either way, bands involving the Si-O-Si stretch can be mitigated by avoiding oxygen impurities which typically enter through crucibles during processing. Employing more expensive float-zone versus Czochralski method Si can be effective at reducing oxygen impurities, therefore reducing the intensity of some interfering bands, but vibrations solely involving silicon atoms will obviously remain. Overall, Figure 4.4 makes clear that decreasing path length is necessary to maintain useful throughput at low frequencies. In the case of the wafer/hemisphere comparison shown here, wafer throughput at low frequencies ranges from 8 to 20 times better than that of the hemisphere.

The consequence for spectroscopy is shown in Figure 4.5, which plots two ATR spectra obtained by dropping neat MOP onto the microgrooved wafer and the Si hemisphere. It is immediately apparent that the hemisphere's near-zero throughput below 1000 cm^{-1}renders the low frequency v_5 and v_{11} ring breathing modes unobservable. Conversely, they are visible with the microgrooved wafer with signal-to-noise comparable to that of any other band in the spectrum. The manufacturer has noted that the optical configuration shown

in Figure 4.1, i.e. beam normally incident on a groove face, results in interference fringing due to multiple internal reflections in a groove. This was only observed when spectra were collected with high spectral resolution (≤ 1 cm^{-1}) which is much lower than that used for condensed phase work reported in this thesis.

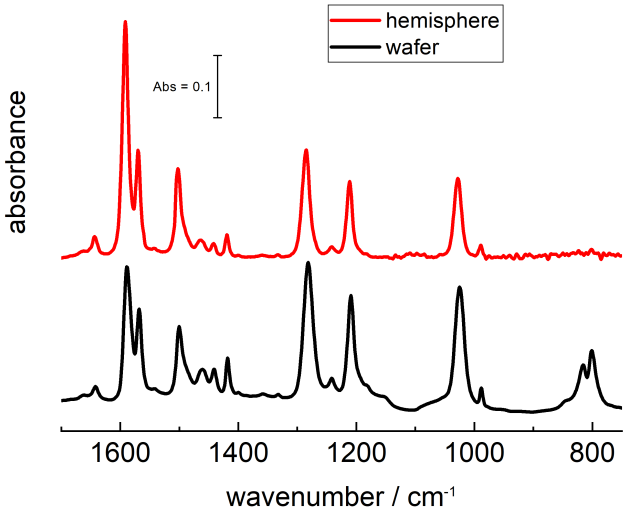

Figure 4.5: Comparison of ATR spectra collected with a hemisphere (black) and a microgrooved IRE (red). The shorter pathlength of the microgrooved IRE improves signal-to-noise at low frequencies.

4.3.2 Electrochemical ATR-SEIRAS measurements

The evidence presented in the preceding section makes a strong case that microgrooved IREs should provide new spectral information when compared to traditional Si hemispheres. The remainder of this chapter is devoted to determining how the limited AOI range affects the ATR-SEIRAS response. As described in the Experimental section, Au films were prepared by sputtering. Both IREs were metallized at the same time to ensure film comparability.

Larger IREs like the hemisphere are better able to accommodate the large beamspots produced at high AOI in specular reflection accessories. This effect is offset by the optical properties of the VeeMAX accessory, as throughput is known to peak around 50°. Indeed, Figure 4.6 shows a series of energy curves with varying AOI and a Si hemisphere placed at focus. The maximum intensity varies weakly around a maximum value at 50° and falls off by less than 10% at the extremes. Notably, maximum throughput is achieved below 70°, an angle which is typical of SEIRAS measurements.

There are several considerations to be made when selecting an AOI for an ATR-SEIRAS study. First is the effect of AOI on polarization. At normal incidence (AOI = 35°), reflection losses are minimized for unpolarized light. However, departures from normal incidence have consequences for the polarization state of reflected and transmitted light. Reflection at the Si/air interface can be calculated using the Fresnel

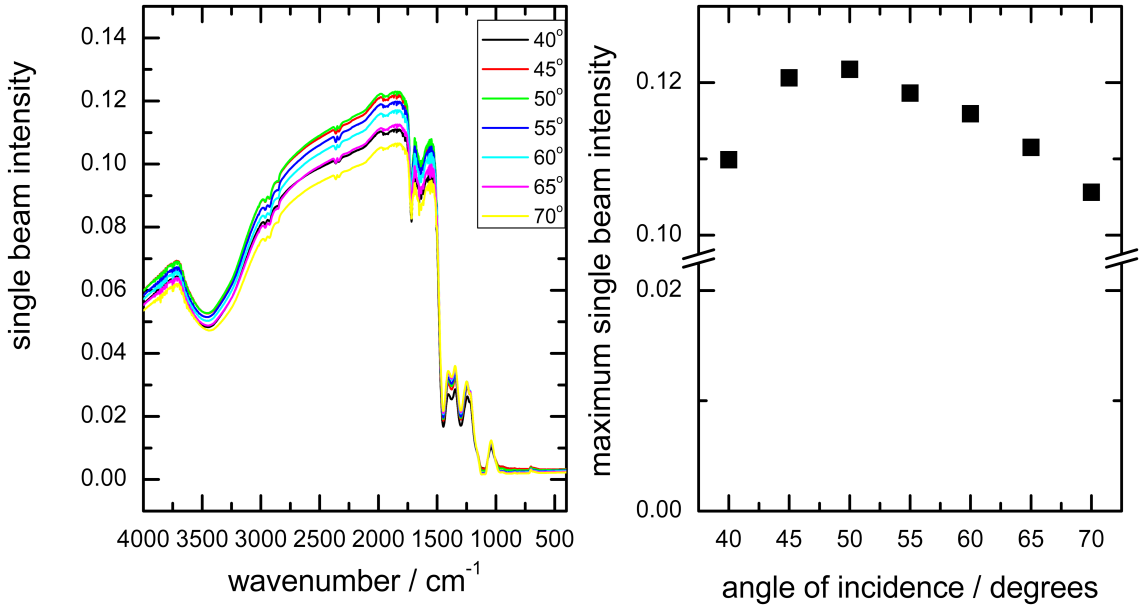

Figure 4.6: Variation of optical throughput as a function of AOI using a Si hemisphere. Single beams are shown at left and the maximum intensity at about 1750 $cm^{-1}$is plotted at right.

equations for s- and p-polarized light:

$$R_s = \left| \frac{n_{air}\cos\gamma - n_{Si}\sqrt{1-(\frac{n_{air}}{n_{Si}}\sin\gamma)^2}}{n_{air}\cos\gamma + n_{Si}\sqrt{1-(\frac{n_{air}}{n_{Si}}\sin\gamma)^2}} \right|^2$$

$$R_p = \left| \frac{n_{air}\sqrt{1-(\frac{n_{air}}{n_Si}\sin\gamma)^2} - n_{Si}\cos\gamma}{n_{air}\sqrt{1-(\frac{n_{air}}{n_Si}\sin\gamma)^2} + n_{Si}\cos\gamma} \right|^2$$

$$R_{avg} = \frac{1}{2}(R_s + R_p)$$

Here, $\gamma = AOI - 35^\circ$ is defined as in Figure 4.3. Figure 4.7 plots the reflection at the Si/air interface for p-, s-, and un-polarized light. The black boxed section indicates the AOI range used in this chapter. While the average reflection is essentially independent of AOI, the relative contributions of p- and s-polarized light vary. Per the surface selection rules of ATR-SEIRAS, only p-polarized light produces signal enhancement. Maximum reflection of p-polarized light occurs at $\gamma = 0^\circ$ (normal incidence) and drops off approximately parabolically on either side. Ideally, one would work at the Brewster angle, but this is at a geometrically unobtainable $\gamma = 74^\circ$. Nevertheless, Figure 4.7 shows that AOI above normal incidence result in larger relative proportions of p-polarized light being transmitted. In experiments using a Si hemisphere, the incoming beam is always at normal incidence, so there is no change in polarization contribution with AOI.

The second consideration is the relationship between AOI and signal enhancement. As described in Chapter 2, the angle of the light travelling through the crystal, ϕ, should be around 70° to achieve the

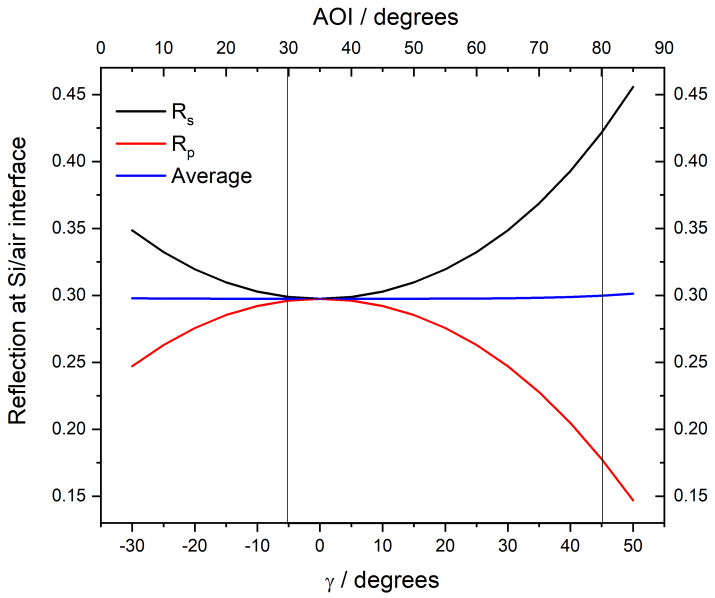

Figure 4.7: Polarisation dependence for reflection at the Si/air interface of a microgrooved IRE. Angles are defined in Figure 4.3.

highest signal enhancement. Because incoming light is mapped to a narrow range of lower angles (recall that $34^\circ \leq 35^\circ + \phi \leq 47^\circ$), the enhancement will likely be lower than ideal.

With these considerations in mind, a series of potential-dependent ATR-SEIRAS measurements were performed as a function of AOI using a Au-coated microgrooved IRE. The resulting spectra are shown in Figure 4.8a. As these are absorbance difference spectra, upward going bands indicate the gain of an adsorbate at the sample potential (E = +200 mV) relative to the reference potential (E = -700 mV), while downward going bands indicate a loss. In Figure 4.8a, upward bands at 1617, 1508, and 1310 $cm^{-1}$are diagnostic of the A'-symmetric modes of an adsorbed monolayer of MOP. Maximum throughput is expected to be around normal incidence (30 to 40°), but SEIRAS signal is rather weak here. Signal intensity appears to increase monotonically until 60°, above which spectral quality begins to deteriorate. At 70° there is no detectable signal (data not shown). The SNR of the C-O-C asymmetric stretching mode at 1310 $cm^{-1}$is plotted in Figure 4.8b. Both absolute signal, s, and SNR peak around 50 – 55°. This observation is surprising considering the discussion above about increasing p-polarization and greater enhancement at higher AOI. This can be partially explained using geometric ray tracing, which reveals that increasing the AOI also increases the proportion of rays undergoing multiple bounces. Figure 4.9 shows three representative cases at AOI = 35, 55, and 65°. At the shallowest AOI of 35°, light incident on terraces is transmitted into the Si and does not achieve TIR, instead exiting into the subphase. Light incident on slopes mostly undergoes a single bounce and exits the crystal before travelling to the detector. Roughly 30% of incident rays complete a single bounce, while 10% complete a double bounce. At AOI = 55°, the detector-facing slopes are shadowed and rays incident on the source-facing side are refracted to less grazing angles. A higher proportion of rays overall

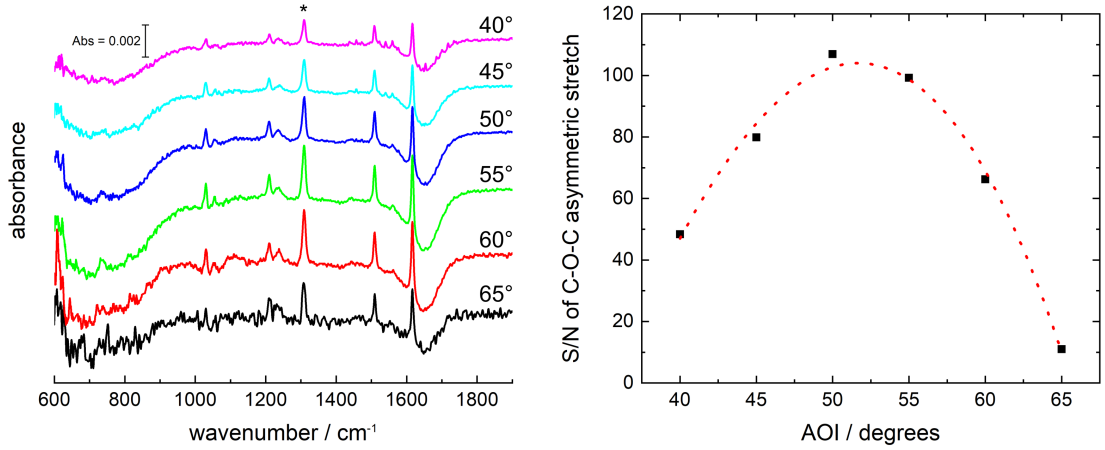

Figure 4.8: ATR-SEIRAS spectra of MOP obtained on microgrooved IRE. a) Potential difference absorbance spectra collected at various AOI. Reference and sample spectra were collected at -700 and +200 mV, respectively. b) Signal-to-noise ratio of the C-O-C asymmetric stretching mode at approximately 1310 $cm^{-1}$with a dotted line fit to guide the eye.

achieve TIR, with 40% undergoing a single bounce and 30% a double bounce. At relatively grazing angles (AOI = 65°) the majority of rays (60%) undergo double bounces while only 10% undergo a single bounce. However, at such high AOI the position of the rays strongly affects the number of rays which escape the crystal.

Most likely the largest influences on losses at high AOI are the size and position of the beamspot at sample. Although the patent for the VeeMAX III optical design claims that the beamspot position is independent of the selected AOI, in practice the beamspot travels off-center by several millimetres over the full range of AOI. Considering the relatively large (typically 10 mm diameter) beamspots which are normally employed with the accessory, this is not problematic for most studies. However, the spot size used in this work is very small. The source size is effectively defined by an aperture diameter, δ. In this work, $\delta = 2$ mm. The source image is further magnified by a factor $M = 1.8$ at sample due to beam expansion optics in the Vertex FTIR. Movement by even a few millimeters is very large on the scale of the focused beamspot. Furthermore, at high AOI the beamspot elongates as it is projected on the substrate. The geometric diagram shown in Figure 4.10 indicates that for a beam of diameter $d = M\delta$, the projected length parallel to the optical axis is $a = M\delta \cos AOI$. At AOI =60°, $a = 7.2$ mm, which is larger than the exposed portion of the wafer. This implies that as AOI increases to grazing incidence, a growing proportion of the incident beam either does not return to the detector or is reflected off the Delrin holder, contributing no analytical signal. Combined, these two factors of beamspot elongation and positional instability drive down SNR at higher AOI beyond what might be expected from arguments about polarization, multiple bounces, and the SEIRAS enhancement mechanism.

Based on Figure 4.8, the empirically optimized AOI is between 50 and 55°. At these angles, SNR is

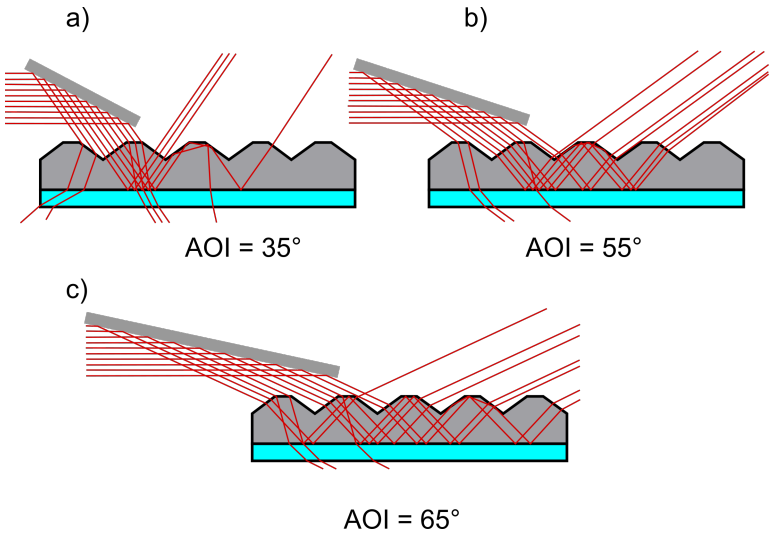

Figure 4.9: Two-dimensional geometric ray-tracing of light incident on the wafer at three different AOI. Rays are incident from the left and reflect off a simple mirror. The proportion of rays undergoing double bounces increases with AOI.

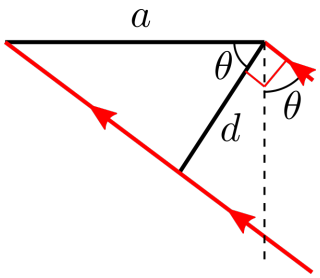

Figure 4.10: Ray diagram of beam projected on wafer.

sufficient to identify several strong MOP vibrations as well as a few relatively weak ones. SEIRAS selection rules requires a component of the transition dipole moment to be aligned normal to the metal surface. The transition dipole moments (TDM) of MOP either possess A' symmetry (in plane of the heterocycle) or A'' symmetry (out of plane). The near-vertical adsorption motif of high-density adsorbed MOP prevents observation of A''-symmetric modes, but several A'-symmetric modes are visible. Positive-going bands at 1562 cm^{-1}(v_{8b} ring vibration), 1237 cm^{-1}(C-O-C asymmetric stretch), 1210 cm^{-1}(v_{9a} ring vibration), and 1028 cm^{-1}(C-O-C symmetric stretch and ring mode) can be seen. The band at 1056 $cm^{-1}$is likely the perchlorate anion Cl-O stretch.[155] Two A'-symmetric modes which are visible in bulk spectra are not observed in SEIRAS as their TDM is aligned orthogonally to the molecular axis.

In addition to the strong signals discussed above, there is a very weak signal at 736 cm^{-1}which is particularly intriguing. At first glance, it may be the v_5 ring vibration which is clearly shown in Figure 4.5, but this is not conclusive. Despite several efforts, this band was not reproduced consistently at SNR above what is shown. Considering that the lowest frequency MOP mode around 800 cm^{-1}has A' symmetry and is aligned with the molecular axis, it is surprising that a stronger band is not evident at low wavenumbers. At

this time, this spectral feature cannot be satisfactorily explained.

Spectral features from water can also be seen in Figure 4.8. The broad downward-going band centred around 1625 cm^{-1}corresponds to the bending mode of H_2O. At the reference potential, H_2O is adsorbed to the Au layer but at the sample potential it is replaced by adsorbed MOP, resulting in a downward going band due to loss. It is particularly exciting that, at low frequencies, another downward-going band is visible at roughly 725 cm^{-1}which can be assigned to water libration modes[156,157] that result from frustrated rotation of hydrogen bonded water molecules.[158] The presence of the H_2O libration mode, which exhibits the same potential dependence as the H_2O bending mode, confirms that the SEIRAS activity extends well below 1000 cm^{-1}. The lower limit of the collected spectra is imposed by the MCT/A detector sensitivity, but preliminary electrochemical experiments at the Far-IR beamline of CLS suggest that the SEIRAS enhancement mechanism is operative in the Far-IR.

4.3.3 Performance Comparison between Si hemisphere and Microgrooved IRE

In order to compare the performance of the microgrooved wafer to that of a traditional Si hemisphere, Figure 4.11 shows an ATR-SEIRAS spectrum from each IRE at its respective optimized AOI. Gold layers were prepared simultaneously to facilitate a direct comparison. The spectra are qualitatively similar above 1200 cm^{-1}, with the hemisphere outperforming the wafer by a factor of about two or three. This is similar to the reported performance of a 200 µm thick Si wafer coupled to a ZnSe IRE relative to that of a conventional Si hemicylinder.[149] However, the stronger phonon absorption in the hemisphere degrades SNR enough that the C-O-C asymmetric stretch at 1300 cm^{-1}actually has 33% lower SNR than that collected with the wafer. Below 1200 cm^{-1}, the SNR degradation is even more severe. The strong oxygen defect mode around 1100 cm^{-1}completely blocks throughput, driving SNR to zero in its vicinity. The perchlorate Cl-O stretch at 1050 $cm^{-1}$is lost in the noise. Without an ATR spectrum to aid assignment, unambiguously identifying the MOP vibration at 1040 cm^{-1}would be difficult if not impossible. By comparison, below roughly 1450 $cm^{-1}$the wafer spectrum exhibits only a modest increase in spectral noise, allowing identification of the MOP, perchlorate, and water libration modes present at low frequencies.

4.4 Conclusions

The data presented in this chapter demonstrate that microgrooved wafers are well-suited to electrochemical ATR-SEIRAS. At frequencies below 1450 cm^{-1}, they provide substantially better optical throughput, allowing otherwise undetectable vibrations to be observed. Above this frequency, wafers are competitive with optimized spectra yielding signal strengths within a factor of two or three. The optimal AOI was empirically found to be 50 – 55° and depends on the several factors: 1) specular accessory throughput, 2) reflection losses incurred at the surface of incidence, 3) refracted AOI through the crystal, and 4) the number of internal reflections. Controlling the position and size of the beamspot more accurately would potentially offer even

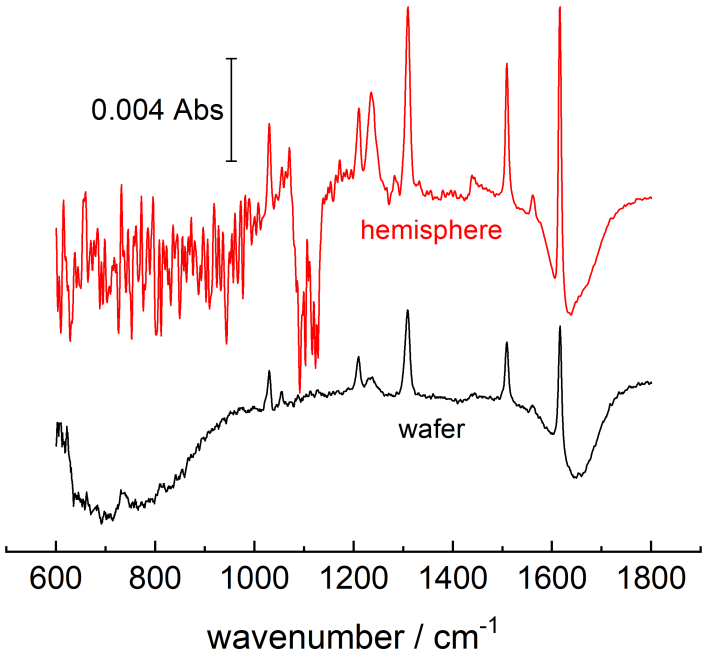

Figure 4.11: Comparison of ATR-SEIRAS spectra of MOP using the 25 mm diameter Si hemisphere (red) and microgrooved IRE (black). Spectra were collected with AOI = 55° for the microgrooved IR and 68° for the hemisphere.

better performance at higher AOI; this will be addressed in the context of microspectroscopy in the next chapter.

Besides the consequences for the overarching thesis goal, perhaps the most impactful outcome of this chapter is the demonstration that the inexpensive microgrooved wafer can be used for electrochemical ATR-SEIRAS with results which are at least comparable to a far more expensive hemisphere and, in the highly important fingerprint region, actually exceed the latter's performance. In subsequent work in the Burgess group, their low cost has been exploited in preparing multiple Au layers by sputtering simultaneously. Au layer preparation and stability have been recognized in this thesis and in the literature as a critical bottleneck in ATR-SEIRAS experiments. Preparing many Au-coated substrates in parallel minimizes the time spent on thin film deposition and allows failed Au layers to be rapidly swapped for new ones. Au layer preparation typically takes several hours, comprising IRE polishing, metal deposition (either chemical or vapour deposition), and post-deposition electrochemical texturing. The metal deposition step is usually rate-limiting. Chemical ("electroless") deposition requires the use of HF and therefore proceeds extremely carefully and cannot be performed in parallel. (To date, no member of the Burgess group has attempted to perform chemical Au deposition on a microgrooved IRE; this is motivated in part by the difficulty associated with doing so and also by subsequent development in hybrid Au layers which is discussed in a later chapter.) Vapour deposition

requires at least several hours for chamber pumpdown, target conditioning, and film deposition. Unlike chemical deposition, vapour deposition can be performed in parallel and is limited only by the chamber capacity; runs of five to ten IREs are typical.

This chapter has demonstrated the utility of the microgrooved wafer for electrochemical ATR-SEIRAS using a conventional FTIR instrument. At focus, the spot size is still much larger than the critical dimension of a groove. The next step in the project was to build a custom horizontal microscope endstation capable of illuminating a single groove with a well-defined spot.

5 Design and Commissioning of a Horizontal ATR Microscope Endstation

Contributions of the Author

The results described in this chapter have been published in the following peer-reviewed publication:

Tyler A. Morhart, Stuart Read, Garth Wells, Michael Jacobs, Scott M. Rosendahl, Sven Achenbach, and Ian Burgess. Attenuated Total Reflection Fourier Transform Infrared (ATR FT-IR) Spectromicroscopy Using Synchrotron Radiation and Micromachined Silicon Wafers for Microfluidic Applications. *Applied Spectroscopy*, **2018**, 89, 21, 1781-1789.

I designed the horizontal ATR microscope and the commissioning experiments with Ian Burgess with input from Scott Rosendahl. Read assisted with beamline setup and optical alignment. Wells and Jacobs assisted with the open channel microfluidic device fabrication with technical input from Sven Achenbach. I wrote the first draft of the manuscript and prepared all figures. Text and figures in this chapter are my own.

5.1 Introduction

In Chapter 3, a successful approach to perform electrochemical ATR-SEIRAS microspectroscopy was discussed. Using an FTIR microscope and a homogeneous Au thin film electrode, good-quality spectra were obtained from a spot approximately 125 μm^2. Although this spot size was sufficient to interrogate a microelectrode, the challenge of achieving this goal was aggravated by the optical characteristics of the hemisphere. Chapter 4 identified a suitable replacement for the hemispherical IRE in the form of a microgrooved IRE. Geometric ray-tracing and electrochemical ATR-SEIRAS spectra were presented that showed the favourable characteristics of the wafer when using a macroscale beamspot. In the context of the larger thesis goal, the promise of the microgrooved Si IRE is that, for a sufficiently small beam, a single groove can be illuminated, spectroscopically addressing a microband electrode on the principal reflecting plane. For reasons discussed below, the microgrooved Si IRE could not be integrated with the existing microscope. Therefore, it was necessary to build a custom endstation capable of illuminating a single groove face.

Although the endstation described in this chapter was conceived for use with ATR-SEIRAS microspectroscopy experiments, the benefits of the design to ATR microspectroscopy was quickly recognized. ATR microspectroscopy is well developed in the scientific literature going back to the work of Harrick on the

"split pea" microspectroscopy accessory.[159] Although early measurements were largely limited to collecting single spectra,[160,161] integration of FT-IR microscopes eventually allowed collection of ATR-FT-IR spectra at multiple points on a sample[162] or in linear scanning or mapping modes.[28,163] These representative examples demonstrate application of ATR microspectroscopy in the non-destructive characterization of art materials,[28] identification of prostate tissue zones in sectioned tissue samples,[162] and in the detection of synthetic microplastics in marine sediments.[163] The higher refractive index of the IRE provides improved spatial resolution but magnification (or equivalently the field of view) depends on the geometry of the IRE. Further details are given in Appendix A.

The excellent beam-steering characteristics of the microgrooved IRE were expected to greatly benefit ATR microspectroscopy. A common problem encountered in the literature is the limited control of the beamspot's position imposed by the beam-steering characteristics of the chosen IRE. This was recognized in reports employing hemispheres[161] and their variants.[160] In those studies, the beam could only be deflected by about 100 µm, significantly limiting the field of view and imposing strict requirements for sample placement on the IRE. Other reports have tried repositioning the sample on the IRE[162] (or *vice versa*) in order to interrogate different areas, but this raises the possibility of sample damage and cross-contamination if good cleaning protocols are not followed between measurements. Furthermore, reproducible sample contact is highly beneficial to quantitatively compare different spots.

This chapter discusses the development of a custom horizontal ATR (HATR) microscope endstation at the Mid-IR beamline. At the time this work was completed, the fabrication of stable, SEIRAS-active microelectrodes was still challenging, and an alternate system with similar spatial dimensions was employed, namely a simple open-channel microfluidic device. A demonstration of the HATR endstation's single-point spectroscopy capabilities with an open-channel microfluidic is presented in this chapter, and reconfiguration of the endstation for vibrational imaging of microfluidics will be subsequently described in Chapter 6.

5.2 Experimental

5.2.1 Materials

Optical components and alignment laser were purchased from Thorlabs. CaF_2 disks (25.4 mm diameter, 1 mm thick) were purchased from Crystran. Si microgrooved IREs were purchased from IRUBIS GmbH. SU-8 2010 resist and developer were purchased from Microchem. AZ1505 photoresist and AZ400K developer were from Merck Performance Materials GmbH. HCl and HNO_3 were from Alfa. Ultrapure water was supplied by a Millipore system.

5.2.2 Fabrication of a Model Microfluidic Device and Transmission Slit

UV photolithography was used to fabricate the open-channel microfluidic device. The layout pattern was created in LayoutEditor and consisted of a 500 µm × 6 mm open channel terminating at each end in a 3.2 mm diameter circular opening.

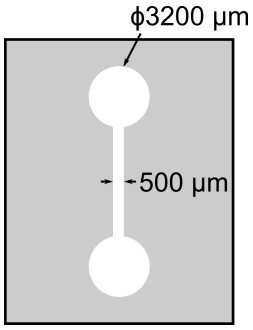

Figure 5.1: Schematic of the open-channel microfluidic device.

A direct-write UV laser system (HIMT DWL66+) equipped with a 355 nm laser was used. As the device was not intended to be sealed and ATR penetration depths are on the order of the IR wavelength, 10 µm thick SU-8 was chosen. Photoresist was spin-coated onto the substrate then baked for 2 min at 95 °C. Then, the coated substrate was exposed with the laser system using a 10 mm working distance write head at 110 mW laser power. After exposure, the substrate was baked for 3 min at 95 °C and allowed to cool. After completion of the post-exposure bake, it was developed in SU-8 developer for 3 min. The developed substrate was immediately rinsed with isopropanol and copious amounts of ultrapure water, blown dry with nitrogen gas, and inspected by optical microscope.

A 5 x 0.4 mm^2 transmission slit was fabricated on an IR-transparent CaF2 window. First, a 30 nm layer of Au was deposited using a Denton Vacuum Desk IV sputtering unit. Then, a 500 nm layer of AZ1505 was spin-coated onto the Au-coated side of the window. The coated substrate was soft-baked at 100 °C for 60 s and allowed to cool. The slit pattern was exposed using the laser system and the substrate was developed for 60 s. A subsequent dip for 5 s in dilute aqua regia (3:1:2 HCl : HNO_3 : H_2O) etched the unmasked Au. The etched substrate was rinsed with ultrapure water and the photoresist mask was removed with acetone before a final cleaning in isopropanol, flowing ultrapure water, and drying with nitrogen.

5.2.3 Spectroscopic Measurements

FTIR measurements were performed at the mid-IR beamline at CLS using a Bruker Vertex 70v FTIR spectrometer coupled to the horizontal microscope by two planar beam transfer optics. The beam angle of incidence (AOI) is measured relative to the normal of the principal reflecting plane on the IRE. In this definition, more grazing angles are closer to 90°. A 150 µm diameter aperture was used for all experiments.

Slit transmission measurements were completed by setting the AOI = 90° i.e. beam parallel to the

floor. The transmission slit was placed at focus and the transmitted power on the detector (analog-to-digital converter counts) was recorded for a set of positions as the slit was scanned in the sample plane.

ATR-FTIR measurements of water and ethanol in the microfluidic channels were collected at AOI = 60°. The dry microgrooved Si IRE was placed at sample focus and the detected power was recorded as a function of x, y, and z (see Figure 5.4 for definitions of the Cartesian coordinate system). Reference spectra of the dry channel were collected at several positions along y and were subsequently re-measured after wetting the channel with a drop of ethanol or water. All spectra were the result of 64 co-added interferograms collected at 16 cm^{-1}resolution.

5.2.4 Total Least Squares Deconvolution

In an effort to measure the inherent IR beam profile in the horizontal microscope, the beam was scanned across a slit of well-known dimension. The detector signal amplitude, S, was measured as a function of position. Mathematically, the measured signal S is the convolution of the inherent beam profile, $P_{beam}(x)$, with the slit, $P_{slit}(x)$. The (continuous) convolution is defined as

$$S = (P_{beam} * P_{slit})(x) = \int_{-\infty}^{\infty} P_{beam}(x-\tau)P_{slit}(\tau)d\tau$$

which can be thought of as translating the beam profile across the slit profile and computing the overlap integral for each position τ. Although in principle one could use the properties of the Fourier transform to recover P_{beam}, in practice the discretely sampled nature of the measurement renders this approach highly sensitive to measurement noise and data density. Instead, a better approach was described by Rahman and Sarkar.[164] Recognizing that the discrete convolution could be cast as a matrix equation $\mathbf{A}x = b$, where $\mathbf{A}$ is the convolution matrix, x is a $(n \times 1)$ vector containing the inherent beam profile P_{beam}, and b is a $(m \times 1)$ vector containing the measured data, they applied total least squares deconvolution (TLS) to recover P_{beam}. The central challenges of solving this matrix equation are 1) the matrix $\mathbf{A}$ is singular, meaning it does not have an inverse, 2) $\mathbf{A}$ is ill-conditioned, meaning that small measurement errors in b result in massive errors in solution vector x, and 3) the system is over-determined, meaning $m \geq n$, and so only an approximate solution exists. TLS deconvolution is a robust means of finding a satisfactory approximation and is tolerant of both measurement error and error in the inherent beam profile due to source instability.

The TLS algorithm proceeds by several steps which are described and justified in reference[164]. First, an augmented matrix $\mathbf{C} = [\mathbf{A} : b]$, where $\mathbf{C}$ is $[m \times (n+1)]$, is constructed. Then, we compute the singular value decomposition of $\mathbf{C}$:

$$\mathbf{C} = \mathbf{U}\mathbf{\Sigma}\mathbf{V}^H$$

where $\mathbf{U}$ and $\mathbf{V}$ are matrices containing the left and right singular vectors of $\mathbf{C}$, so that $\mathbf{U} = [u_1, \cdots, u_m] \in \mathbb{C}^{m \times m}$, $\mathbf{V} = [v_1, \cdots, v_{n+1}] = \mathbb{C}^{(n+1)\times(n+1)}$ with u_i and v_i the left and right singular vectors, respectively. $\mathbf{\Sigma}$

is a diagonal matrix, $\mathbf{\Sigma} = \text{diag}(\sigma_1, \cdots, \sigma_{n+1}) \in \mathbb{R}^{m\times(n+1)}$ with the singular values $\sigma_1 \geq \sigma_2 \geq \cdots \geq \sigma_{n+1} \geq 0$ on the diagonal. Then, the approximate solution $\hat{x}$ is found by approximating $\mathbf{C}$ with a reduced-rank matrix $\hat{\mathbf{C}}$ of rank $r \leq n+1$. (In practice, this means keeping the r largest singular values and setting the other $n+1-r$ singular values to zero.) Thus, we can construct the approximate solution from elements of the right singular values

$$\hat{x} = \frac{\Sigma_{i=1}^{r} v_{n+1,i}[v_{1,i}v_{2,i}\cdots v_{n,i}]^H}{1 - \int_{i=1}^{r} v_{n+1,i}^2}$$

The number of singular values to retain (equivalently, the rank r of the approximate matrix $\hat{\mathbf{C}}$) is varied manually until a suitable approximate solution is found. A suitable solution was determined by convolving the extracted profile with the slit function and comparing the calculated and measured data. For the data shown in this thesis, reducing the rank of the matrix $\mathbf{C}$ by approximately half yielded good results.

5.2.5 Optical Modelling

Two-dimensional geometric ray tracing was performed using OptGeo software (version 2.24). The refractive index of Si was set to 3.4 and monochromatic light was used for all ray traces.

Three-dimensional geometric ray tracing was performed with Zemax OpticStudio 20.2 using a non-sequential modelling environment. A simple model was built to capture the essential features of the horizontal microscope, Figure 5.2. The incident beam was monochromatic ($\lambda = 3.0$ µm) and was generated by an 8×8 mm^2 source rectangle. The size was chosen to match the beam size incident on the sampling parabolics (inset in Figure 5.4). The beam power was set to 1 W. For monochromatic light, a simple converging lens (BaF_2, Edmund Optics part no. BF-BX-25-25.1) with a 25.4 mm focal length can approximate the action of an off-axis parabolic and is substantially easier to model in OpticStudio. Matched converging lenses were used to provide a converging beam at 60° AOI. The microgrooved Si IRE was first modelled in Solidworks based on detailed drawings provided by IRUBIS GmbH and then imported into Zemax. The refractive index of Si was used (OpticStudio library entry SILICON from INFRARED library, modelled with the Sellmeier equation). A matched BaF_2 lens was used to collect the outgoing beam, resulting in a collimated beam. Finally, another matched BaF_2 lens focused the light onto a 500×500 µm^2 detector element.

5.3 Results and Discussion

5.3.1 Design Considerations of the Horizontal ATR Microscope Endstation

The need for a custom microscope was motivated by the shortcomings of the available FTIR microscope. Early experiments with the Hyperion FTIR microscope indicated that focusing through a Schwarzchild objective on the microgrooves did not allow sufficient collection of outgoing rays. Figure 5.3a shows the beampath through a Schwarzchild objective operating in reflection mode with a simple mirror at focus. Figure 5.3b

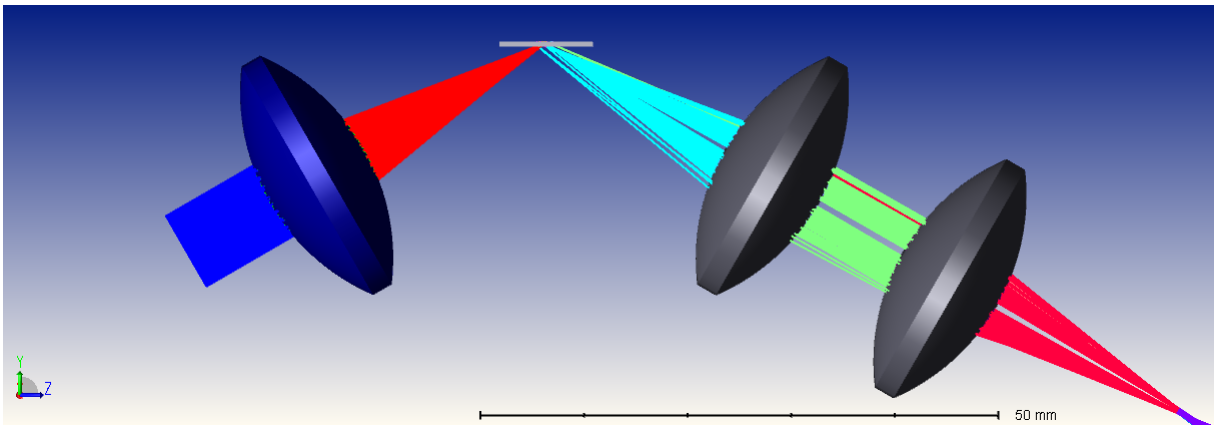

Figure 5.2: Picture of the 3D ray-tracing simulation geometry. The beam is generated at left and is focused onto the microgrooved IRE by a BaF_2 lens (blue) and then is collimated by an equivalent lens before being focused onto the detector. The detector size is matched to the MCT/A detector used in this chapter. Rays are colour-coded by intersection for clarity.

replaces the mirror with the scaled-up microgrooved wafer. Increasing the scale allows the deleterious effect of the wafer to be made more obvious for the purposes of the figure. Light is incident from the top on a primary spherical mirror, reflected onto a concentric secondary spherical mirror, and focused at the sample plane at the bottom of the figure. Reflected rays travel through an identical (though mirrored) path to return to the detector. Placing a microgrooved IRE at focus displaces the beam as it travels through the Si. Although the situation is artificially worsened by increasing the scale of the wafer, the figure illustrates that beam displacement due to refraction in the Si prevents many rays from reaching the detector. Experimental results (not shown) confirmed that only a small fraction of IR light was able to be collected in this geometry.

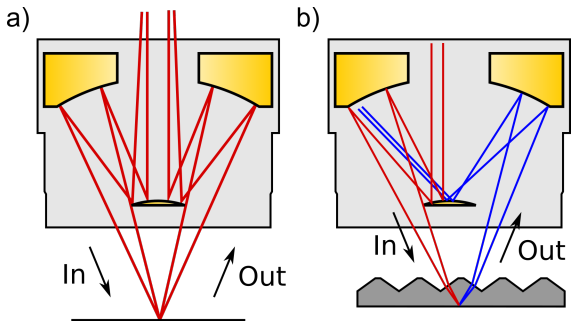

Figure 5.3: Two-dimensional ray-tracing of a Schwarzchild objective (not to scale) in reflection mode with a) a flat mirror at the sample position and b) a microgrooved IRE placed such that the incident radiation is focused on the principal reflecting plane. The blue rays in (b) indicate returning rays which are off-centre and do not reach the detector.

The goal for the microscope was to provide variable AOI, control over the size of the spot at focus, and fine control over the position of the microgrooved wafer. This was accomplished with the design shown in Figure 5.3. SIR or globar radiation was delivered from the external output of the Vertex 70v spectrometer and steered with two planar mirrors toward the Hyperion FTIR microscope. The internal pickoff mirror was moved to the

passthrough position, allowing the IR beam to propagate beyond the Hyperion microscope and into the first leg of the horizontal microscope. The optics necessary for the horizontal microscope were fastened to a 60×60 cm^2 aluminum breadboard fastened to the same optics table as the Vertex 70v and Hyperion microscope. The breadboard and optics table were in electrical contact via metal fasteners to prevent static discharge and grounding problems. (Mounting the detector outside the spectrometer makes the system particularly sensitive to static charge buildup.) The tight confines of the optics table required the breadboard to partially overhang the edge of the table; this cantilever geometry undoubtedly has potential to contribute some noise due to coupling of mechanical vibrations, but this was found to be low in practice. (Subsequent rearrangement of the experimental hutch by Mid-IR beamline staff allows the horizontal microscope to currently be supported on a dedicated optics table; data shown in this thesis were collected before this occurred.)

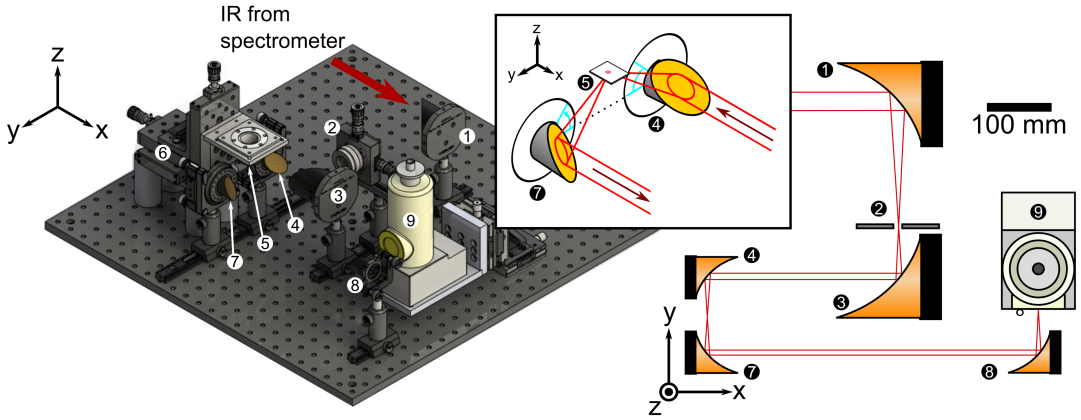

Figure 5.4: Left: CAD drawing of the horizontal ATR microscope. The red arrow indicates the direction that IR is incident. The inset depicts the sampling optics and the sample holder, which is compatible with the microfluidic devices used in this chapter and Chapter 6 and the spectroelectrochemical cell used in Chapter 7. The IRE is mounted such that the grooved side faces down (negative z-axis) toward the incident beam. Right: schematic of optical layout

The SIR beam is collimated and relatively large (diameter roughly 50 mm) when it exits the spectrometer. A 50.8 mm diameter off-axis parabolic, OAP1, (position 1) with $f_1 = 152.4$ mm focal length, collects the beam and focuses it at position 2, the aperture plane, which is conjugate to the sample focal position (*vide infra*). A telescoping aperture holder at position 2 mounted on an optical rail can hold apertures of varying sizes, allowing control of the spot size at sample. The role of the aperture is twofold. First, the aperture size controls the size of the spot which illuminates the sample. Downstream optics serve to image the aperture at 1x magnification onto the sample. This is comparable to the size of the beam at focus. The measured divergence, θ_d, of the collimated SIR beam incident on OAP1 is approximately 1 to 2 mrad. For a Gaussian beam, the diameter of the spot at the aperture plane is given by the product of θ_d and the focal length $f_1 = 152.4$ mm of OAP1, so that the spot diameter is between 150 and 300 µm in diameter. The smallest aperture used in the microscope was 150 µm in diameter, which is close to the lower bound on beamspot size. The second function of the aperture is to act as a spatial filter; the focused spot is strongly structured in

space and frequency, with a slightly V-shaped pattern where the joint of the V has highest intensity. Using a circular aperture selects only the most intense part of the beam in a circular shape.

After the aperture, a 25.4 mm diameter OAP2 (3), $f_2 = 50.8$ mm, collects the diverging beam. The ratio of focal lengths $f_2/f_1 = 3$ so that this section acts as a beam compressor, decreasing the radius of the collimated beam from roughly 50 mm to 17 mm, justifying the smaller diameter optics used in the sampling optics and later sections of the microscope.

The compressed beam is then incident on the sampling optics which are composed of two matched 25.4 mm OAPs (OAP3 and OAP4, $f_3 = f_4 = 50.8$ mm, positions 4 and 7 respectively) held in rotation mounts. Both mounts are supported on optical rails, allowing OAP4 to be moved to accommodate differing AOI. The size of the mounts limits how close OAP3 and OAP4 can be brought together, limiting the lower end of the accessible AOI range to 50˚. These OAPs were chosen to have f/# = 2, imparting a relatively large depth of focus compared to that of the Schwarzchild objectives used in the Hyperion microscope (f/# = 1.1 or less). The sample (a microgrooved Si IRE) is held in a custom holder which can be sealed to form a complete spectroelectrochemical cell. The position of the sample (5) can be controlled by the 3-axis positioner (6) in steps of 10 µm with excellent reproducibility.

After the beam is collected by OAP4, it is collimated and sent to OAP5 (25.4 mm diameter, $f_5 = 50.8$ mm, position 8). OAP5 is also mounted on a rail so that it can be translated to follow OAP4 when the AOI is adjusted. OAP4 focuses the beam onto the MCT/A detector (9), which is mounted on a 3-axis positioner. The detector signal is fed into the spectrometer so that spectra can be collected.

It is often claimed that synchrotron sources outperform globar sources when the diameter of the beamspot at focus is less than around 20 µm. This is potentially misleading, as it is only true for optics with large magnification factors like typical FTIR microscopes, where a typical Schwarzchild objective has at least 15x magnification. Instead, it is more informative to discuss the synchrotron advantage in terms of the geometric etendue, G, introduced in Chapter 2. For maximum throughput efficiency, etendue is perfectly matched at the sample i.e. $G_{sample} = G_{source}$ and S becomes the irradiated area at sample and Ω the solid angle in which incident radiation is collected. Although globars are isotropic sources, optical limitations confine the usable emitted light to at most a half-sphere for which $\Omega_{source} = 2\pi$. (Typical collection optics are usually much smaller.) Thus, for a typical 10 × 1 mm globar, the etendue is at best 0.63 sr cm^2, whereas the measured value of G_{source} for 1600 cm^{-1}radiation at CLS is 4.1×10^{-5} sr cm^2, over 4 orders of magnitude better. The solid angle at the conjugate focus (aperture plane) can be calculated from the numerical aperture of OAP1, which defines the opening angle Θ for the cone in which light is focused. Using the formula for the solid angle of a cone, $\Omega = 2\pi(1 - \cos\Theta)$, the solid angle can be found to equal 0.085 sr. Thus, in order to match the etendue of a globar an aperture of radius 1.52 cm is required. However, 100% coupling efficiency can be achieved using SIR with only a 120 µm radius pinhole. Considering the smallest pinhole radius used in this work is 75 µm, the coupling efficiencies of a Globar and SIR are 0.002% and 37%, respectively.

5.3.2 Quantification of Beamspot Size

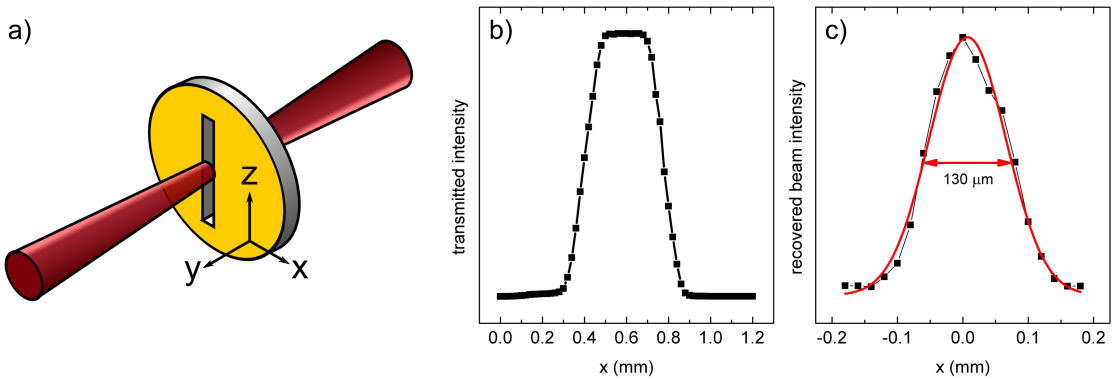

Figure 5.5: Determination of the beamspot profile at focus with a slit. a) Schematic of the experiment showing the focusing beam incident on a CaF_2 wafer with a 400 µm wide transmission slit in an otherwise Au-coated surface. b) Profile of the transmitted intensity falling on the detector. c) Recovered beam profile (black dots) after total least squares deconvolution. The Gaussian fit (solid red line) has FHWM = 130 µm.

In order to quantify the beamspot size at sample focus, a beam profiling experiment was performed. A 5×0.4 mm rectangular slit was fabricated with ultraviolet photolithography on a 1 mm thick CaF_2 disk and mounted in the 3-axis positioner at the sample focus. The AOI was set to 90° (normal incidence on the slit surface) and the long axis of the slit was aligned with the z-axis as shown in Figure 5.5a. Then, the sample was translated so that the slit scanned through the x-axis and the detected power was recorded. Figure 5.5b plots the results. The profile shown has a full-width at half-maximum of 400 µm and is the convolution of the beam profile along the axis and the slit. Performing total least squares deconvolution, as described in the experimental, with the known slit dimensions and the measured intensity profile recovers the beam profile, which is plotted in Figure 5.5c. Note that the profile is an average across the entire measurable spectral range, roughly 8000 to 1000 cm^{-1}, which is bounded by the MCT/A detector sensitivity at the high limit and by absorption in CaF2 at the lower limit. The black dots indicate the recovered profile and the red curve is a Gaussian which fits the data well. There is some slight asymmetry in the recovered profile, and it is hard to determine if this is real without a more detailed analysis of the error. It is possible that the structure in the SIR beamspot is reflected in the deconvolved profile. Whether or not this is the case, the Gaussian fit is strong enough to say that the FWHM of the recovered beamspot is 130 µm, or equivalently that 95% of the intensity falls within a 200 µm wide region. This is close to 150 µm diameter aperture, and the difference is likely due to a slight defocus at either the aperture of sample planes. Finally, it is important to note that this measurement is an average across all wavelengths.

5.3.3 Single-Point Measurements with a Sub-Millimeter Beamspot

The horizontal microscope had been designed to perform ATR-SEIRAS microspectroscopy with the explicit assumption that the small beamspot characterized above in air would provide a small, focused spot capable of 1) irradiating a single groove of the microgrooved Si IRE, and 2) addressing a single microelectrode. The characterization of the beamspot in the previous section suggested that condition 1 was likely satisfied. Before moving onto exploring whether condition 2 was met, an interesting question remained. If the beamspot was small enough to interrogate single grooves, what effect did beam positioning have on the detected power and the ATR signal? To explore that question, a simple ATR experiment was performed by positioning the microgrooved IRE at the sample focus and wetting the principal reflecting plane with a drop of neat ethanol. (The wafer was covered to prevent evaporation.) Then, ATR-FTIR spectra were collected as a function of position along the x- and y-axes, both parallel to the principal reflecting plane. Figure 5.6 plots salient results, with Figure 5.6a showing a schematic cross-section indicating the coordinate directions and the illumination geometry. The power on the detector was first monitored as the beam was translated along the x-axis, i.e. along the face of a single groove. The normalized power, plotted in Figure 5.6b (top panel), exhibits seemingly random variation of about 10 – 20%. Although one might intuitively expect the groove faces to be crystallographically smooth, observation under an optical microscope reveals a scalloped texture. This occurs during the etching process and likely results from angular error in the parent Si wafer crystallography and additional errors incurred during photolithographic mask alignment, as well as the KOH etching chemistry. Nevertheless, the power graph shown in Figure 5.6b has more or less random variations over translation of 1 mm, suggesting the surface texture, and not serious misalignment, is responsible.

The lower panel of Figure 5.6b plots the detected power (in black) as the wafer is scanned along the y-direction from groove to groove. Roughly sinusoidal variation is observed with peaks in the detected power occurring every 700 µm, which closely matches the groove-to-groove pitch (705 µm). The substantial difference between peak and trough suggests that the beam is much smaller than an individual groove. Figure 5.6d plots ATR-FTIR spectra of ethanol collected as the beam is translated over one groove period. The peak height of the OH-stretching band around 3300 $cm^{-1}$was extracted and is co-plotted in Figure 5.6c in red. Intriguingly, the peak absorbance appears out of phase with the peak detector power. To understand the physical origin of the heterogeneity in signal, we turned to 3D ray-tracing using the model described in the Experimental section. Figure 5.7 shows cross-sections of the microgrooved IRE at two positions: one where the detected power is high (Figure 5.7a) and one where the detected power is low (Figure 5.7b). Ray-tracing reveals that in the former situation, incoming radiation is incident on two grooves and is separated into two bundles of rays. Rays incident on the flat terrace are either reflected (about 30%) or transmitted into the IRE where they do not escape the crystal because of their near-normal incident angle on the principal reflecting plane. The important detail captured in Figure 5.7a is that all rays which reach the detector undergo a single internal reflection. However, Figure 5.7b depicts the situation when the detected power is at a minimum. This corresponds to an offset of the crystal along y of approximately 400 µm. Most rays which reach the

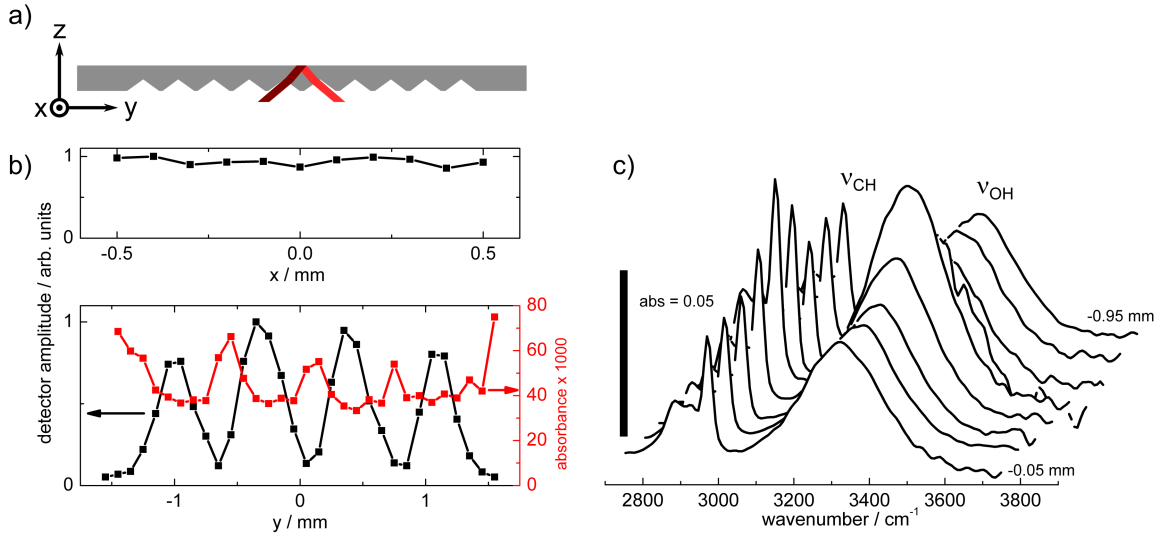

Figure 5.6: a) The microgrooved IRE showing the experimental geometry with the beam incident on a single groove. b) Detected power as a function of IRE translation along the x and y coordinates. c) ATR experiment showing the OH-stretch and hydrocarbon bands of ethanol plotted as a function of y position. The variation in the OH-stretching mode is co-plotted in red alongside the detected power in (b).

detector undergo a double internal reflection, doubling the analytical signal carried by that radiation. (A small fraction of rays escape after a single bounce.) Furthermore, rays exiting the crystal in this configuration are spread out in space, so only a small fraction reach the detector at all. Thus, although the absolute power falling on the detector is very low, those rays which do reach the detector carry a greater analytical signal than for other crystal positions along y. Figure 5.7 plots the normalised power falling on the detector as a function of translation along the y-axis, revealing a sinusoidal trend which matches that shown in Figure 5.6 very well.

The microscope described in this chapter was designed for spectroelectrochemical measurements, the goal being to interrogate microelectrodes with widths on the scale of a few hundred micrometers. At the time, reproducible fabrication of stable, SEIRAS-compatible microelectrodes was still highly challenging, so a different system was sought to test the microspectroscopy capabilities of the endstation. It was recognized that an open-channel microfluidic device would be sufficient. A schematic of the prepared device is shown in Figure 5.8. The microgrooved wafer was coated with a 10 µm layer of SU-8, an epoxy-based photoresist, and a 400 µm wide open channel was lithographically prepared. By filling the channel with water to provide spectral contrast with the photoresist which formed the channel walls, it was hypothesized that the microchannel could be profiled along its width, demonstrating the spatial resolution of the microscope. The 400 µm width of the channel was chosen to be comparable to a typical microelectrode that was expected to be used.

A cartoon of the device is shown in Figure 5.8a, with the cartesian coordinate system preserved from Figure 5.6. The channel (shown filled with water) runs perpendicular to the groove face. ATR-FTIR spectra were collected at discrete positions along the groove face i.e. along the x-coordinate in the figure. Diagnostic

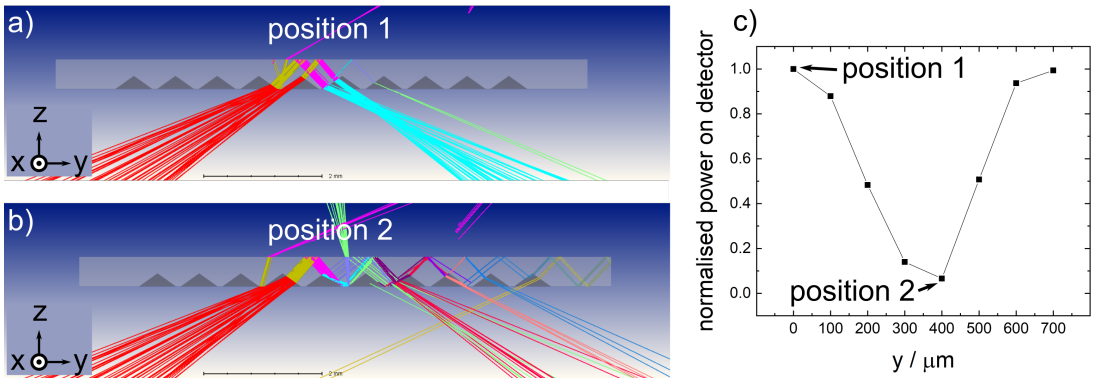

Figure 5.7: 3D raytracing depicting the beampath through the microgrooved IRE. Note that the coordinate system is the same as that used in Figure 5.2, and here the z direction is equivalent to the y direction in other figures. a) Position 1, where the IRE is placed at $z = 0$ µm and maximum intensity falls on the detector. The majority of rays undergo single reflection. b) Position 2, $z = +400$ µm (approximately one half of a groove period) and minimum intensity falls on the detector. The majority of rays undergo multiple internal reflections. c) Normalized intensity falling on the detector as a function of translation along y. The total range of z is 700 µm, or one groove period. A sinusoidal oscillation is observed which matched the experiment shown in Figure 5.6.

bands for water and SU-8 were chosen and their absorbance intensities are plotted in Figure 5.8b. The O-H stretching mode of water at 3365 $cm^{-1}$was chosen along with the phenol C-O stretch of SU-8 at 1240 cm^{-1};[165] the latter was chosen because of its strength and spectral separation from the O-H bend of water. Co-plotting these two band intensities reveals complementary profiles, with the SU-8 profile showing strong constant absorbance outside the channel ($|x| \geq 0.25$ mm) and falling to zero inside the channel (in the vicinity of x = 0.0 mm). Water is detected exclusively inside the channel. The channel dimensions, which were confirmed by optical microscopy to be 400 µm, correspond well to the FWHM of the H_2O profile. The profiles shown are the convolution of the beamspot profile with that of the channel; deconvolution recovers the beamspot profile and is plotted as an inset to Figure 5.8b. A Gaussian fit to the recovered profile has a FWHM of 70 µm. 95% of the area under the Gaussian fit is enclosed in a 150 µm region, which matches the aperture dimension very well. Although this is roughly two time smaller than the spot's FWHM in air, the differences are likely due to better focus quality in this measurement. Although it might be expected that the high refractive index of Si would impart and additional demagnfication of the beamspot similar to that shown in Figure 3, the discussion in Appendix A shows that for prisms such as the microgrooved IRE there is no additional magnfication.

The spectral quality of the microspectroscopy system developed in this chapter is illustrated in Figure 5.8c, which shows representative spectra at three positions along the groove face, marked as positions 1, 2, and 3. At position 1, the beam only interrogates the SU-8 sidewalls of the channel, and spectral features due to SU-8 (red) dominate the spectrum. Close inspection suggests there is a weak, broad band around 3400 cm^{-1}. Although at first glance this may be suggestive of some water inclusion due to partial SU-8 delamination near the edge of the channel, this can be assigned to OH groups in the cross-linked SU-8.[165]

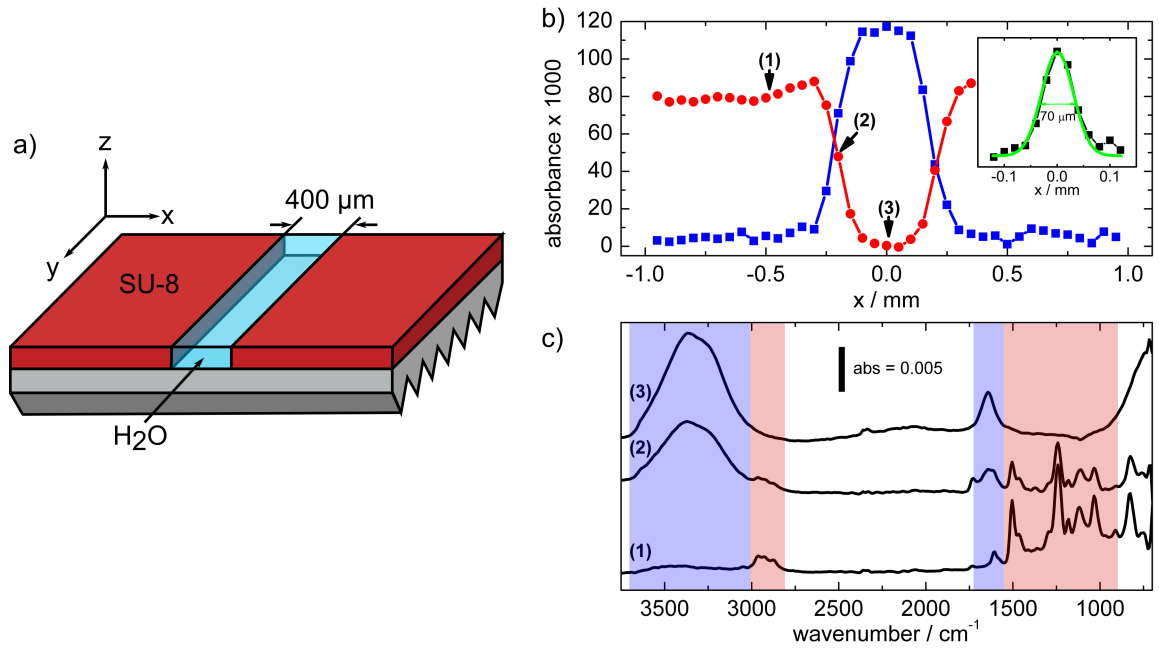

Figure 5.8: a) Schematic of the 400 µm-wide water-filled microfluidic channel patterned in 10 µm thick layer of SU-8. b) Peak ATR absorbance of characteristic H_2O (blue) and SU-8 (red) as a function of x translation. The deconvolved beam profile is shown as an inset and has FWHM = 70 µm. c) Representative spectra at the positions marked in b) with arrows. Spectral features from water and SU-8 are marked in blue and red, respectively.

At Position 2, the beam is poised on the edge of the channel and exhibits approximately equal contributions from water and SU-8. Position 3 probes the center of the channel, and the characteristic O-H stretching and bending modes are visible in the spectrum with no trace of SU-8. In addition, the extended spectral range of the microgrooved Si IRE allows observation of the water libration band (around 750 cm^{-1}) at Position 3 and aromatic C-H out of plane bend of SU-8 (around 800 cm^{-1}) at Positions 1 and 2.

5.4 Conclusions

The design and construction of a horizontal ATR microscope endstation has been described and its successful application to a simple microfluidic measurement has been demonstrated. This chapter marks the completion of a major thesis goal and also the realization of utility beyond the goals of the thesis, namely for microfluidic applications. The microgrooved IRE is highly compatible with conventional UV photolithography techniques. This, coupled with the fine spatial control of the beamspot position, suggest great freedom in designing microfluidic or electrochemical devices (or coupled devices) for multiplexed experiments.

At the time this work took place, the implications for FTIR imaging were obvious and exciting. In principle, the single-element MCT detector could be replaced with a multi-element focal plane array (FPA) detector, allowing imaging of chemical reactions in microfluidic channels. This will be explored in the next

chapter.

The horizontal microscope endstation has now been in use for several years as of this writing and has seen excellent updates from Mid-IR staff. Optical simulations conducted after the completion of this project suggested that a lower AOI offered better throughput and simpler beampaths. This was initially concerning, as it was known from Chapter 4 that relatively high AOIs were desirable for maximum SNR. However, excellent experimental and theoretical work by Ian Andvaag (Burgess group M.Sc. candidate at time of writing) on Au/ITO hybrid films for ATR-SEIRAS showed that lower AOI were best; the benefits of that system and its implications for this thesis will be discussed in a later chapter. With this in mind, Mid-IR staff undertook a program of upgrading the endstation, designing fixed mounts at a different AOI and rebuilding it on a separate optical table.

Before closing this chapter, it is worth considering the effect that contuinuing development of quantum cascade laser (QCL) infrared spectroscopy will have. The endstation described here relies on the low divergence of the SIR beam to provide a small, tightly focused beamspot at sample. This advantage is also provided by QCL laser sources, in addition to the high flux. Furthermore, the power output of the laser can be easily adjusted. That suggests that an ATR-based approach is not strictly necessary, as transmission mode measurements can be performed simply by increasing the laser power (within limits to prevent sample damage) to achieve sufficient throughput. The Spero Chemical Imaging Microscope from Daylight Solutions is a transmission-based IR microscope equipped with a QCL, and it is expected that uptake of that instrument will result in new and exciting imaging studies of microfluidics.

A key aspect of this chapter is the recognition that a sufficiently small beam with good spatial definition can be used to selectively probe the ATR interface, and this is fully amenable to a laser-based spectroscopy as well. Shortly after publication of these results, an IRsweep IRis F1 QCL laser spectrometer was installed at the Mid-IR beamline, and a three-axis positioner similar to that used here was modified by Erick Lins (Burgess group Ph.D. student at time of writing) to accept a version of the ATR-SEIRAS spectroelectrochemical cell described in the previous chapter. Lins demonstrated the time-resolved measurement of dimethyaminopyridine (DMAP) desorption with electrochemical ATR-SEIRAS. The IRis F1 is purpose-built for fast time-resolved studies, with submillisecond time resolution attainable with relative ease, and continued development and commissioning of this instrument is expected to be highly complementary to the work reported in this thesis.

6 Chemical Imaging of a Simple Interfacial Reaction on Flow

Contributions of the Author

The results described in this chapter have been published in the following peer-reviewed publication:

Tyler A. Morhart, Stuart Read, Garth Wells, Michael Jacobs, Scott M. Rosendahl, Sven Achenbach, and Ian Burgess. Micromachined Multigroove Silicon ATR-FTIR Internal Reflection Elements for Chemical Imaging of Microfluidic Devices. *Analytical Methods*, **2019**, 11, 5776 - 5783.

I designed the experiments with Ian Burgess and performed all ray-tracing. I fabricated the microfluidic device with assistance from Wells and Jacobs and technical input from Achenbach. Read assisted with beamline setup, optical alignment, and characterization of the imaging properties of the endstation. Data shown in Figure 6.2 were analyzed by Read. I wrote the first draft of the manuscript and prepared all figures. The text and figures in this chapter are my own.

6.1 Introduction

The previous chapter described the development and construction of a custom horizontal ATR microscope and its application to a very simple microfluidic application. That experiment used an open-channel device: an unsealed device with no active pumping of fluids. This is a far cry from the majority of devices published in the literature, which offer a variety of fascinating geometries and applications. The last chapter ended with the recognition that the endstation described was readily amenable to vibrational imaging. In this chapter, the modifications necessary to perform imaging experiments will be described and a proof-of-concept experiment, the imaging of H/D exchange in co-flowing H_2O/D_2O streams, will be presented.

Microfluidics devices are broadly defined as those which manipulate the flow of fluids at the microscale, typically in fluidic channels with critical dimensions of a few to several hundred microns.[166,167] Fluid flow is fundamentally different than in macroscale systems: the Reynolds number, a dimensionless quantity which quantifies the ratio of inertial to viscous forces, is very low in small channels, leading to purely laminar flow.[168] The implication is that fluid flow is very easily manipulated in microfluidics, with great consequence for the design of analytical devices or microreactors. Additional benefits are low reagent/sample consumption and superb control of heat flow due to the high surface area to volume ratio of microchannels. The latter benefit

is of great importance for chemical synthesis, as typical synthetic methods such as lab-scale preparation or industrial production have at least many hundred milliliters of solution volume, and are known to have thermal gradients and 'hot spots' which contribute to non-uniform reaction rates and conditions.[169] In contrast, microfluidic devices can maintain uniform reaction conditions and are easily variable due to their low thermal mass. This property makes them uniquely suited to investigations of on-flow chemical synthesis. Indeed, a substantial body of literature has developed demonstrating a variety of useful chemical transformations on flow and investigations of reaction condition parameter space.[169]

FTIR spectroscopy or imaging is a natural choice to probe the chemical composition of fluid streams, but transmission-mode measurements of condensed media are complicated by the requirement of a short pathlength (typically 10 µm or less) due to significant absorption by the solvent. Above this pathlength, the incident beam is so greatly attenuated by optical absorption that little or no light reaches the detector, preventing analytical detection. The preparation of thin-layer microfluidic devices has been demonstrated by Mitri *et al.* to circumvent this problem,[170] but the requirement for both optical and infrared transparency limits fabrication to only a few substrates, typically alkali or alkaline earth fluorides like CaF_2 which do not lend themselves to microfluidic device applications. Furthermore, such fluorides are sparingly soluble in water, incompatible with acidic environments, and are usually cytotoxic. An alternative is described by Silverwood *et al.* where deep reactive ion etching was employed to micromachine a 30 µm deep channel in an IR-transparent Si(1 0 0) wafer sealed by anodically bonded glass. Although the short pathlength allowed good optical throughput to be achieved, optical interference fringes complicated data analysis.[171]

An alternative to transmission-mode devices is the use of an internal reflection technique such as ATR-FTIR, where infrared radiation penetrates only a few micrometers into solution. This simultaneously provides sufficient analytical signal and lifts the requirement of thin cavity devices, allowing much greater freedom in fabrication. Multibounce[172] and single-bounce spectroscopy methods[173] have been developed by Jensen's group. imaging has primarily been developed by Kazarian and Chan who have published extensively on micro- and macro-ATR imaging of microfluidic devices[174–176] among other applications. In the macro-ATR method the device (or sample material) is in intimate contact with the principal reflecting plane of the IRE. Spectroscopic measurements can be collected with a single point detector or linear array detector[177] or with a 2D focal plane array (FPA).[178] When illuminating a large field of view (FOV), there is a necessary tradeoff between FOV and resolution, although sub-images can be stitched together at the cost of increased measurement time. This method was employed by Chan and Kazarian to image a large area of a serpentine microfluidic channel.[175] Greener's group has developed a system which supports a multi-channel microfluidic device built on a multibounce IRE coupled to a conventional FT-IR spectrometer and a single point detector.[179] The multibounce design results in spectra which average the spectral response over the length of a channel. The device can be translated through the beam using a three-axis positioner, resulting in a one-dimensional image composited from spectra collected as a function of device position.

In the examples given above, FOV is maximized at the expense of spatial resolution. In this chapter, the

custom microscope endstation developed in Chapter 5 is employed to demonstrate a high-spatial resolution imaging study of a simple chemical reaction at steady state. The compatibility of the microgrooved IREs with conventional photolithography is exploited to prepare a microfluidic device compatible with an ATR imaging approach. The fabrication of an IR-compatible microfluidic device will be described along with the necessary modifications to the microscope to support imaging experiments. Steady-state imaging of H/D exchange between two co-flowing streams of H_2O and D_2O will be demonstrated.

6.2 Experimental

6.2.1 Materials

Microgrooved IREs (Universal ATR wafer) were purchased from IRUBIS GmbH. The experimental solid film photoresist Lamires_XP was donated by micro resist technology GmbH. Isopropanol and propylene glycol monomethyl ether acetate (PGMEA) were purchased from Sigma Aldrich. 3mm thick PMMA sheets were purchased from Acrylite. Tygon tubing (1/16" ID) was purchased from McMaster-Carr. Dymax 1142-M UV-curable glue was purchased from Ellsworth. Ultrapure H_2O was provided by a Millipore water system and D_2O was purchased from Cambridge Isotopes.

6.2.2 Microfluidics Device Fabrication

The primary challenge is in sealing a lid onto the patterned IRE; uneven photoresist frequently prevented good contact between lid and resist, resulting in leaks. This problem was particularly evident when spin-coating photoresist. Although this is the usual method for preparing a thin film on a Si wafer of any form, in early devices the edge bead formed during spin-coating resulted in highly uneven resist layers. The small size of the microgrooved IREs and rectangular geometry prevented typical edge bead removal processing. Instead, the method employed here was to laminate a solid film photoresist (LamiRes_XP), ensuring a uniform thickness and therefore a good seal.

IREs were cleaned by sonication in isopropanol followed by drying in a nitrogen stream. Then, the photoresist was laminated onto the substrate by the following method. A tabletop roll laminator (Royal Sovereign) was used with lower and upper rollers operating at 75 and 80 °C, respectively. The photoresist was cut to size and gently placed on the IRE. This was supported on a thin aluminum plate and covered with an overhead transparency sheet to form a "sandwich." The wafer was oriented such that the long axis of the grooves was oriented parallel to the feed direction. Further fabrication refinement showed that the wafer could also be fed with one corner leading to reduce defects in lamination. The sandwich was fed into the laminator. This step is surprisingly gentle on the IREs, which might be expected to crack along the groove axis, but over twenty-five replicate experiments have been done without a broken wafer. Following the lamination, the wafer was immediately soft-baked at 55 °C for 1 minute before exposure.

The operating principle of the direct write laser system (Heidelberg Instruments DWL66+) is as follows. The DWL66+ incorporates a 250 mW 355 nm diode-pumped solid state frequency-tripled Nd:YAG laser. The laser power, which is variable, was tuned to achieve the correct exposure dose. The internal optics incorporate first an acousto-optic modulator to gate the laser beam and second an acousto-optic deflector to modulate the lateral position of the laser over a total travel of 150 µm. A 10 mm working distance optical objective focuses the laser on the substrate. While the laser is deflected, the vacuum-chucked sample is scanned in the orthogonal direction such that the desired pattern is directly exposed in a series of stripes stitched together. The pattern was prepared with LayoutEditor (build 20180522). In principle the resolution of the exposure is defined by the laser wavelength and optics, but in practice photoresist chemistry and thickness plays a substantial role. Patterns exposed in this work did not incorporate features near the resolution limit of the process so no special steps were taken to optimize exposure resolution.

Following exposure, the wafer was post-exposure baked at 90 °C for 5 minutes then immediately developed for 1 minute in PGMEA at 35 °C. The developed wafer was rinsed with isopropanol and water and allowed to dry in the fume hood.

The device was sealed with a PMMA lid cut from 3 mm sheet stock to 9 x 11 mm^2. A countersunk hole was bored in two stages, first with a 1.5 mm diameter bit to prepare the through hole, then with a 1/8" bit to form the countersink to a depth of roughly 1.5 mm. In order to seal the lid on the device, a thin layer of UV photoinitiated glue (Dymax 1142-M) was spread across the face of the lid with a razor blade, then the lid was carefully placed on the device. The glue then spread across the photoresist. Because the glue is not very viscous, there was a danger during this step of the glue seeping into the channels, but the device was quickly exposed to a UV point source to initiate the cure. Exposure took place at a distance of 10 cm for 10 s using an OmniCure S1000. Although PMMA is UV-opaque, the cure is initiated at the device edges where there is exposed glue, proceeding into the device, allowing the glue layer to cure completely. Finally, Tygon inlet and outlet tubes were pressed into the countersink and secured with UV photoinitiated glue.

For imaging purposes, a checkerboard pattern was prepared with 180 x 180 $µm^2$ checkers with alternating checkers filled with resist. The design was centered on the wafer so that the checkerboard spanned multiple grooves.

6.2.3 ATR-FTIR Imaging

Minor modifications of the horizontal ATR endstation were necessary to adapt the system for imaging, Figure 6.1. The MCT detector was replaced with a 64 × 64 pixel focal plane array (FPA, Santa Barbara Focalplane) on a custom machined mount and M5 was replaced with a 1" diameter 152.4 mm focal length 90 degree OAP. With these changes made, the theoretical magnification is given by the focal length ratio of M5/M4 = 3.0. Because the magnification was relatively low, the globar source was used to enable greater coverage. Hyperspectral images were collected at 8 $cm^{-1}$by averaging 128 scans. The collection time for one image was approximately five minutes. All images were collected with constant integration time, gain, and

DC offset. Background and sample images, I_{bg} and I_s, respectively, were collected with the above settings and an absorbance image was calculated by $A = -\log(I_s/I_{bg})$. A USAF 1951 target (Edmund Optics) was used to assess imaging quality.

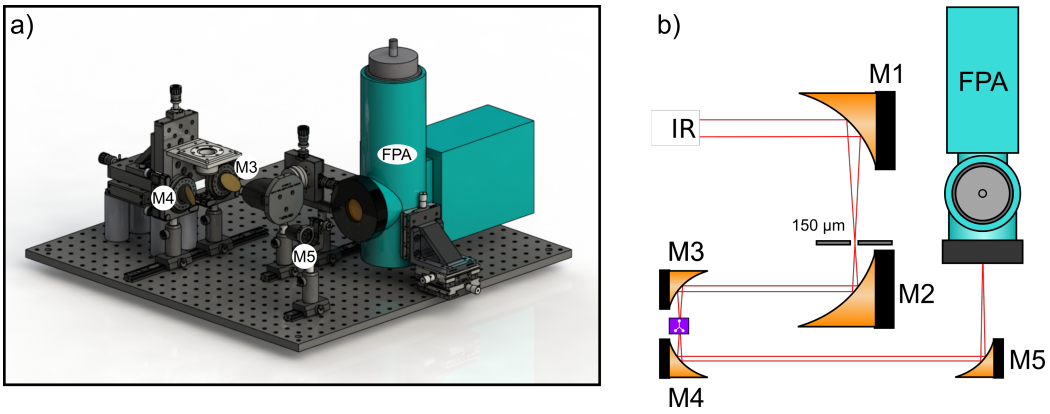

Figure 6.1: Modified HATR end station modified for chemical imaging. a) CAD image with mirrors labelled and the focal plane array's position indicated. b) Plan view of the horizontal microscope.

6.2.4 *In Situ* Microfluidic Device Operation

The microfluidic device was mounted in a custom sample holder such that the grooves were placed at focus and the flow direction was parallel to the optical axis i.e. the fluidic channel was along the y-direction. Fluid inlets were connected to reservoirs of H_2O and D_2O. A single piezoelectric diaphragm pump (mp6, Bartels Mikrotechnik, Dortmund) integrated into a quad channel control, developed in collaboration with Hochschule Niederrhein University of Applied Sciences (Krefeld), was used to drive the fluid flow. Early experiments used two channels to pump fluid into the inlets, but optical microscopy showed that small variations in the channel flow rates resulted in drift of the boundary between the co-flowing fluids. This was significant over the time scale of image acquisition, and negatively impacted image quality, so instead the setup was modified so that fluid was drawn through the outlet using a single pump channel. This resulted in a stable interface as confirmed by optical microscopy.

6.3 Results and Discussion

6.3.1 Characterization of Imaging Capabilities

As discussed in the previous chapter, the custom endstation allows irradiation of the microgrooved IRE with synchrotron IR for spectroscopy experiments. With the adaptations described above, an imaging configuration was realized using a 64 × 64 pixel FPA detector and a theoretical magnification of 3.0. Before performing any imaging experiments, it was necessary to investigate how well the globar source filled the FPA. To do this, a Au mirror was placed at the sample position and focused to collect a reflection image.

The resulting data contain a single beam intensity spectrum at each pixel, so in order to visualize the results Figure 6.2 shows the integrated signal intensity over the 3100 – 3200 cm^{-1}range. (This range was chosen for its proximity to the H_2O bending mode which will be investigated later in this chapter.) Inspection of Fig 6.2a reveals a moderate linear gradient in the signal from the bottom-left to top-right of the image, but otherwise the illumination is quite even. The signal varies by roughly 20% across the image diagonal. The sampling and collection optics rotate the beam by approximately 45˚, resulting in the apparent rotation of the image; this is more obvious in later figures. The pixel noise at the detector is shown in Fig 6.2b, where it is quantified by subtracting a linear fit over the 3100 – 3200 cm^{-1}range then taking the standard deviation. Fig 6.2b shows essentially uniform distribution of noise on the detector. Calculating the signal-to-noise ratio, Fig 6.2c, reveals a similar structure to that shown in Fig 6.2a, with a mild linear gradient but otherwise high S/N. Performing this analysis for other spectral regions yields the same results, indicating that the S/N is more or less constant throughout the spectrum. Therefore, image distortions discussed below are not the result of an inhomogeneous beam at the FPA detector.

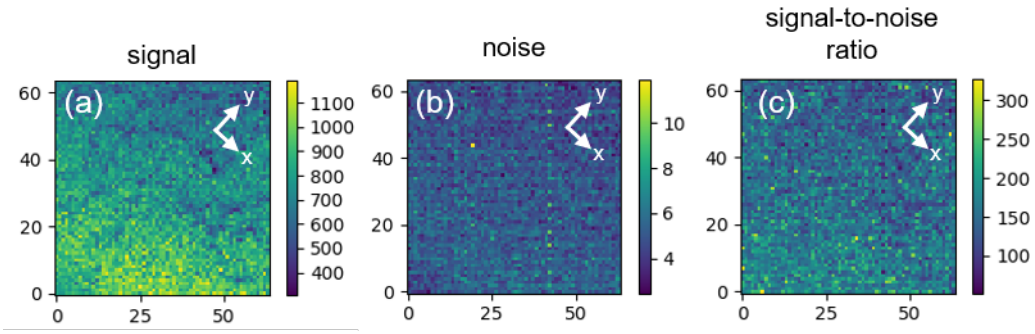

Figure 6.2: Illumination of the FPA detector by placing a mirror at the sample positions. Axes are labelled with pixel number. a) Signal intensity calculated by integrating the single beam intensity around 3100 cm^{-1}. b) Standard deviation of the noise in the same region as (a). c) The signal-to-noise ratio calculated form the preceding images.

The off-normal imaging configuration imparts a compression along the optical axis. From the simple ray diagram shown in Figure 6.3a with $\theta = 50^{\circ}$, the compression factor $d'/d = (\cos\theta) - 1 = 1.56$. That is, the sample is actually 56% longer in the optical axis (y, in Figure 6.2a) than the image would suggest. The cartoon shown in Figure 6.3b illustrates this effect. The compression factor can be experimentally determined by imaging a USAF target (group 2 element 5), an optical micrograph of which is shown in Figure 6.3c. The bars (white) are metallized on a glass substrate (dark grey). At 3200 cm^{-1}glass is IR-transparent, while the metal bars are perfect reflectors. In the reflected power image shown in Figure 6.3d, light grey regions are the metal bars and dark grey regions are the glass substrate. The bottom left region of the image has well-focused bars, but a significant loss of spatial contrast is apparent in the top right portion of the image. The OAPs used in this study have a relatively small depth-of-field, resulting in blurring towards the edge of the image. This is a consequence of the compromise between magnification and field of view, with the former being of greatest interest for this work.

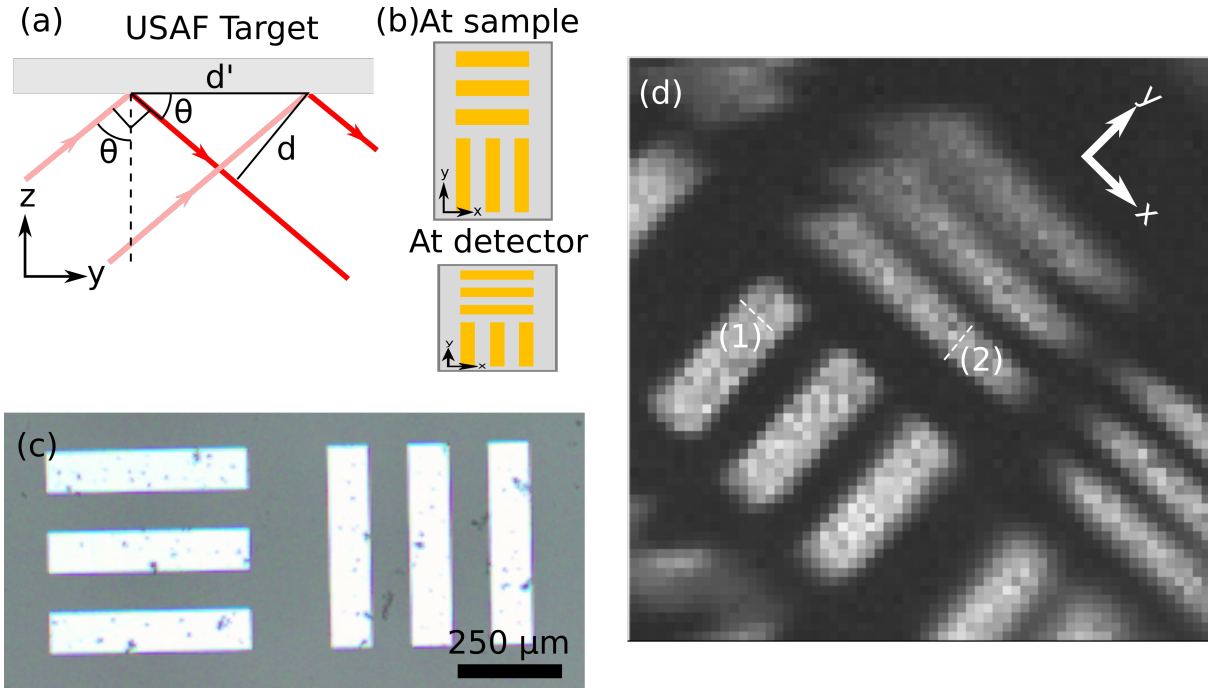

Figure 6.3: External reflection imaging of USAF target. a) Simplified beampath depicting image compression along the y axis. The IR beam (pink rays) is incident from left on the USAF target at an AOI $\theta = 50°$. The beam is projected along the y-direction into an elliptical form with semiaxis d'. b) Illustration of the effect of off-normal illumination. In the top image, the beam samples an extended area. The reflected beam is compressed along the y-axis, resulting in apparent image compression at the detector. c) Optical micrograph of the USAF target group 2 element 5 imaged in (d). Reflected power image of group 2 element 5 in the USAF target.

The effective pixel dimension in the directions parallel (y-axis) and perpendicular to (x-axis) the optical axis can be extracted from Figure 6.3d and the known width of the bar (78.7 µm). Line 1 measures the width of an imaged bar along the x-axis (the uncompressed direction) and provides a pixel dimension of 13.7 µm. Dividing this by the known size of the FPA pixel (40.0 µm) yields an experimental magnification of 2.9, which is in very close agreement with the theoretical value. A similar calculation can be done for Line 2, which is now along the compressed axis. The pixel dimension in the y-direction is 20.4 µm per pixel. The experimental image compression factor can be calculated by the ratio of pixel dimensions along the compressed and uncompressed axes and works out to 1.49. This value agrees closely with the expected compression factor of 1.56.

To assess the image quality of the microgrooved IRE, a checkerboard pattern of 180 × 180 μm^2 voids was fabricated in photoresist. The pattern was prepared on the principal reflecting plane of the IRE. A cartoon depicting the patterned wafer is shown in Figure 6.4a along with an SEM image in Fig 6.4b. The patterned IRE was placed at focus such that the beam illuminated several grooves. Then, a background image was collected of the dry pattern followed by a sample image after it was wetted with water. The water filled the voids, offering chemical contrast in the resulting absorbance image. The H_2O bending mode between roughly 1600 and 1700 $cm^{-1}$was integrated to produce the image shown in Figure 6.4c, where the water integral is

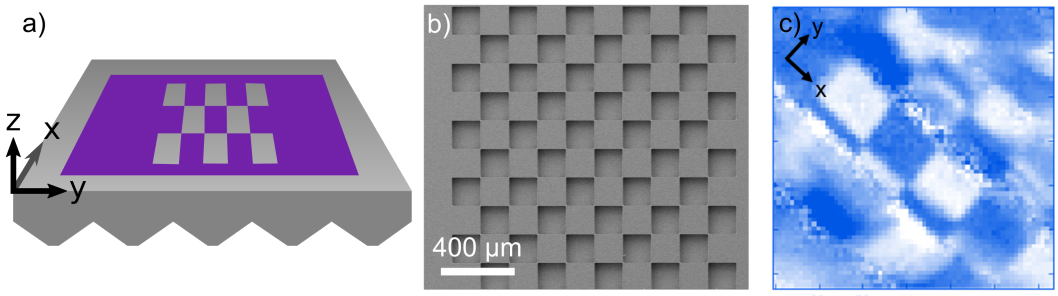

Figure 6.4: c) Cartoon of the microgrooved IRE decorated with a photoresist checkerboard. b) SEM image of the fabricated checkerboard. The square voids in the photoresist are visible with slight shadows in them. c) Full absorbance image of water in the open voids of the checkerboard. The image was obtained by integrating the OH-stretching mode of water.

colour mapped to blue. Inspection of the image reveals a diagonal region parallel to the x-axis, approximately 10% of the FOV, which is well-focused; the rest appears strongly affected by imaging artefacts. To understand this image qualitatively, geometric ray-tracing was used. The following discussion will centre on a cropped and rotated section of Figure 6.4c, shown in Fig 6.5, which spans a single groove period. Annotations mark the three regions of interest. ROI1 has well-focused squares visible with sharp contrast between water and photoresist. ROI2 appears to show some structure from the checkerboards but is significantly blurred. These two regions are separated by a highly noisy region, ROI3. Before discussing the ray-tracing results, analysis of the well-focused squares and comparing to the known dimensions of the checkerboard yields a measured pixel dimension along the x-axis of 14.0 um per pixel, which is in close agreement to that measured in the last section.

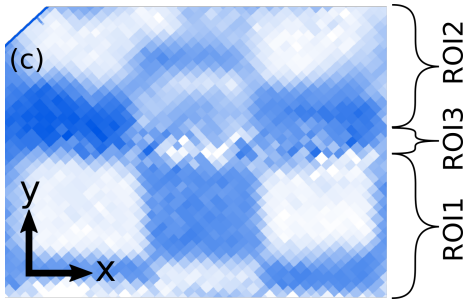

Figure 6.5: Cropped and rotated section of Figure 6.4c showing the image formed from a single groove period. Three regions of interest (ROI) are indicated on the figure. The optical paths leading to the three ROI are explained in Figure 6.6.

It was hypothesized that differing beampaths through (or off) the crystal were responsible for the different regions of interest. This was confirmed by geometric ray-tracing, the results of which are shown in Figure 6.6. To simplify the matter somewhat for presentation purposes, a collimated beam (as opposed to the converging beam used in the experiment) was used in a two-dimensional ray-trace. Figure 6.6 colour-codes several qualitatively different beampaths. No attempt was made to quantify the power transported in each

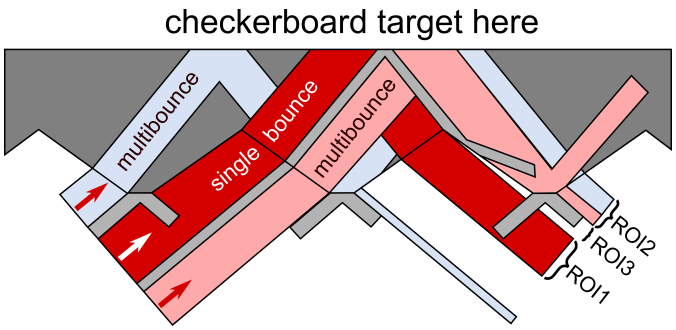

Figure 6.6: Geometric ray-tracing through multiple grooves. The three ROI from 6.5 are shown to arise from differing paths through (or off) the microgrooved IRE. ROI1 arises from light undergoing a single bounce to interrogate the primary imaged area, but light in ROI2 results from the overlap of multiple internal reflections which image primary and secondary areas. ROI3 comes from external reflection on the terraces and carries no analytical signal.

bundle of rays. There are five different paths available to incident rays. The width of the incident beam is set to encompass all of them; extending it would result in multiple overlapping paths which are essentially "copies" of the five components shown here. The grey path is externally reflected off the terrace. Because it never enters the wafer, and thus does not interrogate the principal reflecting plane, it carries no analytical signal and contributes only noise in the final measurement. However, the majority of rays enter the wafer and will ultimately reach the detector carrying signal. The red path is the clearest example of this, where light enters the crystal on one side of a groove, undergoes a single reflection, and exits the crystal on the other side. Note that this path is confined only to rays which enter the groove at the deepest part to midway up the groove wall. No other beampath overlaps with the exiting red beam, so it makes up the well-focused ROI1 in Figure 6.5. The pink path (or, equivalently, the light blue path) is slightly more complex: it enters the IRE midway up the groove to just below the terrace, undergoes a single reflection, but then impinges on the terrace of a neighbouring groove. There are several minor internal reflections which are not shown for clarity; the key point is that part of the beam escapes the crystal on a path toward the detector, but a significant fraction undergoes a second internal reflection at the principal reflecting plane (this is most obvious in the light blue path). The overlap of two beams in this way make up ROI2. The two beampaths interrogate separate regions of the sample but overlap spatially at the detecting, resulting in a blurred part of the image. Finally, a thin bundle of rays incident on the midpoint of the groove (dark grey) never escape the crystal. Based on this simplified diagram, the only rays which reach the detector between ROI1 and ROI2 (i.e. in ROI3) are externally reflected ones which carry only noise. In summary, the ray-tracing shown in Figure 6.6 qualitatively predicts the existence of a well-focused region (ROI1), a highly noisy band (ROI3), and a blurred region which is a composite of the primary and secondary imaged areas weighted by the fraction of rays which undergo multiple versus single internal reflection (ROI2). The situation is not quite so simple, as inspection of ROI3 in Fig 6.5 reveals some structure which is not captured by the ray-tracing. Nevertheless, this ray-tracing exercise demonstrates that only a small fraction of the FPA is filled with light which returns high-fidelity images of the surface.

6.3.2 Steady-State Chemical Imaging in a Microfluidic Channel

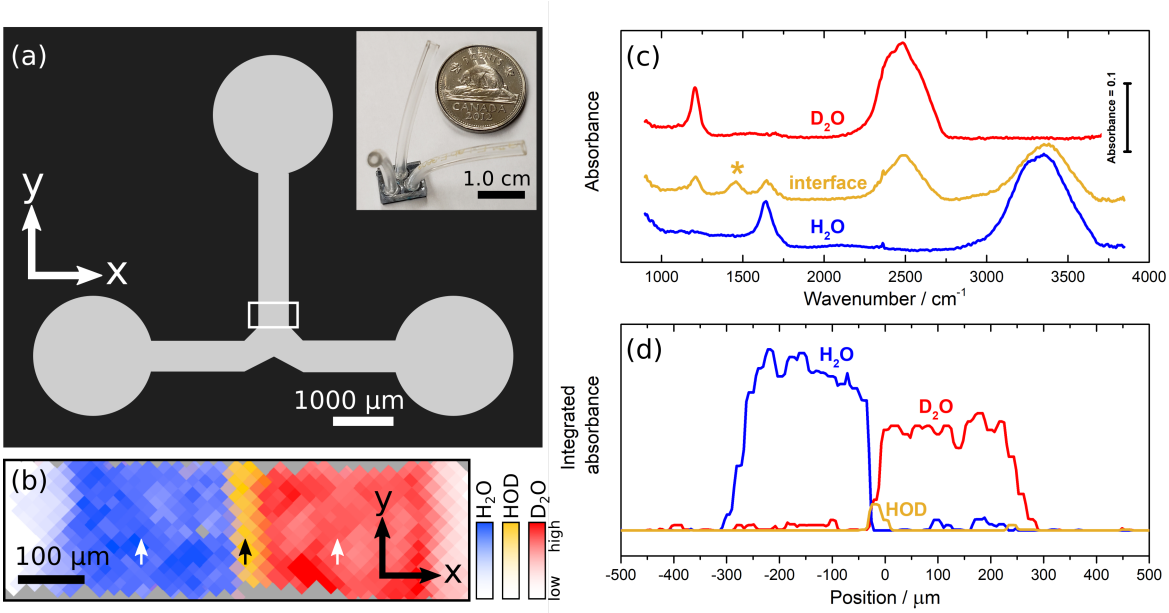

Figure 6.7: ATR imaging of the microfluidic device. a) Schematic of the co-flow channel employed in this chapter. The white rectangle indicates the area imaged in panel b). The inset shows a photograph of the finished device. b) Composite colour-mapped image of H/D exchange in the microchannel under flow. From left to right, integrated band intensities are colour-mapped as follows: H_2O - blue, HOD - orange, D_2O - red. Pixels with no analytical signal are shown in grey. The region shown was extracted from ROI1 on the detector. c) Representative spectra from locations marked with arrows. The asterisk denotes the characteristic H-O-D bending mode. d) Profiles extracted by integrating the relevant bending modes along the line defined by the arrows in (b).

To demonstrate chemical ATR imaging of the microfluidic device discussed above, colaminar flow of two fluids, H_2O and D_2O, in a 500 µm wide microchannel was employed. The exchange of protons and deuterons to form HOD is a popular method of demonstrating chemical contrast in microfluidic systems due to the strong IR absorbance and well-separated vibrations of the three liquids. A schematic of the microfluidic device is shown in Figure 6.7a. Two channel inlets (bottom left and right) lead to 500 µm wide inlet channels. The channels are 55 µm deep (defined by the photoresist thickness). An inset shows a photograph of the completed device with a Canadian nickel for scale. The inlet and outlet tubings are visible protruding from the PMMA lid. The two inlet channels merge into a 500 µm wide reaction channel which runs to a single outlet. The long axis of the grooves is parallel to the x-direction i.e. the reaction channel runs over several grooves. The device was loaded in the endstation such that the reaction channel was parallel to the optical axis (y-direction) and positioned so that the region marked with a white box was imaged. As discussed in a previous section, the FOV is relatively restricted (c.f. ROI1 in Fig 6.7). As a result, the focused region has a relatively wide FOV along the channel width, but is restricted longitudinally. To image co-flowing media in the microchannel, a dry background image was collected, then two streams of H_2O and D_2O were flowed through the device and a sample image was collected. At the interface between the two fluids, hydrogen and deuterium exchange

to form HOD, which can be identified by its characteristic H-O-D bend centred at 1455 cm^{-1}. This band is distinct from the bending modes of H_2O and D_2O, which appear at 1640 and 1205 cm^{-1}respectively. By integrating these three diagnostic bands, the composite image shown in Fig 6.7b is obtained. This image demonstrates steady-state chemical imaging of a reaction occurring at the interface between co-flowing media under laminar flow conditions. In the image, H_2O is mapped to blue, D_2O is mapped to red, and HOD is mapped to yellow. The image has been cropped and rotated to highlight the roughly 10% of the full detector FOV which is well-focused (c.f. ROI 1 in Figure 6.7). In the image, two flows of H_2O and D_2O can be seen flowing along the channel with a narrow diffusion zone containing HOD in between them.

Representative absorption spectra taken from the positions marked with arrows are shown in Figure 6.7c. The curves are coloured and labelled to indicate their locations. The spectra taken in the flowing pure substances are dominated by two peaks: a low frequency bending mode (1205 $cm^{-1}$for D_2O and 1640 $cm^{-1}$for H_2O) and a high frequency stretching mode (2485 $cm^{-1}$for D_2O and 3350 $cm^{-1}$for H_2O). The spectrum at the interface (in the orange region in Fig 6.7b) show spectral signatures of both H_2O and D_2O as well as the characteristic H-O-D bend at 1455 cm^{-1}(marked with an asterix). The absence of HOD in either of the two previous spectra indicates that HOD is formed only where the two laminar flows meet in the centre of the channel.

Integrating the bending modes across the line defined by the three arrows in Fig 6.7b results in the three chemical profiles shown in Fig 6.7d. Note that the higher frequency stretching modes of HOD overlap with those of D_2O and H_2O so they were not chosen for integration despite the higher S/N. The plot shows roughly flat profiles of H_2O and D_2O confined to their sides of the channel with a narrow region containing HOD between them. First, it is notable that the profiles cover a range from -300 to +300 µm, despite the channel being only 505 µm wide. This apparent broadening is due to slight delamination of the photoresist at the edges of the channel. Because IR light penetrates only about $\lambda/4$ in the ATR configuration, a depth of about 1 or 2 µm for the wavelengths used here, even a very small gap between the substrate and the resist will result in appreciable ATR signal. The H_2O profile peaks at -250 µm before falling off to the left, while the D_2O profile peaks at +250 µm. This is much closer to the known channel width. There appear to be slight differences in the widths of the two flows; this is likely due to differences in the hydrodynamic resistances of two fluids being pulled by a single pump. At the boundary between the two flows (roughly around -25 µm), the profiles go rapidly to zero and there is a narrow Gaussian profile of HOD centred at -25 µm. The profile spans roughly four pixels on the FPA detector, or approximately 50 µm.

6.4 Conclusions

In this chapter, chemical imaging of a model chemical reaction has been demonstrated using a custom horizontal ATR endstation over a field of view of 200 × 800 $µm^2$. There are several strategies available for improvement. The FOV is relatively limited and could easily be extended by serially collecting images

downstream in the channel. In principle, this would allow the monitoring of the diffusion profile of the products generated at the interface between the two co-flowing streams. Such a measurement would need to consider the expected rate of diffusion along with the total reaction time of the microfluidic device under study. For a device at steady state, as used here, the elapsed reaction time is mapped to distance along the reaction channel, and careful consideration of the residence time (i.e. by tuning the flow rate and designing a channel of sufficient length, such as a serpentine) is required to ensure that the diffusion profile changes meaningfully over the course of the channel.

Improving the imaging quality is an important goal. Ray-tracing similar to that shown in Fig 6.6 shows that changing the AOI to 55° eliminated spectral cross-talk between grooves, confining all beampaths to single internal reflections. Further benefit could be derived when increasing the magnification, either with a final OAP with a longer focal length or through use of a suitable lens. The current resolution of 14 µm per pixel matches results reported by Chan and Kazarian.[180] Increasing the system magnification to 10× would offer approximately 4 – 6 µm per pixel resolution, near the diffraction limit for mid-IR radiation. The ATR configuration has the advantage of offering improved spatial resolution compared to a transmission or external reflection measurement due to the high refractive index IRE's effect on minimum resolvable distance. (For Si, this is roughly 2.5.) With greater resolution, it is possible to spatially filter the beam with a 250 µm pinhole aperture such as that used in the last chapter. In doing so, a single groove could be illuminated and imaged with high fidelity, opening up the possibility of single devices with many different sample environments on chip for multiplex experimentation, or for tracking the course of a reaction along a single serpentine channel.

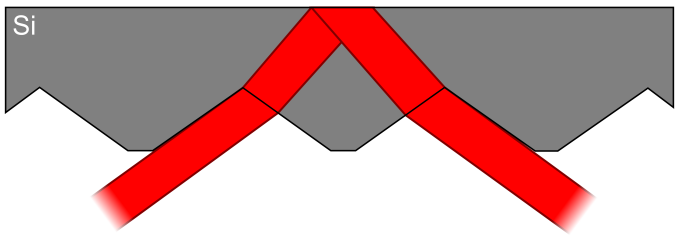

Figure 6.8: Geometric ray-tracing with light incident at 55°. With a sufficiently focused small beam, all rays undergo a single bounce through one groove.

Although the experimental method used here was successful, major drawbacks include the limited availability of beamtime, the difficulty of aligning the invisible IR beam through an optically opaque medium, and the slow feedback due to long acquisition times. Although the measurements described here do not require SIR, the endstation uses a spectrometer with both globar and SIR sources, so measurements are *de facto* limited to scheduled shifts. Although ongoing improvements in magnification are being made with the SIR source in mind, a QCL would seem to be an excellent alternative, particularly given the rise of rapidly tunable broadband sources (e.g. Daylight Solutions MIRcat-QT Mid-IR laser). However, unpublished work from a colleague in the Burgess group (Erick Lins) has shown that the microgrooved IREs exhibit strong

interference fringes when used with a QCL-based spectrometer, so a custom optical design may be necessary to alleviate this problem. Aligning the system might be improved with the addition of a visible microscope and calibrated alignment targets, allowing visual observation of the device under operation. This might offer even more opportunities for coupled analytical techniques such as fluorescence or colourimetry. Finally, the slow feedback seems limited by the choice of detector. The slow response time of the detector requires that any device studied must be capable of operating at steady-state conditions, imposing a significant constraint on future experimental design.

Improvements in the device side are envisioned as well. Recent progress with another solid film photoresist, SUEX (DJ Microdevcorp), has shown great promise. Processing conditions for SUEX are nearly identical, it is commercially available (as opposed to the experimental resist used here), and has excellent chemical stability and adhesion. The problem of edge delamination which contributes to channel widening can be mitigated with slow ramps during baking steps and with a final hard bake step which has been found to heal delaminated areas. Beyond issues of fabrication, increasing complexity of device design will be necessary for developing analytical applications. One possible application is the development of a reactor for electrochemical synthesis. Patterning metal band electrodes in the channel in a two-electrode configuration would allow the electrolysis of a reagent stream to form a reactive intermediate. Addition downstream of a second reagent could result in an interfacial reaction between the electrolytically-formed intermediate and the second reagent, allowing the simultaneous mapping of that reaction's kinetics and the diffusion coefficient of the product in solvent. Designing such a device would likely require an expanded substrate size to fit the requisite fluidic and electronic connectors.

7 ATR-SEIRAS Microspectroscopy of a Model Electrochemical Process on a Microelectrode

Contributions of the Author

The results described in this chapter have not yet been published. I designed the microband electrode, the spectroelectrochemical cell, and the associated experiments under static conditions. I fabricated the electrode with assistance from Garth Wells and technical input from Sven Achenbach. Stuart Read and Scott Rosendahl assisted with beamline setup and optical alignment. Osai Clarke collected the SEM shown in Figure 7.7. Time-resolved data presented in Section 7.3.4 derive from step-scan experiments performed by Dr. Kaiyang Tu using the microelectrode described in this chapter. Data shown in Figures 7.8 and 7.9 were collected and processed by Tu. The text in this chapter is my own.

7.1 Introduction

The preceding chapters can be loosely divided into two sections. The first covered issues specific to ATR-SEIRAS and the second covered optical developments with further application to ATR measurements. In chapters 3 and 4, attempts to perform ATR-SEIRAS microspectroscopy were described along with the experimental challenges that necessitated the development of a protocol using a different IRE. The focus shifted in chapters 5 and 6 to describe the implementation of a custom optical solution and its qualification with single-point FTIR spectroscopy and imaging. In this final experimental chapter, these two sections will be tied together in the demonstration of a time-resolved ATR-SEIRAS spectroscopy experiment on a microband electrode.

A major impediment to the realization of this chapter's goal was the difficulty in preparing a mechanically stable, SEIRAS-active microband electrode. As discussed in the Theory and Background chapter, the substantial lattice mismatch between Au and Si results in a very weak bond. Attempts to post-process prepared metal films into the desired shape of a microelectrode (e.g. by lithographic masking and etching) invariably failed. If the metal film did not delaminate during processing, it would quickly fail during the spectroscopy testing stage. Preparing a microelectrode by first masking the substrate then sputtering metal was slightly more successful from a fabrication standpoint but suffered similar losses under spectroelectrochemical conditions. It is important to note that the film's mechanical instability meant that once assembled

in a spectroelectrochemical cell it could not be dissembled without delamination. This rendered it impossible to perform any quality testing before beamtime at CLS, effectively requiring blind measurements with electrodes which may not be active. The time-consuming nature of film preparation meant that only one or two electrodes could be tested. Given the relatively scarce nature of beamtime, this was highly concerning. The arrival of the microgrooved IREs brought the possibility of preparing multiple electrodes in advance and simply testing one after another, but even this strategy was hindered by the poor stability of the electrodes.

These challenges were finally overcome by excellent work from a fellow student in the Burgess group, Ian Andvaag, during his fourth-year thesis work [181]. His work showed that by electrodepositing Au nanoparticles on a thermally annealed conductive metal oxide adhesion layer, signal enhancement comparable to sputtered or electroless deposition methods could be achieved. A key finding of that project was the excellent mechanical and electrochemical stability. This was demonstrated by reductively desorbing a thiol monolayer from the Au nanoparticles and spectroscopically observing its reassembly at the electrode. This could be repeated several times with no loss in signal enhancement quality, a feat which is otherwise impossible with conventional films. Subsequent development showed that IREs decorated with these so-called "hybrid" films could be removed from the spectroelectrochemical cell and stored for several weeks on the bench at ambient conditions without appreciable changes in their signal enhancement. This represented a major methodological breakthrough in ATR-SEIRAS experiments and was of immediate interest for this thesis work. It was hypothesized that using UV photolithography to template the microelectrode followed by electrodeposition of signal-enhancing Au nanoparticles would result in highly robust, SEIRAS-compatible microelectrodes. This chapter describes their preparation and *in situ* characterization using the HATR endstation. Finally, reporting results obtained in collaboration with Dr. Kaiyang Tu, this chapter achieves the stated goal of this thesis: microsecond time-resolved ATR-SEIRAS microspectroscopy.

7.2 Experimental

7.2.1 Materials

Microgrooved wafers were purchased from IRUBIS GmbH. $HAuCl_4$ and $KClO_4$ were purchased from Aldrich; the latter was recrystallized and stored under vacuum before use. A 50.4 mm diameter, 3.2 mm thick ITO target (90% In_2O_3 and 10% SnO_2 by weight) was purchased from Kurt J. Lesker. AZ1505 positive tone photoresist was purchased from Microchem (now Kayaku Advanced Materials Inc.). HCl and HNO_3 were purchased from Fisher. 4-Methoxypyridine (MOP) was purchased from Alfa Aesar. Ultrapure water was provided from a Millipore system.

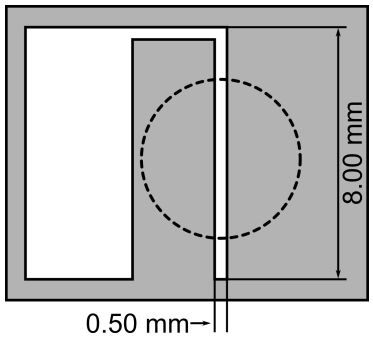

Figure 7.1: Schematic of the microband electrode layout (white) on the microgrooved Si IRE (grey). The dotted circle represents the area which is exposed to electrolyte solution in the assembled spectroelectrochemical cell.

7.2.2 Microelectrode Template Fabrication

A 500 µm wide, 8 mm long microband electrode was prepared using UV photolithography on a microgrooved IRE. A schematic of the layout is shown in Figure 7.1. First, the wafer was placed in a home-built sputter system (Johanson lab, University of Saskatchewan Engineering) and 25 nm of ITO was sputtered at 30 W power at a base pressure of 2×10^{-5} Torr. Then, it was annealed in air at 300 °C for 1 hour to decrease the electrical resistance of the ITO layer. Following annealing, 500 nm of AZ1505 photoresist was spun on using a dynamic dispense for 5 s at 500 rpm, then stepping the spin speed to 3000 rpm and spinning for 30 s. The coated wafer was soft-baked for 60 s at 100 °C then immediately patterned with a Heidelberg Instruments DWL-66+ using 40 mW laser power with a 0% focus setting. Following exposure, the resist was developed for 60 s in AZ400K developer without agitation then rinsed with ultrapure water. At this point, the ITO-coated wafer was covered with a photoresist mask defining the geometry of the microelectrode. The excess ITO was etched in aqua regia (2:1 HCl:HNO_3) until the ITO was completely removed, about 5 s.

7.2.3 Static Spectroelectrochemical Measurements and *in situ* Au Deposition

The spectroelectrochemical cell described in Chapter 4 was adapted for use with the horizontal ATR endstation and is shown schematically in Figure 7.2. The same glassware was used, but the plastic components were changed slightly to allow attachment to the endstation sample stage. A flange on the Teflon body (top of 8 in Figure 7.2) mates to a removable steel plate, allowing the entire cell to be easily removed from the stage. In contrast to the cell designed for the VeeMAX III, the wafer is held suspended below the plane of the stage in a "flying" configuration. This is due to space constraints and allows greater freedom of movement at the sample position. The added benefit is that locking down the cell does not place any pressure on the wafer, mitigating a potential route to breakage. The total mass on the three-axis positioner is well below the maximum tolerance, and no drift in position was observed over the course of several hours. A homemade Ag/AgCl (saturated KCl) reference electrode was used along with a coiled Au wire counter electrode. The counter electrode was flame annealed before use.

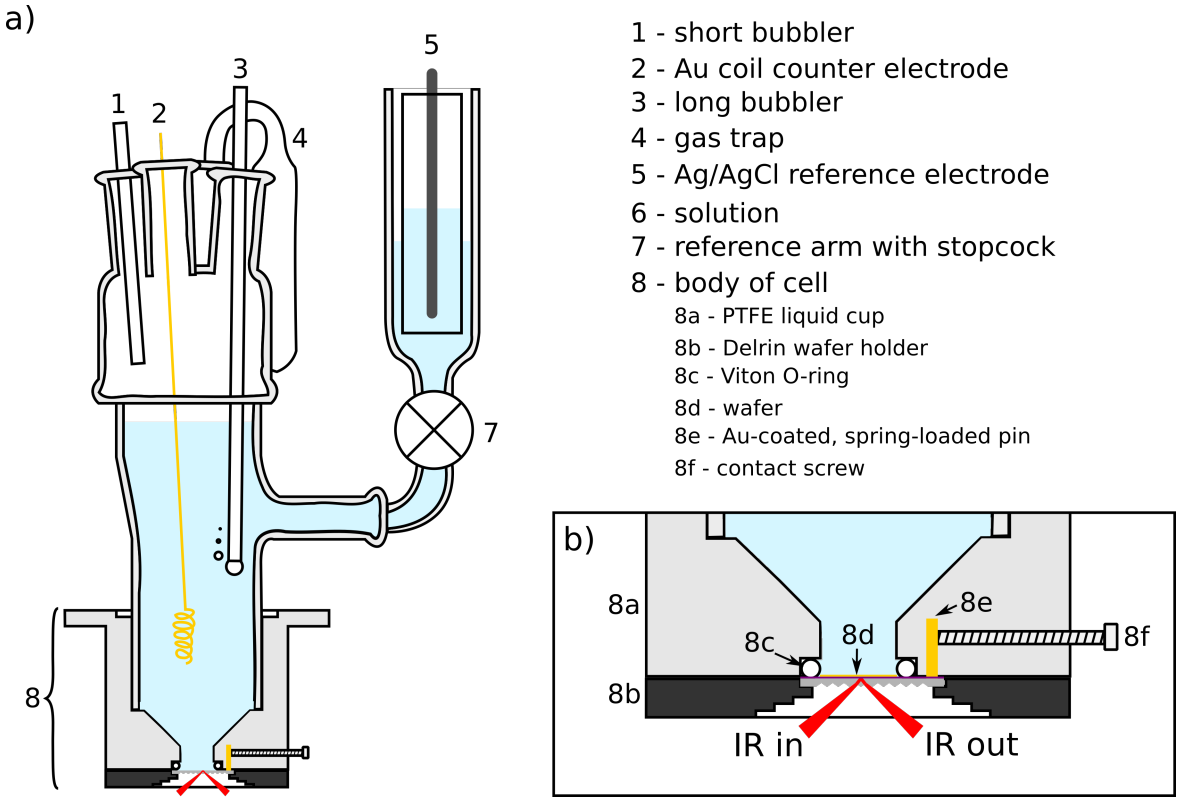

Figure 7.2: Spectroelectrochemical cell for use with microgrooved IREs on the HATR endstation. a) Cross-section illustration of the complete cell, with numbering indicating critical components. b) Detailed view of the region surrounding the microgrooved IRE, indicating the method of electrical contact and the positioning of the incoming IR beam.

Au electrodeposition took place *in situ* to monitor the evolution of the SEIRAS activity. (Some attempts were made to do the deposition offline i.e. with a benchtop spectrometer before beamtime, but the microband electrode was too small to provide meaningful S/N.) The cell was filled first with 0.1 M NaF and purged of dissolved oxygen with Ar for 20 min. Then, aliquots of aqueous $KAuCl_4$ and MOP solutions were added to make the final concentration up to 250 µM and 100 µM, respectively. Electrodeposition was begun immediately with a modified form of the protocol reported in Andvaag *et al.*[181] First, the working electrode potential was scanned starting from OCP (approximately +200 mV vs Ag/AgCl) between +1000 and -1000 mV vs Ag/AgCl. Three such cycles were performed, then a potential difference absorbance measurement was collected to monitor the evolution of the SEIRAS enhancement. (This sequence is termed a "deposition cycle.") The sample potential was +300 mV and the reference potential was -900 mV; MOP adsorbs on Au at the former and is fully desorbed at the latter. Background and reference spectra (I_{bg} and I_s, respectively) were collected at these potentials and an absorbance spectrum was calculated with $A = -\log(I_s/I_{bg})$. This process was repeated several times, electrodepositing more Au with each cathodic excursion until the absorbance measurement showed a suitably high MOP signal. At this point, the solution was exchanged for 0.1 M NaF with 0.1 mM MOP after repeated rinsing with ultrapure water.

7.2.4 Step-Scan Measurements

Data acquisition was triggered by a TTL signal from a National Instruments data acquisition card (DAC) using custom LabVIEW software developed by Kaiyang Tu. The LabVIEW program coordinated control of the Bruker spectrometer and the potentiostat to achieve high-quality synchronization between the applied potential step and detector transient collection. Further details of the LabVIEW program, hardware requirements, and timing of the step-scan measurements are given in Tu's dissertation.[182] In order to reduce the noise in the spectra, a 50 - 150 Hz bandstop filter was applied to the detector transients before reconstructing them into interferograms.

7.3 Results and Discussion

7.3.1 Cyclic Voltammetry of Early-Stage Au Electrodeposition on the Microband Electrode

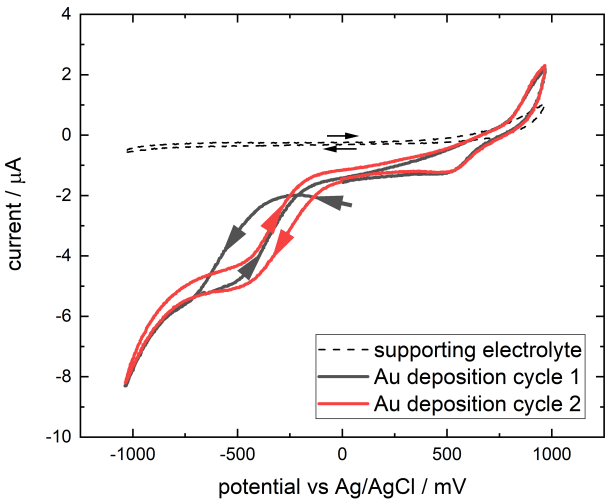

Figure 7.3: Cyclic voltammetry of ITO microband electrode during Au electrodeposition.

Details of the procedure for electrodeposition have been reported by Andvaag *et al.*[181] and mechanistic discussion of the electrochemistry was reported as part of Dr. Sajna Simon's work.[130] Those works were performed on continuous thin films of ITO as opposed to the templated microband used here. Figure 7.3 shows cyclic voltammetry results for the early stages of the electrodeposition process on the microband electrode. The dotted trace in the figure is a cyclic voltammogram (CV) of the unmodified ITO microelectrode in supporting electrolyte (aqueous 0.1 M NaF). The working electrode potential was scanned at 20 mV s^{-1} and the arrows in the figure indicate the scan direction for the anodic (upper) and cathodic (lower) scans.

In the potential region employed, ITO has no redox activity, and the majority of the trace is essentially flat. The current flowing is exclusively due to the capacitive charging of the electrical double layer formed at the working electrode. At extreme potentials, the CV begins to deviate from capacitive behaviour. This is evident from the positive slope that appears at around +750 mV and the negative slope around -900 mV. At positive potentials, anodic current flows from a small amount of electrochemical water oxidation, while at negative potentials the cathodic current is likely from trace dissolved oxygen.

The CV changes radically upon the addition of the electroplating solution (250 µM + 100 µM $KAuCl_4$). An aliquot of solution was spiked in and the electrolyte was briefly sparged with inert gas to remove any added dissolved oxygen. The first two CVs of the deposition are shown in grey and red in the figure. Starting at approximately 0 mV, the working electrode potential is scanned negative to reducing potentials. Around -400 mV, solution-phase $AuCl_4^{1-}$ is reduced to form gold nuclei on the ITO surface, resulting in the flow of cathodic current. On the return scan, it is thermodynamically more favourable to deposit Au on existing nuclei than to nucleate more clusters, so cathodic current continues flowing until much more positive potentials than those observed in the negative-going scan.[130] The crossover of current traces at -250 mV is diagnostic of this process. As the potential is scanned to more anodic potentials, characteristic features of Au oxidation are visible. (Note that the first and second scans overlap at positive potentials.) Starting at +800 mV, oxidation of Au particles results in anodic current, while on the negative-going scan the corresponding reduction process results in a cathodic current wave.

As the second deposition cycle begins (red trace), many Au nuclei have already been formed, and the CV shown in red offers clear evidence of microelectrode behaviour in the region between 0 and -500 mV. The current flowing in this region comes from reduction of $AuCl_4^{1-}$ which has diffused to the working electrode from the solution bulk. The macroscale, planar electrodes used by Andvaag and Simon exhibited a diffusion-limited current wave for heterogeneous reactions, but for microelectrodes the diffusion conditions are fundamentally different and steady-state behaviour is achieved instead.[183] In the figure, the S-shaped region is indicative of such behaviour, as the current is constant between about -400 and -700 mV before other contributions to the current flowing take over at more negative potentials. In summary, the CVs shown here agree well with previously reported electrochemical experiments and steady-state behaviour characteristic of a microband electrode has been observed.

7.3.2 Spectroscopic Monitoring of ATR-SEIRAS Activity During Electrodeposition

Becuase of the small size of the microband electrode, it was not possible to perform electrodeposition on a benchtop spectrometer while monitoring the SEIRAS enhancement. Therefore, in order to monitor the development of ATR-SEIRAS activity during electrodeposition it was necessary to prepare the Au layer *in situ* on the HATR endstation. The IRE was first roughly aligned using the known geometry of the experimental setup i.e. the position of the microband on the IRE's principal reflection plane and its position relative to the

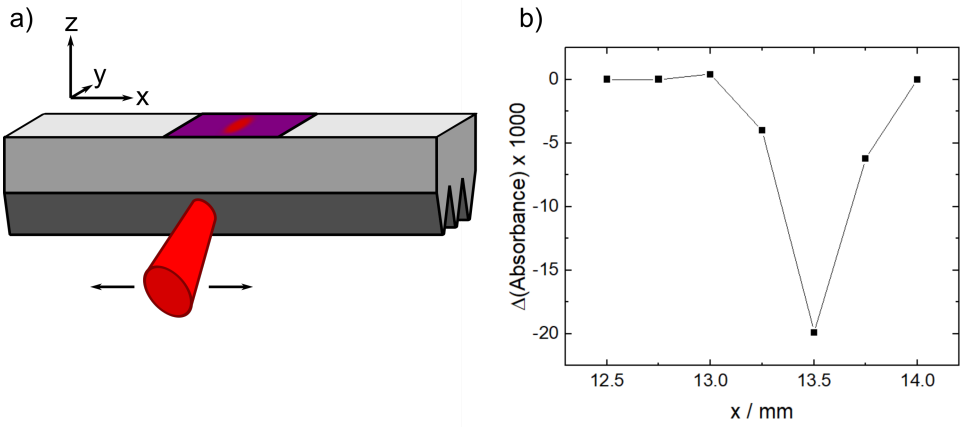

Figure 7.4: a) Depiction of the procedure used to find the microband. A section of the microgrooved IRE is shown with the beam incident on a single groove. The ITO microelectrode is shown in purple. b) Plot of absorbance difference, $\Delta(Absorbance)$, at 1250 cm^{-1}versus x (along a groove face). The strong change in absorbance at $x = 13.5$ mm indicates that the beam is illuminating the microelectrode as its potential is modulated.

aperture in the cell. Then, a fine alignment was performed by exploiting the potential-dependent reflectivity of ITO. To do so, the beam was first aligned on a single groove and then a potential difference experiment was performed with 0.1 M NaF in the cell volume. The microband was biased at two potentials (E_1 = -75 mV vs Ag/AgCl, the open-circuit potential, and E_2 = -900 mV), sample and reference spectra (I_1, I_2, respectively) were collected at each potential, and a potential difference absorbance spectrum was computed. Potential changes on the microband have no effect on the reflectivity of the Si/electrolyte interface, so a flat line centred on $A = 0$ indicated that the beam was not interrogating the microband. The beam was then translated along the groove (x-direction) by 250 µm and another potential difference measurement was performed. When the beam was finally on the microband, an absorbance offset of ΔA = -0.02 at 1250 $cm^{-1}$was observed, indicating that the ITO layer was less reflective at the sample potential than at the reference potential. Plotting the offset ΔA versus x (Fig 7.4b) results in a sparse sampled trace with a feature centered at x = 13.5 mm approximately matching the width of the microband. From this, the middle of the microband was estimated and the beam was positioned there for further experiments.

With the beam properly positioned on the centre of the microband, Au deposition could be monitored *in situ* with the familiar MOP system as a convenient spectroscopic handle. Potential difference absorption measurements were collected with E_{ads} = +200 mV and E_{des} = -900 mV after each deposition cycle (see section 7.2.3). Those curves are plotted in Figure 7.5a. As the deposition progresses the height of diagnostic MOP peaks increase, indicating an increase in the net SEIRAS enhancement factor of the hybrid film as nanoparticles are deposited. A plot of the amplitude of one representative band (the C-O-C asymmetric stretching mode at 1305 cm^{-1}) versus deposition time is shown in Fig 7.5b. This plot is semi-quantitative, as the deposition cycle was controlled manually so that the total time elapsed and charge passed during each cycle varied within about 10%. Nevertheless, a more or less linear increase in enhancement is observed as

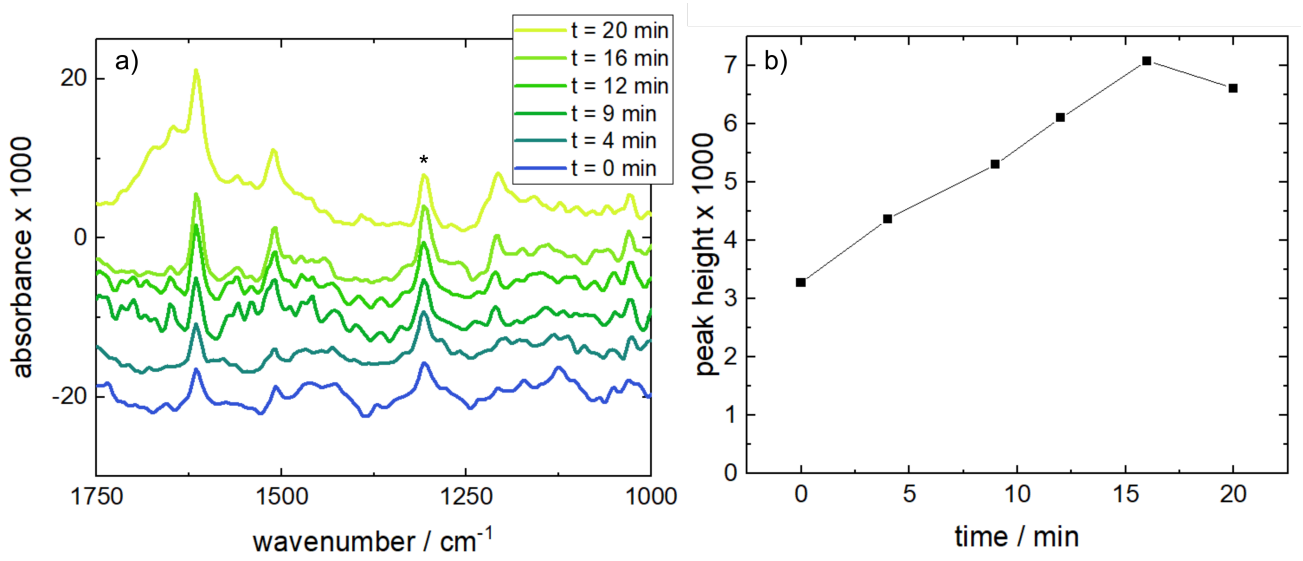

Figure 7.5: *In situ* electrodeposition of Au nanoparticles followed by ATR-SEIRAS. a) Absorbance spectra collected during the electrodeposition process. Growth in vibrational peaks of MOP over time indicate the increasing signal enhancement of the SEIRAS-active nanoparticle film. b) Peak height of the C-O-C asymmetric stretch (marked with an asterisk in (a)) with deposition time.

the deposition progresses. This represents an extremely useful feature of Andvaag *et al.*'s method compared to other methods of ATR-SEIRAS Au layer preparation: The enhancement of the layer can be directly controlled simply by choosing the number of cycles in which Au is deposited and the overall enhancement factor can be monitored *in situ*.[181] It is worth noting that this process is still fairly empirical, and further work from Andvaag and others seeks to understand the mechanistic factors at play. Although extrapolation of the plot in Figure 7.5 suggests that even higher enhancements can be achieved, Andvaag *et al.* showed that prolonged Au deposition results in bimodal absorption bands.[181] These are detrimental for quantitative analysis of ATR-SEIRAS spectra and the deposition in this case was stopped before such a Au layer was achieved.

7.3.3 Demonstration of Spatially-Resolved ATR-SEIRAS Measurement of a Microband Electrode

In Chapter 5, the highly focused spot in the horizontal ATR endstation was demonstrated by scanning across a 500 µm wide water-filled microchannel. A similar experiment was performed here to verify that such spatial resolution could be achieved in a spectroelectrochemical context. Fig 7.6a plots several spectra collected by translating the beamspot along the width of the microband. Spectra which show no traces of MOP signals are shown in gray, while those which do present MOP signals are shown in red. The plot in Fig 7.6b shows the MOP signal (asymmetric C-O-C stretch at 1305 cm^{-1}) as a function of position, and reveals a broadened profile which matches the width of the microband (500 µm) and corresponds well to the position of the ITO microband shown in Figure 7.4. Although in Figure 7.4 maximum reflectivity difference is observed at

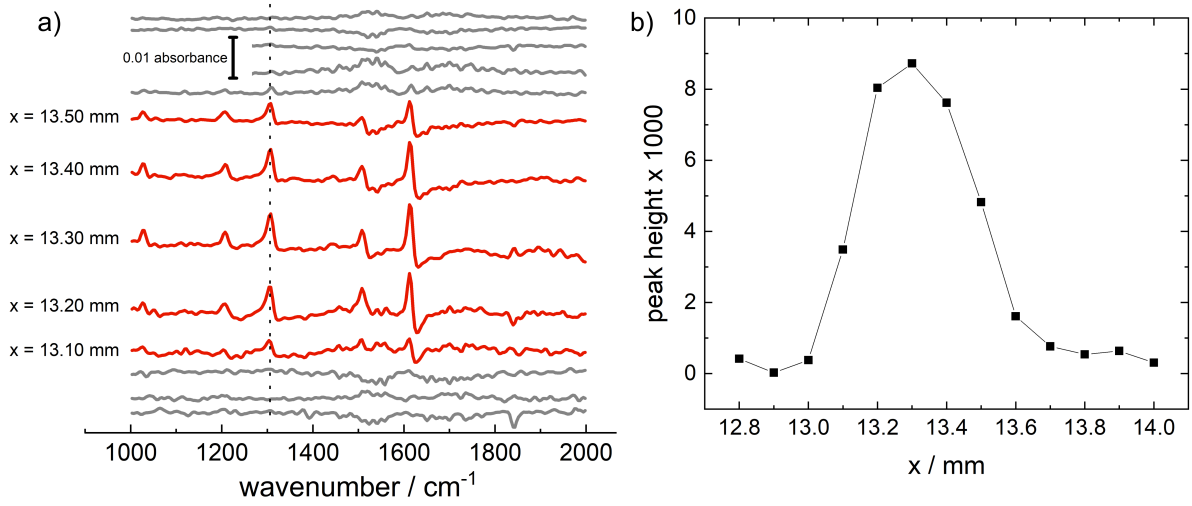

Figure 7.6: a) Potential difference absorbance measurements collected at varying positions across the width of the microband. Spectra on the microband are coloured red, while those off the microband are coloured grey. b) The peak of the C-O-C asymmetric bend as a function of position across the width of the band.

x = 13.5 mm while in Figure 7.6 maximum ATR-SEIRAS signal is observed at x = 13.3 mm, this is most likely a result of the differing sampling interval (250 versus 100 µm respectively). In Chapter 5, it was shown that the FWHM of the beamspot in the x-direction at focus in an ATR configuration was approximately 70 µm. In Figure 7.6, the peak height changes from essentially zero at x = 13.0 mm to its maximum at x = 13.2 mm, a distance of 200 µm. Within the relatively low-resolution measurement shown, this is consistent with a beamspot having FWHM close to 70 µm.

A scanning electron micrograph of the edge of the microband can be seen in Figure 7.7. The microband occupies approximately the top three quarters of the image, and two distinct regions are visible. The top portion of the microband in the image has a relatively low density of nanoparticles of varying size. This region is representative of the middle sections of the band as well. The bottom portion (i.e. at the edge) is covered in a very high density deposit, with a notably high density within approximately 1 - 2 µm of the edge. This is likely due to the differing diffusion profiles near the edge of the microband: far from the edge, diffusion of gold precursor is essentially planar, but near the edge radial diffusion contributes strongly, enhancing mass transport. The effect of nanoparticle density on ATR-SEIRAS signal is challenging to predict, but for isolated particles, increasing density should improve SEIRAS signal by modifying the effective permitivity of the layer.[184] However, particles which are in intimate contact, such as the percolated network visible at the very edge of the microband, generally have a nonlinear effect on the enhancement factor and the spectral lineshape, *vide infra*. Nevertheless, the region shown in Figure 7.7 is only a very small subsection of the sampled area (recall that the FWHM of the focused spot is on the order of 70 µm), so with the comparatively low spatial resolution available in this chapter no effect from this region is seen. With improvements in magnification of the HATR endstation, it may be possible to resolve differing enhancement factors at the

edge versus middle of the microelectrode.

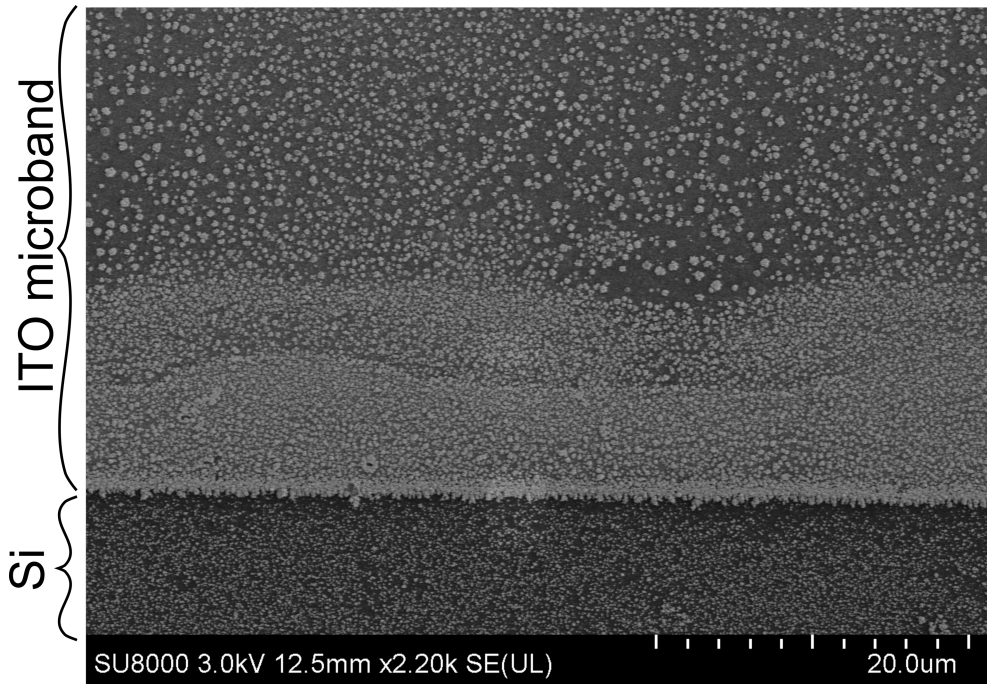

Figure 7.7: SEM micrograph showing the edge of the microband. The ITO microband is at the top of the image and the Si substrate is at the bottom. The region very near the edge (approximately 15 um) has a very high nanoparticle density and the very edge of the electrode is coated in a near-continuous network of nanoparticles.

Finally, it is worth noting that the SEM show nanoparticles on the Si surface surrounding the microband electrode i.e the bottom quarter of the image. A detailed description of Au nanoparticle formation under conditions similar to those employed here was the subject of Sajna Simon's PhD thesis [185] which describes a complex set of homogeneous and heterogeneous reactions. In brief, the method used here likely results in a mixture of surface-bound Au nanoparticles which grow from seed particles nucleated on the ITO surface and physically deposited nanoparticles which form in solution before settling onto the ITO or Si surface under the influence of gravity. Though they likely exhibit some signal enhancement, particles which are simply resting on the Si surface are not electrically addressed and so will contribute no signal to the potential difference measurements employed here.

7.3.4 Time-Resolved Spectroelectrochemistry with Step-Scan FTIR

The motivation for the previous sections of this chapter was to the show that the highly focused beamspot offered by the HATR endstation could be used to obtain surface-sensitive spectra from a 500 µm wide electrode under equilibrium conditions. The next step was to perform a dynamic experiment. The static experiments presented to this point all used the potential-dependent adsorption of MOP as a spectroscopic probe system, and the desorption of MOP was expected to proceed very rapidly. This made it a convenient

test system to verify that time-resolved spectra could be collected using the microband electrode.

The results presented below summarize experiments spearheaded by Dr. Kaiyang Tu, a PhD candidate at the time experiments were performed. Tu's dissertation focused on developing and applying time-resolved FT-IR methods to spectroelectrochemical problems, entailing significant technical contributions in automation *via* Labview, data processing and analysis, and instrumentation. With the technical challenges of implementing step-scan solved, the cell and microband electrode presented in this chapter could be used in time-resolved measurements.

In a separate experiment, the time constant of the microband electrode was measured by Tu at $\tau \approx 5RC = 4$ µs, so it was recognized that a time resolution floor of a few microseconds was sufficient, and therefore the step-scan technique was appropriate. As discussed in the Background chapter, step-scan measurements require approximately 1×10^5 experimental repetitions for sufficient signal-to-noise. With this in mind, the superb stability of the Au/ITO system developed by Andvaag *et al.* was essential for these experiments.

The fundamental problem which was encountered in step-scan time-resolved experiments was the surprisingly high noise inherent to the CLS facility. The noise level was roughly an order of magnitude higher in step-scan than in static potential difference experiments, rendering SNR too poor for meaningful analysis for all but the strongest vibrational bands of MOP. After much experimentation, the source of this noise was determined to be primarily mechanical, likely due to the many vacuum pumps and other sources of vibrational noise in the facility. To measure the environmental noise, a detector transient was collected without any experiment running and Fourier transformed into frequency space. Figure 7.8 depicts the power spectrum of the vibrational noise registering on the MCT detector. Strong peaks at 60 and 120 Hz can be observed, probably resulting from electromagnetic coupling of the mains frequency to mechanical devices such as pumps. Many other line frequencies can be observed, and although there are contributions at higher frequencies than that shown in the graph, they are small relative to those at low frequencies. Furthermore, there is a broad rolling background appearing to peak around 60 and 140 Hz corresponding to many lower intensity noise sources. Noise of the kind measured here is particularly detrimental to step scan measurements, which use DC-coupled detector measurements. In a conventional FT-IR measurement the detector is AC-coupled, and interferograms have effectively been high-pass filtered. This mitigates contamination of spectra by noise at low frequencies. Step-scan measurements with DC-coupled detectors are exposed to low frequency noise. Furthermore, the initial phase of the noise frequencies is different for each mirror position. When the interferogram is reconstructed, two adjacent mirror positions may have completely different phases of noise, resulting in extremely high apparent noise in the interferogram.

Although at first glance it may seem that digital filtering may be possible to remove these troublesome frequency contributions, this was not possible in practice. The transient collected for Figure 7.8 covered a fairly large time interval in order to achieve sufficient frequency resolution for display purposes. Transients collected in step-scan experiments in this chapter were much shorter, and even then data collection took upwards of 12 hours. Extending the measurement time was not practical. Instead, a bandstop filter was

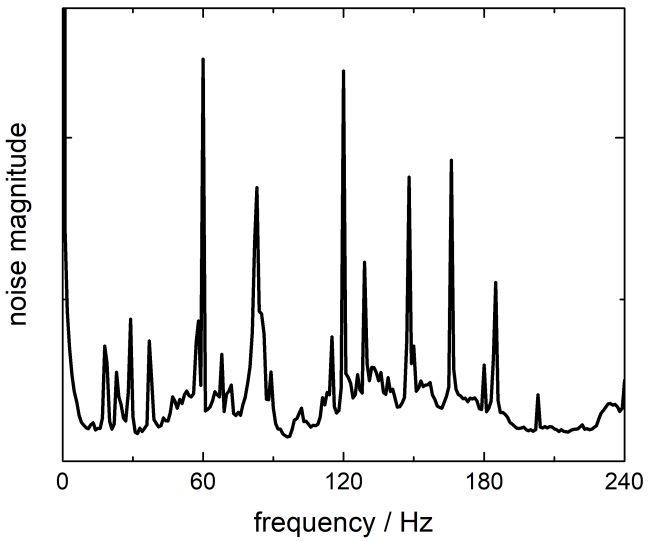

Figure 7.8: Frequency-dependent measurement noise in step-scan measurement with a microband electrode.

applied to the transients from 50 to 150 Hz to remove as much of the noise as possible before reconstructing the interferograms. Some results of this processing are shown in Figure 7.9. A representative spectrum at the end of the desorption process is shown in Figure 7.9a. Because loss of adsorbed material is being monitored, negative (i.e. downward-going) bands are expected. However, the spectrum shown in Figure 7.9a exhibits bimodal bands with strong positive and negative lobes. This effect was originally dubbed anomalous infrared effects (AIRES),[186] but has since been explained using Fresnel's equations for reflection while considering the density of a deposited layer of nanoparticles.[184,187,188] By employing an effective medium model with a variable nanoparticle fill factor, Pecharromán *et al.* showed that as nanoparticle coverage increases, vibrational bands from adsorbed molecules change sign from the expected negative-going direction to positive-going bands.[187,188] Critically, at intermediate fill fractions the bands are bimodal. The data displayed in Figure 7.9 were collected on a different electrode than that shown in Figures 7.5 and 7.6. In this case, Au was slightly over-deposited, resulting in the bimodal features shown in the figure. It is worth noting that in this spectrum, the peak-to-peak absorbance spectral noise is approximately 1×10^{-3} - 2×10^{-3} around 1800 cm^{-1}, while the strongest signal, the negative lobe of the v_{8a} ring vibration around 1600 cm^{-1}, has a peak height of about 10×10^{-3}.

The temporal evolution of the desorption process is depicted by plotting the absorbance intensity of a representative MOP mode in Figure 7.9b. The negative lobe of the strongest MOP peak, the v_{8a} ring vibration at 1610 cm^{-1}, was extracted and plotted in red. The potential function applied to the microband electrode, as measured during the experiment, is co-plotted in grey. The sharp potential step function shown is a result of the very low measured RC time constant, and confirms that the desorption process is not

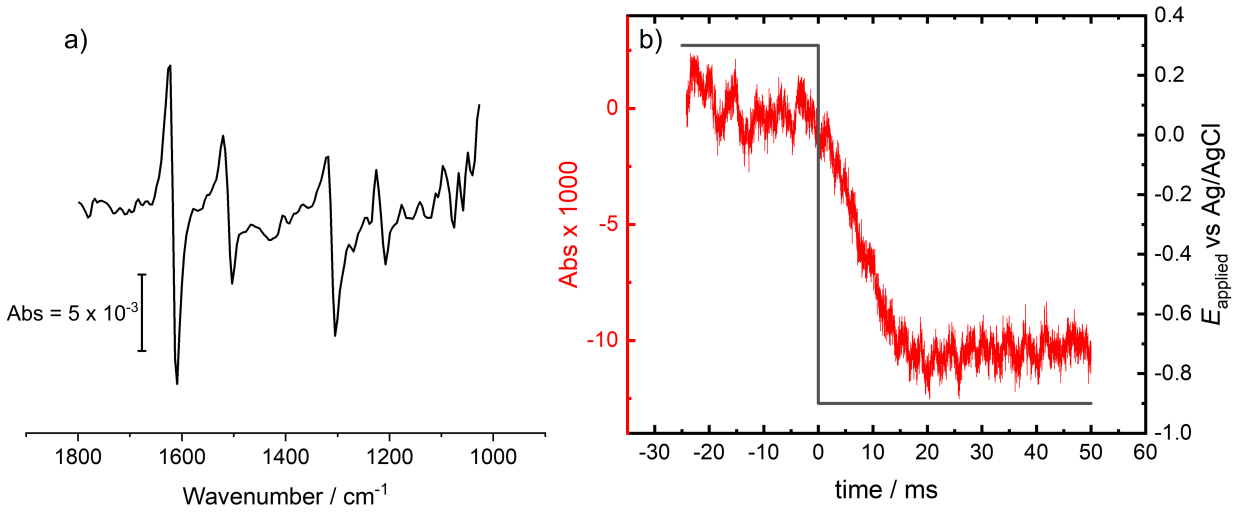

Figure 7.9: Processed results of the step scan experiment. a) Representative ATR-SEIRAS absorbance spectra at long time. The derivative shape of the spectral bands from MOP is a result of excess Au deposition. b) Absorbance transient of the υ_{8a} ring vibration at 1610 cm^{-1}(red) overlaid on the desorptive potential step applied to the microband electrode (grey).

convolved with electrode charging. Interestingly, although electrode charging is essentially instantaneous on the time scale shown in the figure, the desorption apparently takes about 15 ms to complete. This is a surprising result which cannot be explained by diffusion of the analyte out of the spectroscopically probed volume. The enhancement mechanism of ATR-SEIRAS is known to operate up to about 5 - 10 nm from the metal surface.[189] The time required for MOP to diffuse away from the surface and out of the interaction volume can be estimated using $t = d^2/D \approx 1$ µs, assuming a diffusion coefficient $D = 1 \times 10^{-6}$ cm^2/s. Even errors of an order of magnitude in each quantity do not result in a timescale comparable to that observed here, nor do more sophisticated models of desorption which take into account analyte solubility.[14] It is worth noting that the observed timescale of the desorption is very likely perturbed by the bandstop filter, which removes frequency components ranging from 50 - 150 Hz, a frequency range with characteristic time scales similar to the observed process. However, the unfiltered data (not shown), although very noisy, also show a transient process occurring with a timescale of a few milliseconds. While the 15 ms timescale observed here should be considered semi-quantitative, the process is nonetheless clearly slower than double layer charging.

Further quantitative interpretation is stymied by the high experimental noise but a tentative qualitative description can be suggested. Although the electrode potential is stepped to one at which desorption is thermodynamically favourable, it is likely that a kinetic barrier to MOP desorption is encountered. Similar organic monolayers are known to desorb following a nucleation and growth model wherein defects in the film nucleate and grow outward, with the kinetics limited by either the rate of nucleation or growth, depending on overpotential. With the low overpotential used here, the observed kinetics are limited by the rate of growth of the defect domains.[16] Exactly what mechanistic steps limit the rate of film growth are unclear. Desorption of an adsorbed molecule proceeds by reorientation of the adsorbed molecule, reformation of the solvation shell,

and transport out of the double layer and into the solution bulk. Any one of these steps may be sluggish; for example, it might be that the path between the adsorbed molecule and the solvated desorbed molecule requires a high-energy conformation of water molecules. The fluoride anion used as part of the supporting electrolyte in this study is well-known to induce a highly structured water network relative to other typical aqueous electrolytes.[190,191] Breaking that network at the ESI may present a high activation energy barrier, hindering the desorption kinetics. Reference 16 employed chronoamperometry to study monolayer desorption. The addition of spectroscopic data, obtained by repeating these experiments in a lower-noise environment with a range of electrolytes of varying hydrophilicity would provide excellent complementary data to determine the limiting factor. Because ATR-SEIRAS has been demonstrated to be sensitive to molecular orientation,[73,76] the dynamic processes of MOP reorientation and diffusion away from the electrode could be interrogated. Separately, the study of the interfacial water structure would offer valuable information. Vibrational bands of water are well-established as diagnostic markers of the average interfacial structure of water,[75,110] and monitoring their evolution during the desorption process would allow conclusions to be drawn about the changing structure of water as MOP transitions from an adsorbed to solvated state.

7.4 Conclusions

The data reported in this chapter demonstrate a proof-of-principle experiment in which a focused IR beam interrogates a 500 µm wide microband electrode to provide surface sensitive, chemically-specific information. In static potential difference experiments, the signal-to-noise ratio of the hybrid Au/ITO layer was comparable to or even better than more conventionally prepared Au layers. Preliminary step-scan time-resolved measurements showed that the potential-induced desorption of MOP takes place on a timescale three orders of magnitude slower than double-layer charging. Although the signal-to-noise ratio of the time-resolved measurements precluded detailed conclusions from being drawn, it was suggested that molecular reorientation or solvation (or both) constitute a kinetic barrier to desorption. Obtaining higher quality spectra is expected to allow the molecular orientation to be monitored as well as the changing water structure near the ESI.

This chapter serves as a capstone for the thesis goal, and general implications will be discussed in Chapter 8. The remaining technical problem to be solved is the high noise inherent to the CLS facility. Although it is possible to adapt the tools developed here to any suitable synchrotron facility, work could be continued at CLS by modulating the signal of interest into a cleaner frequency range in the manner proposed by Bewick *et al.*[192] Let us assume that the true timescale of the desorption is at most on the scale of 100 µs (or about the 10 kHz range.) Modulating the signal with a tenfold higher carrier wave (100 kHz) would be necessary to extract the lower frequency signal with a lock-in amplifier. The extremely fast potential response of the microelectrode may allow the electrode potential to be modulated by a high frequency, low-amplitude oscillation carrier wave. In the absence of a campaign of vibrational isolation at the Mid-IR beamline, it is likely that any further work will need to employ these double-modulation techniques to improve SNR.

The results presented in this chapter also demonstrate that spatially-resolved ATR-SEIRAS under equilibrium conditions is possible. This is an important development for ATR-SEIRAS generally, as the technique is exclusively used on conventional FT-IR spectrometers with very large spot sizes. The spatial resolution afforded by the HATR endstation is expected to allow further work on structured electrodes with e.g. heterogeneously deposited nanoparticles of varying size or composition. Furthermore, UV lithography allows electrodes of arbitrary shape to be prepared, with critical dimensions limited to a few microns. The flexibility of this fabrication technique combined with developments in metal nanoparticle electrodeposition is expected to be highly important for future catalytic studies.

8 Conclusions and Future Work

8.1 Conclusions

This thesis was motivated by the desire to collect time-resolved spectroscopic data at the electrode/solution interface with microsecond time resolution. As described in the introduction and background chapters, this posed a unique experimental challenge: illuminating an ATR-SEIRAS compatible microband electrode with highly brilliant synchrotron infrared radiation. The work presented in this thesis can be viewed as an extended response to that challenge.

Chapter 3 described what might be considered a "naive" approach to performing ATR-SEIRAS measurements with the existing instrumentation at the Mid-IR beamline. The experimental setup described in that chapter was inspired by typical ATR-SEIRAS experiments performed in the Burgess group and in the wider literature. A custom spectroelectrochemical cell was designed to accommodate a Si hemisphere, a typical internal reflection element for ATR-SEIRAS, and place it at focus of the FT-IR microscope at the Mid-IR beamline of CLS. Working with a very large thin film electrode, it was demonstrated that, in principle, ATR-SEIRAS spectra could be collected from an approximately 125 μm^2 area with femtomole detection limits. Although this was a significant achievement, the diffficulty of positioning the synchrotron IR beamspot prevented application of this experimental setup to work on microband electrodes.

Chapter 3 concluded by highlighting two hurdles in the experimental program: the complex beam steering characteristics of the hemisphere and the instability of patterned Au thin film electrodes. Chapters 4, 5, and 7 can be viewed as the core of the thesis work, where the questions posed at the end of chapter 3 were answered.

Chapter 4 began by considering the potential of a new microgrooved IRE which had recently become commercially available. The microgrooved IRE was obviously amenable to photolithography (a boon for microelectrode preparation) and was expressly designed for single-bounce ATR-FTIR spectroscopy. A detailed analysis of its capabilities for ATR-SEIRAS was conducted in chapter 4, which showed that microgrooved IREs were completely compatible with ATR-SEIRAS along with the following key findings: 1) the empirically optimal AOI was lower than that used for a hemisphere (approximately 55° compared to more typical 70 to 80°) leading to $2-3\times$ lower signals above the Si cutoff; but this was balanced by 2) superior optical throughput below 1450 cm^{-1}(and thus SNR) relative to hemispheres due to lower optical pathlength.

With these results in mind, Chapter 5 presented the design and qualification of a new Mid-IR endstation, a horizontal microscope which was generally capable of ATR-FTIR measurements but was conceived for

use in microspectroscopy experiments with the microgrooved wafers. It was shown that by controlling the beamspot size with an aperture, a spot size (FWHM) of 130 µm in air and 70 µm at the Si/water interface was achievable. The latter quantity deviated from that expected due to the higher refractive index, but the discrepancy was explained in terms of a slight defocus. Nevertheless, high-quality single point spectra were collected across the width of a 400 um wide water-filled channel in SU-8 photoresist, clearly demonstrating the excellent spatial resolution of the endstation.

It was recognized that the benefits of the HATR endstation were greater than the rather narrow focus of this thesis on surface-sensitive spectroelectrochemistry. This was demonstrated in chapter 6, where a two-channel microfluidic device was fabricated on a microgrooved IRE. Imaging of a model chemical reaction, H/D-exchange in co-flowing H_2O and D_2O streams, was demonstrated with a 200×400 µm^2 field of view and approximately 14 µm spatial resolution. This was sufficient to image the formation of HOD at the H_2O/D_2O interface. The relatively large FOV was provided by low magnification and the large-area illumination of a conventional globar source, but application of synchrotron IR was discussed in the context of future work with higher magnification.

Finally, chapter 7 discussed the preparation of a highly stable, ATR-SEIRAS-compatible microband electrode which capitalized on contemporary work in the Burgess group. UV photolithography was used to prepare a 500 µm wide microband electrode aligned perpendicular to the long of axis of the microgrooves. The spatial resolution of the HATR endstation was sufficient to collect spectra across the microband's width, demonstrating the high fidelity of the measurement. Preliminary time-resolved measurements were presented, with the key challenge being the high environmental noise at the CLS. Nevertheless, the electrochemically induced desorption of MOP from a Au surface was followed with 12.5 µs resolution, and it was shown to proceed at a rate three orders of magnitude slower than double layer charging. A preliminary explanation was offered by invoking a kinetic barrier to solvation as desorption proceeded.

Overall, there have been two concrete developments that have come out of this thesis work. First, the HATR microscope endstation is a permanent installation at the Mid-IR beamline and is now managed by beamline staff. At the time of writing, it has attracted an increasing number of new external users. Ongoing development and scientific application will be discussed in the Future Work section. Second, a robust and well-developed spectroelectrochemical cell has been developed around microgrooved wafer IREs. By drawing on previous designs in the Burgess group, cells have been designed which make it possible to perform high-quality ATR-SEIRAS experiments using microgrooved wafers on either FT-IR benchtop spectrometers or the HATR microscope as CLS. In fact, the benchtop cell reported in Chapter 4 is now a commercial product and is in use by multiple laboratories worldwide.[193]

8.2 Future Work

8.2.1 Technical Developments

Although the developments summarized above demonstrate a way forward to perform kinetic experiments on electrochemical systems with microsecond time resolution, the high environmental noise at CLS remains a significant obstacle. Without exhaustive vibrational isolation or improved digital filtering of the noise, the feasibility of such measurements are in doubt. However, the optics and spectroelectrochemical proposed here are easily amenable to any synchrotron facility which has a Mid-IR beamline. Also, fourth generation synchrotron sources such as that proposed for CLS 2.0 are characterized by extremely small source sizes and require correspondingly higher vibrational isolation than third generation facilities. Such facilities or other third generation sources with lower noise environments are excellent candidates for a research program such as that described in this thesis.

A better option may be to continue development of microelectrode spectroscopy using the dual-comb quantum cascade laser (QCL) based IRis-F1 spectrometer which has been commissioned at the Mid-IR beamline. The IRis-F1 is built for time-resolved measurements using relatively broadband IR QCLs (bandwidth about $50 - 100$ cm^{-1}) which can be exchanged to change the spectral coverage.[194–197] The instrument is designed with microsecond time resolution in mind, and as a stand-alone instrument it can more easily be isolated from mechanical noise. (Compare the Mid-IR beamline, where mechanical noise can be coupled in at a variety of sources starting at the transfer optics which pipe the beam from its exit port at the synchrotron to the spectrometer.) However, the preliminary work of Erick Lins (Burgess group Ph.D student) has shown that optical interference fringes develop over typical experimental durations. Although it was initially hypothesized that multiple internal reflections of the coherent laser beam in the microgrooved wafer were responsible, painstaking experimental work by Lins has shown that laser instability is the more likely culprit. While it is possible to manually tune laser parameters to improve stability, this remains highly challenging and will benefit greatly from continued engineering work on the part of laser manufacturers and authors of control software.

As of this writing, the HATR endstation is now managed by Mid-IR beamline staff and has benefited greatly from their input. Chapter 6 showed that multiple internal reflections complicated interpretation of chemical imaging experiments in microfluidic devices built on the microgrooved wafers. Subsequent geometric ray-tracing suggested that changing the AOI to 55° would result in the largest possible fraction of rays undergoing single internal reflections, improving imaging quality. This change has been made by Mid-IR staff, along with upgrades to the three-axis positioner and the very useful addition of an optical microscope.

The magnification of the HATR microscope can be improved to take advantage of the synchrotron source. Addition of a high-refractive index lens (e.g. Ge) or Cassegrain objective could improve the effective magnification from 3× to 10×; coupling this with the SIR beam would increase the spatial resolution to about 5

µm which is comparable to the diffraction limit of IR light. Greater resolution would allow for higher data density in single point measurements across channels or microelectrodes. Greater resolution would benefit imaging work as well. Collecting several high resolution images over the length of a fluidic channel would potentially allow mapping of reaction products as they diffuse in the channel. Improving resolution would decrease measurement error when attempting to quantify reaction rates and diffusion coefficients from such images. However, the relatively high detection limits of ATR-FTIR microspectroscopy have to be taken into account, and it seems likely that reactants and products with strong absorption coefficients will yield the best results in the near future.

8.2.2 Static and Dynamic Spectroelectrochemistry

Leaving aside the technical problems encountered in time-resolved measurements, it is worth revisiting the original motivation of electrocatalysis. This thesis began with the example of methanol oxidation, a prototypical electrocatalytic reaction, and the outlook for studying it and similar systems is positive. High spatial resolution microspectroscopy developed in this thesis could be productively applied to electrocatalysis. Many electrocatalysts consist of metal nanoparticles on a support material such as that shown in the introductory chapter. The ability to probe the local activity of a heterogeneous electrocatalyst, for example a catalyst with variable nanoparticle density or composition, could have important implications in combinatorial catalyst engineering. It is important to note that many important electrocatalytic systems are amenable to study by infrared. Although the proof-of-principle measurements discussed in Chapter 7 were stymied by high environmental noise, the tools developed in this thesis are generally applicable to any number of electrocatalytic systems such as the reduction of methanol, CO_2, or other small organic molecules. In fact, even systems without an obvious infrared target, such as nitrogen or oxygen reduction or the hydrogen evolution reaction, might be studied by monitoring the dynamics of water structure at the ESI. This is potentially of great consequence for the chemical industry. It seems likely that any successful industrial electrocatalysis application will work with aqueous media simply based on the abundance and benign nature of water. Furthermore, reaction at the ESI must be accompanied by changes in the solvation shell of the reactants and is mediated by the solvent structure.[198–201] Nonlinear spectroscopy has been used extensively to characterize the structure of water in the electrical double layer formed at the silica/water[202] interface, water/surfactant/air interface[203], and the water/air interface as well.[204] However, dynamic studies with nonlinear methods at the ESI remain challenging, partly due to the complex phase shift imparted by metallic surfaces.[205] ATR-SEIRAS offers excellent sub-monolayer sensitivity and avoids the difficult data analysis associated with such techniques, and is an excellent candidate to study the dynamics of water structure under electrocatalytic conditions.

A unique advantage of the platform developed in this thesis is that it can also monitor the libration mode of water due to wide frequency window offered by the microgrooved Si IRE. In contrast to the H-O-H bending and O-H stretching modes, the frequencies of which are determined by the hydrogen bonding network's effects on the H_2O molecule's vibrational potential, the libration mode probes the rotational potential of the water

molecule. This is a fundamentally different intermolecular interaction which has otherwise been difficult to probe in surface-sensitive experiments. Vibrational sum frequency generation experiments have shown that interfacial water structuring retards the associated rotation with consequences for heterogeneous kinetics.[206] The broadband nature of synchrotron radiation and wide spectral window afforded by the microgrooved IREs allows a complete inventory of water stretching and libration modes to be collected in one measurement. Failing improvements in the signal-to-noise ratio of step-scan experiments, tunable or broadband QCLs might be used with a similar experimental setup. Alternatively, spectroscopy at the Far-IR beamline of CLS would likely generate interesting results. Although rudimentary Far-IR experiments were performed during the course of this thesis work, it was not developed further. Early results suggest that the SEIRAS mechanism is operative in the Far-IR region and electrochemically induced changes in the water libration band could be monitored.

Applying the imaging techniques developed in this thesis to electrochemical problems is expected to yield insights which are not otherwise obtainable with single-point microspectroscopy measurements. An intriguing opportunity exists in imaging non-equilibrium systems. When chemical systems are driven far from equilibrium, as in an operational electrocatalyst, it is well known that highly nonlinear effects may occur. A classic example from pure chemistry is the Belousov-Zhabotinsky reaction,[207] a reaction-diffusion system which exhibits complex pattern formation. For electrochemical systems, the fundamental basis is the coupling of the electrode potential, mass transport to the electrode, and in some cases cooperative effects in surface chemistry. So-called electrochemical turbulence has been observed by driving a rotating ring disk at varying potentials, with the potential driving the formation of periodic reaction fronts at low voltages and chaotic defect formation at higher voltages.[208] Behm and coworkers have productively applied these insights to study the oxidation of CO on a Pt thin film electrode using ATR-SEIRAS coupled with differential electrochemical mass spectrometry.[209] Only single-point measurements were collected in that work, with the spectroscopic response averaging over the entire electrode surface. Krischer and coworkers coupled an ATR-SEIRAS experiment with relatively low spatial resolution (40 $\times$ 80 µm) using an FPA detector to demonstrate steady-state pattern formation in the CO/Pt system under galvanostatic conditions.[210] They found that with increasing current density, CO surface coverage transitioned from one completely covered by high-density linear bonded CO to a mixed surface with completely passivated islands of linear bonded CO and unpassivated islands of bare Pt which accounted for all of the reactivity. Interestingly, they noted at intermediate current densities the boundaries of CO-passivated islands were not sharp, but instead showed a gradual decrease in CO signal intensity with no change in peak frequency. The lack of peak shift indicated that decreasing monolayer coverage could not explain their results. They proposed two possible explanations: either fluctuations in the size of the high coverage islands which occur on faster time scales than image collection, or in the formation of high-coverage micro islands which were below the relatively low spatial resolution of the measurement. Considering the potential improvements in spatial resolution proposed in this Conclusions chapter to near the diffraction limit of infrared radiation, the tools developed in this thesis

might be usefully applied to studying electrochemical pattern formation for the purposes of differentiating between these two explanations.

8.2.3 Electrochemical Microfluidics

The unique coupling of microfabricated devices and surface-sensitive microspectroscopy will enable the study of electrochemical microfluidic devices. There is a substantial body of literature devoted to developing flow reactors (electrochemical or not) for the synthesis of fine chemicals.[169,211–214] Most published reports monitor the product distribution by sampling the effluent[215,216] but detailed information about reaction conditions and intermediates could be obtained by directly imaging the reaction mixture on-chip,[217–219] particularly at the interface between two co-flowing media. Taking advantage of the innate compatibility of Si microgrooved IREs with conventional microfabrication techniques, electrodes could be incorporated into a device like that discussed in Chapter 6. Early proof-of-principle experiments might focus on simply detecting an electrogenerated product downstream from a single band electrode. Alternatively, by using a conductive metal oxide such as ITO, which is transparent in the visible and IR regimes, the entire channel could act as an electrode and the buildup of electrogenerated product could be monitored. At a greater level of complexity, this product stream might be introduced to a separate reactant stream, and the reaction occuring at the interface between the streams could be imaged. Current materials limit such a program to aqueous systems with relatively moderate pH, but efforts are underway to evaluate materials compatible with organic solvents and more aggressive conditions. Overall, these experiments sketch the work necessary to begin developing an analytical device capable of *in situ* imaging of organic reactions on flow.

References

[1] SaskPower, Queen Elizabeth Power Station. 2021; https://www.saskpower.com/Our-Power-Future/Our-Electricity/Electrical-System/System-Map/Queen-Elizabeth-Power-Station.

[2] Bard, A. J.; Faulkner, L. R. *Electrochemical Methods: Fundamentals and Applications*, 2nd ed.; John Wiley & Sons, Ltd: New York, 2001.

[3] Pletcher, D.; Walsh, F. *Industrial Electrochemistry*, 2nd ed.; Springer Netherlands, 1993; p 672.

[4] Hamnett, A. Mechanism and electrocatalysis in the direct methanol fuel cell. *Catalysis Today* **1997**, *38*, 445–457.

[5] Scott, K.; Taama, W. M.; Argyropoulos, P. Engineering aspects of the direct methanol fuel cell system. *Journal of Power Sources* **1999**, *79*, 43–59.

[6] Lozeman, J. J.; Führer, P.; Olthuis, W.; Odijk, M. Spectroelectrochemistry, the future of visualizing electrode processes by hyphenating electrochemistry with spectroscopic techniques. *Analyst* **2020**, *145*, 2482–2509.

[7] Antonio, M. R.; Soderholm, L.; Song, I. Design of spectroelectrochemical cell for in situ X-ray absorption fine structure measurements of bulk solution species. *Journal of Applied Electrochemistry* **1997**, *27*, 784–792.

[8] Risch, M.; Grimaud, A.; May, K. J.; Stoerzinger, K. A.; Chen, T. J.; Mansour, A. N.; Shao-Horn, Y. Structural changes of cobalt-based perovskites upon water oxidation investigated by EXAFS. *Journal of Physical Chemistry C* **2013**, *117*, 8628–8635.

[9] Rao, R. R. et al. Towards identifying the active sites on RuO2(110) in catalyzing oxygen evolution. *Energy and Environmental Science* **2017**, *10*, 2626–2637.

[10] Oum, K.; Lohse, P. W.; Flender, O.; Klein, J. R.; Scholz, M.; Lenzer, T.; Du, J.; Oekermann, T. Ultrafast dynamics of the indoline dye D149 on electrodeposited ZnO and sintered ZrO2 and TiO2 thin films. *Physical Chemistry Chemical Physics* **2012**, *14*, 15429–15437.

[11] Hewitt, J. T.; Vallett, P. J.; Damrauer, N. H. Dynamics of the 3MLCT in Ru(II) terpyridyl complexes probed by ultrafast spectroscopy: Evidence of excited-state equilibration and interligand electron transfer. *Journal of Physical Chemistry A* **2012**, *116*, 11536–11547.

[12] Abramczyk, H.; Brozek-Płuska, B.; Kurczewski, K.; Kurczewska, M.; Szymczyk, I.; Krzyczmonik, P.; Błaszczyk, T.; Scholl, H.; Czajkowski, W. Femtosecond transient absorption, Raman, and electrochemistry studies of tetrasulfonated copper phthalocyanine in water solutions. *Journal of Physical Chemistry A* **2006**, *110*, 8627–8636.

[13] Bewick, A.; Kunimatsu, K.; Pons, B. S. Infra Red Spectroscopy of the Electrode-Electrolyte Interphase. *Electrochimica Acta* **1980**, *25*, 465–468.

[14] Pesika, N. S.; Stebe, K. J.; Searson, P. C. Kinetics of desorption of alkanethiolates on gold. *Langmuir* **2006**, *22*, 3474–3476.

[15] Robinson, R. S.; McCurdy, C. W.; McCreery, R. L. Microsecond Spectroelectrochemistry by External Reflection from Cylindrical Microelectrodes. *Analytical Chemistry* **1982**, *54*, 2356–2361.

[16] Yang, D. F.; Morin, M. Chronoamperometric study of the reduction of chemisorbed thiols on Au(111). *Journal of Electroanalytical Chemistry* **1997**, *429*, 1–5.

[17] Hossain, M. D.; Huang, Y.; Yu, T. H.; Goddard, W. A.; Luo, Z. Reaction mechanism and kinetics for CO2 reduction on nickel single atom catalysts from quantum mechanics. *Nature Communications* **2020**, *11*, 1–14.

[18] Osawa, M.; Ataka, K.-i.; Yoshii, K.; Yotsuyanagi, T. Surface-enhanced infrared ATR spectroscopy for in situ studies of electrode/electrolyte interfaces. *Journal of Electron Spectroscopy and Related Phenomena* **1993**, *64-65*, 371–379.

[19] Rosendahl, S. M.; Borondics, F.; May, T. E.; Burgess, I. J. Step-scan IR spectroelectrochemistry with ultramicroelectrodes: Nonsurface enhanced detection of near femtomole quantities using synchrotron radiation. *Analytical Chemistry* **2013**, *85*, 8722–8727.

[20] Lardner, M. J.; Tu, K.; Barlow, B. C.; Rosendahl, S. M.; Borondics, F.; Burgess, I. J. Quantitative analysis of electrochemical diffusion layers using synchrotron infrared radiation. *Journal of Electroanalytical Chemistry* **2016**, 6–11.

[21] Tu, K.; Lardner, M. J.; Morhart, T. A.; Rosendahl, S. M.; Creighton, S.; Burgess, I. J. Spatial Mapping of Methanol Oxidation Activity on a Monolithic Variable-Composition PtNi Alloy Using Synchrotron Infrared Microspectroscopy. *Journal of Physical Chemistry C* **2016**, *120*, 23640–23647.

[22] Griffiths, P. R.; De Haseth, J. A. In *Fourier Transform Infrared Spectrometry*, 2nd ed.; Winefordner, J. D., Ed.; John Wiley & Sons, Ltd: Hoboken, 2007; p 560.

[23] McQuarrie, D. A. *Quantum Chemistry*, 2nd ed.; University Science Books: Sausalito, 2008; p 690.

[24] Harris, D. C.; Bertolucci, M. D. *Symmetry and Spectroscopy: An Introduction to Vibrational and Electronic Spectroscopy*; Oxford University Press: New York, 197; p 550.

[25] May, T. E.; Appadoo, D.; Ellis, T.; Reininger, R. Infrared beamlines at the Canadian Light Source. AIP Conference Proceedings. 2007; pp 579–582.

[26] May, T.; Ellis, T.; Reininger, R. Mid-infrared spectromicroscopy beamline at the Canadian Light Source. *Nuclear Instruments and Methods in Physics Research, Section A: Accelerators, Spectrometers, Detectors and Associated Equipment* **2007**, *582*, 111–113.

[27] Hackett, M. J.; Caine, S.; Liu, X.; May, T. E.; Borondics, F. Development of single-beam wide-field infrared imaging to study sub-cellular neuron biochemistry. *Vibrational Spectroscopy* **2015**, *77*, 51–59.

[28] Prati, S.; Joseph, E.; Sciutto, G.; Mazzeo, R. New advances in the application of FTIR microscopy and spectroscopy for the characterization of artistic materials. *Accounts of Chemical Research* **2010**, *43*, 792–801.

[29] Kuimova, M. K.; Chan, K. L.; Kazarian, S. G. Chemical imaging of live cancer cells in the natural aqueous environment. *Applied Spectroscopy* **2009**, *63*, 164–171.

[30] Gelfand, P.; Smith, R. J.; Stavitski, E.; Borchelt, D. R.; Miller, L. M. Characterization of Protein Structural Changes in Living Cells Using Time-Lapsed FTIR Imaging. *Analytical Chemistry* **2015**, *87*, 6025–6031.

[31] Wallace, G. Q.; Foy, H. C.; Rosendahl, S. M.; Lagugné-Labarthet, F. Dendritic Plasmonics for Mid-Infrared Spectroscopy. *Journal of Physical Chemistry C* **2017**, *121*, 9497–9507.

[32] Holman, H. Y. N.; Miles, R.; Hao, Z.; Wozei, E.; Anderson, L. M.; Yang, H. Real-time chemical imaging of bacterial activity in biofilms using open-channel microfluidics and synchrotron FTIR spectromicroscopy. *Analytical Chemistry* **2009**, *81*, 8564–8570.

[33] Rosendahl, S. M.; Borondics, F.; May, T. E.; Pedersen, T. M.; Burgess, I. J. Synchrotron infrared radiation for electrochemical external reflection spectroscopy: A case study using ferrocyanide. *Analytical Chemistry* **2011**, *83*, 3632–3639.

[34] Rosendahl, S. M. Advances in in-Situ spectroelectrochemical Fourier Transform Infrared Spectroscopy. Ph.D. thesis, University of Saskatchewan, 2013.

[35] Lardner, M. J.; Tu, K.; Rosendahl, S. M.; Borondics, F.; Burgess, I. J. Spatiotemporal Mapping of Diffusion Layers Using Synchrotron Infrared Radiation. *Electrochimica Acta* **2015**, *162*, 72–78.

[36] Milosevic, M. Internal reflection and ATR spectroscopy. *Applied Spectroscopy Reviews* **2004**, *39*, 365–384.

[37] Rödig, C.; Chizhov, I.; Weidlich, O.; Siebert, F. Time-resolved step-scan Fourier transform infrared spectroscopy reveals differences between early and late M intermediates of bacteriorhodopsin. *Biophysical Journal* **1999**, *76*, 2687–2701.

[38] Schultz, B. J.; Mohrmann, H.; Lorenz-Fonfria, V. A.; Heberle, J. Protein dynamics observed by tunable mid-IR quantum cascade lasers across the time range from 10 ns to 1 s. *Spectrochimica Acta - Part A: Molecular and Biomolecular Spectroscopy* **2018**, *188*, 666–674.

[39] Xiao, X.; Bard, A. J. Observing single nanoparticle collisions at an ultramicroelectrode by electrocatalytic amplification. *Journal of the American Chemical Society* **2007**, *129*, 9610–9612.

[40] Fan, F. R. F.; Bard, A. J. Electrochemical detection of single molecules. *Science* **1995**, *267*, 871–874.

[41] Amemiya, S.; Bard, A. J.; Fan, F. R. F.; Mirkin, M. V.; Unwin, P. R. Scanning electrochemical microscopy. *Annual Review of Analytical Chemistry* **2008**, *1*.

[42] Barnes, E. O.; Lewis, G. E.; Dale, S. E.; Marken, F.; Compton, R. G. Generator-collector double electrode systems: A review. *Analyst* **2012**, *137*, 1068–1081.

[43] Hu, M.; Fritsch, I. Application of Electrochemical Redox Cycling: Toward Differentiation of Dopamine and Norepinephrine. *Analytical Chemistry* **2016**, 5574–5578.

[44] Murarka, S. P.; Hymes, S. W. Copper Metallization for ULSI and Beyond. *Critical Reviews in Solid State and Materials Sciences* **1995**, *20*, 87–124.

[45] Murarka, S. P. Multilevel interconnections for ULSI and GSI era. *Materials Science and Engineering R: Reports* **1997**, *19*, 87–151.

[46] Wells, G.; Achenbach, S.; Subramanian, V.; Jacobs, M.; Klymyshyn, D.; Iyer, S.; Moazed, B.; Hanson, J. SyLMAND: a microfabrication beamline with wide spectral and beam power tuning range at the Canadian Light Source Garth. *Journal of Synchrotron Radiation* **2019**, *26*, 565–570.

[47] Achenbach, S.; Hegsbach, S.; Schulz, J.; Mohr, J. Optimization of laser writer-based UV lithography with high magnification optics to pattern X-ray lithography mask templates. *Microsystem Technologies* **2019**, *25*, 2975–2983.

[48] Achenbach, S.; Wells, G.; Jacobs, M.; Moazed, B.; Iyer, S.; Hanson, J. Polymer-based X-ray masks patterned by direct laser writing. *Review of Scientific Instruments* **2018**, *89*.

[49] Plieth, W.; Wilson, G. S.; Gutiérrez De La Fe, C. Spectroelectrochemistry: A survey of in situ spectroscopic techniques (Technical Report). *Pure and Applied Chemistry* **1998**, *70*, 1395–1414.

[50] Zhai, Y.; Zhu, Z.; Zhou, S.; Zhu, C.; Dong, S. Recent advances in spectroelectrochemistry. *Nanoscale* **2018**, *10*, 3089–3111.

[51] León, L.; Mozo, J. D. Designing spectroelectrochemical cells: A review. *TrAC - Trends in Analytical Chemistry* **2018**, *102*, 147–169.

[52] Garoz-Ruiz, J.; Perales-Rondon, J. V.; Heras, A.; Colina, A. Spectroelectrochemical Sensing: Current Trends and Challenges. *Electroanalysis* **2019**, *31*, 1254–1278.

[53] Dunsch, L. Recent Advances in in situ multi-spectroelectrochemistry. *Journal of Solid State Electrochemistry* **2011**, *15*, 1631–1646.

[54] Cowan, A. J.; Hardwick, L. J. Advanced Spectroelectrochemical Techniques to Study Electrode Interfaces Within Lithium-Ion and Lithium-Oxygen Batteries. *Annual Review of Analytical Chemistry* **2019**, *12*, 323–346.

[55] Heineman, W. R.; Burnett, J. N.; Murray, R. W. Optically Transparent Thin-Layer Electrodes: Ninhydrin Reduction in an Infrared Transparent Cell. *Analytical Chemistry* **1968**, *40*, 1974–1978.

[56] Aroca, R. F.; Ross, D. J.; Domingo, C. Surface-Enhanced Infrared Spectroscopy. *Applied Spectroscopy* **2004**, *58*, 324A – 338A.

[57] Shao, M. H.; Adzic, R. R. Electrooxidation of ethanol on a Pt electrode in acid solutions: In situ ATR-SEIRAS study. *Electrochimica Acta* **2005**, *50*, 2415–2422.

[58] Samjeské, G.; Miki, A.; Ye, S.; Osawa, M. Mechanistic study of electrocatalytic oxidation of formic acid at platinum in acidic solution by time-resolved surface-enhanced infrared absorption spectroscopy. *Journal of Physical Chemistry B* **2006**, *110*, 16559–16566.

[59] Cuesta, A.; Cabello, G.; Osawa, M.; Gutiérrez, C. Mechanism of the electrocatalytic oxidation of formic acid on metals. *ACS Catalysis* **2012**, *2*, 728–738.

[60] Samjeské, G.; Miki, A.; Ye, S.; Yamakata, A.; Mukouyama, Y.; Okamoto, H.; Osawa, M. Potential oscillations in galvanostatic electrooxidation of formic acid on platinum: A time-resolved surface-enhanced infrared study. *Journal of Physical Chemistry B* **2005**, *109*, 23509–23516.

[61] Miyake, H.; Okada, T.; Samjeské, G.; Osawa, M. Formic acid electrooxidation on Pd in acidic solutions studied by surface- enhanced infrared absorption spectroscopy. *Physical Chemistry Chemical Physics* **2008**, *10*, 3607–3608.

[62] Miki, A.; Ye, S.; Senzaki, T.; Osawa, M. Surface-enhanced infrared study of catalytic electrooxidation of formaldehyde, methyl formate, and dimethoxymethane on platinum electrodes in acidic solution. *Journal of Electroanalytical Chemistry* **2004**, *563*, 23–31.

[63] Watanabe, M.; Zhu, Y.; Uchida, H. Oxidation of CO on a Pt-Fe Alloy Electrode Studied by Surface Enhanced Infrared Reflection-Absorption Spectroscopy. *Journal of Physical Chemistry B* **2000**, *104*, 1762–1768.

[64] Watanabe, M.; Zhu, Y.; Igarishi, H.; Uchida, H. Mechanism of CO Tolerance at Pt-Alloy Anode Catalysts for Polymer Electrolyte Fuel Cells. *Electrochemistry* **2000**, *68*, 244–251.

[65] Chen, D. J.; Tong, Y. J. Irrelevance of Carbon Monoxide Poisoning in the Methanol Oxidation Reaction on a PtRu Electrocatalyst. *Angewandte Chemie - International Edition* **2015**, *54*, 9394–9398.

[66] Wuttig, A.; Yaguchi, M.; Motobayashi, K.; Osawa, M.; Surendranath, Y. Inhibited proton transfer enhances Au-catalyzed CO2-to-fuels selectivity. *Proceedings of the National Academy of Sciences of the United States of America* **2016**, *113*, E4585–E4593.

[67] Shao, M. H.; Adzic, R. R. Spectroscopic identification of the reaction intermediates in oxygen reduction on gold in alkaline solutions. *Journal of Physical Chemistry B* **2005**, *109*, 16563–16566.

[68] Yao, Y.; Zhu, S.; Wang, H.; Li, H.; Shao, M. A Spectroscopic Study on the Nitrogen Electrochemical Reduction Reaction on Gold and Platinum Surfaces. *Journal of the American Chemical Society* **2018**, *140*, 1496–1501.

[69] Wan, L. J.; Terashima, M.; Noda, H.; Osawa, M. Molecular orientation and ordered structure of benzenethiol adsorbed on gold(111). *Journal of Physical Chemistry B* **2000**, *104*, 3563–3569.

[70] Li, Z.; Han, B.; Meszaros, G.; Pobelov, I.; Wandlowski, T.; Błaszczyk, A.; Mayor, M. Two-dimensional assembly and local redox-activity of molecular hybrid structures in an electrochemical environment. *Faraday Discussions* **2006**, *131*, 121–143.

[71] Han, B.; Li, Z.; Wandlowski, T.; Błaszczyk, A.; Mayor, M. Potential-Induced Redox Switching in Viologen Self-Assembled Monolayers : An ATR - SEIRAS Approach. *Journal of Physical Chemistry C* **2007**, *111*, 13855–13863.

[72] Cai, W. B.; Wan, L. J.; Noda, H.; Hibino, Y.; Ataka, K.; Osawa, M. Orientational phase transition in a pyridine adlayer on gold(111) in aqueous solution studied by in situ infrared spectroscopy and scanning tunneling microscopy. *Langmuir* **1998**, *14*, 6992–6998.

[73] Quirk, A.; Unni, B.; Burgess, I. J. Surface Enhanced Infrared Studies of 4-Methoxypyridine Adsorption on Gold Film Electrodes. *Langmuir* **2016**, *32*, 2184–2191.

[74] Wandlowski, T.; Ataka, K.; Pronkin, S.; Diesing, D. Surface enhanced infrared spectroscopy - Au(1 1 1-20 nm)/sulphuric acid - New aspects and challenges. *Electrochimica Acta* **2004**, *49*, 1233–1247.

[75] Uchida, T.; Osawa, M.; Lipkowski, J. SEIRAS studies of water structure at the gold electrode surface in the presence of supported lipid bilayer Dedicated to Professor Kingo Itaya on the occasion of his 65th birthday and in recognition of his seminal contributions to electrochemistry. *Journal of Electroanalytical Chemistry* **2014**, *716*, 112–119.

[76] Quirk, A.; Lardner, M. J.; Tun, Z.; Burgess, I. J. Surface-Enhanced Infrared Spectroscopy and Neutron Reflectivity Studies of Ubiquinone in Hybrid Bilayer Membranes under Potential Control. *Langmuir* **2016**, *32*, 2225–2235.

[77] Ataka, K.; Stripp, S. T.; Heberle, J. Surface-enhanced infrared absorption spectroscopy (SEIRAS) to probe monolayers of membrane proteins. *Biochimica et Biophysica Acta - Biomembranes* **2013**, *1828*, 2283–2293.

[78] Ataka, K.; Giess, F.; Knoll, W.; Naumann, R.; Haber-Pohlmeier, S.; Richter, B.; Heberle, J. Oriented attachment and membrane reconstitution of his-tagged cytochrome c oxidase to a gold electrode: In situ monitoring by surface-enhanced infrared absorption spectroscopy. *Journal of the American Chemical Society* **2004**, *126*, 16199–16206.

[79] Ataka, K.; Heberle, J. Use of Surface Enhanced Infrared Absorption Spectroscopy (SEIRA) to Probe the Functionality of a Protein Monolayer. *Biopolymers* **2006**, *82*, 415–419.

[80] Kriegel, S.; Uchida, T.; Osawa, M.; Friedrich, T.; Hellwig, P. Biomimetic Environment to Study E. coli Complex I through Surface- Enhanced IR Absorption Spectroscopy. *Biochemistry* **2014**, *53*, 6340–6347.

[81] Busalmen, J. P.; Berna, A.; Feliu, J. M. Spectroelectrochemical examination of the interaction between bacterial cells and gold electrodes. *Langmuir* **2007**, *23*, 6459–6466.

[82] Han, B.; Li, Z.; Wandlowski, T. Adsorption and self-assembly of aromatic carboxylic acids on Au/electrolyte interfaces. *Analytical and Bioanalytical Chemistry* **2007**, *388*, 121–129.

[83] Armstrong, F. A.; Hill, H. A. O.; Walton, N. J. Direct Electrochemistry of Redox Proteins. *Accounts of Chemical Research* **1988**, 407–413.

[84] Armstrong, F. A.; Evans, R. M.; Hexter, S. V.; Murphy, B. J.; Roessler, M. M.; Wul, P. Guiding Principles of Hydrogenase Catalysis Instigated and Clarified by Protein Film Electrochemistry. *Accounts of Chemical Research* **2016**, 884–892.

[85] Megarity, C. F.; Esselborn, J.; Hexter, S. V.; Wittkamp, F.; Apfel, U.-p.; Happe, T.; Armstrong, F. A. Electrochemical Investigations of the Mechanism of Assembly of the Active-Site H - Cluster of [FeFe]-Hydrogenases. *Journal of the American Chemical Society* **2016**, 15227–15233.

[86] Ash, P. A.; Vincent, K. A. Spectroscopic analysis of immobilised redox enzymes under direct electrochemical control. *Chemistry Communications* **2012**, *48*, 1400–1409.

[87] Ash, P. A.; Reeve, H. A.; Quinson, J.; Hidalgo, R.; Zhu, T.; McPherson, I. J.; Chung, M.-W.; Healy, A. J.; Nayak, S.; Lonsdale, T. H.; Wehbe, K.; Kelley, C. S.; Frogley, M. D.; Cinque, G.; Vincent, K. A. Synchrotron-based Infrared Microanalysis of Biological Redox Processes under Electrochemical Control. *Analytical Chemistry* **2016**, *88*, 6666–6671.

[88] Ash, P. A.; Vincent, K. A. *Advances in Biochemical Engineering / Biotechnology*; Springer Berlin Heidelberg: Heidelberg, 2016; pp 1–36.

[89] Ash, P. A.; Carr, S. B.; Reeve, H. A.; Skorupskaitė, A.; Rowbotham, J. S.; Shutt, R.; Frogley, M. D.; Evans, R. M.; Cinque, G.; Armstrong, F. A.; Vincent, K. A. Generating single metalloprotein crystals in well-defined redox states: electrochemical control combined with infrared imaging of a NiFe hydrogenase crystal. *Chem. Commun.* **2017**, *53*, 5858–5861.

[90] Clarke, O. J.; Burgess, I. J. Electrodeposited Gold Nanodaggers on Conductive Metal Oxide Films Provide Substrates for Dual-Modality Surface Sensitive Vibrational Spectroscopy. *Journal of Physical Chemistry C* **2020**, *124*, 13356–13364.

[91] Shen, Y. R. Basic theory of surface sum-frequency generation. *Journal of Physical Chemistry C* **2012**, *116*, 15505–15509.

[92] Rey, N. G.; Dlott, D. D. *Journal of Electroanalytical Chemistry*; 2017; Vol. 800; pp 114–125.

[93] Ji, N.; Ostroverkhov, V.; Chen, C. Y.; Shen, Y. R. *Journal of the American Chemical Society*; 2007; Vol. 129; pp 10056–10057.

[94] Stiopkin, I. V.; Jayathilake, H. D.; Bordenyuk, A. N.; Benderskii, A. V. *Journal of the American Chemical Society*; 2008; Vol. 130; pp 2271–2275.

[95] Nihonyanagi, S.; Mondal, J. A.; Yamaguchi, S.; Tahara, T. *Annual Review of Physical Chemistry*; 2013; Vol. 64; pp 579–603.

[96] Yang, W.-C.; Hore, D. K. Determining the Orientation of Chemical Functional Groups on Metal Surfaces by a Combination of Homodyne and Heterodyne Nonlinear Vibrational Spectroscopy. *Journal of Physical Chemistry C* **2013**, 48–84.

[97] Hatta, A.; Ohshima, T.; Suëtaka, W. Observation of the enhanced infrared absorption of p-nitrobenzoate on Ag island films with an ATR technique. *Applied Physics A Solids and Surfaces* **1982**, *29*, 71–75.

[98] Ding, S. Y.; You, E. M.; Tian, Z. Q.; Moskovits, M. Electromagnetic theories of surface-enhanced Raman spectroscopy. *Chemical Society Reviews* **2017**, *46*, 4042–4076.

[99] Osawa, M.; Kuramitsu, M.; Hatta, A.; Suëtaka, W.; Seki, H. ELECTROMAGNETIC EFFECT IN ENHANCED INFRARED ABSORPTION OF ADSORBED MOLECULES ON THIN METAL FILMS. *Surface Science* **1986**, *175*, 787–793.

[100] Suzuki, Y.; Osawa, M.; Hatta, A.; Suëtaka, W. Mechanism of absorption enhancement in infrared ATR spectra observed in the Kretschmann configuration. *Applied Surface Science* **1988**, *33-34*, 875–881.

[101] Bruggeman, D. Berechnung verschiedener physikalischer Konstanten von heterogenen Substanzen. I. Dielektrizitätskonstanten und Leitfähigkeiten der Mischkörper aus isotropen Substanzen. *Annalen der Physik* **1935**, *416*, 636–664.

[102] Stoner, E. C. XCVII. The Demagnetizing Factors for Ellipsoids. *The London, Edinburgh, and Dublin Philosophical Magazine and Journal of Science* **1945**, *36*, 803–821.

[103] Osawa, M.; Yoshii, K.; Ataka, K.-i.; Yotsuyanagi, T. Real-Time Monitoring of Electrochemical Dynamics by Submillisecond Time-Resolved Surface-Enhanced Infrared Attenuated-Total-Reflection Spectroscopy. *Langmuir* **1994**, 640–642.

[104] Osawa, M.; Yoshii, K. In situ and real-time surface-enhanced infrared study of electrochemical reactions. *Applied Spectroscopy* **1997**, *51*, 512–518.

[105] Osawa, M. Dynamic Processes in Electrochemical Reactions Studied by Surface-Enhanced Infrared Absorption Spectroscopy (SEIRAS). 1997.

[106] Frey, H., Khan, H. R., Eds. *Handbook of Thin-Film Technology*; Springer: Berlin, 2015; p 380.

[107] Miyake, H.; Ye, S.; Osawa, M. Electroless deposition of gold thin films on silicon for surface-enhanced infrared spectroelectrochemistry. *Electrochemistry Communications* **2002**, *4*, 973–977.

[108] Kato, M.; Yazawa, Y.; Okinaka, Y. Electroless Gold Plating Bath Using Ascorbic Acid as Reducing Agent - Recent Improvements. *Hyoumengijutus* **1991**, *41*, 729.

[109] Magagnin, L.; Maboudian, R.; Carraro, C. Gold deposition by galvanic displacement on semiconductor surfaces: Effect of substrate on adhesion. *Journal of Physical Chemistry B* **2002**, *106*, 401–407.

[110] Garcia-Araez, N.; Rodriguez, P.; Bakker, H. J.; Koper, M. T. Effect of the surface structure of gold electrodes on the coadsorption of water and anions. *Journal of Physical Chemistry C* **2012**, *116*, 4786–4792.

[111] Delgado, J. M.; Orts, J.; Perez, J. M.; Rodes, A. Sputtered thin-film gold electrodes for in situ ATR-SEIRAS and SERS studies. *Journal of Electroanalytical Chemistry* **2008**, *617*, 130–140.

[112] Pronkin, S.; Wandlowski, T. Time-resolved in situ ATR-SEIRAS study of adsorption and 2D phase formation of uracil on gold electrodes. *Journal of Electroanalytical Chemistry* **2003**, *550-551*, 131–147.

[113] Pronkin, S.; Hara, M.; Wandlowski, T. Electrocatalytic properties of Au(111)-Pd quasi-single-crystal film electrodes as probed by ATR-SEIRAS. *Russian Journal of Electrochemistry* **2006**, *42*, 1177–1192.

[114] Weaver, C. Adhesion of Thin Films. *J Vac Sci Technol* **1974**, *12*, 18–25.

[115] Chapman, B. N. Thin-Film Adhesion. *J Vac Sci Technol* **1974**, *11*, 106–113.

[116] Cordill, M. J.; Bahr, D. F.; Moody, N. R.; Gerberich, W. W. Adhesion Measurement. *Adhesion Aspects of Thin Films, volume 2* **2005**, *4*, 177–177.

[117] Stuart, P. R. Some measurements of stress in thin films prepared by low pressure triode sputtering. *Vacuum* **1969**, *19*, 507–511.

[118] Chason, E.; Guduru, P. R. Tutorial: Understanding residual stress in polycrystalline thin films through real-time measurements and physical models. *Journal of Applied Physics* **2016**, *119*.

[119] Davey, W. P. Precision measurements of the lattice constants of twelve common metals. *Physical Review* **1925**, *25*, 753–761.

[120] Baker, J.; Douma, M.; Kotochigova, S. The 2018 CODATA Recommended Values of the Fundamental Physical Constants (Web Version 8.1). 2020.

[121] Koch, R. The intrinsic stress of polycrystalline and epitaxial thin metal films. *Journal of Physics: Condensed Matter* **1994**, *6*, 9519–9550.

[122] Vakilov, A. N.; Mamonova, M. V.; Prudnikov, V. V. Adhesion of metals and semiconductors analyzed by a dielectric formalism. *Physics of the Solid State* **1997**, *39*, 864–867.

[123] Landree, E.; Grozea, D.; Collazo-Davila, C.; Marks, L. UHV high-resolution electron microscopy and chemical analysis of room-temperature Au deposition on Si(001)-2×1. *Physical Review B - Condensed Matter and Materials Physics* **1997**, *55*, 7910–7916.

[124] Cros, A.; Muret, P. Properties of noble-metal/silicon junctions. *Materials Science Reports* **1992**, *8*.

[125] Yang, X. M.; Zhong, Z. W.; Diallo, E. M.; Wang, Z. H.; Yue, W. S. Silicon wafer wettability and aging behaviors: Impact on gold thin-film morphology. *Materials Science in Semiconductor Processing* **2014**, *26*, 25–32.

[126] Windischmann, H. Intrinsic stress in sputter-deposited thin films. *Crtitical Reviews in Solid State and Materials Sciences* **1992**, *17*, 547–596.

[127] Tabard-Cossa, V.; Godin, M.; Beaulieu, L. Y.; Grütter, P. A differential microcantilever-based system for measuring surface stress changes induced by electrochemical reactions. *Sensors and Actuators, B: Chemical* **2005**, *107*, 233–241.

[128] Smetanin, M.; Viswanath, R. N.; Kramer, D.; Beckmann, D.; Koch, T.; Kibler, L. A.; Kolb, D. M.; Weissmüller, J. Surface stress-charge response of a (111)-textured gold electrode under conditions of weak ion adsorption. *Langmuir* **2008**, *24*, 8561–8567.

[129] Danger, B. R.; Fan, D.; Vivek, J. P.; Burgess, I. J. Electrochemical studies of capping agent adsorption provide insight into the formation of anisotropic gold nanocrystals. *ACS Nano* **2012**, *6*, 11018–11026.

[130] Simon, S.; Olumorin, T. I.; Guo, B.; Burgess, I. J. Role of Au(I) intermediates in the electrochemical formation of highly anisotropic gold nanostructures with near-IR SERS applications. *Journal of Physical Chemistry C* **2016**, *120*, 26150–26158.

[131] Unni, B.; Simon, S.; Burgess, I. J. Electrochemical Investigations of 4-Methoxypyridine Adsorption on Au(111) Predict Its Suitability for Stabilizing Au Nanoparticles. *Langmuir* **2015**, *31*, 9882–9888.

[132] Spinner, E.; White, J. The Vibration Spectra of the Cations of Methoxypyridines. *Journal of the Chemical Society* **1962**, 3115–3118.

[133] Rosendahl, S. M.; Danger, B. R.; Vivek, J. P.; Burgess, I. J. Surface enhanced infrared absorption spectroscopy studies of DMAP adsorption on gold surfaces. *Langmuir : the ACS journal of surfaces and colloids* **2009**, *25*, 2241–2247.

[134] Burshtein, R. No Title. *Electrokhimiya* **1967**, *3*, 349.

[135] Angerstein-Kozlowska, H.; Conway, B. E.; Hamelin, A.; Stoicoviciu, L. Elementary steps of electrochemical oxidation of single-crystal planes of Au-I. Chemical basis of processes involving geometry of anions and the electrode surfaces. *Electrochimica Acta* **1986**, *31*, 1051–1061.

[136] Kaiser, W.; Keck, P.; Lange, C. Infrared Absorption and Oxygen Content in Silicon and Germanium. *Physical Review* **1956**, *101*, 1264–1268.

[137] Carr, G. L.; Reffner, J. A.; Williams, G. P. Performance of an infrared microspectrometer at the NSLS. *Review of Scientific Instruments* **1995**, *66*, 1490–1492.

[138] Ohta, N.; Nomura, K.; Yagi, I. Electrochemical modification of surface morphology of Au/Ti bilayer films deposited on a Si prism for in situ surface-enhanced infrared absorption (SEIRA) spectroscopy. *Langmuir* **2010**, *26*, 18097–18104.

[139] Holloway, P. H. Gold/Chromium Metallizations for Electronic Devices. *Solid State Technology* **1980**, *23*, 109–115.

[140] Schumacher, H.; Kuenzelmann, U.; Vasilev, B.; Eichhorn, K. J.; Bartha, J. W. Applications of microstructured silicon wafers as internal reflection elements in attenuated total reflection Fourier transform infrared spectroscopy. *Applied Spectroscopy* **2010**, *64*, 1022–1027.

[141] Kovacs, G. T.; Maluf, N. I.; Petersen, K. E. Bulk micromachining of silicon. *Proceedings of the IEEE* **1998**, *86*, 1536–1551.

[142] Koç, M.; Karabudak, E. History of Spectroscopy and Modern Micromachined Disposable Si ATR-IR. *Applied Spectroscopy Reviews* **2017**, *4928*, 0–0.

[143] Karabudak, E. Micromachined silicon attenuated total reflectance infrared spectroscopy: An emerging detection method in micro/nanofluidics. *Electrophoresis* **2014**, *35*, 236–244.

[144] Karabudak, E.; Mojet, B. L.; Schlautmann, S.; Mul, G.; Gardeniers, H. J. Attenuated total reflection-infrared nanofluidic chip with 71 nL detection volume for in situ spectroscopic analysis of chemical reaction intermediates. *Analytical Chemistry* **2012**, *84*, 3132–3137.

[145] Hersig-Marx, R.; Queeney, K. T.; Jackman, R. J.; Schmidt, M. A.; Jensen, K. F. Infrared spectroscopy for chemically specific sensing in silicon-based microreactors. *Analytical Chemistry* **2004**, *76*, 6476–6483.

[146] Queeney, K. T.; Fukidome, H.; Chaban, E. E.; Chabal, Y. J. In-Situ FTIR Studies of Reactions at the Silicon/Liquid Interface: Wet Chemical Etching of Ultrathin SiO2 on Si(100). *Journal of Physical Chemistry B* **2001**, *105*, 3903–3907.

[147] Karabudak, E.; Kas, R.; Ogieglo, W.; Rafieian, D.; Schlautmann, S.; Lammertink, R. G.; Gardeniers, H. J.; Mul, G. Disposable attenuated total reflection-infrared crystals from silicon wafer: A versatile approach to surface infrared spectroscopy. *Analytical Chemistry* **2013**, *85*, 33–38.

[148] Shao, M. H.; Liu, P.; Adzic, R. R. Superoxide anion is the intermediate in the oxygen reduction reaction on platinum electrodes. *Journal of the American Chemical Society* **2006**, *128*, 7408–7409.

[149] Xue, X. K.; Wang, J. Y.; Li, Q. X.; Yan, Y. G.; Liu, J. H.; Cai, W. B. Practically modified attenuated total reflection surface-enhanced IR absorption spectroscopy for high-quality frequency-extended detection of surface species at electrodes. *Analytical Chemistry* **2008**, *80*, 166–171.

[150] Otto, A. Excitation of nonradiative surface plasma waves in silver by the method of frustrated total reflection. *Zeitschrift für Physik* **1968**, *216*, 398–410.

[151] Medernach, J. W. Infrared Characterization of Device-Quality Silicon. *Handbook of Vibrational Spectroscopy* **2006**,

[152] Karabudak, E.; Yüce, E.; Schlautmann, S.; Hansen, O.; Mul, G.; Gardeniers, H. On the pathway of photoexcited electrons: Probing photon-to-electron and photon-to-phonon conversions in silicon by ATR-IR. *Physical Chemistry Chemical Physics* **2012**, *14*, 10882–10885.

[153] Pajot, B.; Stein, H. J.; Cales, B.; Naud, C. Quantitative Spectroscopy of Interstitial Oxygen in Silicon. *Journal of The Electrochemical Society* **1985**, *132*, 3034–3037.

[154] Susarrey-Arce, A.; Tiggelaar, R. M.; Sanders, R. G.; Geerdink, B.; Lefferts, L.; Gardeniers, J. G.; Van Houselt, A. Temperature dependence of the 1727 cm-1 interstitial oxygen absorption band studied by attenuated total internal reflection infrared spectroscopy in a newly developed microreactor. *Journal of Physical Chemistry C* **2013**, *117*, 21936–21942.

[155] Zhumaev, U. E.; Lai, A. S.; Pobelov, I. V.; Kuzume, A.; Rudnev, A. V.; Wandlowski, T. Quantifying perchlorate adsorption on Au(1 1 1) electrodes. *Electrochimica Acta* **2014**, *146*, 112–118.

[156] Bertie, J. E.; Lan, Z. Infrared intensities of liquids XX: The intensity of the OH stretching band of liquid water revisited, and the best current values of the optical constants of H2O(1) at 25 °C between 15,000 and 1 cm-1. *Applied Spectroscopy* **1996**, *50*, 1047–1057.

[157] Maréchal, Y. The molecular structure of liquid water delivered by absorption spectroscopy in the whole IR region completed with thermodynamics data. *Journal of Molecular Structure* **2011**, *1004*, 146–155.

[158] Bergonzi, I.; Mercury, L.; Brubach, J. B.; Roy, P. Gibbs free energy of liquid water derived from infrared measurements. *Physical Chemistry Chemical Physics* **2014**, *16*, 24830–24840.

[159] Harrick, N. J.; Milosevic, M.; Berets, S. L. Advances in Optical Spectroscopy: The Ultra-Small Sample Analyzer. *Applied Spectroscopy* **1991**, *45*, 944–948.

[160] Lewis, L.; Sommer, A. J. Attenuated total internal reflection microspectroscopy of isolated particles: an alternative approach to current methods. *Applied Spectroscopy* **1999**, *53*, 375–380.

[161] Lewis, L. L.; Sommer, A. J. Attenuated total internal reflection infrared mapping microspectroscopy of soft materials. *Applied Spectroscopy* **2000**, *54*, 324–330.

[162] German, M. J.; Hammiche, A.; Ragavan, N.; Tobin, M. J.; Cooper, L. J.; Matanhelia, S. S.; Hindley, A. C.; Nicholson, C. M.; Fullwood, N. J.; Pollock, H. M.; Martin, F. L. Infrared spectroscopy with multivariate analysis potentially facilitates the segregation of different types of prostate cell. *Biophysical Journal* **2006**, *90*, 3783–3795.

[163] Harrison, J. P.; Ojeda, J. J.; Romero-González, M. E. The applicability of reflectance micro-Fourier-transform infrared spectroscopy for the detection of synthetic microplastics in marine sediments. *Science of the Total Environment* **2012**, *416*, 455–463.

[164] Rahman, J.; Sarkar, T. K. Deconvolution and Total Least Squares in Finding the Impulse Response of an Electromagnetic System from Measured Data. *IEEE Transactions on Antennas and Propagation* **1995**, *43*, 416–421.

[165] Tan, T. L.; Wong, D.; Lee, P.; Rawat, R. S.; Patran, A. Study of a chemically amplified resist for X-ray lithography by fourier transform infrared spectroscopy. *Applied Spectroscopy* **2004**, *58*, 1288–1294.

[166] Whitesides, G. M. The origins and the future of microfluidics. *Nature* **2006**, *442*.

[167] Whitesides, G. Microfluidics in Late Adolescence. **2018**,

[168] Bruus, H. Theoretical microfluidics. *Choice Reviews Online* **2008**, *45*, 45–5602–45–5602.

[169] Elvira, K. S.; Casadevall, X.; Wootton, R. C. R.; Andrew, J. The past, present and potential for microfluidic reactor technology in chemical synthesis. *Nature Chemistry* **2013**, *5*, 905–915.

[170] Mitri, E.; Pozzato, A.; Coceano, G.; Cojoc, D.; Vaccari, L.; Tormen, M.; Grenci, G. Highly IR-transparent microfluidic chip with surface-modified BaF 2 optical windows for Infrared Microspectroscopy of living cells. *Microelectronic Engineering* **2013**, *107*, 6–9.

[171] Silverwood, I. P.; Al-Rifai, N.; Cao, E.; Nelson, D. J.; Chutia, A.; Wells, P. P.; Nolan, S. P.; Frogley, M. D.; Cinque, G.; Gavriilidis, A.; Catlow, C. R. A. Towards microfluidic reactors for in situ synchrotron infrared studies. *Review of Scientific Instruments* **2016**, *87*.

[172] Hersig-Marx, R.; Queeney, K. T.; Jackman, R. J.; Schmidt, M. A.; Jensen, K. F. Infrared spectroscopy for chemically specific sensing in silicon-based microreactors. *Analytical Chemistry* **2004**, *76*, 6476–6483.

[173] Moore, J. S.; Jensen, K. F. Batch kinetics in flow: Online IR analysis and continuous control. *Angewandte Chemie - International Edition* **2014**, *53*, 470–473.

[174] Sergei G. Kazarian,; Chan, K. L. A. Micro- and Macro- Attenuated Total Reflection Fourier Transform Infrared Spectroscopic Imaging. *Applied Spectroscopy* **2009**, *64*, 135A–152A.

[175] Chan, K. L. A.; Gulati, S.; Edel, J. B.; Mello, J. D.; Kazarian, S. G. Chemical imaging of microfluidic flows using ATR-FTIR spectroscopy. *Lab on a Chip* **2009**, *9*, 2909–2913.

[176] Andrew Chan, K. L.; Kazarian, S. G. Attenuated total reflection Fourier-transform infrared (ATR-FTIR) imaging of tissues and live cells. *Chemical Society Reviews* **2016**, *45*, 1850–1864.

[177] Chan, K. L. A.; Govada, L.; Bill, R. M.; Chayen, N. E.; Kazarian, G. ATR-FTIR Spectroscopic Imaging of Protein Crystallization. *Analytical Chemistry* **2009**, *81*, 3769.

[178] Boulet-Audet, M.; Byrne, B.; Kazarian, S. G. High-throughput thermal stability analysis of a monoclonal antibody by attenuated total reflection FT-IR spectroscopic imaging. *Analytical Chemistry* **2014**, *86*, 9786–9793.

[179] Pousti, M.; Joly, M.; Roberge, P.; Amirdehi, M. A.; Bégin-Drolet, A.; Greener, J. Linear Scanning ATR-FTIR for Chemical Mapping and High-Throughput Studies of Pseudomonas sp. Biofilms in Microfluidic Channels. *Analytical Chemistry* **2018**, *90*, 14475–14483.

[180] Chan, K. L.; Kazarian, S. G. New opportunities in micro- and macro-attenuated total reflection infrared spectroscopic imaging: Spatial resolution and sampling versatility. *Applied Spectroscopy* **2003**, *57*, 381–389.

[181] Andvaag, I. R.; Morhart, T. A.; Clarke, O. J. R.; Burgess, I. J. Hybrid Gold–Conductive Metal Oxide Films for Attenuated Total Reflectance Surface Enhanced Infrared Absorption Spectroscopy. *ACS Applied Nano Materials* **2019**, *2*, 1274–1284.

[182] Tu, K. Developing Time-Resolved Synchrotron Infrared Spectroscopy for Spectroelectrochemical Measurements. Ph.D. thesis, University of Saskatchewan, 2020.

[183] Aoki, K. Theory of Ultramicroelectrodes. *Electroanalysis* **1993**, *5*, 627–639.

[184] Bjerke, A. E.; Griffiths, P. R.; Theiss, W. Surface-enhanced infrared absorption of CO on platinized platinum. *Analytical Chemistry* **1999**, *71*, 1967–1974.

[185] Simon, S. On the role of 4-methoxypyridine in the electrochemical formation of plasmonic gold nanoparticles. Ph.D. thesis, University of Saskatchewan, 2020.

[186] Zheng, M. S.; Sun, S. G. In situ FTIR spectroscopic studies of CO adsorption on electrodes with nanometer-scale thin films of ruthenium in sulfuric acid solutions. *Journal of Electroanalytical Chemistry* **2001**, *500*, 223–232.

[187] Pecharromán, C.; Cuesta, A.; Gutiérrez, C. Comments on the paper by M.-S. Zheng and S.-G. Sun entitled 'In situ FTIR spectroscopic studies of CO adsorption on electrodes with nanometer-scale thin films of ruthenium in sulfuric acid solutions' [J. Electroanal. Chem. 500 (2001) 223]. *Journal of Electroanalytical Chemistry* **2002**, *529*, 145–154.

[188] Pecharromán, C.; Cuesta, A.; Gutiérrez, C. Calculation of adsorption-induced differential external reflectance infrared spectra of particulate metals deposited on a substrate. *Journal of Electroanalytical Chemistry* **2004**, *563*, 91–109.

[189] Osawa, M.; Ikeda, M. Surface-enhanced infrared absorption of p-nitrobenzoic acid deposited on silver island films: Contributions of electromagnetic and chemical mechanisms. *Journal of Physical Chemistry* **1991**, *95*, 9914–9919.

[190] Frank, H. S.; Wen, W. Y. Ion-solvent interaction. Structural aspects of ion-solvent interaction in aqueous solutions: A suggested picture of water structure. *Discussions of the Faraday Society* **1957**, *24*, 133–140.

[191] Reiners, G.; Lorenz, W.; Hertz, H. Tracer Diffusion Coefficients in Aqueous Electrolyte Solutions of Various Structure Forming and Breaking Ions. *Berichte Der Bunsengesellschaft Für Physikalische Chemie* **1978**, *82*, 738–744.

[192] Bewick, A.; Kunimatsu, K.; Pons, B. S.; Russell, J. W. Electrochemically modulated infrared spectroscopy (EMIRS). Experimental details. *Journal of Electroanalytical Chemistry* **1984**, *160*, 47–61.

[193] Manufacturing, J. S. Jackfish SEC Manufacturing. 2021; `https://jackfishsec.com/`.

[194] Faist, J.; Villares, G.; Scalari, G.; Rösch, M.; Bonzon, C.; Hugi, A.; Beck, M. *Nanophotonics*; 2016; Vol. 5; pp 272–291.

[195] Vitiello, M. S.; Scalari, G.; Williams, B.; De Natale, P. *Optics Express*; 2015; Vol. 23; p 5167.

[196] Villares, G.; Hugi, A.; Blaser, S.; Faist, J. Dual-comb spectroscopy based on quantum-cascade-laser frequency combs. *Nature Communications* **2014**, *5*, 1–3.

[197] Klocke, J. L.; Mangold, M.; Allmendinger, P.; Hugi, A.; Geiser, M.; Jouy, P.; Faist, J.; Kottke, T. Single-Shot Sub-microsecond Mid-infrared Spectroscopy on Protein Reactions with Quantum Cascade Laser Frequency Combs. *Analytical Chemistry* **2018**, *90*, 10494–10500.

[198] Fawcett, W. R.; Foss, C. A. Solvent effects on simple electron transfer reactions. A comparison of results in Debye and non-Debye solvents. *Journal of Electroanalytical Chemistry* **1991**, *306*, 71–85.

[199] Weaver, M. J.; Gennett, T. Influence of solvent reorientation dynamics upon the kinetics of some electron-exchange reactions. *Chemical Physics Letters* **1985**, *113*, 213–218.

[200] Gennett, T.; Milner, D. F.; Weaver, M. J. Role of solvent reorganization dynamics in electron-transfer processes. Theory-experiment comparisons for electrochemical and homogeneous electron exchange involving metallocene redox couples. *Journal of Physical Chemistry* **1985**, *89*, 2787–2794.

[201] Weaver, M. J. Dynamical Solvent Effects on Activated Electron-Transfer Reactions: Principles, Pitfalls, and Progress. *Chemical Reviews* **1992**, *92*, 463–480.

[202] Darlington, A. M.; Jarisz, T. A.; Dewalt-Kerian, E. L.; Roy, S.; Kim, S.; Azam, M. S.; Hore, D. K.; Gibbs, J. M. *Journal of Physical Chemistry C*; 2017; Vol. 121; pp 20229–20241.

[203] Sartin, M. M.; Sung, W.; Nihonyanagi, S.; Tahara, T. *Journal of Chemical Physics*; 2018; Vol. 149; pp 48–84.

[204] Nihonyanagi, S.; Yamaguchi, S.; Tahara, T. *Chemical Reviews*; 2017; Vol. 117; pp 10665–10693.

[205] Yang, W. C.; Hore, D. K. Determining the Orientation of Chemical Functional Groups on Metal Surfaces by a Combination of Homodyne and Heterodyne Nonlinear Vibrational Spectroscopy. *Journal of Physical Chemistry C* **2017**, *121*, 28043–28050.

[206] Tong, Y.; Kampfrath, T.; Campen, R. K. Experimentally probing the libration of interfacial water: The rotational potential of water is stiffer at the air/water interface than in bulk liquid. *Physical Chemistry Chemical Physics* **2016**, *18*, 18424–18430.

[207] Epstein, I. R.; Pojman, J. A.; Steinbock, O. *Chaos*; 2006; Vol. 16; pp 48–84.

[208] Varela, H.; Beta, C.; Bonnefont, A.; Krischer, K. Transitions to electrochemical turbulence. *Physical Review Letters* **2005**, *94*, 1–4.

[209] Heinen, M.; Chen, Y. X.; Jusys, Z.; Behm, R. J. In situ ATR-FTIRS coupled with on-line DEMS under controlled mass transport conditions-A novel tool for electrocatalytic reaction studies. *Electrochimica Acta* **2007**, *52*, 5634–5643.

[210] Morschi, R.; Bolten, J.; Bonnefont, A.; Krischer, K. Pattern formation during CO electrooxidation on thin Pt films studied with spatially resolved infrared absorption spectroscopy. *Journal of Physical Chemistry C* **2008**, *112*, 9548–9551.

[211] Atobe, M. Organic electrosynthesis in flow microreactor. *Current Opinion in Electrochemistry* **2017**, *2*, 1–6.

[212] Song, H.; Chen, D. L.; Ismagilov, R. F. Reactions in droplets in microfluidic channels. *Angewandte Chemie - International Edition* **2006**, *45*, 7336–7356.

[213] Taghavi-Moghadam, S.; Kleemann, A.; Golbig, K. G. Microreaction technology as a novel approach to drug design, process development and reliability. *Organic Process Research and Development* **2001**, *5*, 652–658.

[214] Hartman, R. L.; McMullen, J. P.; Jensen, K. F. Deciding whether to go with the flow: Evaluating the merits of flow reactors for synthesis. *Angewandte Chemie - International Edition* **2011**, *50*, 7502–7519.

[215] Nichols, K. P.; Azoz, S.; Gardeniers, H. J. Enzyme kinetics by directly imaging a porous silicon microfluidic reactor using desorption/ionization on silicon mass spectrometry. *Analytical Chemistry* **2008**, *80*, 8314–8319.

[216] Ratner, D. M.; Murphy, E. R.; Jhunjhunwala, M.; Snyder, D. A.; Jensen, K. F.; Seeberger, P. H. Microreactor-based reaction optimization in organic chemistry - Glycosylation as a challenge. *Chemical Communications* **2005**, 578–580.

[217] Pfeiffer, S. A.; Rudisch, B. M.; Glaeser, P.; Spanka, M.; Nitschke, F.; Robitzki, A. A.; Schneider, C.; Nagl, S.; Belder, D. Continuous purification of reaction products by micro free-flow electrophoresis enabled by large area deep-UV fluorescence imaging. *Analytical and Bioanalytical Chemistry* **2018**, *410*, 853–862.

[218] Sui, X.; Zhou, Y.; Zhang, F.; Chen, J.; Zhu, Z.; Yu, X. Y. Deciphering the aqueous chemistry of glyoxal oxidation with hydrogen peroxide using molecular imaging. *Physical Chemistry Chemical Physics* **2017**, *19*, 20357–20366.

[219] Schafer, D.; Squier, J. A.; Van Maarseveen, J.; Bonn, D.; Bonn, M.; Müller, M. In situ quantitative measurement of concentration profiles in a microreactor with submicron resolution using multiplex CARS microscopy. *Journal of the American Chemical Society* **2008**, *130*, 11592–11593.

[220] Hecht, E. *Optics*, 5th ed.; Pearson, 2015; p 720.

[221] Burka, E. M.; Curbelo, R. Imaging ATR Spectrometer. 2000.

[222] Sommer, A. J.; Tisinger, L. G.; Marcott, C.; Story, G. M. Attenuated total internal reflection infrared mapping microspectroscopy using an imaging microscope. *Applied Spectroscopy* **2001**, *55*, 252–256.

[223] Sergei G. Kazarian,; Chan, K. L. A. Micro- and Macro- Attenuated Total Reflection Fourier Transform Infrared Spectroscopic Imaging. *Applied Spectroscopy* **2009**, *64*, 135A–152A.

[224] Mansfield, S. M.; Kino, G. S. Solid immersion microscope. *Applied Physics Letters* **1990**, *57*, 2615–2616.

[225] Richards, B.; Wolf, E. Electromagnetic diffraction in optical systems, II. Structure of the image field in an aplanatic system. *Proceedings of the Royal Society of London. Series A. Mathematical and Physical Sciences* **1959**, *253*, 358–379.

[226] Lang, M.; Aspnes, E.; Milster, T. D. Geometrical analysis of third-order aberrations for a solid immersion lens. *Optics Express* **2008**, *16*, 20008.

[227] Chen, R.; Agarwal, K.; Zhong, Y.; Sheppard, C. J. R.; Phang, J. C. H.; Chen, X. Complete modeling of subsurface microscopy system based on aplanatic solid immersion lens. *Journal of the Optical Society of America A* **2012**, *29*, 2350.

[228] Chen, R.; Agarwal, K.; Sheppard, C. J. R.; Phang, J. C. H.; Chen, X. A complete and computationally efficient numerical model of aplanatic solid immersion lens scanning microscope. *Optics Express* **2013**, *21*, 14316.

[229] Hu, L.; Chen, R.; Agarwal, K.; Sheppard, C. J. R.; Phang, J. C. H.; Chen, X. Dyadic Green's function for aplanatic solid immersion lens based sub-surface microscopy. *Optics Express* **2011**, *19*, 19280.

[230] Ramsay, E.; Serrels, K. A.; Thomson, M. J.; Waddie, A. J.; Warburton, R. J.; Taghizadeh, M. R.; Reid, D. T. Three-dimensional nanometric sub-surface imaging of a silicon flip-chip using the two-photon optical beam induced current method. *Microelectronics Reliability* **2007**, *47*, 1534–1538.

[231] Ramsay, E.; Serrels, K. A.; Thomson, M. J.; Waddie, A. J.; Taghizadeh, M. R.; Warburton, R. J.; Reid, D. T. Three-dimensional nanoscale subsurface optical imaging of silicon circuits. *Applied Physics Letters* **2007**, *90*, 1–4.

[232] Serrels, K. A.; Ramsay, E.; Dalgarno, P. A.; Gerardot, B. D.; O'Connor, J. A.; Hadfield, R. H.; Warburton, R. J.; Reid, D. T. Solid immersion lens applications for nanophotonic devices. *Journal of Nanophotonics* **2008**, *2*, 021854.

[233] Chan, K. L.; Kazarian, S. G. Attenuated total reflection-fourier transform infrared imaging of large areas using inverted prism crystals and combining imaging and mapping. *Applied Spectroscopy* **2008**, *62*, 1095–1101.

Appendix A

Magnification in Macro- and Micro-ATR Experiments

A.1 Introduction

The experimental results presented in the main body of the thesis reveal situations where the higher refractive index of the IRE provides additional magnification (Chapter 3), yet elsewhere this is not the case (most obviously in Chapter 6). This is explained in the text on the basis of collimated versus focusing light, but it is important to note that this was not obvious at the time and therefore these results were highly surprising when they were collected. The literature seemed to indicate that magnification should be uniformly improved in a micro-ATR geometry, so much effort was expended on understanding whether the results shown in Chapter 6 were legitimate.

In this Appendix, I show in greater detail why the results in this thesis are consistent with the literature. I first review definitions of magnification, numerical aperture, and resolution, the former two using geometric optics. With reference to the literature on solid immersion lenses, I discuss the optics of Micro- and Macro-ATR and the resulting effect on magnification in each case. Finally, I show that the results of the thesis can be conclusively explained with geometric ray-tracing and are fully consistent with the literature. The key result is that magnification is provided by lens geometry and not by higher refractive index *per se*.

A.2 Definitions

We can define *magnification* as follows. Consider an optical system where an object of height x_{object} is placed at the object plane. The object is then imaged at the image plane (usually the detector/camera sensor in a microscopy experiment) and the image has height x_{image}. Then, we define magnification as the ratio of the two heights, $M = x_{image}/x_{object}$.

Numerical Aperture, NA, is a dimensionless quantity which characterizes the range of angles over which an optical system can collect light.[220] For a microscope objective such as that shown in Figure A.1, NA is defined as $\mathrm{NA} = n \sin\theta$. Increasing the collection angle θ or increasing the refractive index of the medium improves numerical aperture.

Numerical aperture is related to *spatial resolution* in the following way. There are several resolution criteria which are used in the literature on Micro- and Macro-ATR, including the Abbe, Rayleigh, and Sparrow criteria. The differences are fairly subtle, so for this discussion it is sufficient to use the Abbe criterion which is applicable to microscopy and is relatively common. For light of radiation λ focused through a lens of numerical aperture NA, the Abbe diffraction criteria states that minimum distance at which two separate points can be resolved is $d == \frac{\lambda}{2NA}$. The consequence is that spatial resolution improves with increasing numerical aperture and decreasing probe wavelength.

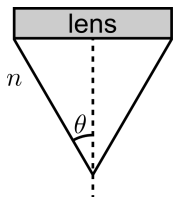

Figure A.1: Numerical aperture. Radiation with wavelenght λ is focused in a cone characterized by half-angle θ in a medium of refractive index n.

A.3 Optical Geometries in Micro- and Macro-ATR

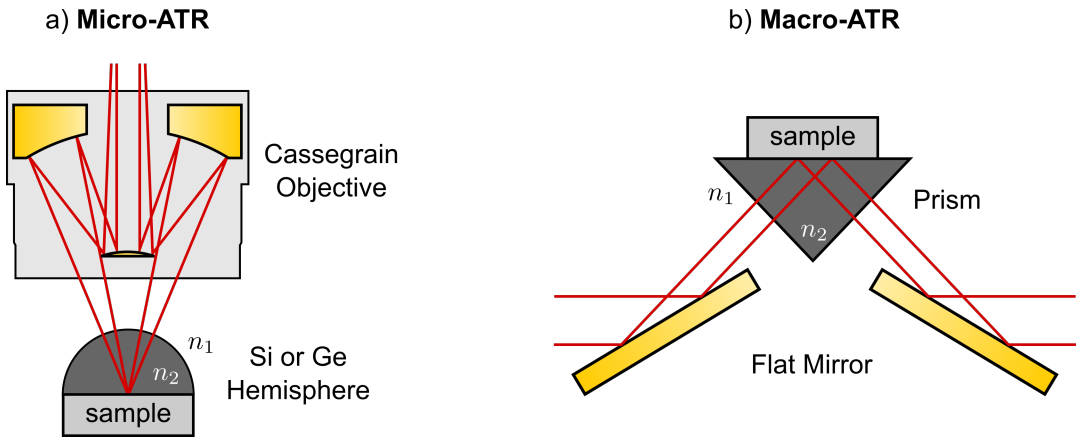

Figure A.2: ATR imaging geometries. a) Micro-ATR uses a hemispherical IRE in combination with a focusing objective to image a small area. b) Macro-ATR uses a prism and flat mirrors to interrogate a large area with a collimated beam.

There are two main optical geometries used in ATR imaging work which are depicted in Figure A.2. The two methods, *micro-* and *macro-ATR*, are so named based on their relative fields of view, with micro-ATR offering a smaller FOV than macro-ATR.

A.3.1 Micro-ATR

Micro-ATR is usually implemented in the configuration shown in Fig. A.2a, where a hemispherical IRE is placed at focus of a microscope objective operating in reflection mode.[221] The hemisphere has a higher refractive index n_2 than the surrounding medium (usually air), n_1. An immediate consequence of the difference in refractive index is that spatial resolution increases. The maximum achievable spatial resolution is given by the Rayleigh criterion,[222,223] where the minimum resolvable distance d is related to free-space wavelength λ by

$$d = \frac{\lambda}{2n\sin\theta} = \frac{\lambda}{2NA}$$

where the denominator has been rewritten using the definition of numerical aperture $NA = n\sin\theta$. Inspecting the Abbe criterion reveals that the improvement in resolution imparted by the Micro-ATR geometry is a direct consequence of the differing refractive indices of the IRE and air. Focusing the beam in e.g. Si ($n_{Si} = 3.4$) imparts a 3.4-fold improvement in resolution over air ($n_{air} = 1$).

The additional magnification provided by the micro-ATR geometry is less obvious. Although it is often stated in the literature that magnification is improved by a factor equal to n_{IRE}, this is not obvious from common depictions of the technique such as that shown in Figure A.2a. Furthermore, at least in the infrared literature a detailed description of the physical origin is rarely given. Experimental evidence, however, is conclusive: by comparing a feature of well-known size to the image obtained on an FPA detector with known pixel sizes, Sommer *et al.* have shown that working in this geometry imparts an additional magnification factor equal to n_{IRE}.[222]

A deeper description of the optics can be found in the literature on solid immersion lenses. The solid-immersion lens (SIL) was invented in 1990 by Mansfield and Kino[224] and was eventually extended to infrared imaging in 1999 by Burka and Paul of BioRad Laboratories.[221] Solid immersion lenses take advantage of an optical feature of a spherical lens, namely that it behaves as an aplanatic system. By definition, an aplanatic system has zero coma and spherical aberration, and Richards and Wolf showed in 1959 with rigorous electromagnetic theory that this allows imaging at very high angular aperture θ (i.e. high NA).[225] Furthermore, they showed that there are two so-called aplanatic points in a spherical lens: one precisely

at its origin (center), and another displaced some distance beyond the origin. Light focused at either of these two aplanatic points will be free of coma and spherical aberration, with the consequence that either hemispherical lenses or superhemispherical lenses can be used. Although superhemispherical lenses are more commonly used in the literature for their more favourable resolution and magnification characteristics, the discussion here will focus on hemispherical lenses in order to facilitate comparison to results shown in Chapter 3.

Beginning with the rigorous developments of Richards and Wolf, optical descriptions of hemispherical lenses have been provided using paraxial (i.e. geometric)[226] or electromagnetic theories.[227–229] For this discussion, I show in Fig. A.3 a geometric ray-tracing simulation (Optgeo) to graphically explain the magnification factor of micro-ATR.

Fig. A.3a shows a simple two-dimensional model of an infrared microscope, with some liberties taken in order to simplify the problem for presentation. The layout of the simulation is as follows: the source plane is marked at the top, followed by thin lens $L1$ ($f = 25$ mm, $DIA = 200$ mm) and beam steering mirror $M1$ to direct the beam(s) toward the sample. (More will be said about the two beams below.) The Schwarzchild objective lens is modelled with a thin lens $L2$ ($f = 25$ mm, $DIA = 625$ mm, $NA = 0.4$). A 25 mm diameter hemisphere ($n = 3.4$) is placed with its origin (point O in the figure) at the focus of $L2$. Light passes through one side of the hemisphere to a focus, is totally internally reflected, and is collected by the $L2$ as it exits the crystal. The beam is collimated as it leaves $L2$, and finally, a lens $L3$ (same parameters as $L2$) focuses it on the detector.

In order to graphically depict the crystal's focusing effect and its consequence on the system magnification, two beampaths (red and blue) are drawn through the system. At the source, two point sources are placed, one (red beam) at the center of the source i.e. on the optical axis, and another (blue) off-axis by 1.5 mm. (The red points exactly at the focal point of $L1$.) This is a simplified but highly instructive way to model the finite-sized globar source. In a real globar, each of these points on the source emit light isotropically, but in this figure only rays which are captured by the left half of $L1$ are shown for simplicity. Comparing the paths traced out by the red and blue beam paths reveals an important detail. Because the red source is placed at the focus of $L1$ (on-axis) while the blue source is off-axis, the two beam paths enter and leave $L1$ at slightly different angles. This grows more apparent as the beams travel downstream toward $L2$, to the point that when they impinge on the hemisphere it is clear that the blue beampath is significantly translated with respect to the red beam.

The red path (the on-axis radiation) is essentially identical to the path shown in Fig. A.2, and it is this beampath which is commonly depicted in simple figures of micro-ATR. Because the hemisphere origin is placed at the focus of $L2$, each red ray impinges on the crystal surface at normal incidence and enters unrefracted, coming to a focus at the origin of the hemisphere. Those rays are totally internally reflected, leave the crystal (again, unrefracted) and ultimately are focused at the center of the detector. In contrast, the off-axis radiation (blue), which is displaced relative to the red path, enters the crystal at angles slightly off of normal incidence, Fig. A.3b. Without the hemisphere in place, the rays would follow the blue dotted path, focusing at a spot displaced laterally from the focus of $L2$ by 1.5 mm. However, upon entering the hemisphere the beam is refracted and follows the blue solid path. Surface normals are drawn as black dashed lines, and it is clear that despite entering the crystal a few degrees off-normal the high refractive index of the hemisphere acts to "pull" them toward the origin of the crystal. This has been called the "optical lever" effect by Ramsay *et al.*[230–232] and forms the basis of the hemisphere's magnification.

As the blue off-axis rays leave the crystal, they are again refracted and are ultimately focused at the detector. Comparing the differing focal positions of the two beams at sample and detector, Fig. A.3c, demonstrates the magnification imparted by the hemisphere. The top panel of Fig. A.3c places an object (magenta arrow) in the focal plane of the hemisphere, with the red on-axis beam focusing at its tail and the blue off-axis beam focusing at its head. The bottom panel shows that the image of the object is now larger by a factor of $n_{Si} = 3.4$. In summary, due to refraction off-axis beams are mapped to a smaller area inside the high refractive index crystal than outside, and this is the basis for image magnification.

A.3.2 Macro-ATR

In contrast to Micro-ATR, Macro-ATR is frequently implemented in work which requires lower spatial resolution or, equivalently, wider field of view. While there is generally an improvement in spatial resolution

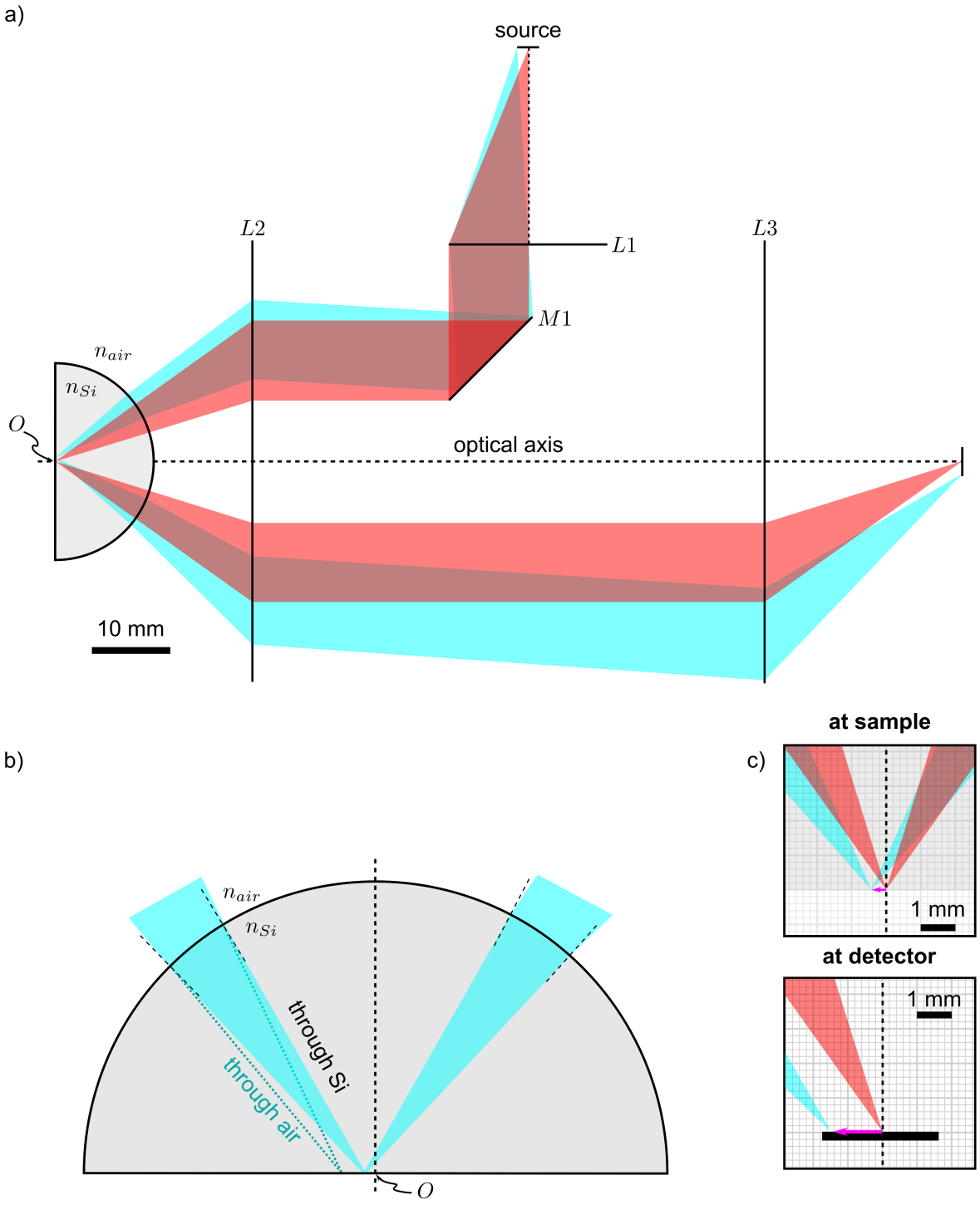

Figure A.3: Geometric ray-tracing to visualize magnification in micro-ATR. a) Simplified IR microscope showing two beampaths from points on the source. The red path travles from the focal point of lens $L1$ (on-axis) while the blue path propagates from a point 1.5 mm to the left (off-axis). b) Expanded view of the hemisphere's effect on the off-axis beam. The blue beam in air would follow the dotted path, but due to refraction the beam follows the solid path through the hemisphere. Surface normals are drawn as black dashed lines. c) Graphical depiction of magnification. Due to the high refractive index's effect on the two beampaths, an imaged object (magenta arrow) at sample (top image) is mapped to a larger image at the detector (bottom). The magnification factor is equal to n_{Si} = 3.4.

imparted by the increased refractive index, the collection angle for Macro-ATR systems is generally very low, so overall spatial resolution is poorer than for Micro-ATR. The image shown in Figure A.2b depicts a collimated beam incident on a prism with no additional magnification, but it is more common to use a focused i.e. converging beam such as in combined imaging and mapping work by Kazarian.[233] In either case, the prism geometry provides no additional magnification to the image, although we will see that there is compression of the image along one axis.

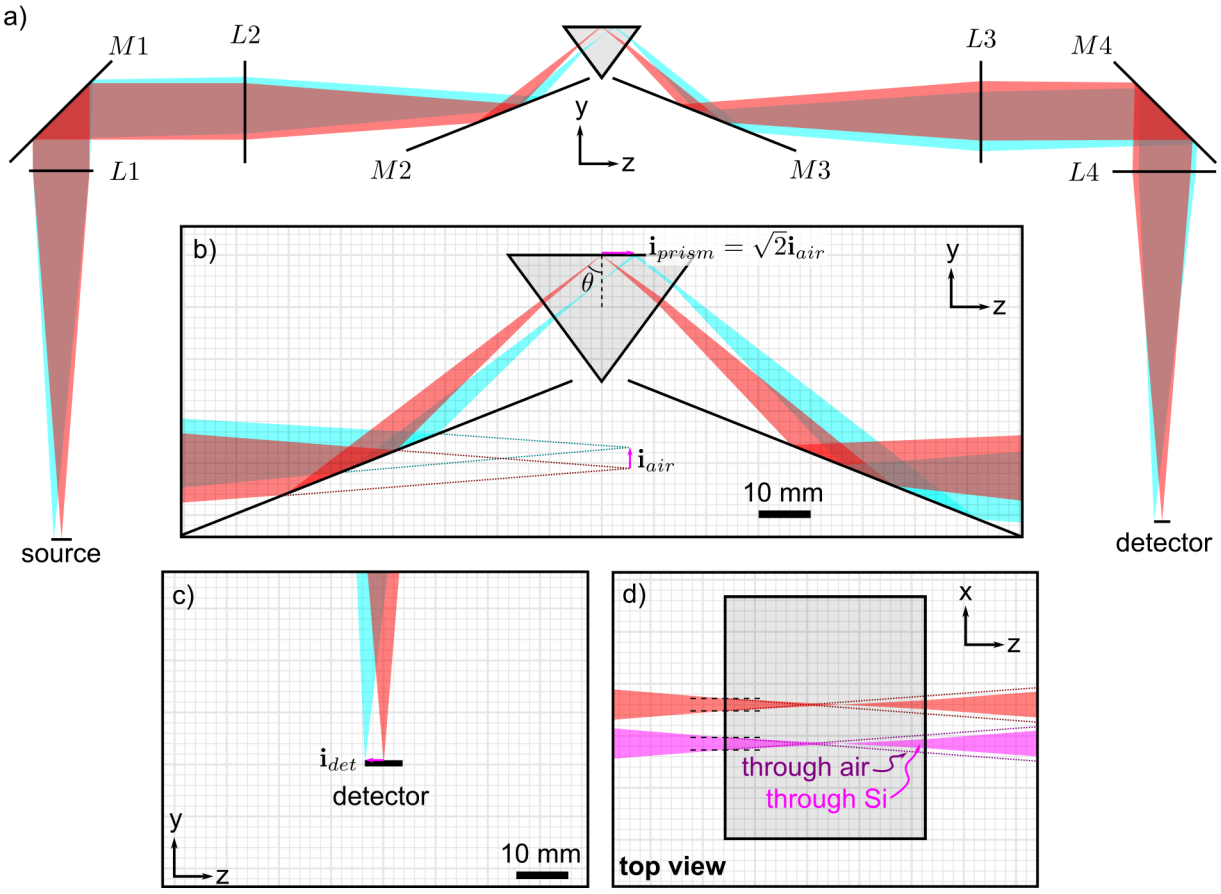

Figure A.4: Geometric ray-tracing to visualize magnification in macro-ATR.

Figure A.4a shows a two-dimensional model of typical optics which are used in Macro-ATR. As in Figure A.3a, the source is depicted with two beampaths, red on-axis radiation and blue off-axis radiation. Light is collected by $L1$ ($f = 180$ mm, $DIA = 50$ mm), redirected by beam-steering mirror $M1$, then focused by lens $L2$ which has the same properties as $L1$. Two flat mirrors deflect the beam onto IRE and collect the internally reflected beam ($M2$ and $M3$, respectively). A Si prism ($n = 3.4$, height = 25 mm) is placed in the beam path. The right-hand side of the optics is symmetric to the left-hand side, and ultimately focuses the two beams to points on the detector.

Figure A.4b depicts the effect of the IRE. The dotted lines show the focal points of the two beampaths in air without $M2$ and $M3$ in place and thus the height of the image formed, $\mathbf{i}_{air}$. (Because the focal lengths of $L1$ and $L2$ are identical, the image is the same size as that of the source object i.e. magnification is unity. Note that the source object is not shown.) Because light is incident on the principal reflecting plane of the prism at $\theta = 45^{\circ}$, $\mathbf{i}_{air}$ is projected longitudinally on the crystal, resulting in an elongation of the image such that $\mathbf{i}_{prism} = \sqrt{2}\mathbf{i}_{air}$. Ultimately, the image spot on the prism $\mathbf{i}_{prism}$ is mapped to an image formed at the detector, $\mathbf{i}_{det}$. The size of $\mathbf{i}_{det}$ is equal to the size of the image in air $\mathbf{i}_{air}$ irrespective of the presence of the IRE. The net effect is that the image formed on the detector is compressed along one direction by a factor

$1/\sqrt{2}$. (This was shown already in Chapter 6.) Finally, careful inspection of Fig. A.4b reveals that the two beams do not both focus on the principal reflecting plane of the IRE; the red beam comes to a focus there but the blue beam focuses some distance below the principal reflecting plane. The implication is that image quality deteriorates rapidly toward the edge of an image.

Figure A.4a through c demonstrate the image compression along the optical axis by following two beampaths which impinge on the crystal at different positions in the $y-z$ plane. We can also consider a top view, as shown in Fig. A.4d, where two beams impinge at different spots in the $x-z$ plane. Put another way, the two beams illuminate the IRE at the same height but at different points along the face of the prism. Once again, the dotted lines indicate the beampaths without the crystal in place while the solid path indicates the beampaths with the crystal present. Although the focal positions of the two beams is different in air and Si (a consequence of the dissimilar refractive indices of the two media) there is no change in the distance δx between the two foci. Therefore, the lateral dimension of the image along the x-axis is unchanged in Si, and there is no additional magnification imparted by the Si IRE.

A.3.3 Summary of the Differences between Macro- and Micro-ATR

Micro-ATR provides high spatial resolution over a small field-of-view. High spatial resolution is a result of both the high refractive index of Si and the very high collection angles which are possible when working with hemispherical lenses. In contrast, Macro-ATR provides poorer spatial resolution due to lower collection angles.

The relative magnification factors (and therefore field-of-view) are direct consequences of the IRE used. We saw that in Micro-ATR, the spherical geometry of the hemisphere resulted in a focusing effect toward the origin of the crystal, shrinking the size of the focused beamspot by a factor of n. This is the basis of the additional magnification factor of Micro-ATR, and can be considered a unique consequence of the aplanatic points of a hemispherical lens. In contrast, Macro-ATR provides no additional magnification because there are no special points in a hemisphere. In fact, we saw that because the focused beamspot is project longitudinally along the IRE's principal reflecting plane, the image at the detector is actually compressed by a factor related to the AOI used.

A.4 Magnification in This Thesis

In Chapter 3, optical simulations demonstrated that the hemisphere acted to shrink the focused beamspot by a factor equal to the refractive index. Later, ATR images of microfluidics presented in Chapter 6 showed that there was no additional magnification provided by the microgrooved IRE. This was unexpected at the time, as I naively expected that both Si IREs should provide magnification due to their high refractive index. However, the discussion above shows that although spatial resolution is certainly improved by the high refractive index, additional magnification is imparted by the lens geometry, not by the refractive index *per se*. In summary, the results in this thesis are fully consistent with the literature on Micro- and Macro-ATR.